River Rapids

Conference Proceedings of the Society for Experimental Mechanics Series

Dynamic Evironments and Durability Testing, Volume 7

Dagny Beale
Cora Taylor
Shannon Danforth

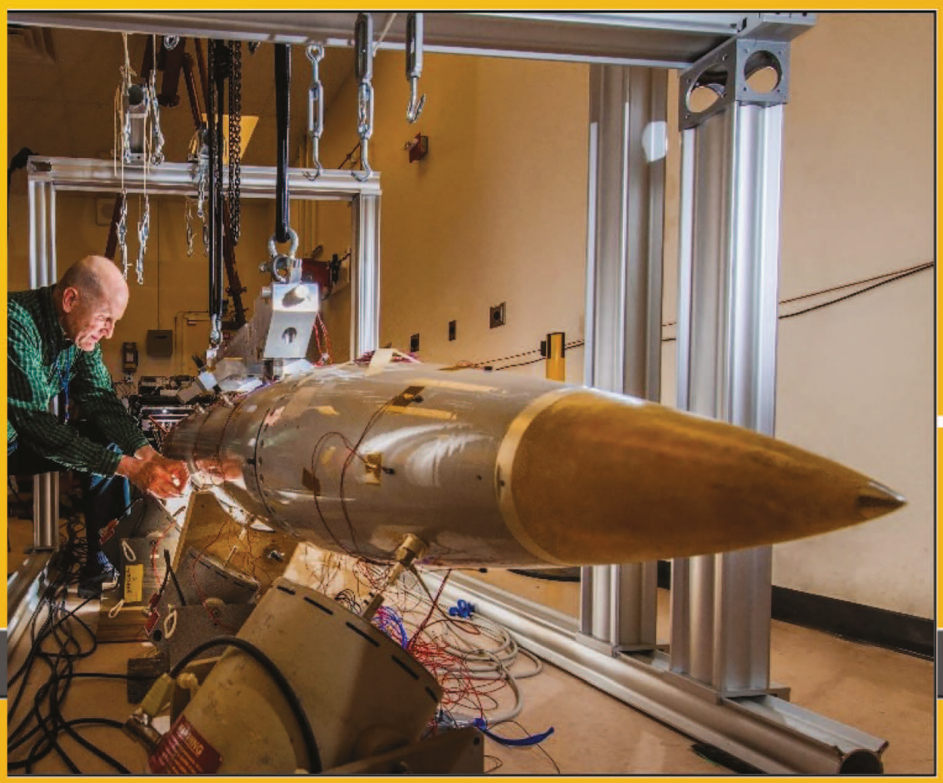

Proceedings of the 44th IMAC, A Conference and Exposition on Structural Dynamics 2026

River Publishers

Conference Proceedings of the Society for Experimental Mechanics Series

Series Editor

Kristin B. Zimmerman
Society for Experimental Mechanics, Inc.,
Bethel, USA

The Conference Proceedings of the Society for Experimental Mechanics Series presents early findings and case studies from a wide range of fundamental and applied work across the broad range of fields that comprise Experimental Mechanics. Series volumes follow the principle tracks or focus topics featured in each of the Society's two annual conferences: IMAC, A Conference and Exposition on Structural Dynamics, and the Society's Annual Conference & Exposition and will address critical areas of interest to researchers and design engineers working in all areas of Structural Dynamics, Solid Mechanics and Materials Research.

Dagny Beale · Cora Taylor · Shannon Danforth
Editors

Dynamic Evironments and Durability Testing, 2026, Vol. 7

Proceedings of the 44th IMAC, A Conference and Exposition on Structural Dynamics 2026



River Publishers

Published, sold and distributed by:

River Publishers
Broagervej 10
9260 Gistrup
Denmark

www.riverpublishers.com

ISBN 97887-438-1446-7 (Hardback)

ISBN 97887-438-1418-4 (eBook)

https://doi.org/10.13052/rp-9788743814184

Conference Proceedings of the Society for Experimental Mechanics

An imprint of River Publishers

© The Society for Experimental Mechanics, Inc. 2026

This work is subject to copyright. All rights are solely and exclusively licensed by the Publisher, whether the whole or part of the material is concerned, specifically the rights of translation, reprinting, reuse of illustrations, recitation, broadcasting, or reproduction in any other physical way, and transmission or information storage and retrieval, electronic adaptation, computer software, or by similar or dissimilar methodology now known or hereafter developed.

The use of general descriptive names, registered names, trademarks, service marks, etc. in this publication does not imply, even in the absence of a specific statement, that such names are exempt from the relevant protective laws and regulations and therefore free for general use. The publisher, the authors, and the editors are safe to assume that the advice and information in this book are believed to be true and accurate at the date of publication. Neither the publisher nor the authors or the editors give a warranty, expressed or implied, with respect to the material contained herein or for any errors or omissions that may have been made. The publisher remains neutral with regard to jurisdictional claims in published maps and institutional affiliations.

Preface

Dynamic Environments and Durability Testing represents one of ten volumes of technical papers presented at the 44th IMAC, A Conference and Exposition on Structural Dynamics, organized by the Society for Experimental Mechanics, and held January 19-22, 2026. The full proceedings also include volumes on Nonlinear Structures & Systems; Dynamic Substructuring & Transfer Path Analysis; Model Validation and Uncertainty Quantification; Dynamic Substructuring & Transfer Path Analysis; Special Topics & Experimental Techniques in Structural Dynamics; Computer Vision & SLDV for Structural Dynamics; Topics in Modal Analysis & Parameter Identification in Structural Dynamics; Data Science in Engineering; and Structural Health Monitoring, Metamaterials, Metastructures & Additive Manufacturing and Dynamics of Biomedical and Bioinspired Systems.

Each collection presents early findings from experimental and computational investigations on an important area within Dynamic Environments and Durability Testing & other Structural Dynamics areas.

The organizers would like to thank the authors, presenters, session organizers, and session chairs for their participation in this track.

Editors:

Dagny Beale – Sandia National Laboratories, NM, USA;
Cora Taylor – Michigan Technological University, MI, USA;
Shannon Danforth – Los Alamos National Laboratories, NM, USA

Contents

1 Application of the Impedance Matched Multi-Axis Testing Theme of Smart Dynamic Testing 1
Michael T. Hale, William A. Barber, and Jacob A. Davis

2 Combined Electromagnetic and Piezoelectric Shaker System for High Frequency Environment Testing 13
Jacob Cox, McKaelin Edralin, Matthew S. Allen, Michael Denison, Troy J. Skousen, and Washington De Lima

3 Investigating Three-Axis Shock and Vibration with a "Supplemental Shaker" Frame 35
R. Krieghbaum and S. M. Danforth

4 Smart Dynamic Testing of Aero Engine Externals: Challenges and Directions 51
Simon Euler, Ibrahim Sever, and Bernd Beirow

5 Correlating Damage in Vibration Environments Using Fixed-Base Modal Responses 59
Marcus Behling, Matthew S. Allen, Randy Mayes, and Washington DeLima

6 A Multivariate Specification Development Approach Using Principal Component Analysis 69
Colin M. Haynes and Sean T. Kelly

7 NASA Armstrong's Thermal Vibration Test System (TVTS) Pathfinder Capability 75
Jessica J. De la Cruz, Keerti K. Bhamidipati, Chris B. Kostyk, Jackson T. Winter, Natalie D. Spivey, Phillip C. Nguyen, and Samson S. Truong

8 A Recommended Procedure and Best Practices for MIMO Vibration Testing 95
Ryan Schultz and Steven Carter

9 Test-to-Failure Characterization and Acceleration Signal Feature Analysis of Electronic Systems Under Repeated Shock Loading 109
Trotter Roberts, Hugo Luck, Joud N. Satme, Mohsen Gol Zardian, Sina Navidi, Ryan Yount, Austin R.J. Downey, and Chao Hu

10 Structural Response Characterization under Multi-Axis Excitation via Video Motion Magnification 119
Davide Mastrodicasa, Alberto Garcia de Miguel, Andrea Cavagnolo, Ruben Araujo, Umberto Musella, Emilio di Lorenzo, and Enrico Zappino

11 Shaker Testing of a Fuel Cell Stack: Modal Survey, FE Model Updating, and Fixture Coupling Neutralization 125
Giancarlo Kosova, Vittoria D'Alessio, Emilio Di Lorenzo, Lorenzo Dozio, Simone Gallas, Hervé Denayer, Giovanni Fasulo, Mattia Barbarino, and Oskar Ekblad

Chapter 1
Application of the Impedance Matched Multi-Axis Testing Theme of Smart Dynamic Testing

Michael T. Hale, William A. Barber, and Jacob A. Davis

Abstract Execution of vibration testing without imparting major impedance mismatches between the field and laboratory test environments has long been a challenge in the dynamic test community. The historic technique of designing vibration fixtures such that the first mode is beyond the maximum frequency of the test is based on the false premise that the vibration levels imparted to the unit under test (UUT) are uniform at all input points. Testing in a serial single degree-of-freedom (SDOF), further diverges the classical laboratory test from the true nature of the multiple degree-of-freedom (MDOF) tactical field environment. The use of a stiff cradle fixture to address captive carry or free-flight environments of a missile system is a prime example of a test configuration that severely restricts the UUT's natural modal characteristics, and the resulting mechanical impedance has no correlation to the field conditions. The Impedance Matched Multi-Axis Testing (IMMAT) theme of Smart Dynamic Testing (SDT), aims to provide a reasonable representation of the global vibration response of operating environments such as those that are aerodynamic or acoustic in nature (e.g., captive carriage, free-flight vibration). This paper will discuss IMMAT and associated SDT themes and illustrate the concepts through a laboratory-based application on a dynamically accurate missile surrogate using a reconfigurable test stand.

Keywords Dynamic · Impedance · Multi-shaker · Modal · Test

Background

The traditional approach of the use of rigid fixturing attached to a high impedance SDOF shaker for replicating aerodynamic environments in the laboratory is known to be poor. This has been recognized by dynamicist and test engineers for many years; however, in the early years of dynamic testing there were test equipment limitations that restricted testing options [1]. In recent years, significant advances have been made in instrumentation, test hardware and control systems that have opened the possibilities for more advanced test approaches. Daborn, Ind and Ewins proposed implementation of multiple small exciters to conduct MDOF testing on a freely suspended structure [2]. Roberts and Ewins focused further on the concepts of impedance matching and MDOF testing, demonstrating significant improvements over traditional SDOF approaches [3]. The early work with the use of multiple small shakers and impedance optimization by Daborn, Ind, Roberts and Ewings led to the term Impedance Matched Multi-Axis Testing (IMMAT). Daborn used the phrase "Smarter Dynamic Testing" in his dissertation [4].

Professor David Ewins was a champion of the work referenced above, and he worked tirelessly with the dynamic test community in an effort to formalize the approach [5]. A Workshop and informal Community of Practice (CoP) was

Michael T. Hale
Trideum Corporation, 675 Discovery Dr NW Suite 300, Huntsville, AL 35806
e-mail: mhale@trideum.co

William A. Barber
AI Signal Research, Inc., 201 Nichols Dr SW Suite 300, Huntsville, AL 35802
e-mail: bbarber@aisignal.com

Jacob A. Davis
Redstone Test Center, Bldg. 7856, Redstone Arsenal, AL 35898
e-mail: jacob.a.davis91.civ@army.mil

© The Author(s), under exclusive license to River Publishers 2026

Kristin B. Zimmerman, PhD (eds.), *Dynamic Evironments and Durability Testing, 2026, Vol. 7*, Conference Proceedings of the Society for Experimental Mechanics Series, https://doi.org/10.13052/rp-9788743814184

established in 2018 and the term "Smart Dynamic Testing" (SDT) was adopted. Understanding the risks of unrealistic laboratory conditions and opportunities to merge test and analysis was recognized by all participants as keys to future test planning and development [6].

During the 2018 Workshop, the underlying technologies that form the basis of SDT were discussed, and these were presented as 4 themes which provide a well-defined structure for future development of new testing techniques and of their eventual documentation and reference. The Technology Themes identified were:

I. Test Specification: Environmental capture and definition.
II. Boundary Conditions and Fixture Design.
III. Excitation Strategy (IMMAT).
IV. Test Optimization and Integration

While engineering associated with each of the four themes is common, developing a more synergetic test approach integrating across all themes is the objective of SDT.

The Redstone Test Center's (RTC) Dynamic Test Division has the primary mission of providing vibration, acoustics, mechanical shock and pyrotechnic shock testing for the US Army and DoD at large. The lab has a wide range of traditional electrodynamic and servo hydraulic excitation systems in both SDOF and MDOF configurations. In recent years RTC and other Dynamic Test facilities have begun to integrate SDT concepts into the test paradigm. The presented example is intended to illustrate a typical SDT approach as related to captive carriage of a typical fixed wing aircraft store.

The example UUT, as illustrated in Figure 1, is characteristic of a typical aircraft store for which captive carry vibration testing will be included as part of the qualification program. Due to the sensitivity of the test payload, detailed pictures and specific engineering units were not included in this document.



Fig. 1 Five Shaker IMMAT Setup

SDT theme I (Test specification)

For the example UUT, the objectives were to conduct captive carry buffet and non-buffet vibration tests. Ideally, the product of Theme I, will be a fully populated Spectral Density Matrix (SDM) based on field measurements that would serve as the test reference criteria. Auto Spectral Density (ASD) reference criteria in each of the three mutually orthogonal directions were provided at six locations along the length of the test item. Unfortunately, and is often the case, Cross-Spectral Density (CSD) profiles were not provided. The alternate approach is to utilize the modal characteristics in the test configuration to compute a CSD. In these scenarios, reproducing all 18 ASDs within traditional MIL-STD-810 tolerances is highly unlikely and success depends greatly on the enveloping or averaging methods utilized in the original specification development.

SDT theme II (Boundary conditions and fixture design)

Mechanical Setup

It is acknowledged that the best impedance match to aircraft captive carry boundary conditions would consist of the UUT attached to an isolated launcher assembly with the isolation frequency tuned to the first bending mode of the aircraft wing. However, limitations of launcher availability often restrict this approach and require alternative levels of attachment to the vibration source. As discussed in Reference [1], each alternative comes with a level of compromise with respect to impedance, but some are certainly better than others. For example, the historically acceptable practice of conducting a vibration test by placing the UUT in a cradle fixture significantly influences the natural modal characteristics of the test article yielding structural responses with minimal correlation to that of the fielded configuration. Unfortunately, such practices continue today across the industry. Other techniques such as exciting the UUT with a single shaker stinger assembly at one end of the payload have limitations in that only the portion of the UUT nearest the drive point would come close to the desired reference criteria. The use of dual exciters for a single axis test with some level of rotational relief (e.g., stingers, radial bearings) at the attachment points has shown significant improvement for captive carry vibration especially when coupled with a launcher interface, but this approach is typically limited to a single translational axis of vibration and does not fully capture the effects of the coupled degrees of freedom. All the techniques described above employ large, fixed base high force exciters with large spatial footprints that are heavy and not practical to configure for multiple translational DOF excitation.

For the test example, a launcher was not available and the UUT was simply supported with elastic cordage. This setup is most representative of free-free boundary conditions, although analysis has shown that the captive carry boundary conditions are not significantly different from the free-free boundary conditions. It is acknowledged that this mechanical setup does not induce loads through the launcher interface, but this was not an objective of this particular test.

Test Fixtures

The collar fixtures that allowed connection of the stingers to the UUT were repurposed from previous dual shaker trials. Due to the relatively large mass of the collars (approximately 10 pounds each), the free-free modes of the UUT were reduced by approximately 5% as shown in Figures 2 & 3 and Table 3. While not ideal, they provide a rigid connection to the UUT across the bandwidth of interest and were considered sufficient for initial trials.

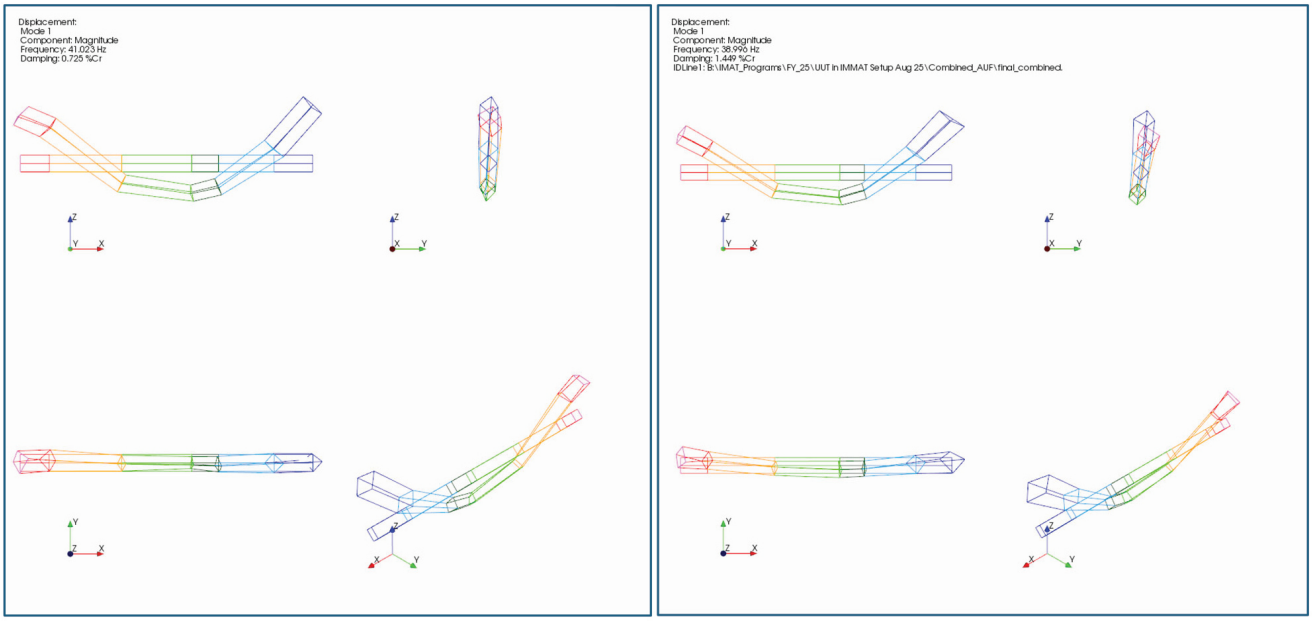

Fig. 2 Left: Free-Free: Mode 1. Right: Configured for IMMAT: Mode 1

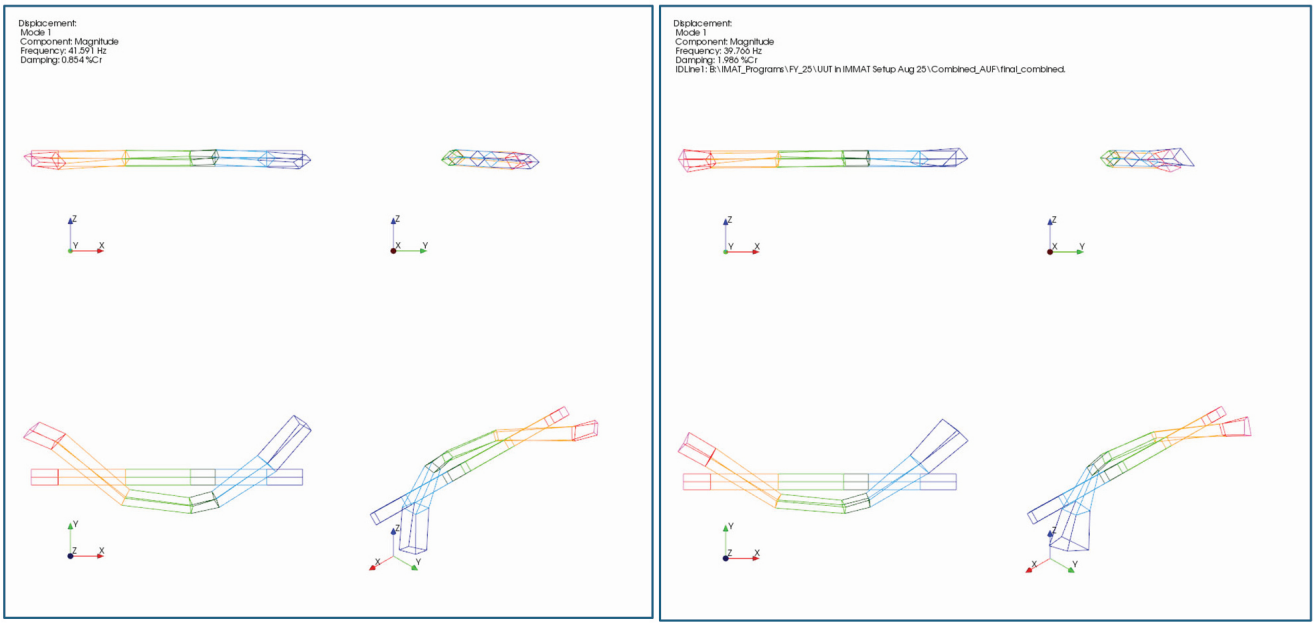

Fig. 3 Left: Free-Free: Mode 2. Right: Configured for IMMAT: Mode 2

SDT theme III (excitation strategy)

While SDT themes I, II, and IV are primarily analysis based, the Theme III Excitation Strategy requires infrastructure and test hardware. For replication of the captive carriage vibration environments, it is important to select an excitation strategy such as the IMMAT technique that provides distributed excitation while avoiding over-constraint of the test article's structural modes. With the inclusion of the IMMAT method in the pending release of MIL-STD-810J Method 527, it is important to understand the practical implementation and limitations associated with the IMMAT approach.

The RTC IMMAT infrastructure consists of eight electro-dynamic exciters and a reconfigurable framework from which the exciters could be mounted were integrated into an existing test facility. The random force ratings of the original suite of shakers range from approximately 120 to 500 lbf rms. The shaker displacements vary from ± 0.25 inch to ± 0.5 inch. Figure 1 illustrates the reconfigurable IMMAT platform in the five-shaker arrangement used for this example.

Shaker Setup

An IMMAT test configuration appears to look very similar to a multiple exciter modal test, however, there is a significant difference in that the shakers will be required to impart significantly higher acceleration levels to the UUT. For this reason, the stinger attachment between the shaker and UUT will need to be more robust and still allow relative motion in DOFs other than the drive direction without damaging the shaker itself and minimizing the effect on the overall mechanical impedance. This of course, is a premise of Theme II. The stingers employed for this example initially were a preloaded cable/strut design with an elastomer joint at each end that allows rotational and cross axis translational motion [7]. While these would have been sufficient for vibration up to 500 Hz, the losses between 500-2000 Hz required the struts to be replaced with solid threaded rods (5/8" diameter) to provide more efficient transfer of high frequency vibration into the UUT structure. Initial indications are that the threaded rods provide improved axial stiffness and sufficiently low rotational stiffness to protect the shaker armatures from side loading during test. Variations of the threaded rods, including reduction of the rod diameter, will continue to be assessed in an ongoing effort to maximize axial stiffness while minimizing rotational stiffness of connection.

Drive Points and Control Accelerometer Locations

A traditional right hand rule Cartesian coordinate system was used to define the motion degrees-of-freedom. The origin was considered to be the forward centerline tip of the UUT with +X assigned to the direction of flight and +Z upward. Triaxial accelerometers were placed along the length of the top of the UUT at the positions defined in Table 1.

Table 1 Accelerometer Locations

CH	Location	DOF	Type
1	1	+X	Control
2	1	+Y	Control
3	1	+Z	Control
4	2	+X	Control
5	2	+Y	Control
6	2	+Z	Control
7	3	+X	Control
8	3	+Y	Control
9	3	+Z	Control
10	4	+X	Control
11	4	+Y	Control
12	4	+Z	Control
13	5	+X	Measure
14	5	+Y	Measure
15	5	+Z	Measure
16	6	+X	Control
17	6	+Y	Control
18	6	+Z	Control
19	7	+X	Control
20	7	+Y	Control
21	7	+Z	Control

The accelerometer positions correlate directly to the positions from which field data was measured to develop the test reference profiles. For the initial trials, the drive points, as defined in Table 2, were selected to match the captive carry attachment points used in previous dual-shaker tests. Optimization of the drive points, a product of Theme IV, is planned for subsequent trials and will be discussed later in this document.

Table 2 Drive Point Locations

Drive	Location	DOF	Shaker Mdl
3	6	+X	V − 100
5	6	-Y	V − 300
6	4	-Y	V − 300
7	4	-Z	V − 350
8	6	-Z	V − 350

Strain Gage/Bending Moment Instrumentation

The use of tactically placed strain gage measurements during the field data acquisition phase of a test program is always highly recommended. The direct relationship between strain and fatigue and the ability to estimate moments imparted on the test item of interest can serve as key parameters in evaluating laboratory test fidelity. For the example UUT, strain gages were installed at six locations (three vertical and three lateral) and bending moment calibration was conducted by applying static loads to the structure at predetermined distance from the measurement points.

Formulation of the Spectral Density Matrix

As discussed for Theme I, ASD reference criteria in each of the three mutually orthogonal directions were provided at six locations along the length of the test item. Unfortunately, and is often the case, CSD profiles were not provided. Ideally, the product of Theme I, will be a fully populated SDM based on field measurements that would serve as the test reference criteria.

For the cases in which CSD terms are not provided, the approach outlined below is employed. It is essentially a minimum drive approach and is based on the assumption that the impedance match between field and laboratory is close and that the forcing function was uncorrelated between DOF's. The process below takes advantage of the Hermitian structure of the $n\ x\ n\ x\ d$ structure of the SDM, preserving the phase and scaling the magnitude as coherence squared.

Step I: Send a set of uncorrelated drive signals with a flat spectrum shape over the bandwidth of interest to each of the shakers and measure the drive and control point time histories.

Step II: Compute the following: Φ_{xx} (Cumulative Input Auto-Spectrum Estimate)
Φ_{yx} (Cumulative Cross-Spectrum Estimate)
H_{yx} (Transfer Function Estimate)

Step III: Compute $\Phi_{yy} = H_{yx}\Phi_{xx}H_{yx}^{*'}$

Step IV: Assign the spectral density matrix (SDM) as Φ_{yy} at each spectral line.

Step V: Compute normalized spectral density matrix (SDMn) by dividing each cross terms SDM(j,k) term at each spectral line d by $\sqrt{G_{jj}G_{kk}}$.

Step VI: Replace the diagonal (ASD) terms of SDMn with the Reference ASD terms for the test of interest.

Step VII: Convert SDMn back to SDM by multiplying each of the cross terms SDM(j,k) term by $\sqrt{G_{jj}G_{kk}}$ where the diagonal terms are now represented by the Auto-Spectrum of the desired Reference. This will yield the reference criteria for the test as a fully populated SDM.

Note that the cumulative (average) spectral estimates above will have errors associated with the number of averages taken, therefore estimates with 100 measurement DOF or more are recommended. Using the reference ASD's that were provided for each of the control points defined in Table 2 and the CSD development process outlined above, the natural coupling between DOFs will be preserved. Reference SDM's were established for the Buffet (10-500 Hz) and non-Buffet (10-2000 Hz) environments of interest. A frequency resolution of 1.25 Hz was selected for both cases. Multi-Shaker random testing was then conducted for each case. Time histories were captured during each trial run and processed posttest.

Trial Results

The results of the IMMAT trials are discussed in terms of three primary test objectives: 1) Modal Similarity, 2) Control of the Spectral Density Matrix, and 3) Bending Moment Characterization.

1) Modal Similarity

As a check to quantify the effects of the natural modal characteristics of the UUT while configured for the subject IMMAT test, a modal survey was conducted on the UUT in a free-free mode and again with the collar fixtures installed and attached to the freely suspended shakers as configured for the IMMAT test. Figures 2 & 3 illustrate the first bending modes of the highly symmetric UUT as computed for the free-free and the IMMAT configuration.

The Modal Assurance Criterion (MAC) matrix in Table 3 provides a comparison of the free-free modes to the modes of the UUT as configured for the IMMAT test. Observe that there is an approximate 5% reduction of the frequency of the first bending modes and an increase in estimated damping, both associated with the combination of the additional collar mass and attachment to the shakers. Very similar differences were also observed for the second and third bending modes.

2) Control of the Spectral Density Matrix

The initial 5-shaker IMMAT test configuration yielded strong similarities to the Buffet reference criteria across the 18 control channels of interest. Illustrating the SDM results for the 18-channel control scheme is difficult in the limited size of a traditional manuscript, so a reduced version illustrating only the dominant Z-Axis control channels is provided in Figure 4. The graphic takes advantage of the Hermitian nature of the SDM by plotting the ASD's down the diagonal with phase information on the lower triangular region and the associated coherence in the upper triangular region. The test yielded very similar results for the X and Y-Axis control channels as well.

Table 3 CMAC between free-free and IMMAT configured UUT

Cross-MAC Table											90 - 100
			Shapes (IMMAT)							Test	CRSS	50 - 89
			1	2	3	4	5	6	7			
MACtg	Shapes (free-free)		39.00	39.77	67.12	108.09	112.42	177.62	185.05	3%	All	0 - 49
100	1	41.02	96							99	99	
95	2	41.59		97						99	99	
90	3	68.69			93		38			96	98	
85	4	109.15				97				99	99	
80	5	114.89			43		97			98	99	
75	6	187.41						93		97	98	
70	7	197.40							95	97	98	
65	FEM	3%	99	99	96	99	98	97	97			
60	CRSS	All	99	99	98	99	99	98	98			

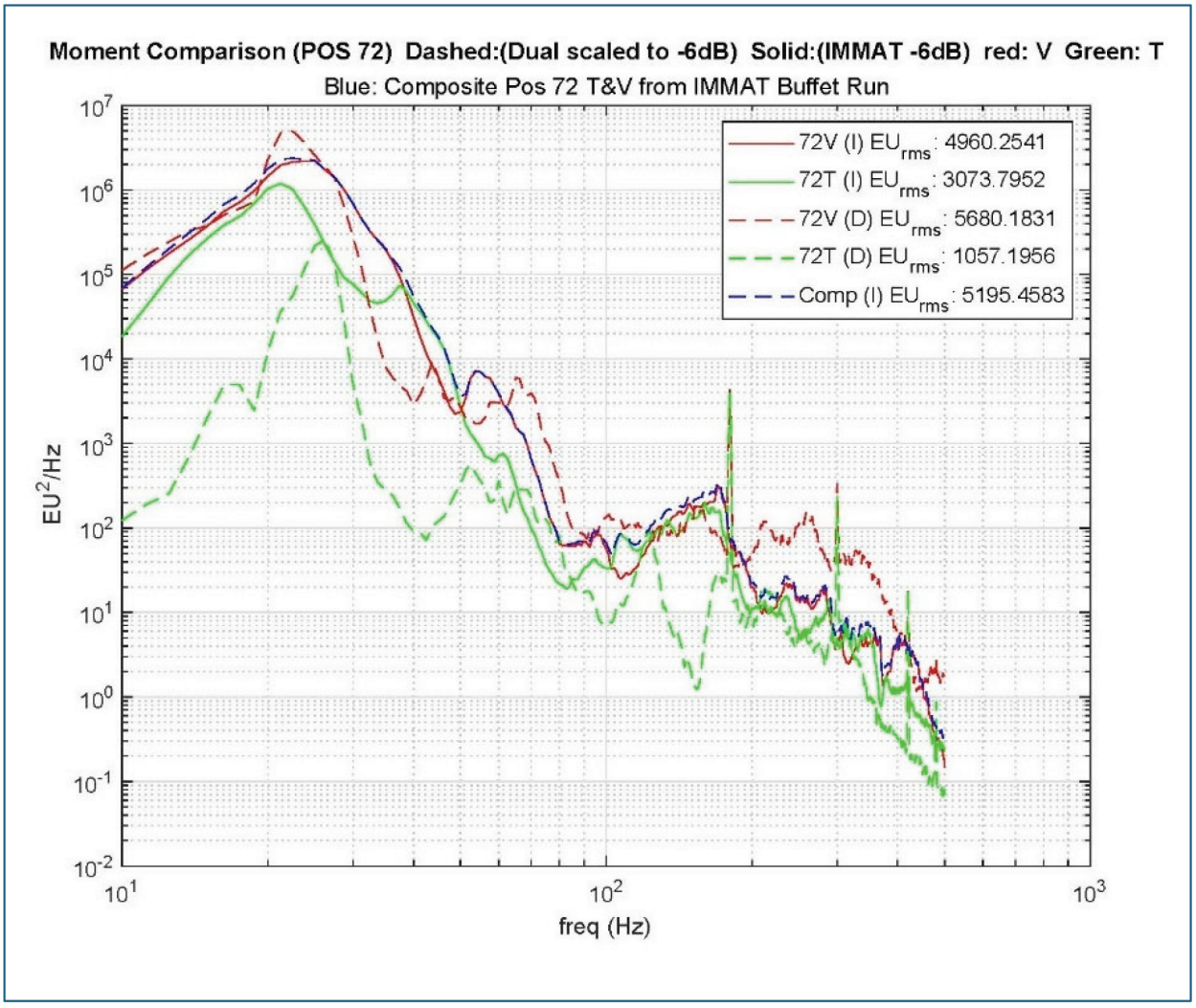

Fig. 4 SDM of the Z-Axis control channels. Red: Reference vs. Blue: IMMAT Trial

A compact review of the test results is shown in Figure 5 as a summation of the first five singular value ASD plots and the associated percentage of the total system response as provided in Table 4. The singular value ASDs are generated from taking a singular value decomposition of the full SDMs. This process is detailed in reference [8]. This compact view contains information from all the translational ASD's and associated CSD's. The associated singular vectors will contain estimates of the associated operational deflection shapes.

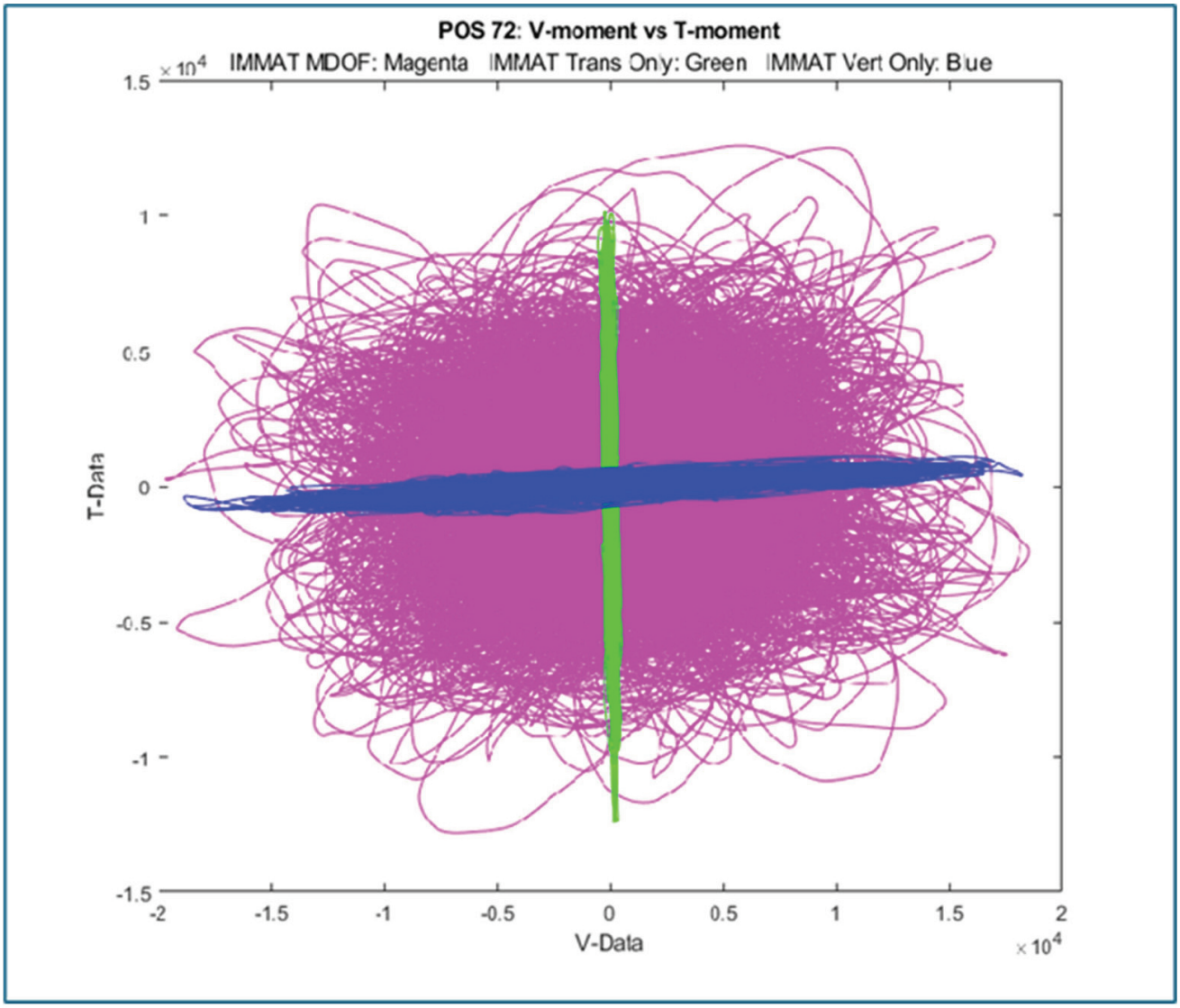

Fig. 5 Line by line sum of the five Singular Value ASD's (Left: Buffet Reference & Right: Non-Buffet)

Table 4 Tabular view of Laboratory test results relative to Reference Singular Value ASD RMS values

	Buffet		
	Lab2Ref (rms) %	**Ref2RefSum (rms) %**	**RunSum2RefSum (%)**
SV01	96.7	40.60	40.60
SV02	101	27.70	68.30
SV03	102	16.70	85.00
SV05	104	11.10	96.20
SV05	118	3.82	99.92

	Non-Buffet		
	Lab2Ref (rms) %	**Ref2RefSum (rms) %**	**RunSum2RefSum (%)**
SV01	71.60	40.60	40.60
SV02	67.70	25.40	66.00
SV03	66.30	16.10	82.10
SV05	63.50	11.40	93.50
SV05	67.90	6.50	100.00

The left-hand graphic in Figure 5 is associated with the Buffet vibration as was Figure 4. The right-hand graphic in Figure 5 is associated with the non-Buffet environment. Observe the wider test bandwidth and significantly different spectral shape of the non-Buffet reference. In the initial non-Buffet trials, it proved difficult to couple the higher frequency energy (> 1000 Hz) into the UUT with the initial shaker configuration as illustrated in the right-hand graph of Figure 5 and associated Table 4 results. The less-than-favorable results are also in part due to the specification variations between closely spaced control locations. This issue is typically an unintended artifact of the specification development process and may indicate a local response on the measurement vehicle that is not present in the test article (e.g., loose fins or internal components). In test, this requires some level of averaging or notching between the control locations which effectively reduces the overall similarity to the reference ASDs at these locations. The combination of difficulty in coupling the high frequency energy into the structure and the nature of the proposed reference criteria restricted the maximum attainable non-Buffet test level of the current test configuration to approximately -3 dB of the current reference criteria.

As vibration specifications are refined and models are developed for the example UUT, optimization studies will be conducted targeted at addressing the current deficiencies in addressing the higher frequency reference criteria of the non-Buffet environment.

3) Bending Moment Characterization

The bending moment test results presented below are based on the Buffet reference criteria since that is the scenario for which maximum bending moments are expected. For the subject UUT, as demonstrated above via modal analysis the key bending modes have been minimally affected by the test setup. Figure 6 illustrates measured moment comparisons between previous dual exciter vertical axis testing and the IMMAT trials. Observe that the shape of the moments induced by vertical axis motion and associated rms levels are comparable between previous dual shaker vertical trials in which the drive points correlated to the bomb rack attachment points, and the current 5-shaker IMMAT trials. Also observe that the IMMAT trials simultaneously yielded the moments induced by the transverse axis as well. The green dashed curve illustrates the cross-axis

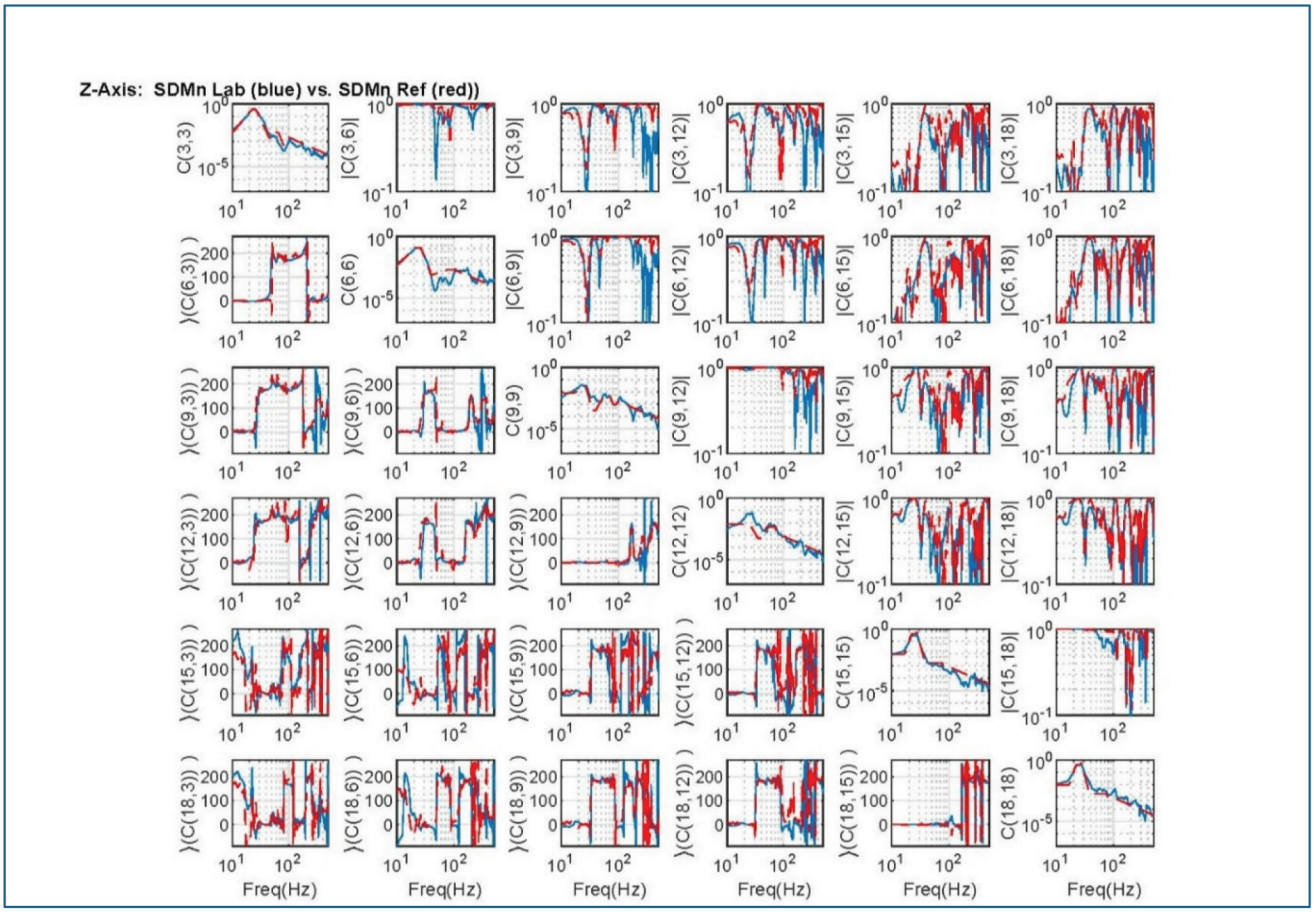

Fig. 6 Comparison of measured Moments between IMMAT and previous Z-axis only testing

moment measured during the vertical axis dual shaker trials. Note that the much smaller set of shakers employed in the IMMAT yield the expected bending moments.

Prior trials with the same UUT used in this example have been conducted with dual shakers to perform sequential axis vibration testing. Such trials have shown evidence of uneven joint wear associated with dwelling in a uniaxial state. Figure 7 illustrates through a scatter plot of bending moment time histories as measured during the 5-shaker IMMAT trial vs. exciting the structured in the Y and Z axes in a 1-DOF manner. While the peak bending moments in each axis are similar, observe the distribution of bending moment vectors that is clearly evident in the IMMAT approach, eliminating the aforementioned uneven wear issues associated with the 1-DOF approach.

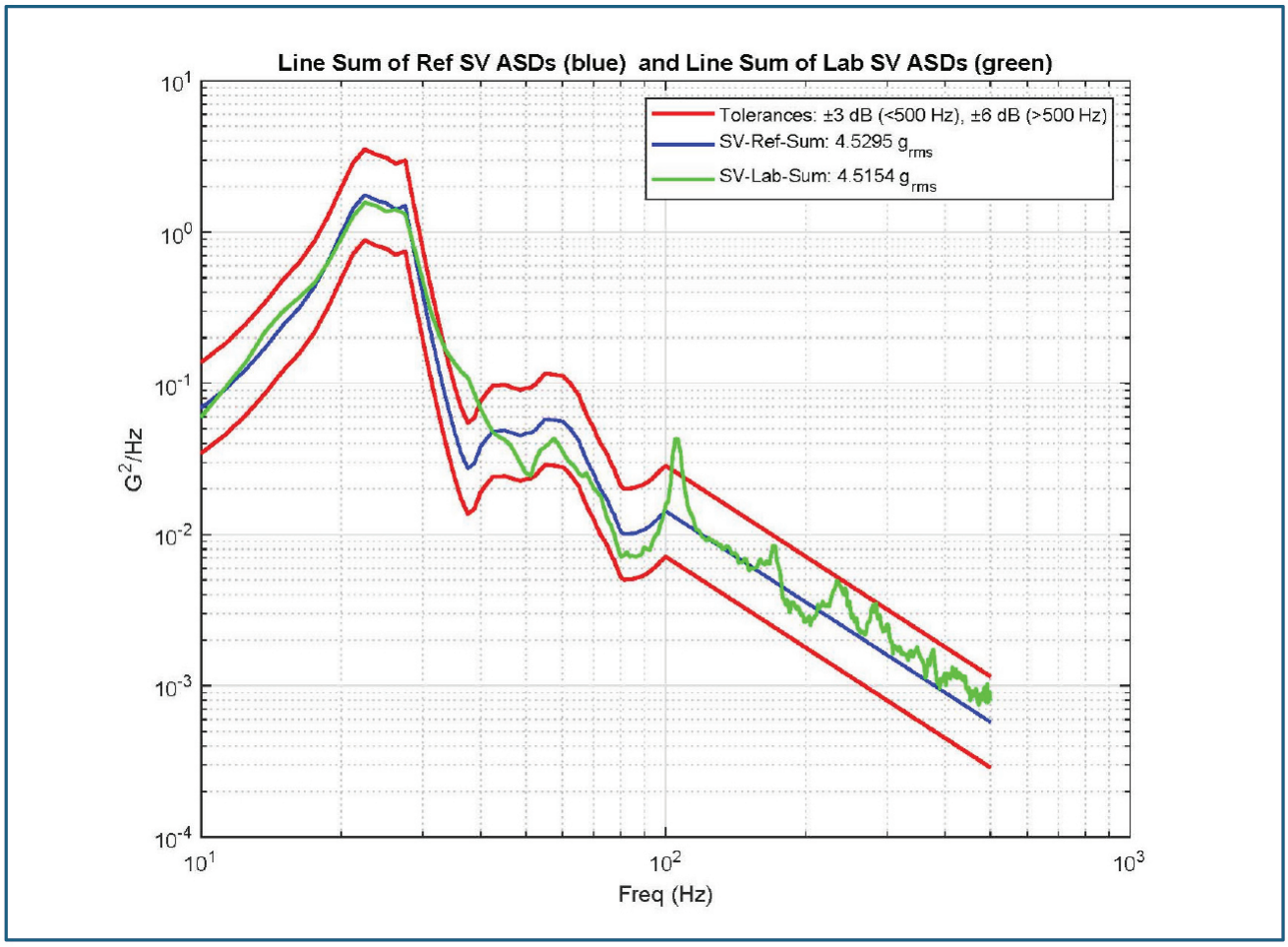

Fig. 7 Scatter of Moment Data Between IMMAT Approach and serial 1-DOF

Theme IV (Test Optimization and Integration)

The objectives of Theme IV are largely associated with identifying opportunities to improve the fidelity of the test by addressing gaps in the environment definition, test boundary conditions, and excitation strategy. Comprehensive analytical models that utilize modal characteristics of the system to identify optimal drive and control points have the potential to be valuable optimization tools but often require high fidelity models and a significant level of expertise. In the absence of validated finite element or other analytical models, iterative changes to the test setup and excitation strategy can help to improve correlation to the objective ASDs, but may also lead to costly mechanical changes that rely on engineering judgement as opposed to analytical assessments. As with many test scenarios, the tradeoff between analytical and iterative approaches is often dictated by cost and schedule constraints.

In the example presented, analytical models were not available to fully optimize the drive points into the UUT structure. Instead, initial attachments points were defined at locations corresponding to the launcher interfaces and the shaker sizes were initially based on engineering judgement. Several iterations in the stinger design were evaluated and some improvements were observed especially in the higher frequency transmissibility. Overall, satisfactory results were achieved with a reasonable number of iterations in the setup. However, deficiencies were identified that may require more substantial and costly changes (e.g., procurement of additional shakers) in order to achieve the defined higher level qualification environment(s). To address these deficiencies, analytical methods will be employed to mitigate the risk of ineffective solutions.

Conclusions

Clearly the implementation of the four themes of SDT takes considerable forethought. As demonstrated in the example employed in this document, it is still possible to conduct a quality IMMAT test without having all the desired information to fully address each of the four themes of SDT. Iterative approaches to test optimization are typical in the classical laboratory environment and expected to be so for IMMAT trials as well.

While initial trials have been limited to half-level vibration, the captive carriage example above yielded very favorable preliminary results for both the 10-500 Hz Buffet and the 10-2000 Hz non-Buffet vibration environments. Current projections are that both environments can be achieved up to approximately -3 dB, but some adjustments of the shaker configuration will be required to achieve full level. For both the buffet and non-buffet environments, spectral control in each axis at the six control points were in family with results from prior 1-DOF trials, but the ability to excite all axes simultaneously provides much more realistic loading of the UUT structure.

There are clear benefits that have been identified in the application of IMMAT testing techniques. As illustrated above in the Figure 7 discussion, issues such as uneven wear of joints associated with dwelling in a uniaxial state are avoided. While a properly planned IMMAT test allows the UUT to flex in a natural manner, it also yields the advantage of only requiring the test to be configured once and requires only one-third of the run-time as compared to traditional serial 1-DOF testing. This is very advantageous when dealing with a UUT that is being tested at temperature extremes with significant amount of instrumentation. IMMAT tests address the four themes of SDT well and allow rapid changes in setup to improve results.

Future Work

While the initial IMMAT trials discussed proved successful, there are still significant improvements possible that should yield additional fidelity. Specific planned improvements associated with the four SDT themes are as follows:

Theme I: Continue to highlight the need to develop IMMAT references that are highly correlated to the tactical deployment environment. Techniques such as significant sky lining of multiple events with dissimilar spectral characteristics should be avoided. To address such cases, multiple reference criteria are preferred and easy to implement once the test is configured.

Theme II: Design and integration of a lighter/reconfigurable collar assembly to provide greater flexibility in placement of shakers while minimizing added mass to the test setup. Design and integration of a stinger assembly with improved high frequency transmissibility characteristics is in progress.

Theme III: Integration of additional midsize shaker systems to address current test level limitations.

Theme IV: Build/acquire a FEM of the UUT and experiment with the use of ATA IMAT modal pre-test utilities to further optimize instrumentation and drive point selections [9].

Acknowledgments The authors wish to acknowledge the Redstone Test Center's Dynamic Test Division for their support of this research and the NASA Loads and Dynamics Technical Data team for their continued support of the concept of SDT through discussions across the industry at forums such as IMAC.

References

1. Gertel M (1962) Derivation of Shock and Vibration Tests Based on Measured Environments. The Shock and Vibration Bulletin 7: 25–33
2. P. R. Daborn and D. J. Ewins. “Replicating aerodynamic excitation in the laboratory.” *Proceedings of the 31st International Modal Analysis Conference*, Ca, 2013.
3. C. Roberts and D. J. Ewins. “Multi-Axis Vibration Testing of an Aerodynamically Excited Structure.” *Journal of Vibration and Control*, April 2016. doi: 10.1177/1077546316642064
4. Daborn, P.M.: Smarter dynamic testing of critical structures PhD Thesis, University of Bristol, Bristol (2014).
5. D. Ewins, “Exciting vibrations: the role of testing in an era of supercomputers and uncertainties”, DOI 10.1007/s11012-016-0576-y, Springer-link.com, 2016.
6. M. Allen, M. Hale, W. Barber, S. Herold, W. deLima, D. Maio, C Roberts. “Systematic Fixture Design to Address Deficiencies in Dynamic Environmental Testing”, https://mywikis-wiki-media.s3.us-central-1.wasabisys.com/sem/SDTCoP_WP2_v6.pdf
7. Etegent Technologies, https://etegent.com/contact/
8. Hale, M., Davis, J., Barber, W., Akers, J. “Use of Spectral Analysis of Singular Values as a Test Metric for IMMAT Trials”, SAVE Conference Proceedings 2024.
9. IMAT V8.5 [Computer software], ATA Engineering. https://www.ata-e.com/software/ata-software/imat/

Chapter 2
Combined Electromagnetic and Piezoelectric Shaker System for High Frequency Environment Testing

Jacob Cox, McKaelin Edralin, Matthew S. Allen*, Michael Denison, Troy J. Skousen, and Washington De Lima†

Abstract A prior work [1] showed that piezoelectric actuators could be combined with electrodynamic shakers to impart wideband random vibration input to a Device Under Test (DUT) up to 5kHz, while significantly reducing the drive voltages required for an electrodynamic shaker alone. The goal of such a system is to use electrodynamic shakers and piezoelectric actuators together for low and high frequencies respectively, where each is most effective. At the same time, the piezoelectric actuators provide additional inputs that may overcome the anti-resonances at the electrodynamic shaker head, where the nodes of a major mode reside in the single input system. This work builds on that effort, presenting the design and characterization of a general system that incorporates several piezoelectric actuators in series with a large electrodynamic shaker to impart a wider broadband input to a DUT. A model is presented which was used to facilitate the design. The model was calibrated by comparing measured and predicted transfer functions between the DUT accelerations and the actuator input voltages. Particular attention is given to the model for the piezoelectric actuator and amplifier. This is shown to be a limiting factor which depends on the number of actuators available and the current that the amplifiers can supply. Measurements are presented from the completed system with quantified capabilities.

Keywords Electrodynamic shaker · Piezoelectric actuator · Random vibration environment

Jacob Cox · McKaelin Edralin
Undergraduate Students, Brigham Young University, Department of Mechanical Engineering
e-mail: jgc53@byu.edu; bedralin@byu.edu

Matthew S. Allen
Professor, Brigham Young University, Department of Mechanical Engineering
e-mail: matt.allen@byu.edu

Michael Denison · Troy J. Skousen
Technical Staff, Sandia National Laboratories[1]
e-mail: mdeniso@sandia.gov; tjskous@sandia.gov

Washington De Lima
Honeywell Federal Manufacturing and Technologies[2]
e-mail: wdelima@kcnsc.doe.gov

*Sandia National Laboratories is a multi-mission laboratory managed and operated by National Technology & Engineering Solutions of Sandia, LLC (NTESS), a wholly owned subsidiary of Honeywell International Inc., for the U.S. Department of Energy's National Nuclear Security Administration (DOE/NNSA) under contract DE-NA0003525. This written work is authored by an employee of NTESS. The employee, not NTESS, owns the right, title and interest in and to the written work and is responsible for its contents. Any subjective views or opinions that might be expressed in the written work do not necessarily represent the views of the U.S. Government. The publisher acknowledges that the U.S. Government retains a non-exclusive, paid-up, irrevocable, world-wide license to publish or reproduce the published form of this written work or allow others to do so, for U.S. Government purposes. The DOE will provide public access to results of federally sponsored research in accordance with the DOE Public Access Plan.

†Honeywell Federal Manufacturing & Technologies, LLC operates the Kansas City National Security Campus for the United States Department of Energy / National Nuclear Security Administration under Contract Number DE-NA0002839. **NSC-614-7407 08/2025 Unclassified Unlimited Release**

© The Author(s), under exclusive license to River Publishers 2026

Kristin B. Zimmerman, PhD (eds.), *Dynamic Evironments and Durability Testing, 2026, Vol. 7*, Conference Proceedings of the Society for Experimental Mechanics Series, https://doi.org/10.13052/rp-9788743814184

Introduction

Mechanisms and electronics in rockets, aircraft, and automobiles are often subject to a high-vibration environment. To ensure the reliability and durability of these components, they are tested using electrodynamic shakers, which use an electromagnetic force to generate controlled vibrations. While current electrodynamic shakers are capable of producing large forces, they do have failure limits. One such limit is associated with high frequency resonances as studied in [2], that lead to mechanical failure of the shaker armature which in turn limits their frequency range to below about 2000 Hz. Attempting to exceed this frequency range can cause catastrophic failure, as shown in Figure 1, requiring expensive and project-delaying repair or maintenance. This limitation poses an issue because many mechanical and electrical components experience significant vibration environments up to 5000 Hz.



Fig. 1 Catastrophic failure due to an electrodynamic shaker being driven at a resonance in which the armature bends, leading to excessive stresses in the cylindrical part that is shown.

Romero et al. [3] seem to have been the first to combine piezoelectric actuators such as these with other systems to reproduce combined environments. This work builds on a recent study by Singh et al. [1], who demonstrated that piezoelectric actuators could be integrated with an electrodynamic shaker to enable testing from 2000 - 5000 Hz. In that work, the electrodynamic shaker was operated between 100-2000 Hz, with the piezoelectric actuators providing the forces needed from 2-5kHz, thus creating a high-frequency environment. Despite Singh's promising results, much remains to be understood regarding the best practices in designing and modeling practical piezo actuator configurations. Furthermore, we desired to create a system that was modular, with a plate where test articles could be mounted just as they are in conventional shaker systems.

During the 2023-2024 academic year, Sandia National Laboratories enlisted a team of undergraduate Mechanical Engineering students to create a modular system that combined a large shaker with a set of PPA40XL piezoelectric actuators, to enable regular environmental tests at high frequencies, using the approach envisioned by Singh et al. [1]. The system consisted of a base plate that interfaced with a 2000-lbf LDS V830–335 Shaker at BYU, but with a bolt pattern that would also be compatible with Unholtz-Dickie shakers at Sandia Labs. The system was to consist of a top plate with a standard bolt pattern, where a variety of test articles could be attached. The team completed the design, as detailed in this report, yet did not have time to resolve all of the issues with the modeling and testing of the system. Authors Cox and Allen subsequently completed testing and resolved issues with the modeling, and their findings are summarized here, as well as the design that was created and the analysis and considerations that led to the design.

Hence, this paper builds on the work of Singh et al. [1] by presenting the design of the piezo/electromagnetic shaker system that the students developed and presenting models that capture its axial dynamic behavior. Measurements from the completed system are provided, highlighting its capabilities, the accuracy of our models, and offering suggestions for future iterations on the MIMO test system.

Methods

System Design

The final design is shown in Figure 2. The five major components are more thoroughly detailed in Figures 2-4 and the descriptions that follow.

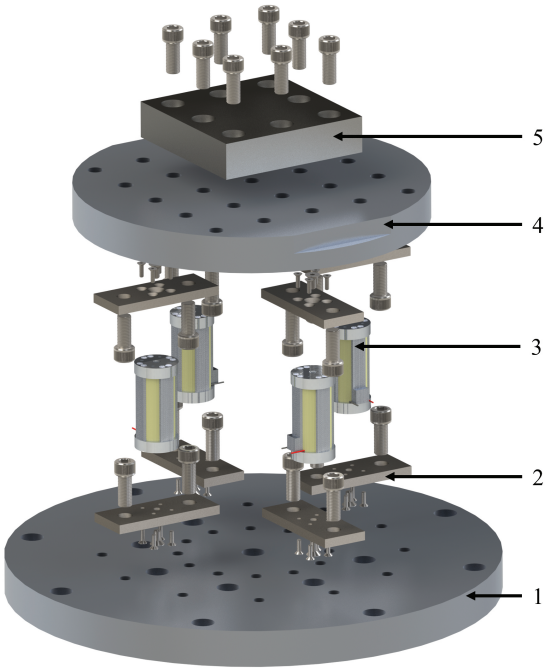

Fig. 2 Exploded CAD view of the piezo assembly with the following components: 1) base plate (designed to be mounted to the top of a large shaker), 2) mounting brackets, 3) PPA40XL piezoelectric actuator, 4) top plate, and 5) mass that simulates the loading of a DUT.

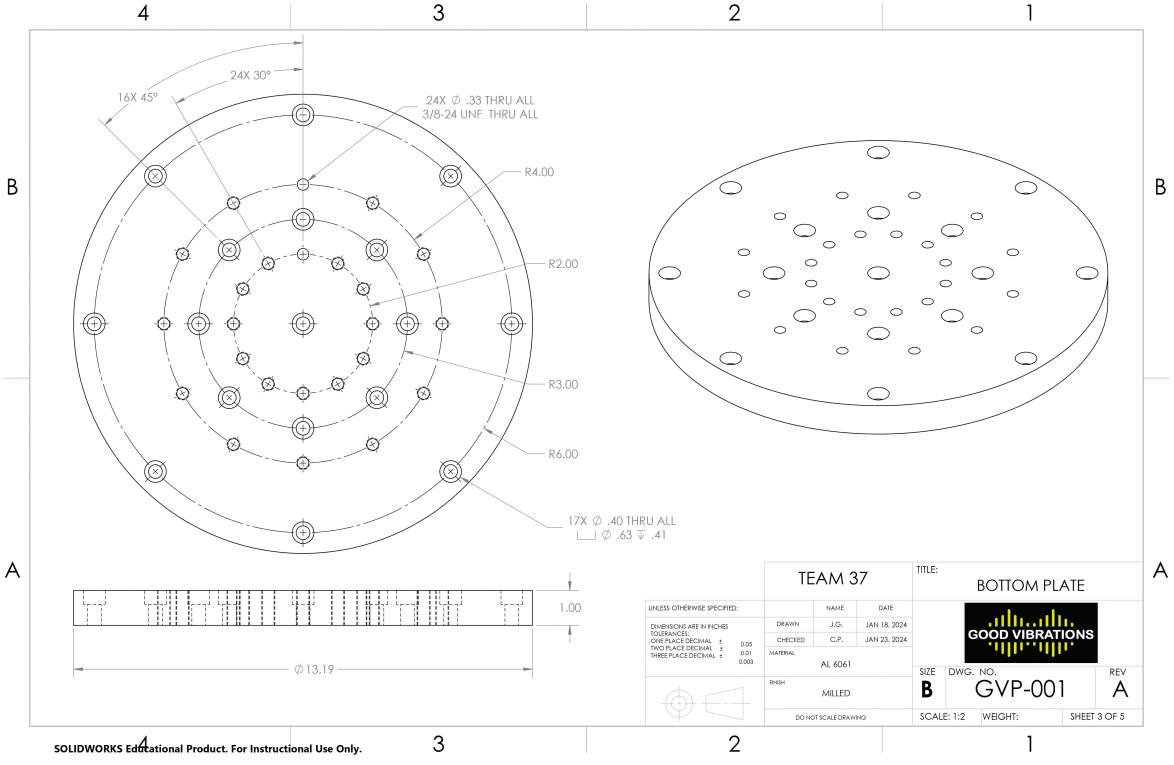

Fig. 3 Bottom plate part drawing. This design allows for a 2, 4, 6, and 8 piezo actuator configuration.

1. The base plate serves as the foundation of the system, connecting the electrodynamic shaker and piezoelectric actuators. The dimensions and hole layout can be seen in Figure 3. The plate features two hole patterns: one for connecting it to the electrodynamic shaker and the other for attaching the piezo actuator mounting brackets, as shown in Figures 2 and 4.

2. The mounting brackets secure the piezo actuators to the top and bottom plates and ensure they are level to prevent overstraining. According to the manufacturer, the piezo actuators are machined with a height tolerance of 200 μm. However, their maximum tensile strain is 15.5 μm. Hence, there was concern that they could exceed this strain when bolted into the assembly. To address this, the bracket design shown in Figure 4 allows shim stock to be used between each bracket and the top and bottom plate, so one can avoid over-straining when assembling the system. The mounting brackets were also precisely machined and sanded to within 2.5μm. (It should be noted that this design only works for a maximum of four piezo actuators because the edges would interfere if more piezo actuators were used. A modified mounting bracket was also designed that allows for more piezo actuators but was not used in this study. This modified design can be seen in Figure 24 in the Appendix.)

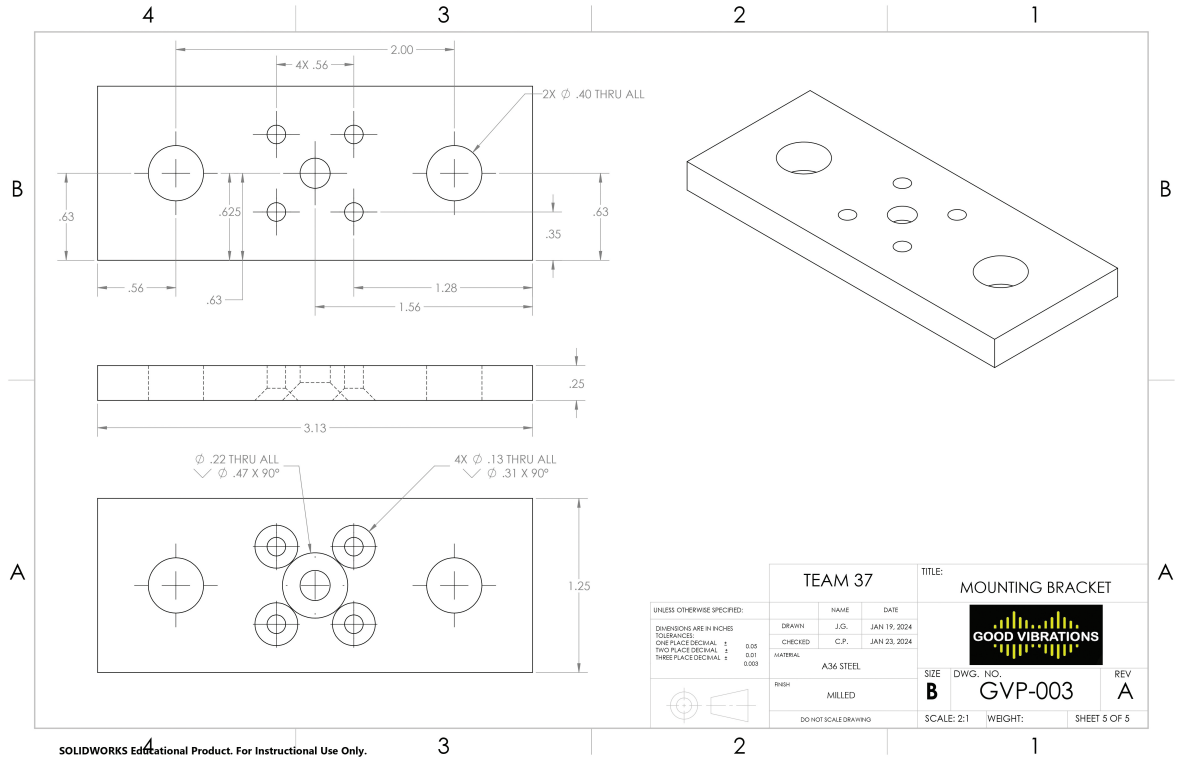

Fig. 4 Mounting bracket design used for four or fewer piezo actuators

3. The piezoelectric actuators utilized in this research were PPA40XL parallel pre-stressed actuators from Cedrat. Piezoelectric actuators convert an electrical signal into a displacement through the use of quartz crystals. In this system, the piezoelectric actuators exert a force between the EM shaker and the top plate to supplement that provided by the EM shaker.

4. The top plate interfaces with the mounting brackets and transfers forces to the DUT. A finite element model (FEM) was used to predict the modes of the plate in free-free conditions and are shown in Fig. 6. Most of the modes have nodes at the plate center, so they won't affect the displacement of a DUT mounted there. Hence, the focus was on maximizing the frequency of Mode 3 so as to minimize its influence on the DUT motion. Furthermore, when the piezos and top plate are mounted to the shaker, there is a mode in which the top plate bounces on the piezos. This reveals that a tradeoff exists. The plate should be small and thick to maximize the frequency of the flexible mode, and yet it should be as light as possible (and hence as thin as possible) to maximize the bounce mode frequency. Ultimately, a 9.5 × 1-inch plate was chosen to balance these competing objectives. However, as will be seen later, the final results suggest that more should have been done to minimize the mass of the top plate.

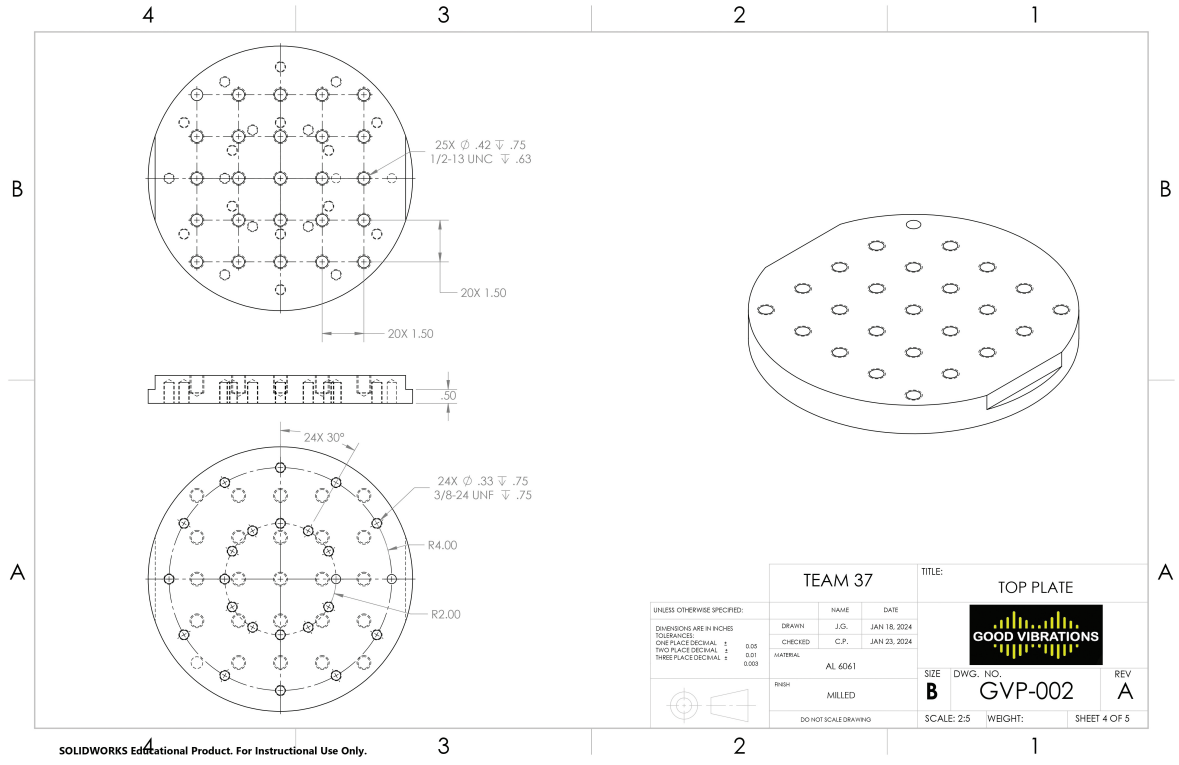

Fig. 5 Top plate part drawing

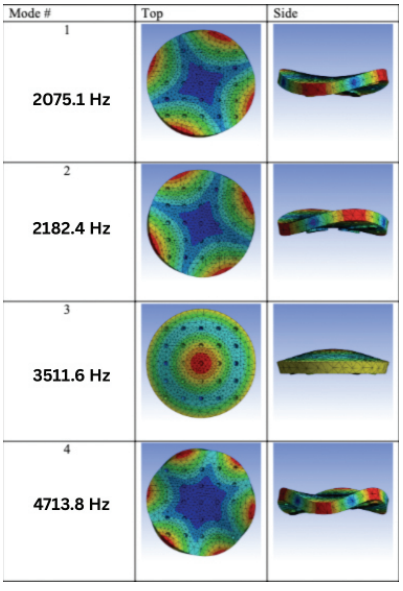

Fig. 6 Modes of the Top Plate as predicted by FEM

5. The DUT is the mechanical or electrical device subjected to testing. For this research, the DUT is a rigid block of aluminum that has similar mass and stiffness to a typical DUT. Unfortunately, time constraints did not allow the system to be tested with the DUT attached, so all results presented in this paper are for the system with a bare top plate.

Many components of the piezo assembly are costly. To ensure that the piezo assembly would not break, could survive repeated use, and would meet desired performance metrics, a discrete mass model was created that predicts the dynamic behavior of the system in the axial direction. Using this model, two major failure criteria were analyzed, the voltage and strain limits of the piezo actuators. Later, the current limit of our amplifier was found to be a limiting factor and was added to this analysis.

Once the system was assembled these models were evaluated against experimental measurements. The models were then tuned using experimental data. Using these updated models, we hope to more confidently predict the behavior of other design variations. Therefore, in the following sections, results are presented for both the initial and updated models.

Discrete Mass Model: MATLAB

A discrete spring-mass model of the system was created to size the actuators and obtain preliminary performance estimates. Simulations of this model were implemented in a MATLAB script. The system was modeled as a 3DOF system, shown in Figure 7. Two masses represent the EM shaker and capture its first axial mode, while the other mass represents the top plate and DUT, both of which sit on top of the piezo actuators.

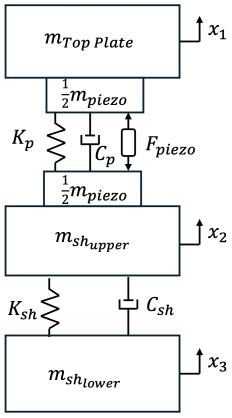

Fig. 7 3DOF model of the shaker assembly. The top mass represents the top plate, with K_p the total equivalent spring constant of all four piezo actuators, C_p the total equivalent damping coefficient, and m_{piezo} the mass of four piezos and required brackets. The shaker is modeled as a two DOF system, with the armature mass split between the upper mounting surface $m_{\text{sh,u}}$ and the lower portion $m_{\text{sh,l}}$. K_{sh} is the shaker stiffness and C_{sh} is the damping coefficient of the shaker.

Using this model, a mathematical model of the system was developed as follows:

$$\mathbf{M}\ddot{\mathbf{x}} + \mathbf{C}\dot{\mathbf{x}} + \mathbf{K}\mathbf{x} = \mathbf{F} \tag{1}$$

where $\mathbf{x} = [x_1, x_2, x_3]^{\mathrm{T}}$ are the displacements of the masses shown in Figure 7.

$$\mathbf{M} = \begin{bmatrix} m_{\text{Top Plate}} + \frac{1}{2}m_{\text{piezo}} + m_{\text{payload}} & 0 & 0 \\ 0 & m_{\text{sh,u}} + \frac{1}{2}m_{\text{piezo}} & 0 \\ 0 & 0 & m_{\text{sh,l}} \end{bmatrix}, \quad \mathbf{C} = \begin{bmatrix} C_p & -C_p & 0 \\ -C_p & C_p + C_{\text{sh}} & -C_{\text{sh}} \\ 0 & -C_{\text{sh}} & C_{\text{sh}} \end{bmatrix}, \tag{2}$$

$$\mathbf{K} = \begin{bmatrix} K_p & -K_p & 0 \\ -K_p & K_p + K_{\text{sh}} & -K_{\text{sh}} \\ 0 & -K_{\text{sh}} & K_{\text{sh}} \end{bmatrix}, \quad \mathbf{F} = \begin{Bmatrix} F_{\text{piezo}} \\ -F_{\text{piezo}} \\ F_{\text{sh}} \end{Bmatrix}, \tag{3}$$

It is worth noting a deviation from the model presented by Singh et al. [1]. In their model, the shaker force was applied to the upper shaker mass. In contrast, our model applies the shaker force to the lower mass. This aligns with the functionality

of our electrodynamic shaker, where the applied force is generated by coils at the bottom of the armature. This approach was also found to better match the experimental behavior of our system, which is presented later.

The values of all of the constants used are listed in Table 1. Initially, values from Singh et al. [1] were used, supplemented by measured mass characteristics of the new system. However, damping and stiffness values were later tuned, matching the theoretical transfer functions to the experimental ones (see Sections and for additional information on experimental transfer function collection and tuning results).

Table 1 The parameters used in the 3DOF MATLAB model.

Parameter	Definition	Initial Method	Initial Value	Final Method	Final Value
m_{piezo}	Mass of piezo (kg)	Direct Meas.	0.195	Direct Meas.	0.195
m_b	Mass of Brackets (kg)	Direct Meas.	0.17	Direct Meas.	0.17
m_{sh}	Total mass of shaker armature (kg)	Shaker Spec.	12.83	Shaker Spec.	12.83
$m_{\text{sh,u}}$	Upper mass of shaker armature (kg)	Exper. Calib.	10.89	Exper. Calib.	10.89
$m_{\text{sh,l}}$	Lower mass of shaker armature (kg)	Exper. Calib.	1.94	Exper. Calib.	1.94
m_{TP}	mass of top plate (kg)	Direct Meas.	2.905	Direct Meas.	2.905
K_p	Piezo stiffness (N/m)	CEDRAT catalog	1.59e8	Exper. Calib.	3.66e7
C_p	Damping within the piezo (N*s/m)	CEDRAT catalog	90.74	Exper. Calib.	544.44
K_{sh}	Shaker armature stiffness (N/m)	Exper. Calib.	3e8	Exper. Calib.	2.97e8
C_{sh}	Damping within the shaker (N*s/m)	Modal Analysis	7.82e3	Exper. Calib.	1.56e2
m_{payload}	Mass of payload being driven (kg)	-	0	-	0
F_f	Force Factor (N/V)	CEDRAT catalog	186.7	Exper. Calib.	46.7

Once the mechanical system was defined, transfer functions relating the shaker and piezo input forces to the displacement of each mass were found as follows. Starting with Eq. (1), the force vector can be separated into components, resulting in Eq. (4).

$$\left[-\omega^2\mathbf{M} + i\omega\mathbf{C} + \mathbf{K}\right]\mathbf{X}(\omega) = F_{\text{sh}}(\omega)\begin{bmatrix}0\\0\\1\end{bmatrix} + F_{\text{piezo}}(\omega)\begin{bmatrix}1\\-1\\0\end{bmatrix} \tag{4}$$

Treating each force individually, the transfer functions become Eqs. (5) and (6), where the rows of $\mathbf{H}_{x,F_i}$ refer to the transfer functions from the input force to the displacement of: 1.) the top plate, 2.) the top of the EM shaker, and 3.) the bottom of the EM shaker, respectively.

$$\mathbf{H}_{x,F_{\text{sh}}}(\omega) = \left[-\omega^2\mathbf{M} + i\omega\mathbf{C} + \mathbf{K}\right]^{-1}\begin{bmatrix}0\\0\\1\end{bmatrix} \tag{5}$$

$$\mathbf{H}_{x,F_{\text{piezo}}}(\omega) = \left[-\omega^2\mathbf{M} + i\omega\mathbf{C} + \mathbf{K}\right]^{-1}\begin{bmatrix}1\\-1\\0\end{bmatrix} \tag{6}$$

The required forcing signal was then calculated using Eq. (7), where $a(\omega)$ represents the desired acceleration environment, and the transfer function H_{1,F_i} in the denominator is multiplied by $-\omega^2$ to convert the displacement transfer functions in Eqs. (5) and (6) from displacement to acceleration over force.

$$F_i(\omega) = \frac{a(\omega)}{-\omega^2 H_{1,F_i}(\omega)}, \quad \text{where } i = (\text{sh},\ \text{piezo}) \tag{7}$$

This was done for both the shaker and piezo input forces as if they were individually responsible for recreating the entire environment. Afterwards, the forcing signals were set to zero over certain frequency ranges so that the shaker was fully responsible for recreating the environment up to a cut-off frequency (typically 1700 Hz) and the Piezos provided the environment from the cut-on frequency (typically 500 to 1700 Hz) up to the maximum frequency (typically 5000 Hz). Then the forcing signals were multiplied by the displacement transfer functions to simulate the movements of each of the masses.

$$\mathbf{X}(\omega) = \mathbf{H}_{x,F_i}(\omega)F_i(\omega) \tag{8}$$

Piezo Voltage Limits

In addition to the mechanical system, the electronics also needed to be characterized in order to correctly size the actuators and predict failure. As in Singh [1], a linear force to voltage relationship was assumed and characterized by a force factor (F_f), as given in Eq. (9). Combining this relation with our forcing functions, the time domain voltage signal for any acceleration environment could be calculated and compared to the voltage limits of the piezo actuators.

$$V_{piezo} = F_{piezo}\frac{V_{max}}{F_{max}} = \frac{F_{piezo}}{F_f} \tag{9}$$

The allowable voltage range for the piezo actuators is -20 to 150V. They are driven through an amplifier that increases the voltage by a factor of 20 with a DC bias so that the input to the amplifier can be centered at zero. With a DC bias of 65V, the maximum sinusoidal signal is 85V (or 85/20 = 4.25V at the output of the control software). To account for the DC bias and amplifier inaccuracies, the amplitude was limited to 75V in this study, which provided a 10V buffer.

Piezo Strain Limits

The manufacturer specifies the maximum tensile strain for the actuator to be 15.5 μm. The maximum compressive strain is not given, but the maximum resonant displacement is specified to be 27 μm peak-to-peak, so that the maximum vibration amplitude is approximately the same as the maximum tensile strain. They also state the maximum strain of the piezoelectric material is 0.12%, which would correspond to a total displacement of about 48 μm. The largest displacement that the piezo actuators can create is nominally 43 μm [6]. In operation, the displacement consists of the dynamic movement of the system during testing and a static displacement caused by the 65V DC bias. Hence, it seems that the system can survive 21.5 μm of displacement about the biased state.

In this work, the dynamic portion of the displacement was estimated by transferring the displacements obtained from Eq. (8) into the time domain and then taking the difference $(x_2 - x_1)$ to find the stretch in the piezos. The static portion (D_s) is calculated using the force factor and stiffness of the piezos as follows:

$$D_s = \frac{V_{bias}F_f}{K_p} \tag{10}$$

While some of this stretch may actually be taking place in the bolted bracket assembly, it is conservatively assumed that the stretch takes place entirely inside of the piezos.

Amplifier Current Limits

The electrical current capabilities of the amplifier provide another limitation. In this research, two amplifiers were utilized, each capable of outputting 6.8A, which was found to limit the maximum frequency and displacement amplitude the actuators could achieve. The piezo actuator expansion is dependent on the speed with which the amplifier can fill the capacitance of the quartz. At 0V and room temperature, the capacitance of an individual actuator is reported as c = 17 μF. For our modeling, the capacitance was multiplied by a factor to account for temperature and voltage effects per the recommendations found here [4]. These effects seem consistent with those mentioned in Sherrit et al. [5], yet the authors were not able to find any literature that reported actual data as was available on [4]. In this work, a factor of 1.4 was selected, based roughly on our maximum voltage amplitude and operation at room temperature.

Using the fundamental equation for current through a capacitor,

$$I = c\frac{dV}{dt} \tag{11}$$

The frequency domain current signal can then be calculated from the voltage signal and then converted to the time domain using an inverse Fourier transform. The amplifier current was found to be the strongest limiting factor for shaker performance. Consequently, two analyses were performed to better understand the effects of exceeding our current limits. First, the amplifier limits were quantified by considering sinusoidal inputs at various frequencies. While each piezo actuator could be driven by a separate amplifier, in this work, only two amplifiers were available and so each amplifier drove two piezo actuators. Given the limits on I (two amplifiers) and c (four piezos with 17 μF each and a temperature factor of 1.4), the maximum value of the derivative $\frac{dv}{dt}$ = 13.6 A / 95.2 μF = 142857 $\frac{V}{s}$. The value of $\frac{dv}{dt}$ that is needed depends on frequency. If we desired to supply a sinusoidal voltage to the piezo actuators at a voltage amplitude of V_p, i.e.

$$V(t) = V_p \sin(\omega t) \tag{12}$$

then the derivative would be

$$\frac{dV}{dt} = V_p \omega \cos(\omega t) \tag{13}$$

and its maximum value is $V_p\omega$. Hence, when $V_p = 75$ V the highest frequency at which the amplifier can achieve the required $\frac{dV}{dt}$ is 303.2 Hz. Conversely, the voltage amplitude V_p would have to be limited to reach the desired peak frequency of 5 kHz. The largest input voltage at 5 kHz is thus found to be 4.55 V.

To verify these calculations, tests were performed in which a sinusoidal input was supplied to the amplifier with two piezo actuators connected to each channel and the voltage out of the amplifier was recorded and is shown in Figure 8. When a low voltage was used, for example, the curves labeled 50 mV (the entries in the legend are the voltage amplitude sent to the amplifier), the output is 0.91 V (1 V expected) whether the frequency is 2 kHz or 5 kHz. As the input voltage increases to 200 or 250 mV the output from the amplifier scales nearly as expected to 3.42 V (4 V expected) and 4 V (5 V expected) when the frequency is 2 kHz. Both of these are within the 11.37 V limit computed using the equations above. Specifically,

$$\frac{dV}{dt} = 142857 \frac{\text{V}}{\text{s}} = 11.37 \frac{\text{V}}{\text{Channel}} \times (2000 \times 2\pi) \frac{\text{rad}}{\text{s}} \tag{14}$$

In contrast, when the frequency is increased to 5 kHz, the output from the amplifier distorts noticeably and the voltage amplitude is only 3.18 V when 5 V were expected. The peak voltage computed for the amplifier for this case, using Eq. (13) is 4.55 V, which is about 40% higher than the voltage that seems to have been achieved. These tests provide evidence that our amplifier current limits likely inhibit the performance of our system, and that the model in the equations above gives a reasonable approximation of the system's behavior.

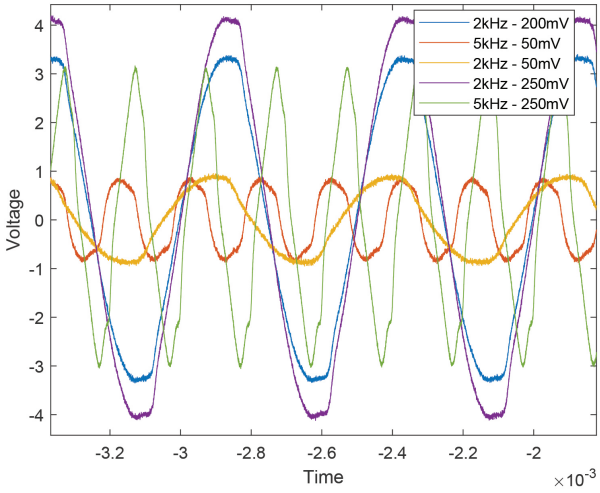

Fig. 8 Voltages from piezo amplifier for various input levels

The current limits were also evaluated using our discrete mass model. When simulating the performance of the system, the required current signal calculated from Eq. (11) was crudely clipped, more specifically, all current values exceeding our limits were set to the limit (in the time domain). Then, this updated current was run through the relations presented previously to find the resultant acceleration environment (i.e. Eq. (11), (9), and (7) in that order). The results are presented in Sec. .

Experimental Test Procedure

After the initial round of modeling, the system was designed, manufactured and tested. All tests were performed without a DUT attached, as shown in Fig. 9. Experimental transfer functions were measured between the input voltages to the shaker and piezos and the different accelerometers using DataPhysics SignalCalc software. These are compared with those from the model in the following sections.

Environment Testing was performed using SignalStar Matrix vibration controller software. For these tests, the software was set to utilize two output signals, one for the electromagnetic shaker and one for the piezos. A single output channel was split to the two piezo amplifiers, each of which fed two of the four piezos. That signal first passed through a high pass filter

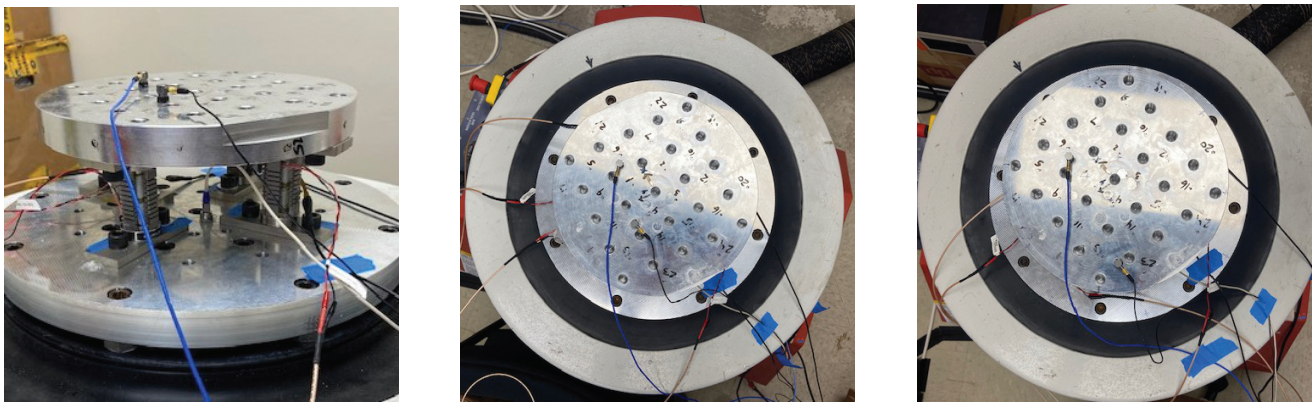

(a) Isometric view of original accelerometer placement

(b) Top-Down view of original accelerometer placement

(c) Top-Down view of adjusted accelerometer placement

Fig. 9 Accelerometer placement during environment testing

(Krohn-Hite Variable Filter 3341) with a cutoff frequency of f_{HP} =500 to 1400 Hz, depending on the test. The control signal for the big shaker was fed through a low pass filter (same model) with a cutoff frequency of f_{LP} =1800 Hz. Originally, one of the two accelerometers on the top plate, placed as shown in Figure 9a and 9b, was used as the control. However, further testing revealed that moving one accelerometer outward, to the position shown in Figure 9c, allowed the controller to recreate somewhat more powerful environments.

Results

Model Verification: Modal Test

To better understand the potential limitations of the lab setup, a roving hammer test was performed on the whole piezo assembly while attached to the shaker as shown in Figure 9a. Three accelerometers were included in the test, two on the top plate and one in the center of the base plate, and twenty force locations were used: 8 on the base plate and 12 on the top plate. The approximate accelerometer and forcing locations are labeled in Figure 10. The accelerometers were uniaxial,

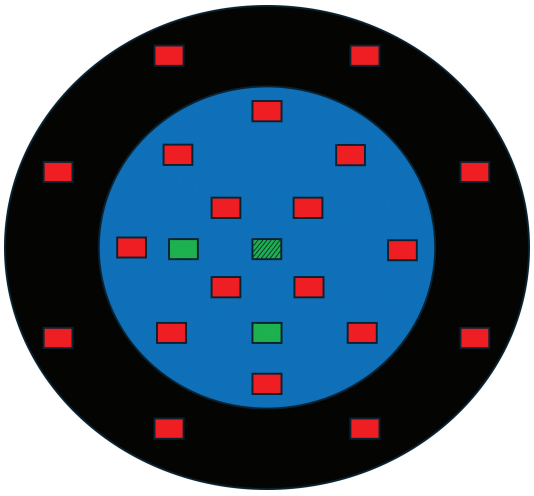

Fig. 10 Approximate accelerometer (green rectangles) and force (red rectangles) locations on the top plate (blue) and base plate (black). Note that the center accelerometer was actually on the base plate.

pointed in the direction of the shaker's force, and remained at the same locations in the qualification tests as shown in 9b, and were judged to be sufficient to observe all modes. The forcing locations were selected to allow the mode shapes of the system to be adequately visualized.

The composite FRF measured in the modal test is shown in Figure 11. There are seven clearly identifiable modes in the FRF. The natural frequencies and damping ratios, along with the descriptions of these mode shapes are given in Table 2. The operating deflection shape at 1427 Hz is also included in Figure 12, since this frequency is of interest later.

The key modes of interest are the bounce mode of the top plate on the piezos and the axial mode of the shaker. Mode 3 at 1179.5 Hz is likely the bounce mode, although the identified mode shape shows that it also involves some rotation of the top plate and perhaps slight deformation or bubbling. This suggests that the DUT might not move uniformly in the vertical direction even if it is mounted at the center of the top plate. (The system also has two lateral modes at lower frequencies of 815.6 and 991.1 Hz.) The axial mode of the shaker can be discerned to reside between 2022.5 and 2180.9. The top plate should have two asymmetric bending modes in this frequency range, yet the measurements show three, so the shaker's axial mode is likely coupled with these, causing an additional resonance that manifests with a similar shape.

The first bubble mode of the top plate is found to occur at 3057.7, which is similar to the 3511.6 Hz frequency predicted by the free-free FEM in Fig. 6, presumably lowered due to the mass added by the piezos.

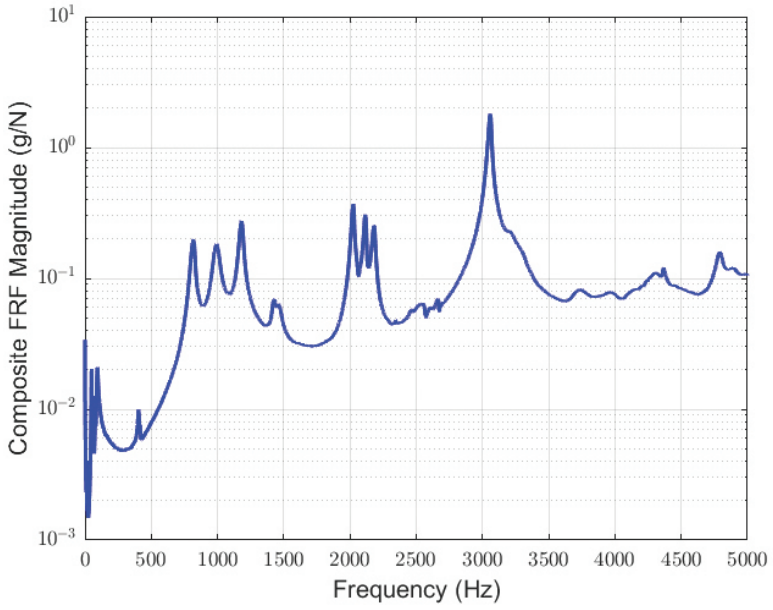

Fig. 11 Composite FRF Measured in Modal Test

Table 2 Natural frequencies, damping ratios, and descriptions of measured mode shapes

Mode Number	Natural Frequency (Hz)	Damping Ratio (%)	Top Plate Motion	Base Plate Motion
1	815.6	1.8	Rocking	Vertical Translation
2	991.1	2.2	Rocking	Slight Rocking
3	1179.5	1.2	Rocking and Bubble	Vertical Translation
4	2022.5	0.5	Asymm. Bending	Slight Asymm. Bending
5	2115.7	0.4	Asymm. Bending	Slight Translation
6	2180.9	0.5	Asymm. Bending	Base Plate Twist
7	3057.7	0.4	Bubble	Vertical Translation

Discrete Mass Model

The 3DOF discrete mass model of the shaker has two elastic modes. One would expect the first mode to be one in which the top plate bounces on the shaker, and the second to be the axial mode of the shaker. However, the actual modes generally

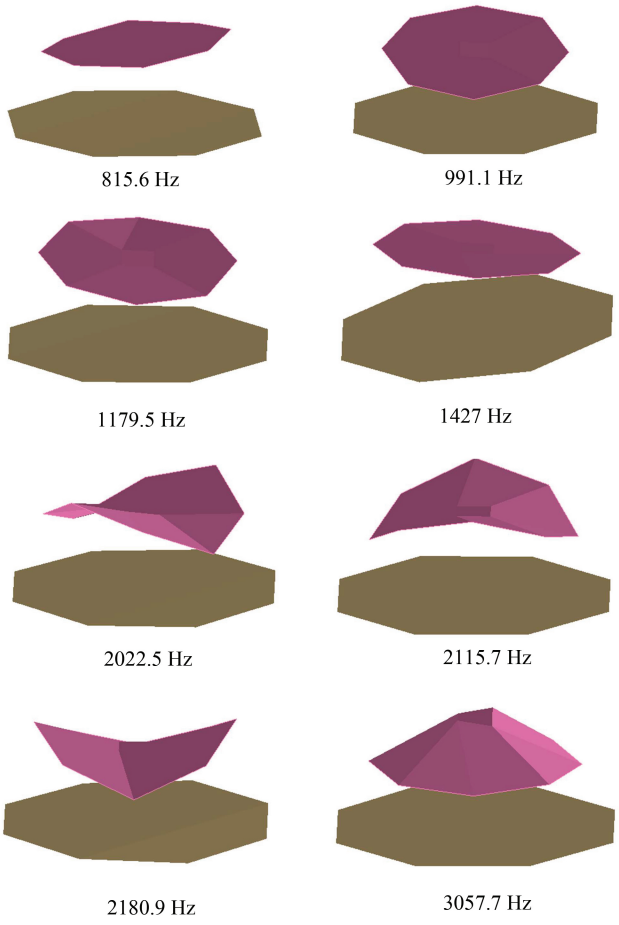

Fig. 12 Operating deflection shapes near natural frequencies as measured in the modal test

involved motion of all three masses. In any event, using the original model parameters, the elastic modes occurred at 1989.6 and 2448.2 Hz, considerably higher than the values found in the modal test. The model was tuned in order to better capture the frequency responses presented below, and after this tuning the elastic modes occurred at 1087.8 and 2136.7 Hz.

The discrete mass model was used to reproduce the FRFs of the system, and also to simulate environmental tests, as presented in the figures below. For clarity, results from the initial model are always shown in blue while the updated model is shown in black.

In Figs. 13a-b, the resulting transfer functions from our discrete mass model are compared with the experimental results. The initial model only shows one peak in the FRF (at about 2500 Hz); the lower frequency mode apparently does not respond. The updated model captures both of the experimentally observed resonances. Except for the transfer function from the shaker to the bottom of the piezos, the initial model tends to follow the same general trend of the experimental data. Although the updated model significantly improves in capturing the true behavior of the system at frequencies below 2500 Hz. As shown in Table 1, the model updating primarily consisted in reducing the piezo stiffness and damping from the values in the catalog and reducing the shaker damping relative to the value that was initially assumed. The model does not include any of the asymmetric modes nor any modes beyond 2500 Hz, so it is not expected to match the measurements above that frequency.

Recall that the control scheme used in these simulations only employs the electromagnetic shaker below 1700 Hz and then only the piezos above that frequency. Hence, the predictions of strain, voltage, and current presented in the following only use a portion of each of the transfer functions shown in Figs. 13. Therefore, the significant discrepancy between the shaker's experimental and updated model at high frequencies, for example, does not affect the accuracy of our results.

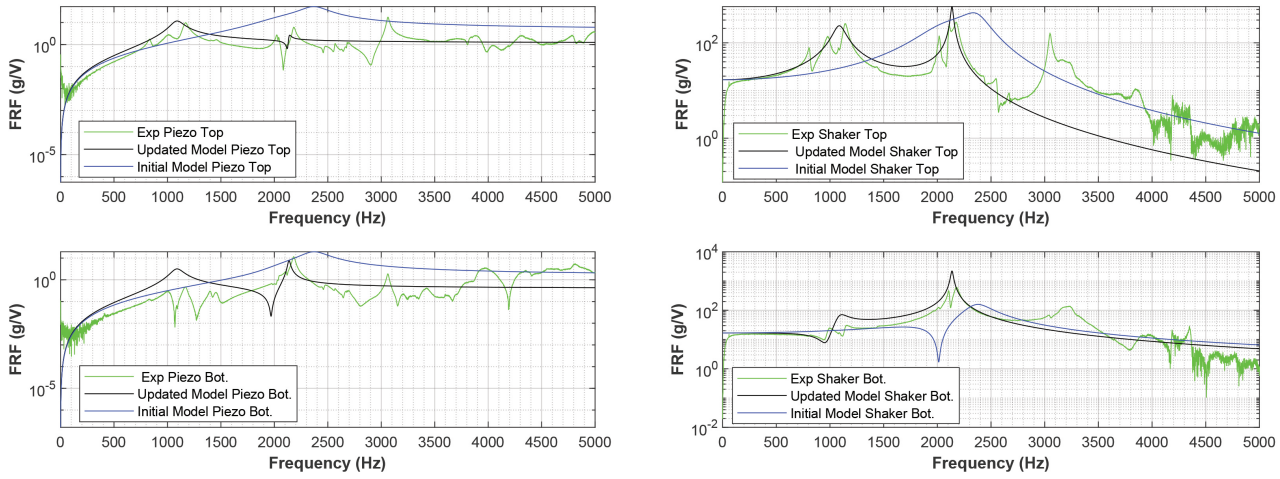

(a) $H_{1,F_{\text{piezo}}}$ and $H_{2,F_{\text{piezo}}}$ (piezo as input)

(b) $H_{1,F_{\text{sh}}}$ and $H_{2,F_{\text{sh}}}$ (shaker as input)

Fig. 13 Experimental and theoretical transfer functions from the force inputs to the accelerations at the top and bottom of the piezos. Since the voltage-to-force relationship of the shaker is unknown, the models for Figs. 13b show the transfer functions after multiplying by a factor to match the general magnitude of the experimental data. The experimental data for the Piezo top is an average of the transfer functions of both accelerometers.

The rest of the results presented in this section concern the case in which piezo and shaker forces were determined to replicate a target environment of 0.1 g^2/Hz at the DUT from 10 to 5000 Hz. The required forces were computed using Eq. (7). We approximate the system as behaving as a perfect high/low pass filter at 1700 Hz, so the electromagnetic shaker forces were set to zero from 1700.25 to 5000 Hz and the piezoelectric actuator forces were set to zero from 0 to 1700 Hz. These forces were applied to the models in Eqs. (5) and (6) to find the displacements and hence the accelerations of each mass, and those responses were added to find the response of the DUT and of the rest of the system. The resulting environment had a root mean square amplitude of 22.4 g.

Figure 14 displays the predicted stretching in the piezo actuators as a function of time. Notably, the maximum stretch does not exceed the stated limits (43 μm) for these actuators. Initially, the magnitude of stretching may seem surprising, considering the overall amplitude of the vibration environment and the low frequencies involved. Further analysis shows that

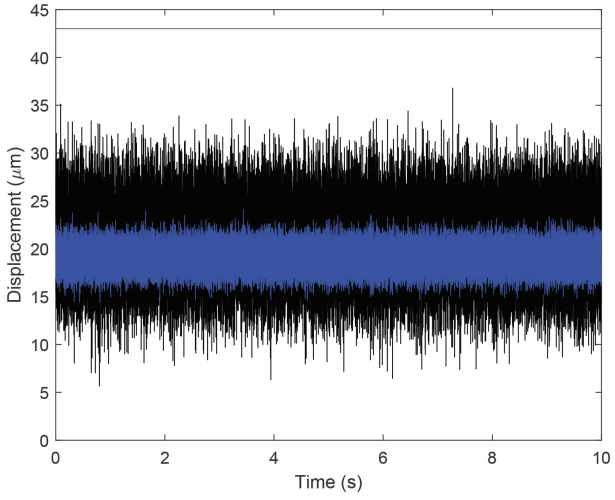

Fig. 14 Stretch in the piezo actuators versus time for the (blue) initial model and (black) updated model.

the shaker input at low frequencies does cause larger displacements. However, the top plate and upper shaker mass move in tandem, causing little to no stretching in the actuators as seen in the time domain in Figure 15.

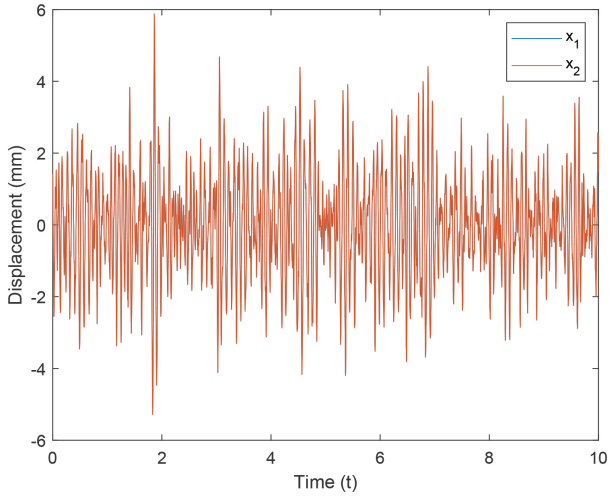

Fig. 15 Displacements of the top and middle masses over time taken from the simulation of the updated model.

Similarly, the voltage capacities of the piezos were not found to be a limiting factor for this level of environment. The time histories were created by taking the inverse Fourier transform of the piezo driver signal (see Eq. (9), which is zero from 10-1700Hz. Figure 16 shows the voltage signals from our initial and updated models. Interestingly, the two plots show a strong difference. While the initial model predicts a max voltage of 8.6 V, the updated model predicts a max voltage of 60.6 V, more than a 7-times difference. This isn't surprising considering the fact that the transfer function of the initial model was an order of magnitude larger at high frequencies, as shown in Figure 13a. One large contributing factor is that when tuning the model, the force factor (F_f) for the piezos was reduced by a factor of 4 in order to match the overall magnitude of the experimentally measured transfer functions.

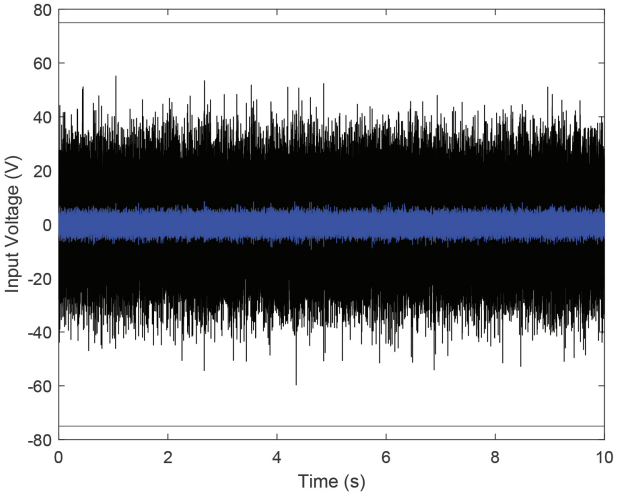

Fig. 16 Voltage signal to the piezo actuators versus time for the (blue) initial model and (black) updated model.

As previously noted, the current limit proved to be the largest limiting factor to the shaker's performance. Figure 17 shows the electrical current signals from the initial and updated models, respectively. Again, the current signal for the updated model is about 7 times greater than that of the preliminary model. However, in contrast to our voltage signals, neither current signal falls within their specified limits. In the initial case, the current signal barely exceeds the proposed current limits. In the updated case, the current limits vastly exceed the limits.

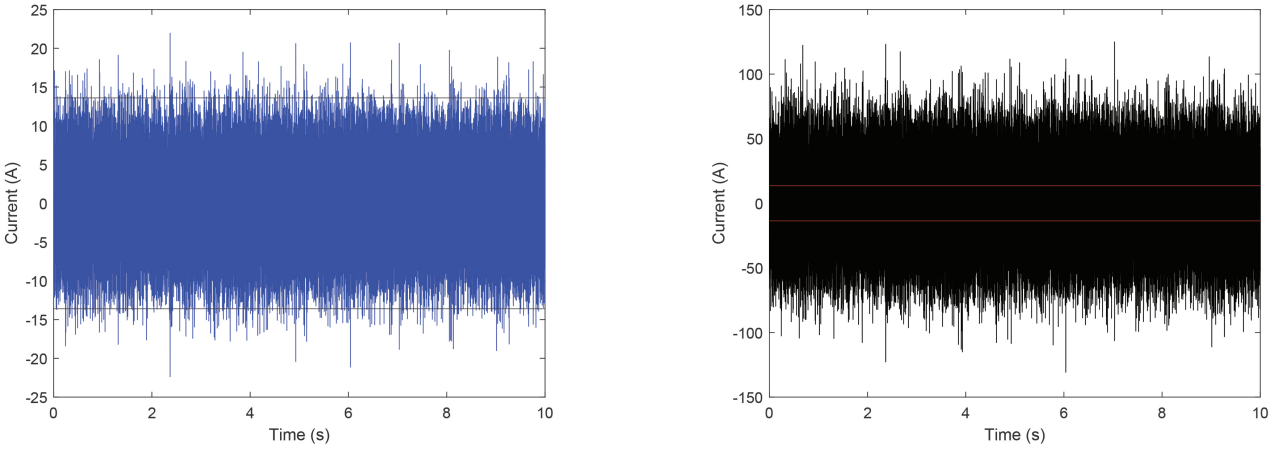

(a) Initial model

(b) Updated model

Fig. 17 A time history of the current to the piezo actuators across our simulated time.

In order to understand the effect that the electrical current limits might have on the response of the system, the simulation was repeated, but this time clipping the current by setting it to its maximum or minimum value any time it exceeded the limits, as was described in Section . The clipped current signal was used to compute the voltage in the piezos, using Eq. (11) in the frequency domain. This was then used in Eq. (9) to recompute the forces in the piezo actuators. Those were applied to the system using Eq. (6). The resulting PSD of the environment at the DUT is shown in Fig. 18 and compared to that which would have been obtained if the amplifier had infinite current capability. The environment obtained using the initial model matches the original environment quite closely, because very little clipping occurred. In contrast, the current in the updated model is clipped dramatically. This changes the spectrum of the piezo force, reducing its amplitude from 1700-5000 Hz, while at the same time increasing its amplitude from 0 to 1700 Hz, which was initially zero. This spurious low-frequency content excites the 1200Hz resonance of the system, as seen in Fig. 13, because we did not reduce the force to the large shaker to compensate. At the same time, the response at higher frequencies reduces from 0.1 g^2/Hz to roughly 0.018 g^2/Hz because the spectrum of the piezo force was much lower at those frequencies due to the clipping. A shaker control system

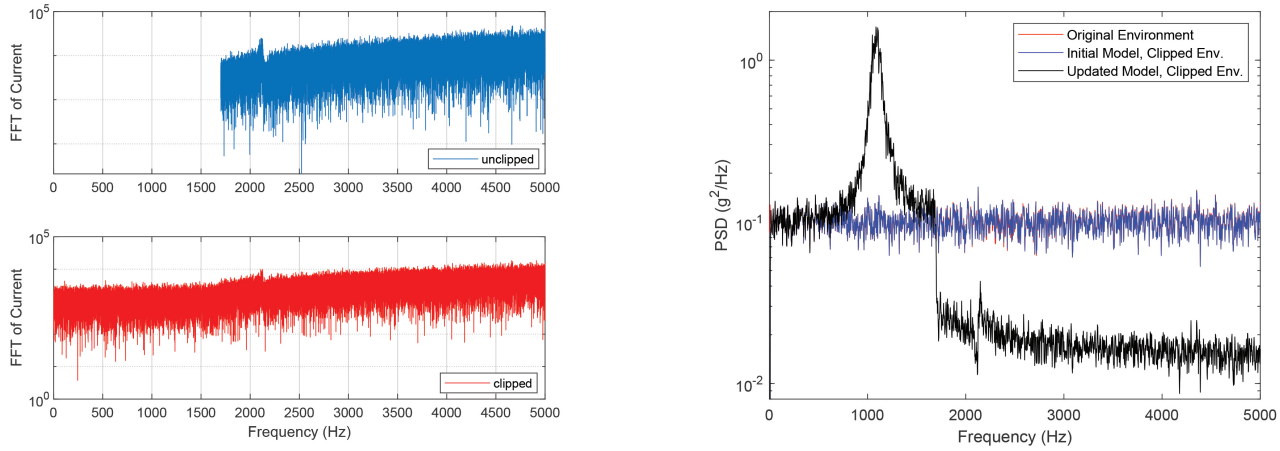

(a) Spectrum of the electrical current to the Piezo (blue) before and (red) after clipping.

(b) PSD of Environment at the DUT with the electrical current clipped.

Fig. 18 Simulation of the effect of clipping the electrical current on the environment reconstructed at the control accelerometer.

would update the forces in each of these actuators to compensate, but would be unable to reach the environment because any increase in the voltage to the piezos would cause increased clipping.

Experimental Results

A variety of environmental tests were performed on the hardware that was manufactured as discussed in Sec. . The Data-Physics system was used to control to one of the accelerometers on the top plate, using the configuration discussed in Sec. . The exact settings for the low and high pass filters used for the shaker and piezos are given in the caption for each result.

The goal was to recreate a target environment of 0.1 g^2/Hz, yet the system was not capable of reproducing an environment at that level. The maximum recreated environment had a mean power spectral density of 0.03 g^2/Hz, although this was a result of asking for 0.05 g^2/Hz from the controller. Figure 19 shows the auto-power spectra of the control accelerometer for this environment and also 0.01 g^2/Hz and 0.001 g^2/Hz environments. Somewhat similar to what was observed in the simulations with current clipping, the response for the 0.05 g^2/Hz environment shows over-excitation of the 1200 Hz resonance, and under-excitation of the high frequencies. In contrast, the controller was able to more accurately recreate the 0.01 g^2/Hz environment. Even then, both environments were not reproduced very accurately, with several frequencies exceeding the 6 dB tolerances that are shown with horizontal lines.

One notable feature of both experimental environments is the presence of strong anti-resonances at about 820 and 860 Hz. The system contains two rocking modes at 815.6 and 991.1 Hz, as seen in Figure 12. This suggests that the 820 and 860 Hz anti-resonances involve rocking motion of the system. Originally, the high-pass filter applied to the piezo actuators was set at 1400 Hz, forcing the shaker and piezos to create the low and high frequency portions of the environment, respectively. However, during testing, these anti-resonances resulted in excessive voltages being sent to the shaker, limiting the achievable acceleration environment. For this reason, the high-pass filter was set below 800 Hz, allowing the piezo actuators to assist the shaker in overcoming these anti-resonances. This anti-resonance is also associated with a significant peak in the stretching of the piezos, as can be seen in Figure 22, which is discussed later.

The responses in Figure 12 also show large spikes in acceleration at about 3800 Hz. These seem to come about because of the current clipping; these spikes were not visible in the data when controlling to an environment of 0.001 g^2/Hz; in that case our simulation model suggests that clipping would not occur. None of the measurements acquired in this work showed a mode at 3800 Hz.

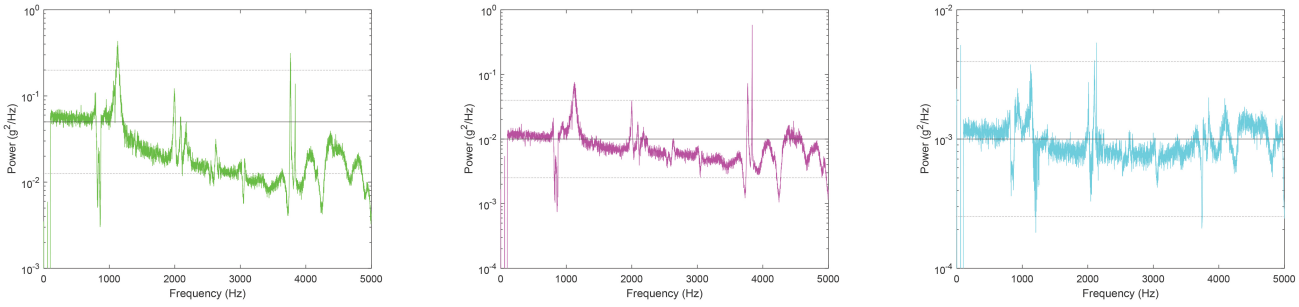

(a) Control environment of 0.05 g^2/Hz with high- and low-pass filters applied at f_{HP} =700 and f_{LP} =1800 Hz.

(b) Control environment of 0.01 g^2/Hz with high- and low-pass filters applied at f_{HP} =500 and f_{LP} =1800 Hz.

(c) Control environment of 0.001 g^2/Hz with high- and low-pass filters applied at f_{HP} =1400 and f_{LP} =1800 Hz.

Fig. 19 PSD of the control accelerometer for the actual experiments for the target environment listed, with the high- and low-pass filters configured as described in Section . Controlled to the outside accelerometer as seen in 9c.

Comparison to model

Figure 20 compares these experimental environments to those predicted by our clipping model. Interestingly, at high frequencies, the measured spectrum at the control accelerometer for the highest amplitude (0.05 g^2/Hz) environment roughly matches the predicted output by the updated model, which included current clipping. Additionally, the experimental results include a large acceleration peak at about 1200 Hz, similar to the distortion caused in the model that included current clipping. Both these facts seem to indicate that our electrical current model reasonably tracks the true experimental behavior of the system.

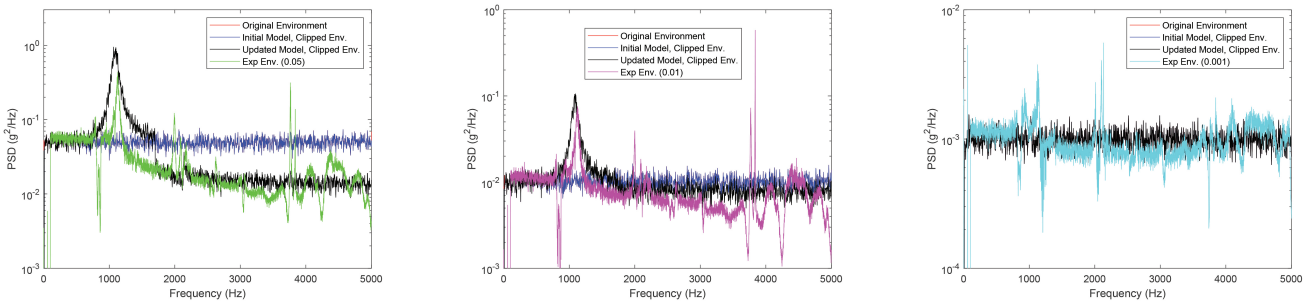

(a) 0.05 g^2/Hz (b) 0.01 g^2/Hz (c) 0.001 g^2/Hz

Fig. 20 Comparison between ideal, experimental, and modeled acceleration environments at the control accelerometer.

The voltage sent to the piezos is compared to that predicted by the model in Fig. 21. The case considered is that of the 0.001 g^2/Hz target environment, where clipping should be minimal. Figure 21 shows that the updated model captures the overall magnitude of the piezo voltages reasonably well. The RMS voltages of the updated model and experiment are 1.33 and 1.15, respectively; the model slightly overestimates the piezo voltages. The model does not capture the variations in the voltage with frequency, which are quite significant in the experimental results. These presumably arise due to higher modes in the system that were not included in the model.

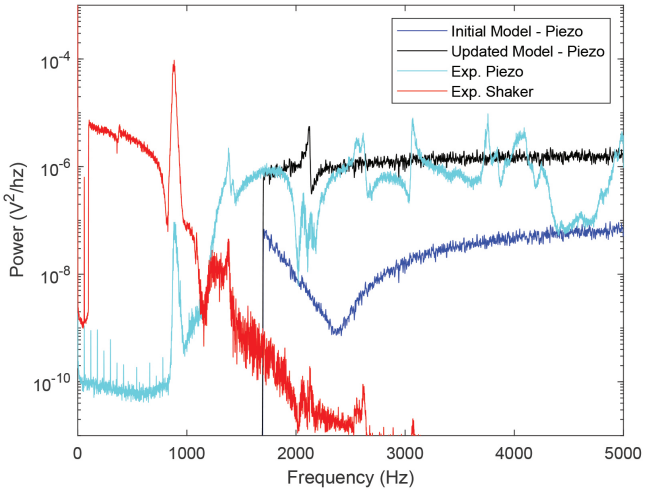

Fig. 21 Comparison between auto power spectra of Piezo and Shaker voltage of the experiment and models for an environment of 0.001 g^2/Hz. Voltage powers are calculated from the control signals before amplification.

The measured strain is compared to the model predictions in Figure 22. Again, the case considered is that of the 0.001 g^2/Hz target environment, with high- and low-pass filters applied at $f_{\text{HP}} = 1400$ and $f_{\text{LP}} = 1800$ Hz respectively. The RMS values of the initial and updated models were 0.115 and 0.360 μm, respectively, and the figure shows that most of the displacement in the piezos occurred in the low frequency range. The experimentally measured strains show strong variations with frequency. The RMS of the measured strains from gauges 1 and 2 were 0.235 and 0.183 μm, respectively. They are dominated by a component at about 950 Hz and many other narrow-band components at various frequencies. The overall magnitude of the strain at low frequencies matches the initial model better than the updated model, but in any event it is clear that the model would need to include higher frequency dynamics to accurately capture the strain.

Shaker Power Reduction

An additional experiment was performed to better understand the reduction in power required when incorporating piezo actuators. For this experiment, a given environment was created by only the shaker. Then, the same environment was recreated with the help of the piezo actuators. In this way, the required shaker voltage could be compared with and without the piezos.

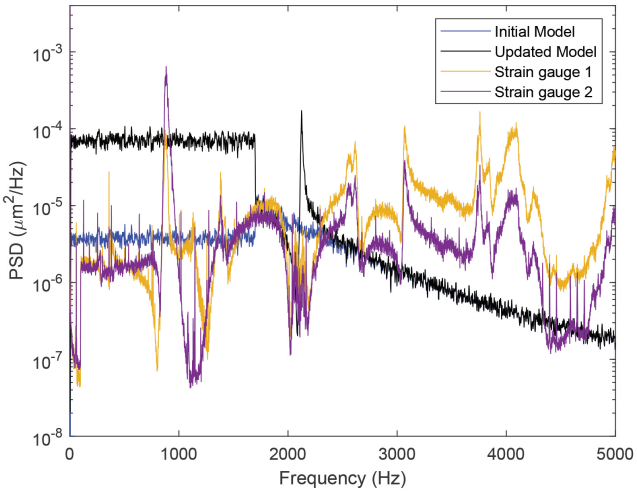

Fig. 22 Comparison between auto power spectra of the piezo stretch of the experiment and models for an environment of 0.001 g^2/Hz. Strain gauges 1 and 2 refer to two different piezo actuators during a single test.

The test was attempted with the original frequency range (0-5000Hz), but even for small environments the shaker encountered anti-resonances and could not adequately recreate high frequency environments by itself. Therefore, the upper frequency was reduced to 2800 Hz and to avoid any possibility of damage to the shaker, the environment level was decreased to (0.001 g^2/Hz) for this test.

As seen in Figure 23, the introduction of the piezo actuators significantly reduces the voltage sent to the shaker from roughly 10^{-6} to 10^{-10} V^2/Hz at high frequencies. At these frequencies, the piezos almost single-handedly recreate the environment requiring voltage levels that are similar to those required in the shaker-only test. Note that the voltages shown are those sent to the respective amplifiers. The amplifier for the electromagnetic shaker is a three-phase, 480 volt amplifier that measures $1.8 \times 0.8 \times 0.5$ m and weighs 500 kg. It can produce up to 80 amps of output current RMS and requires a large and noisy cooling system. In contrast, the piezo amplifiers each measure about $100 \times 150 \times 400$ mm (contained in a case the size of a desktop computer) and produce a total of 6.8 amps each. Hence, even though the voltage sent to these systems is similar, the total power required is dramatically different.

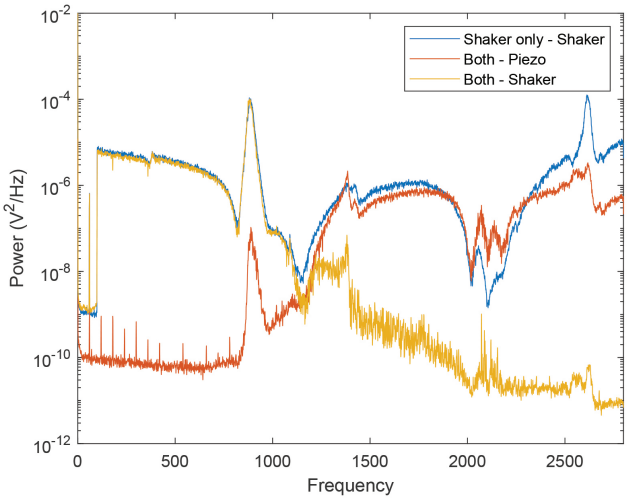

Fig. 23 Comparison of shaker and piezo effort for an environment of 0.001 g^2/Hz from 50 to 2800 Hz for two cases. In the first, only the shaker is active. In the second, both shaker and piezo work together to create the environment. High- and low-pass filters applied at $f_{\text{HP}} = 1400$ and $f_{\text{LP}} = 1800$ Hz, as described in Section . The voltages shown are those sent to the respective amplifiers.

Conclusion

This work presented the design, modeling and testing of a system that integrates four piezoelectric actuators with a traditional, large electromagnetic shaker system. The goal of the system was to enable testing to higher frequencies, while avoiding damage to the electromagnetic shaker or piezo actuators. In its current form, the system failed to reproduce the 0.1 g^2/Hz environments that it was designed to reproduce, and it exhibited many spurious resonances and hence was generally not able to produce the PSD at the control accelerometer with reasonable fidelity. However, the effort so far has validated many aspects of modeling and provides several valuable insights into how such a system could be designed.

The most important finding was that the piezoelectric actuators require far more current than was expected in order to move a sizable DUT at high frequencies. The main limitation of the present design was linked to the electrical current limits of the amplifiers that were used to drive the piezoelectric actuators. If we had access to four of the present amplifiers, so that one could be used for each piezo, then our updated model predicts that we could have reproduced an environment up to $0.008\frac{g^2}{Hz}$ with little to no clipping. That is for an upper frequency limit of 5 kHz. If the upper limit were reduced to 4 kHz, then the system with four amplifiers would be able to reach an environment of $0.016\frac{g^2}{Hz}$. Alternatively, if unlimited current was available, our updated model predicts that we could have reproduced a 5 kHz environment up to $0.19\frac{g^2}{Hz}$ or driven a payload of roughly 1.2 kg at the target environment of $0.10\frac{g^2}{Hz}$ before other limitations posed an issue. According to our updated model, the next limitation to be reached is voltage, not strain. The present design could also be easily modified to allow up to eight piezo actuators (see the Appendix, Figure 25), increasing the capabilities further.

In designing the system, it was decided to maximize the frequency of the bubble mode of the top plate. In the final design, the natural frequency of the bubble mode was 3500 Hz with free boundary conditions; a similar mode appeared at 3000 Hz in the assembled system. However, the top plate that was designed was quite heavy and this exacerbated the problems with the piezo current. Furthermore, the assembled system still has a mode at only 1200 Hz where the top plate bounces on the piezo actuators. In retrospect, it may have been more effective to have designed the system to minimize the weight of the top plate, driving the bounce mode up and allowing the top plate bubble mode to decrease somewhat. The models developed here could be used to predict the behavior of such a system and develop a more optimal design. For example, according to the updated model, cutting the mass of the top plate in half would reduce the RMS current required by the piezos (i.e. see Fig. 17) from 28.6 A to 17.4 A, and the maximum current from 125 A to 72 A.

The test results showed several narrow ranges of frequencies in which the response exceeded or fell short of the desired environment. These frequencies are presumed to correspond to resonances and antiresonances of the system. The present configuration of the system does not seem to be sufficient to eliminate all of the antiresonances that occur below 5 kHz. Indeed, the modal test results in Sec. show that the system has several resonances, and that the resonances all exhibited motions that coupled with axial motion of the system. Some experiments were performed in which pairs of piezo actuators were controlled separately, in hopes of allowing the system to overcome the antiresonances, but none of these was successful. For future designs, we recommend using a higher fidelity finite element model to predict the resonances and antiresonances of the system, and then to see if the piezo actuators can be placed in such a way that they eliminate the antiresonances below 5 kHz.

Finally, some minor design improvements are suggested. For example, with the present design, a special low-profile socket wrench was needed to tighten the bolts to the piezo mounting brackets, because of the tight clearance between the piezo actuators. As shown in Fig. 25, the top plate and piezo mounting brackets could be modified to allow the central bolts to be tightened from above, greatly simplifying the assembly process.

Acknowledgments The original shaker-piezo design configuration was developed by a BYU capstone team consisting of: McKaelin Edralin, Jonathan Paul, Nicholas Harris, Christian J. Johanson, Joel Gibb, and Corry Price. The authors are grateful for each of their contributions, which made this work possible.

References

1. A. Singh, M.S. Allen, M. Schmidt-Landin, and W.J. DeLima. Multi–Input Multi–Output Hybrid Active Vibration Control for High Frequency Random Vibration. *Experimental Techniques*, 46(1):67–79, February 2022.
2. Washington J DeLima and Melanie N Ambrose. Experimental Characterization and Simulation of Vibration Environmental Test. In *Topics in Modal Analysis*, volume 10, pages 45–55. Springer, 2015.
3. Vicente J. Romero, John V. Burkardt, Max D. Gunzburger, and Janet S. Peterson. Comparison of pure and "Latinized" centroidal Voronoi tessellation against various other statistical sampling methods. *Reliability Engineering and System Safety*, 91(10-11):1266–1280, 2006. Number: 10-11.

4. Physik Instrumente. Electrical operation of piezo actuators. https://www.physikinstrumente.com/en/expertise/technology/piezo-technology/properties-piezo-actuators/electrical-operation, 2025. Accessed: 2025-06-17.
5. S. Sherrit, Christopher Jones, Jack Aldrich, Chad Blodget, Xiuliang Bao, Mircea Badescu, and Yoseph Bar-Cohen. Multilayer piezoelectric stack actuator characterization. *Proceedings of SPIE - The International Society for Optical Engineering*, 6929, 05 2008.
6. Cedrat Product Catalog, Cedrat Technologies, 2016, https://cedrat-technologies.com/products/

Appendix

Alternative Mounting Bracket Design

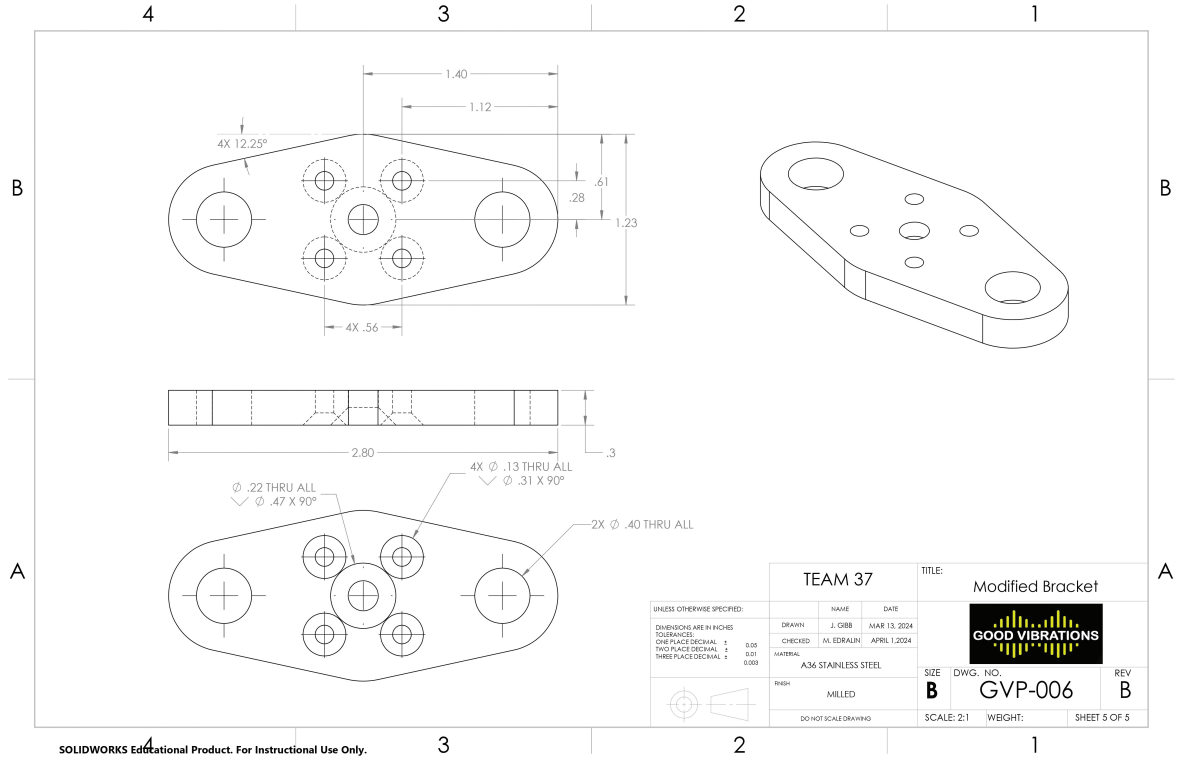

Fig. 24 Modified mounting bracket that allows for four to eight piezo actuators.

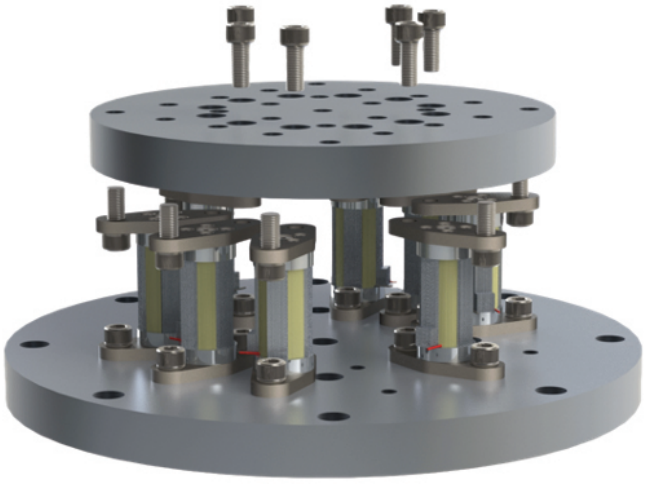

Fig. 25 CAD rendering of an improved design with 8 piezo actuators and mounting screws accessible from above.

Assembly Instructions

The setup of the piezo assembly must be done meticulously to prevent damage and ensure proper functionality. The following are the steps and precautions used to set up a full piezo assembly test, with four piezo actuators.

1. Prepare all components: All parts must be properly prepared before assembly. For instance, the mounting brackets, top plate, and bottom plate need to be deburred, sanded down to a smooth finish, and cleaned. There should be no edges that would prevent the mounting bracket from sitting flush with its contact surfaces.
2. Check flat head screw clearances: The piezoelectric actuators contain a quartz crystal, which expands when a voltage is applied. The mounting screw locations on piezo actuators are through holes. This means that if the screws are tightened too much, it could crack the quartz and therefore break the piezo actuators. During assembly, put the screws in the mounting bracket and measure how much the screw extrudes. If it measures more than 6 mm, the mounting bracket should not be used.
3. Piezo and mounting bracket assembly: Mount a bracket to each end of the piezo actuator, using two brackets per piezo actuator.
4. Measure the piezo and bracket assembly: This is done to ensure the piezo actuator and mounting brackets are level and to determine the height of this assembly. It is best to measure two locations to ensure the piezo actuators are flush with the mounting brackets and level.
5. Base Plate: Mount it to the electrodynamic shaker
6. Bracket - Piezo assembly: Mount the piezo actuator bracket assemblies to the base plate. Tighten the brackets to the base plate with equal torque. Use shim stock as needed to keep the piezo actuators level.
7. Top Plate: Attach the top plate to the top of the mounting brackets
8. DUT: Attach the DUT to the top plate
9. Power and Software: power the piezo actuators and electrodynamic shaker. Also, run the software needed for tests.

This order of operations was sufficient to prevent any piezo actuators from being damaged during assembly.

Chapter 3
Investigating Three-Axis Shock and Vibration with a "Supplemental Shaker" Frame

R. Krieghbaum and S. M. Danforth

Abstract Traditional single-axis environmental testing methods have been shown to over-test components by means of cross-axis excitation, leading to potential damage to test objects that would not be experienced in the field. Multi-input, multi-output testing seeks to address cross-axis excitation by controlling all principal axes during the test, but these methods have had difficulty reaching high-amplitude flight environments. This paper seeks to explore a new method of multi-axis excitation, using a large shaker for axial excitation with additional "supplemental" shakers in the remaining principal axes. A test frame was designed to enable attachment of two supplemental shakers. The test frame was evaluated by subjecting a representative test assembly to transport vibration, flight vibration, and flight shock environments, and these results are compared to a similar test completed using single-axis methodology.

Keywords Environmental shock and vibration testing · Multi-axis shock and vibration testing · Flight environments

Abbreviations

DOF – Degree of freedom
GOBLET – Generic OBject for Laboratory Environmental Testing
PSD – Power spectral density
GRMS – Root-mean-square acceleration, in units of g
SRS – Shock response spectrum
LANL – Los Alamos National Laboratory
MIMO – Multi-input, multi-output
SISO – Single-input, single-output

Introduction

The Shock and Vibration Team at Los Alamos National Laboratory (LANL) seeks to recreate environments of test objects as accurately as possible in a laboratory setting as an alternative to the costly process of performing field tests. Current qualification test methods use single-input, single-output (SISO) testing, where test objects are excited using a single shaker and rotated for sequential excitation in all three principal axes. This test method has been preferred because of the requirement of high excitation levels, such as those experienced during flight stages, that only large, single-axis shakers can provide. However, constraining test articles to single-axis testing may fail to accurately depict the multi-axis forces present during field environments, such as aerodynamic loading that occurs during flight environments and rocket propulsion. Additionally, segmenting test environments into sequential SISO tests has shown to result in cross-axis excitation, yielding elevated excitation levels from the environment specification [1]. Excitation greater than the environmental specification may produce excess damage to production components that would not be experienced during the lifetime of the component.

R. Krieghbaum · S. M. Danforth
Bikini Atoll Rd, Los Alamos, NM 87544
e-mail: rkrieghbaum@lanl.gov; sdanforth@lanl.gov

© The Author(s), under exclusive license to River Publishers 2026

Kristin B. Zimmerman, PhD (eds.), *Dynamic Environments and Durability Testing, 2026, Vol. 7*, Conference Proceedings of the Society for Experimental Mechanics Series, https://doi.org/10.13052/rp-9788743814184

Multi-input, multi-output (MIMO) testing has been shown to provide more field-relevant boundary conditions and address cross-axis excitation concerns by controlling to multiple degrees of freedom (DoFs) using multiple excitation sources during a single test [1]. One method of MIMO excitation uses multiple small, distributed shakers to recreate distributed-loading environments [2]. While this method of MIMO testing addresses current environment replication concerns, the smaller shakers used in these tests are often incapable of supplying the necessary excitation for high-amplitude flight environments.

In previous work, LANL test engineers aimed to address the low excitation levels of distributed shaker testing by using a high-force-output, single-axis shaker for axial excitation and a smaller modal shaker for lateral excitation [3]. We labeled this method as "supplemental shaker" testing because the smaller lateral shaker(s) could supplement the high force provided in the axial direction. The previous supplemental shaker studies showed promising multi-axis control performance for both flight and transportation environments. However, the excitation was limited to two axes because the test area did not have room to suspend a second supplemental shaker.

In this paper, we build upon previous research by introducing a custom test frame that can suspend multiple small shakers with a compact footprint, enabling supplemental shaker testing for flight environments in the three principal axes of a test body. Our goal is to compare the acceleration response of a representative test assembly between three-axis supplemental shaker testing and traditional single-axis testing, with a focus on analyzing viability of the new test method. In Section 2.0, we introduce the test assembly and three test environments that are of interest to LANL's weapons programs. Section 3.0 describes the test frame used during testing, including its features and design considerations. Sections 4.0 and 5.0 describe the equipment, procedure, and notable events experienced during single-axis and multi-axis testing, respectively. Test results are reported in Section 6.0, with discussion presented in Section 7.0 and overall conclusions presented in Section 8.0.

Test Article and Proposed Test Environments

In this study, we conducted testing on an article called the GOBLET (Generic OBject for Laboratory Environmental Testing). The GOBLET was designed to investigate the coupling dynamics of a rigid and compliant component, shown in Figure 1. Part A is thin and bell-shaped, making it compliant when coupled with Part B, a rigid cylinder. A fixture plate was used to attach the GOBLET to the shaker armature or slip table for environmental shock and vibration testing.

Part A of the GOBLET was connected to Part B using three bolted "legs." This study uses the leg oriented 270° clockwise from the +Y direction, referred to as the "270 Leg," as a location for control. In addition to instrumenting the 270 Leg, we

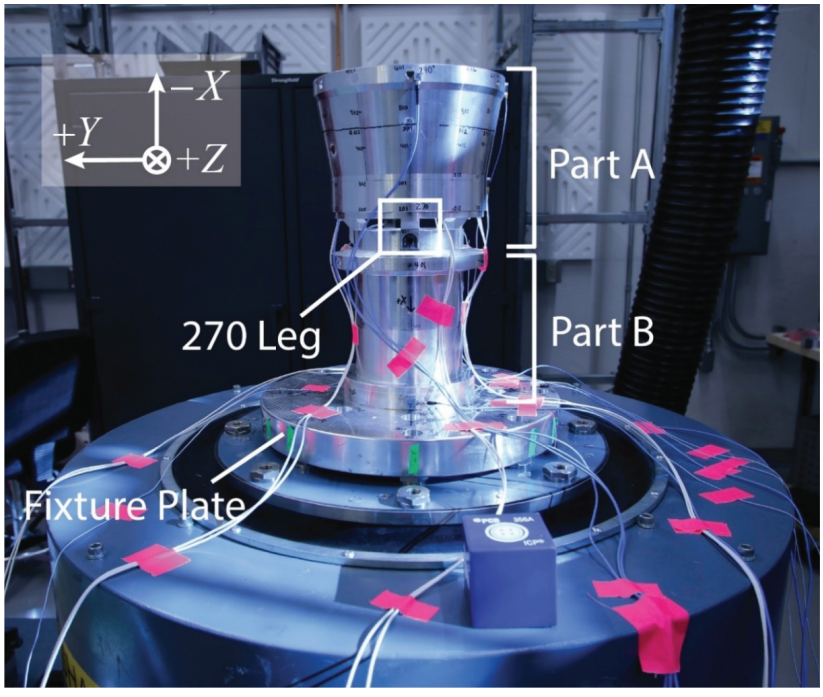

Fig. 1 Overview of the GOBLET test assembly with system axes and notable locations specified

placed accelerometers (PCB and Endevco, 22 channels) and strain gauges (Vishay Measurements Group, 8 channels) at other locations throughout Part A, Part B, and the fixture plate. These extra sensors will aid in evaluating differences in global test article response between testing methods, although the strain data are not evaluated in this study.

We selected three environments for our initial evaluation of the supplemental shaker test frame: a Transport Random vibration environment, Flight Random vibration environment, and a Flight Shock environment. The Transport Random environment contains lower-level transportation vibrations with a higher makeup of low-frequency content, yielding larger displacements that pose a challenge to the supplemental axes. Additionally, LANL team members successfully tested the Transport Random environment at a truncated frequency range in previous two-axis supplemental shaker work, and additional testing of this specification will enable comparison to previous methods [3]. The Flight Random environment contains higher excitation levels with broader frequency content, challenging the capacity of the supplemental shakers to provide sufficient drive voltage in their respective axes. Finally, the Flight Shock environment was chosen because LANL test engineers have not yet attempted multi-axis shock and sought to evaluate its viability in the supplemental shaker test method. When compared to vibration environments, shock environments often involve high displacement, pose unique control challenges, and exacerbate nonlinear system behavior. The Flight Shock environment represents a low-level shock, yielding a reasonable starting point for exploring use of supplemental shakers for MIMO shock testing.

Both random vibration environments, Transport Random and Flight Random, are implemented in the laboratory by controlling to power spectral densities (PSDs) in the frequency domain. The average amplitude of vibration signals synthesized using these PSDs can be estimated by integrating each PSD over its frequency range and taking the square root of the result, yielding the GRMS (root-mean-square acceleration, in g) value for the profile. Figure 2 shows plots of these PSDs along each DoF at the 270 Leg, and Table 1 provides the GRMS of each environment. The SISO testing described in Section 4.0 controls each DoF sequentially, while the supplemental MIMO testing described in Section 5.0 controls the DoFs simultaneously. Note that the PSDs specified in this section are auto spectral densities, but in MIMO testing, cross power spectral densities additionally play a role in environment specification. Our approach to addressing the cross powers is described in Section 5.0.

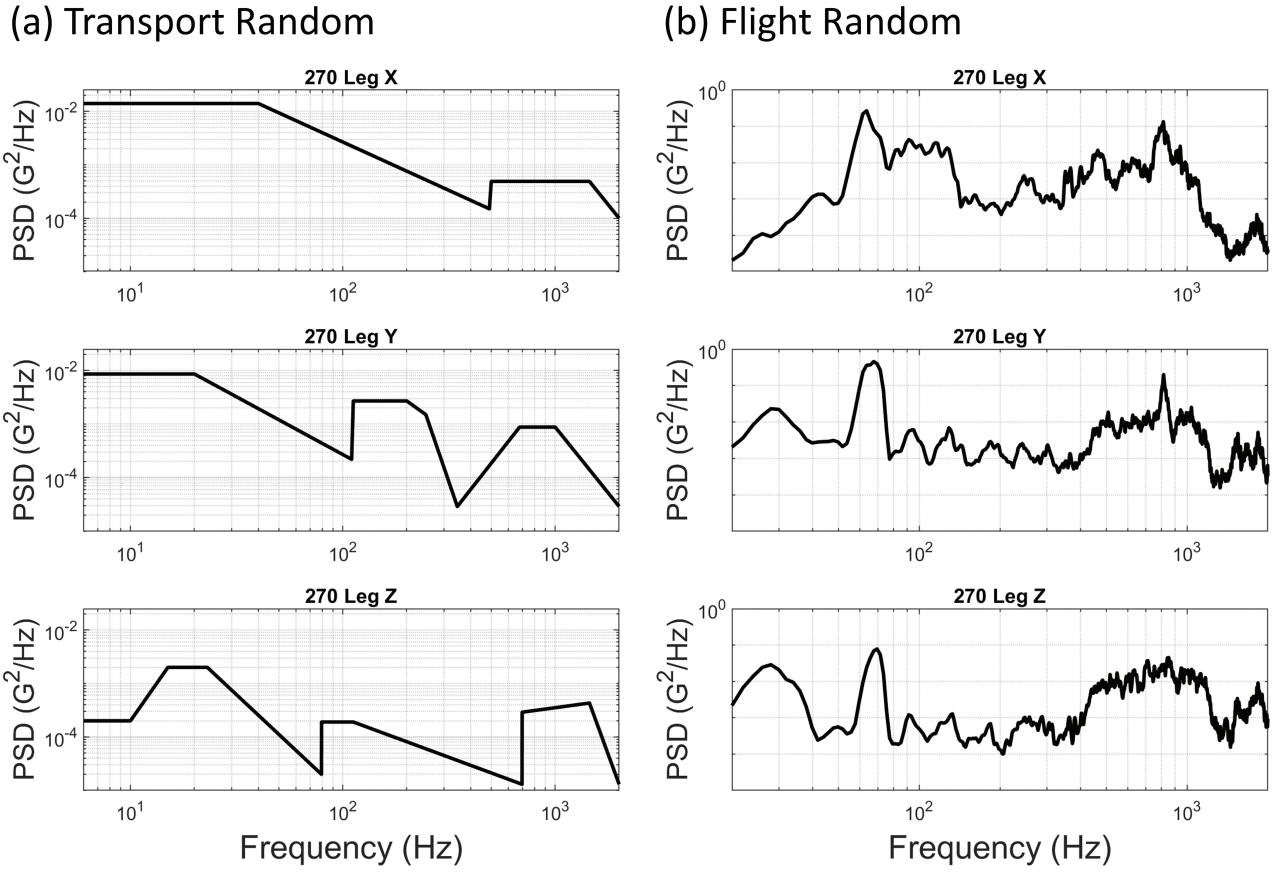

Fig. 2 Random vibration environments used during testing, specified at the principal axes of the 270 Leg

Table 1 GRMS Values for Random Vibration Environments

Environment Name	Frequency Range (Hz)	Axis	GRMS
Transport Random	6–2000	X	1.29
		Y	1.11
		Z	0.64
Flight Random	20–2000	X	3.89
		Y	4.16
		Z	3.63

The Flight Shock environment is specified as a shock response spectrum (SRS) maxi-max absolute acceleration (MMAA), shown in Figure 3(a) for X, Y, and Z at the 270 Leg from 20 Hz–2000 Hz [4]. We worked with the V-14 Data Analysis Team to synthesize a time waveform that achieves this SRS profile. Figure 3(b) shows the synthesized time waveforms for the Flight Shock environment for X, Y, and Z at the 270 Leg.

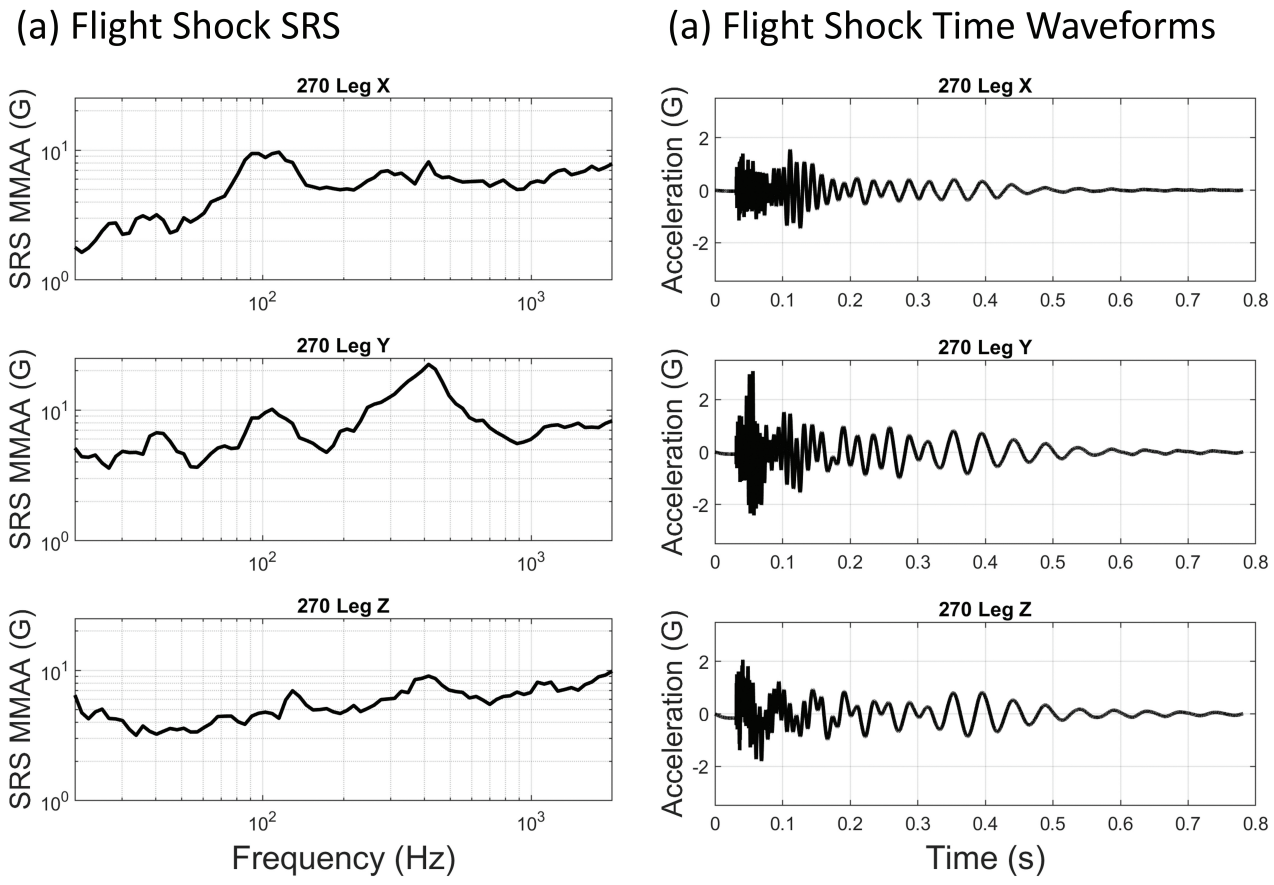

Fig. 3 Shock environment (a) SRS and (b) Time Waveforms used during testing, specified at the principal axes of the 270 Leg

In addition to evaluating control performance, we are interested in comparing system response at non-control locations between single-axis and supplemental test methods. We selected the X, Y, and Z channels of Point 2504 as response DoFs, since Point 2504 is located close to the rim of Part A of the GOBLET. With Part A's bell-like characteristics, we expected interesting motion amplification between our control DoFs at Point 2101 and the response DoFs at Point 2504. Figure 4 highlights Point 2504's location relative to Control Point 2101.

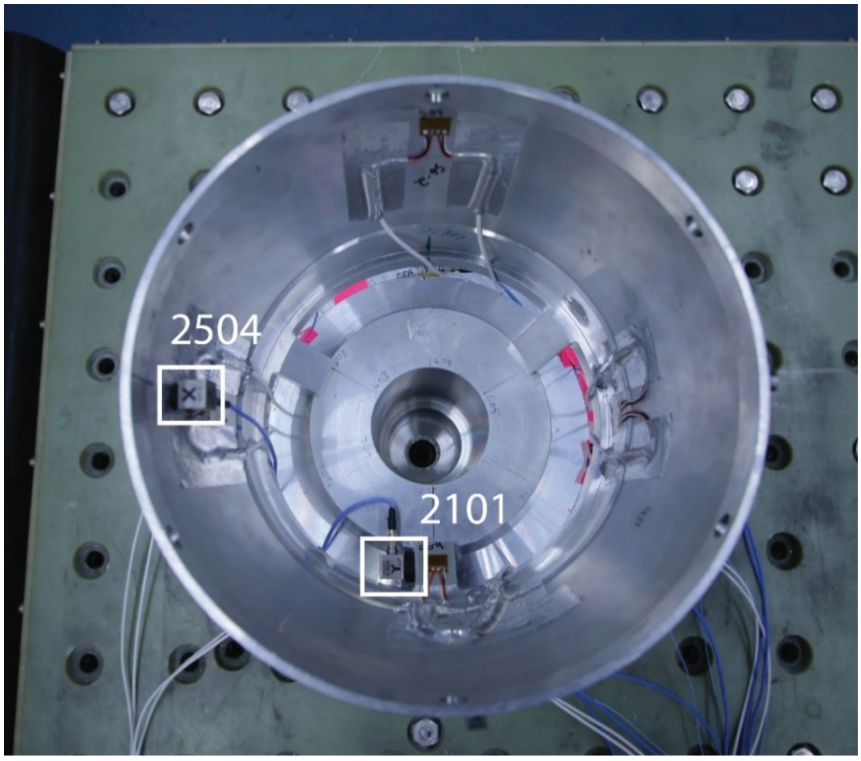

Fig. 4 Locations of Point 2504, near the rim of Part A, and Control Point 2101, located on the 270 Leg

Test Frame Design

As with previous supplemental shaker studies, we identified the Unholtz-Dickie H560 shaker as the large shaker for providing axial excitation. This shaker does not have an associated slip table, which provided more room for a supplemental test frame. Previous supplemental shaker testing used a Lateral Excitation Stand from The Modal Shop to suspend one Modal Shop 2100E11 100-lbf shaker for supplemental excitation [3]. This excitation stand was difficult to reconfigure around the H560 shaker, and because of the size of the stand, only one supplemental shaker was capable of being suspended. To enable the use of multiple shakers from both fixed and suspended attachment as well as increased movement of the small shakers around the test object, we designed a test stand for future multi-axis testing.

The general layout of the test frame is shown below in Figure 5(a), with an approximate size of 6x6x6 ft and weight of 500 lb. The frame consists of Bosch-Rexroth 90x90L aluminum extrusion forming an external structure with "tree-and-branch" internal structures enabling shaker alignment. The "trees" refer to the vertical beams spanning the height of the frame, which can be moved laterally, and the "branches" refer to the cantilevered beams that hold the shakers. The branch height can be adjusted, and multiple branches can be added to each tree if more than one shaker is desired in each axis. We chose the general frame design after discussion with Sandia National Laboratories, who implemented a similar frame design and noted the benefits of high maneuverability for smaller shakers. We selected the 90x90L profile on the recommendation of the manufacturer of the frame, Pacific Integrated Handling, who was provided with the intended shaker size, weight, and applications the frame would experience. In a previous project, we designed a frame with 2-in. aluminum extrusion, but because of scheduling issues, the frame was not used in testing. While assembling the previous frame, V-14 engineers noted high displacements from manual excitation, providing further motivation for the use of 90x90L in the new test frame.

The test frame enables three-dimensional (3D) positioning of the supplemental shakers by means of movement of the vertical support beam (tree), movement of the horizontal arm (branch), and movement of the adapter plate along the arm. We purchased additional lengths of extrusion to enable further adjustment of the shaker's proximity to the test object and avoid interference with larger test objects. Machined $\frac{1}{4}$-in. aluminum adapter plates rigidly mount the trunnions of the shakers to the frame and can be placed on any surface of the horizontal arm. Additionally, these adapters may be used to suspend the shakers below the horizontal arm if non-rigid attachment proves beneficial for shaker isolation. Figure 5(b) shows an implementation of the supplemental shakers on a mock single-axis shaker, with indicator arrows highlighting adjustment capabilities.

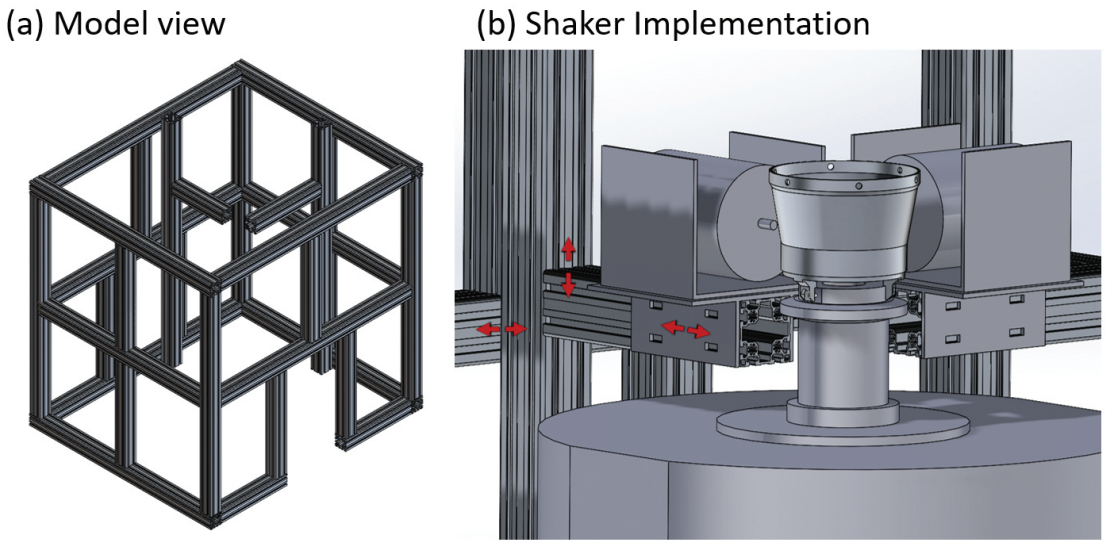

Fig. 5 Supplemental frame design, showing (a) an isometric view of the test frame and (b) mounted shakers with arrows indicating adjustment capabilities

We also purchased rubber padding and additional stiffening gussets to explore optimization of the dynamic characteristics of the test frame. Previous research found that while the dynamics of the test article are the greatest contributing factor in MIMO control efficacy, modification of the dynamic characteristics of the test frame did yield notable change in test performance [5]. These changes are not currently well-understood and may be amplified or reduced by factors such as test frame size, frame or supplemental shaker weight, test environment levels, and any shaker-frame coupling present in the shaker attachment method for a given test setup. Use of these additional components and attachment methods could increase the overall stiffness and damping of the test frame, which may enable alteration of high-amplitude resonances experienced by the test frame during testing.

Single-input, Single-output Testing

We conducted SISO shock and vibration tests on the GOBLET for a baseline comparison to the planned multi-axis supplemental shaker tests. All single-axis tests were conducted using the Unholtz-Dickie S452 shaker. The S452 (SISO tests) and H560 (MIMO tests) differ in characteristics, but we were comfortable using the S452 as a comparison because our goal was to compare a traditional test method to a new one rather than compare SISO versus MIMO with identical shakers.

We first ran the X-axis test with the S452 in its vertical configuration, then we ran the Y- and Z-axis tests with the shaker rotated horizontally and attached to the slip table. We torqued all socket head cap screws between the fixture plate and shaker armature or slip table to the same specification in each axis to ensure similar boundary conditions. Figure 6 shows the SISO test setups for each axis.

In all SISO tests, we used Simcenter Testlab software for control and Simcenter SCADAS hardware for data acquisition. For safety and data quality purposes, Simcenter Testlab allows the user to specify alarm and abort profiles above and below the reference PSD. In LANL qualification tests, we specify alarm profiles at ± 3 dB and abort profiles at ± 6 dB and direct Simcenter Testlab to stop the test if the computed test PSD exits the alarm or abort limits for 5% or 3% of frequency lines, respectively.

The S452 was able to achieve the Transport Random vibration environment for the full frequency range (6 Hz–2000 Hz) in all three axes. The Flight Random vibration environment was successful for the full frequency range (20 Hz–2000 Hz) in the X- and Y-axes, but we had to truncate the Z-axis frequency range to 20 Hz–1000 Hz. Above 1000 Hz, system resonances caused the test PSD to exit the abort limits for greater than 3% of frequency lines. After truncating the environment, the test satisfied our qualification control criteria. We achieved the Flight Shock environment but had the most difficulty with the X-axis waveform, which has the lowest acceleration magnitude.

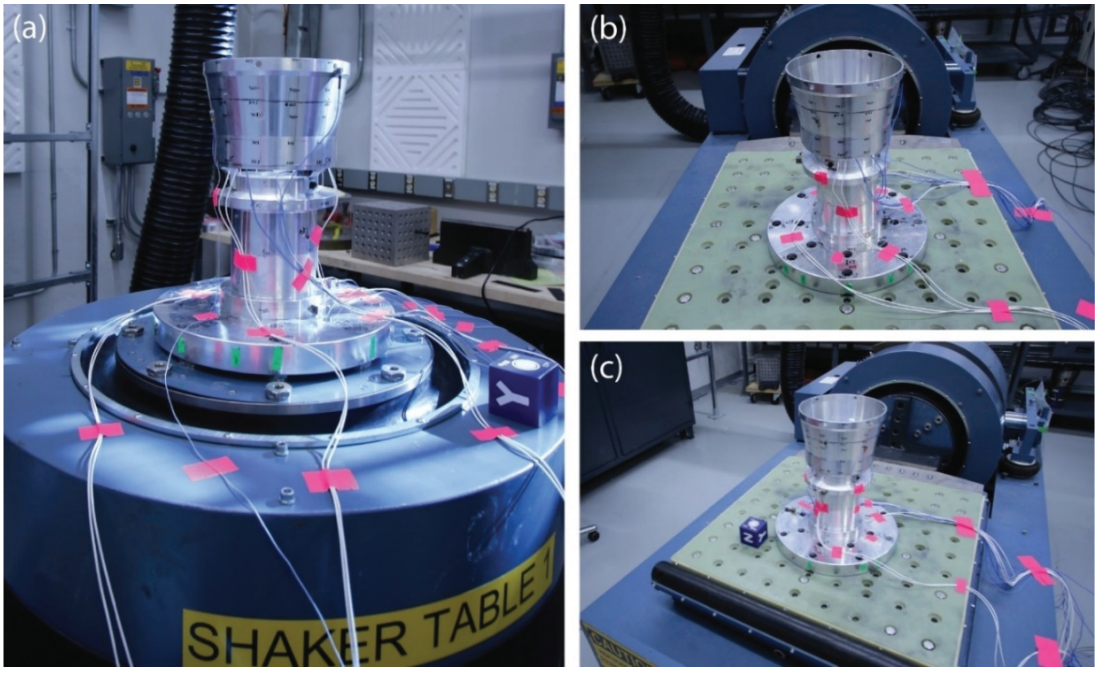

Fig. 6 Single-axis testing setups on the S452 shaker in the (a) X-axis test, (b) Y-axis test, and (c) Z-axis test

Multi-input, Multi-output Testing

After constructing the supplemental shaker frame, we conducted multi-axis testing over a 2-week period. The Unholtz-Dickie H560 shaker provided X-axis excitation, and two 110-lbf shakers (2110E from The Modal Shop) provided excitation in the Y- and Z-axes. We used Simcenter Testlab software and Simcenter SCADAS data acquisition hardware for all multi-axis tests. Each supplemental shaker imparted force through a compliant metal rod called a stinger that was threaded into a load cell, which was in turn threaded into a 3D-printed drive block. The drive block attached to the GOBLET using dental cement (DuraKore, Reliance Dental MFG and X60 Cold Curing Glue, HBK).

Before conducting a shock or vibration test, the Simcenter Testlab software completes a System Identification step. In this step, the controller outputs uncorrelated drive voltage signals to each shaker's amplifier at a flat, low-level PSD that spans the intended testing frequency spectrum. It then measures the response at the control DoFs (2101 X, Y, and Z) and computes system frequency response functions (FRFs). Using these FRFs, the software predicts whether the environment can be achieved by the shakers without exceeding the allowable drive voltage limits (10 V). If the environment requires too much drive voltage, we truncate the frequency range until the test is achievable.

Unlike the SISO tests, we relaxed the alarm/abort limit percentages to allow for test completion. Because the addition of multiple excitation sources and control DoFs creates a more challenging control problem, it is likely that the 5%-alarm and 3%-abort limits will need to be adjusted for MIMO qualification tests, but there has been no investigation into what percentage of excursion is allowable.

In Section 2.0, we presented the auto PSDs for the multi-axis test. In MIMO tests, cross power spectral densities (CPSDs), which describe the co-variance between two signals, are also present. The Simcenter Testlab software has two multi-input control modes: "Matrix" and "PSD." In Matrix mode, the user specifies CPSDs as a matrix at each frequency line. Because CPSDs are not currently included in the specification development process, the common practice within the Department of Energy Complex is to compute the CPSDs during the System Identification step, then populate the specification with the in-situ CPSD values. In PSD mode, the user specifies only the auto PSDs for control and allows in-situ CPSD population.

For our first test series with the supplemental shaker frame, we tried implementing Matrix mode control with the CPSDs from the System Identification step. However, the predicted required drive voltage levels were too high. We switched to PSD mode, which reduced the required drive voltage for the supplemental shakers. All results in Section 6.0 report auto PSD results from PSD mode control. Future work will make additional attempts to control using Matrix mode.

We began testing with the two supplemental shakers rigidly attached to the test frame branches (Figure 7(a)) and the drive blocks attached to Part B, the rigid cylinder, of the GOBLET. First, we ran the Transport Random environment. Although the Transport Random environment specification was defined from 6 Hz–2000 Hz in Section 2.0, we could not reach the low-

frequency, high-displacement values with our MIMO setup. This limitation was expected as displacements in a multi-input test cause shaker misalignment. We therefore truncated the environment to 20 Hz–2000 Hz. Despite truncating the lower frequencies, the rigid shaker attachment caused excessive, visible frame displacement during testing. We re-configured the test setup to have bungee attachment (Figure 7(b)) and were able to complete the transportation environment from 20 Hz–2000 Hz.

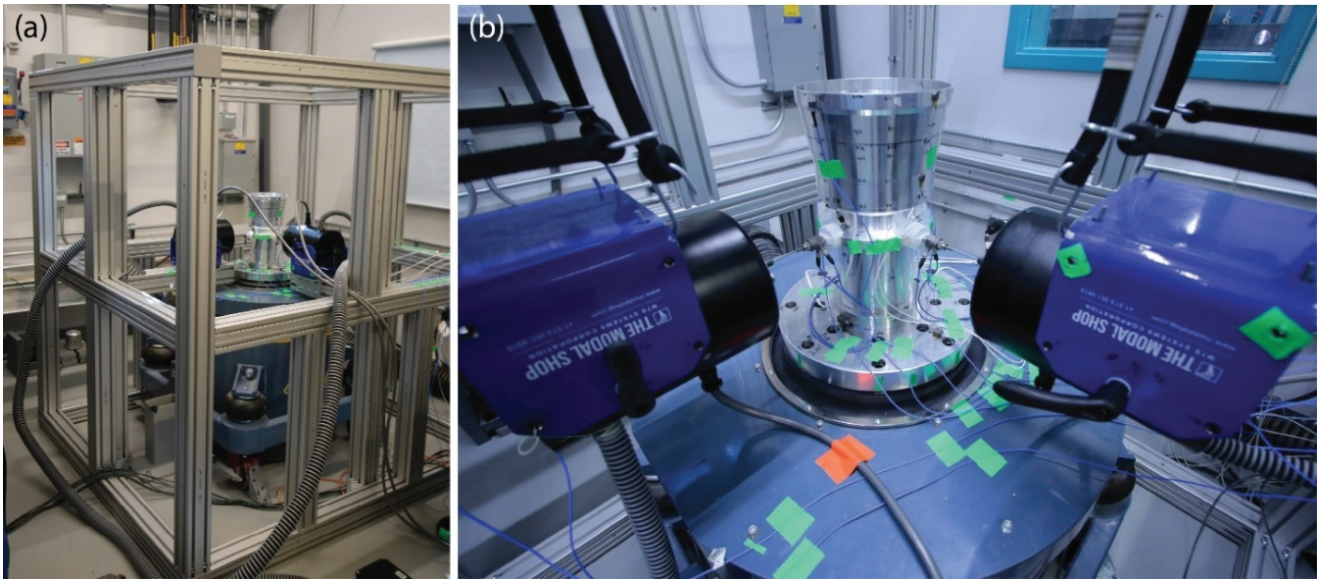

Fig. 7 In-situ test setup showing (a) the assembled frame, and (b) suspended supplemental shakers

Early in testing, we noticed that the print quality of the drive block influenced test success. Our first round of testing used polylactic acid filament and had the print layers oriented perpendicular to the application of shaker force, increasing the chance of delamination. We updated the print material to a carbon fiber and nylon filament and adjusted the print layer orientation so that the layers were parallel to the shaker force vector. We noticed that the estimated drive voltage required for the supplemental shakers was reduced after installing the new drive blocks, but it is important to note that other small changes, such as slight shaker alignments, could have influenced drive voltage as well.

We began to test the Flight Random vibration flight environment with the shakers imparting force on Part B of the GOBLET. In this configuration, we ran into issues with high required drive voltage. We determined that attaching the shakers to Part A, which is more compliant, might help create the same acceleration at Control Point 2101 with less shaker force (and therefore drive voltage). After we re-attached the drive blocks to the compliant portion of the GOBLET, we completed the test from 75 Hz–800 Hz. Below 75 Hz and above 800 Hz, the smaller supplemental shakers were unable to re-create the environment because of drive voltage limitations.

Lastly, we moved to the Flight Shock environment. Note that in Section 2.0, we provide a time waveform for the shock profile that creates the desired SRS profile. Common practice at LANL is to define the time waveforms for shocks to ensure consistency across different tests. While initializing the multi-axis shock program, we discovered that Simcenter Testlab's Shock & MIMO Shock Control does not allow the user to upload a time waveform for multiple control DoF shocks. Instead, the user must specify the SRS, then the software will generate an arbitrary time waveform. We also found that the software needs all output channels (i.e., the channels sending drive voltage to shakers) to be located on the same card in the data acquisition unit for shock testing, likely due to time synchronization. With only three shakers in this test, we were able to use a three-output card in our SCADAS data acquisition system, but this limit will be a problem for tests with more than three shakers. In our MIMO setup, the shock pulses had difficulty with accurate control and resulted in an over-test.

Results

Figure 8 shows the control performance for each DoF at the 270 Leg in comparison to the specification for the Transport Random environment. In single-axis testing, each of these tests was performed sequentially, resulting in independent data acquisition for each axis. For quantitative comparison of the specification and control performance, Table 2 reports the

G_{RMS} values for the specification, previously shown in Table 1, compared to the G_{RMS} values of the signal measured at the control location. Note that the G_{RMS} values of the MIMO specifications are lower than the SISO specifications because of truncation to a 20-Hz minimum control frequency. A positive percent difference between the specification and control G_{RMS} indicates an over-testing of the system in the respective axis, while a negative percent difference indicates an under-test. Similar analysis of the control performance and G_{RMS} values for the Flight Random environment are presented in Figure 9 and Table 3, respectively. Truncation to 20 Hz–1000 Hz of the Z-axis results in a decreased G_{RMS} value for the

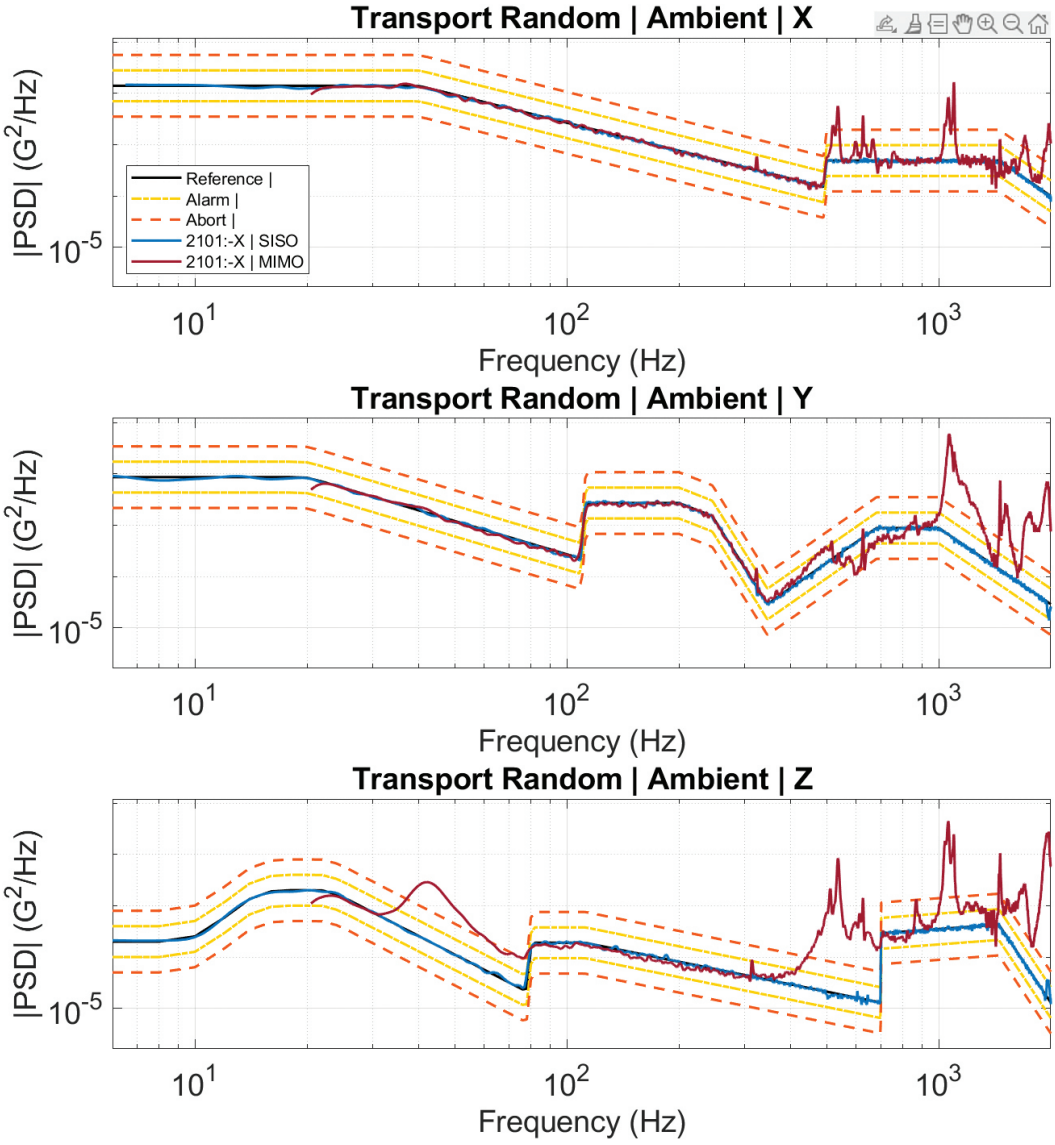

Fig. 8 Control PSD performance comparison for the Transport Random environment

Table 2 GRMS Comparison at Control Point 2101 for the Transport Random environment

	Channel Direction	Specification(GRMS)	Control(GRMS)	% Difference
Single-Axis	X	1.29	1.27	-2.00
	Y	1.11	1.09	-1.27
	Z	0.64	0.63	-0.79
Multi-Axis	X	1.22	1.44	16.5
	Y	1.04	2.20	71.6
	Z	0.62	2.05	107

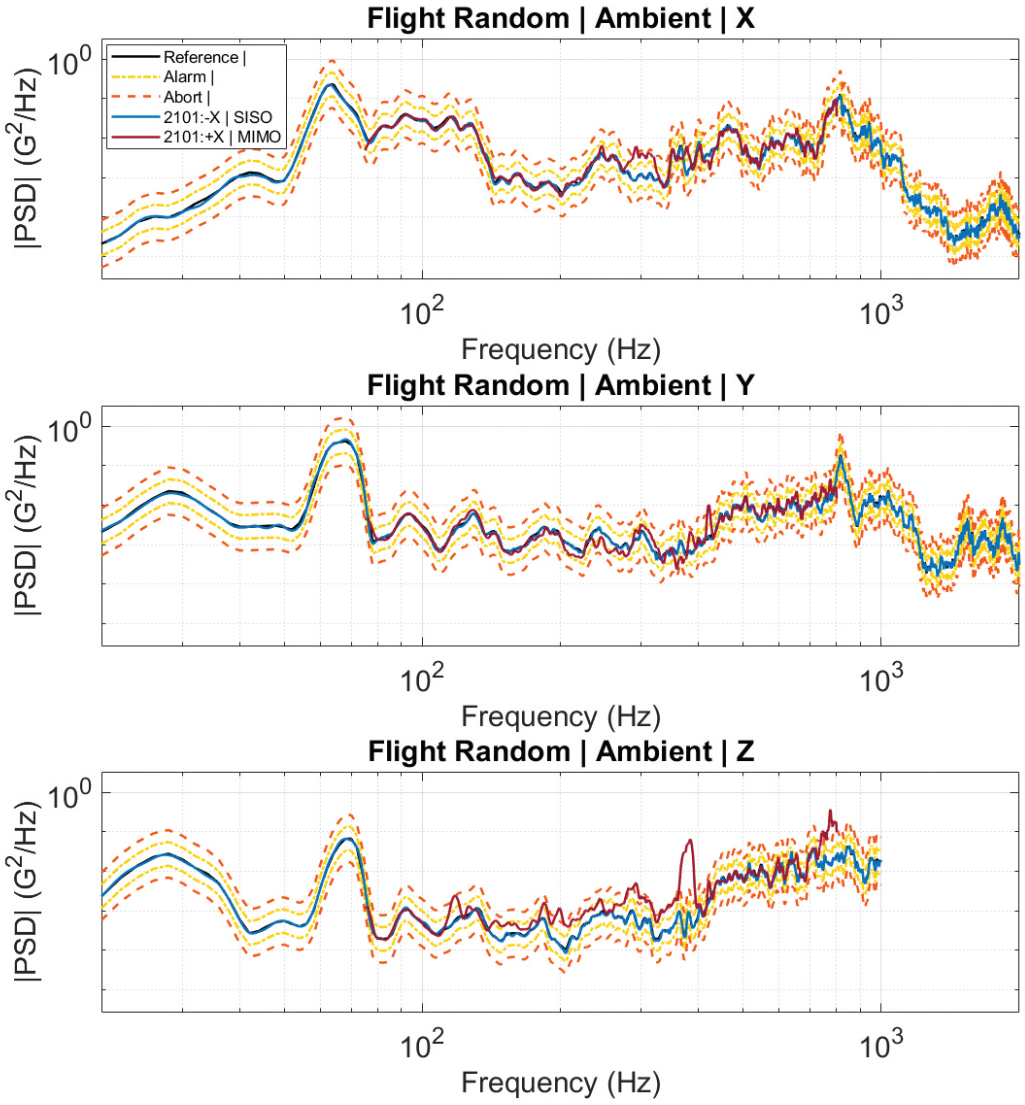

Fig. 9 Control PSD performance comparison for the Flight Random environment

Table 3 GRMS Comparison at Control Point 2101 for the Flight Random environment

	Channel Direction	Specification(GRMS)	Control(GRMS)	% Difference
Single-Axis	X	3.89	3.82	-1.77
	Y	4.16	4.10	-1.59
	Z	3.08	3.04	-1.36
Multi-Axis	X	2.63	2.70	2.63
	Y	2.09	2.25	7.37
	Z	2.19	3.79	53.5

SISO specification compared to Table 1, and truncation of the MIMO specification to 75 Hz–800 Hz further decreased specification G_{RMS} values.

Figure 10 compares the SRS between specification and test for the post-boost shock environment. Visual deviation of the test SRS profile from the reference SRS indicates over-testing or under-testing of the system. As discussed in Section 4.0, we controlled to the time waveforms for the shock environment, so Figure 11 shows the reference and test time data. While the SISO configuration controlled close to the specification value, seen in Figure 3, the MIMO configuration contains a significant spike in maximum acceleration of up to 16.1 G in the Y-axis, far higher than the maximum Y-axis specification

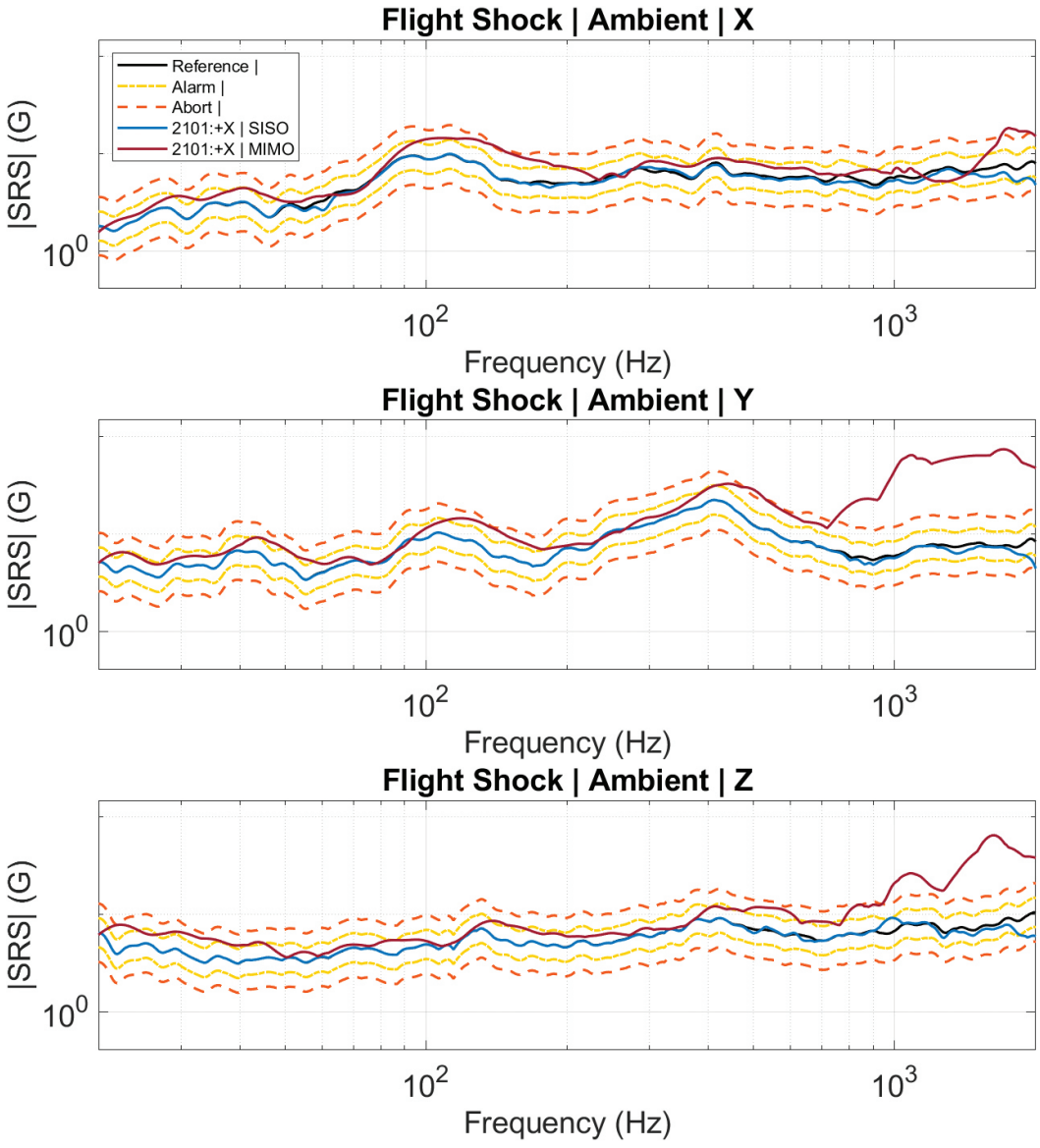

Fig. 10 SRS performance comparison for the Flight Shock environment

acceleration of 3.08 G. Comparison between these waveforms is difficult because the Simcenter Testlab software adds a buffer to the waveform, shifting the pulse further back in time.

In addition to assessing control performance, we evaluated the response at a non-control point of interest, Point 2504 (Figure 4). Instead of analyzing PSDs, we chose to evaluate the transmissibility between the control DoFs at Point 2101 and the in-axis response DoFs at Point 2504. Transmissibility computes the relative acceleration between a control and response channel and contains both amplitude and phase. Peaks in transmissibility amplitude correspond to system resonances, where there is higher acceleration at a response channel than at the control channel. Transmissibility phase describes the relative timing of the acceleration between control and response channels as a function of frequency. For example, a phase of 0° means the two channels are in phase, or exhibiting rigid-body motion. A phase not equal to 0° means the two channels are out of phase, or exhibiting flexion.

Coherence, plotted from 0 to 1 as a function of frequency, examines how much of the response channel data is explained by the measured control signal(s). For MIMO testing, we computed multiple coherence, which examines how much of the response channel can be explained by the combined effect of the control signals. This method allows for a distinction between response attributed to control signals and response attributed to noise, though the participation of individual control channels is not identifiable. Drops in coherence have three main causes: (1) dropouts or saturation in reference and/or response signals,

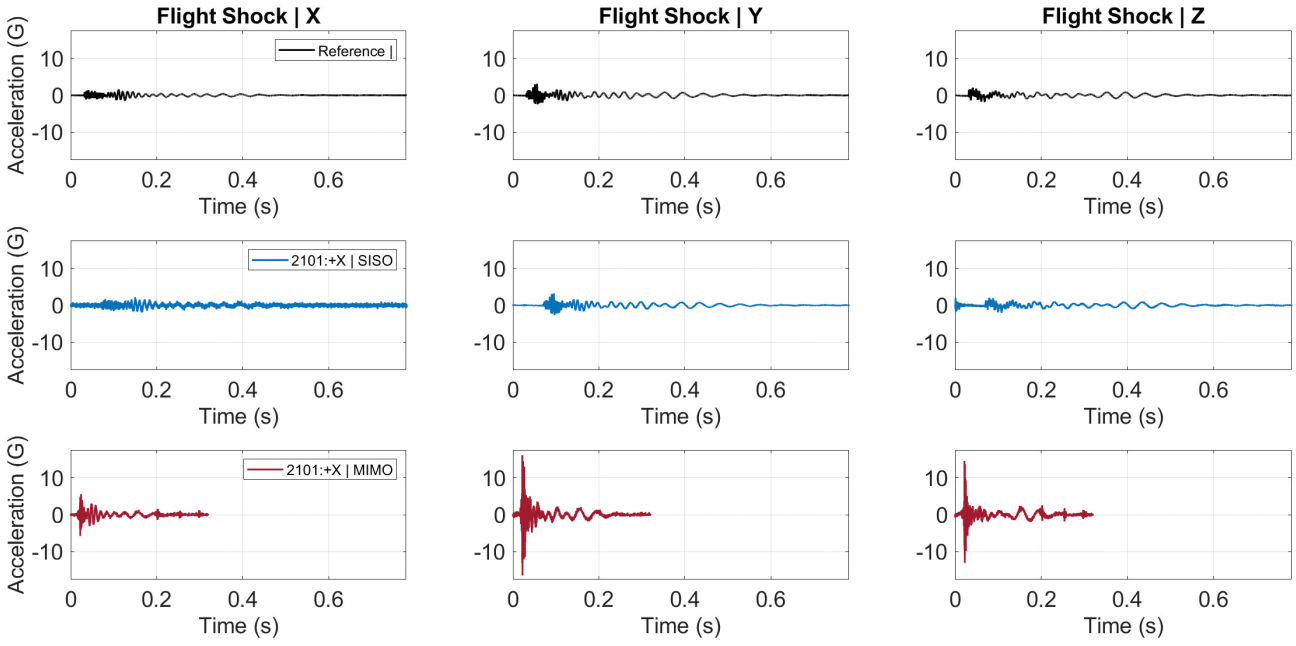

Fig. 11 Time waveform performance comparison at Control Point 2101 for the Flight Shock environment

(2) sensor problems such as faulty hardware or mounting conditions, or (3) system nonlinearity. Most often coherence drops when the response signal is low (e.g., at a system anti-resonance) or if there is rattling or other nonlinear mechanics in the system. Figures 12 and 13 show the coherence, transmissibility phase, and transmissibility magnitude between the control

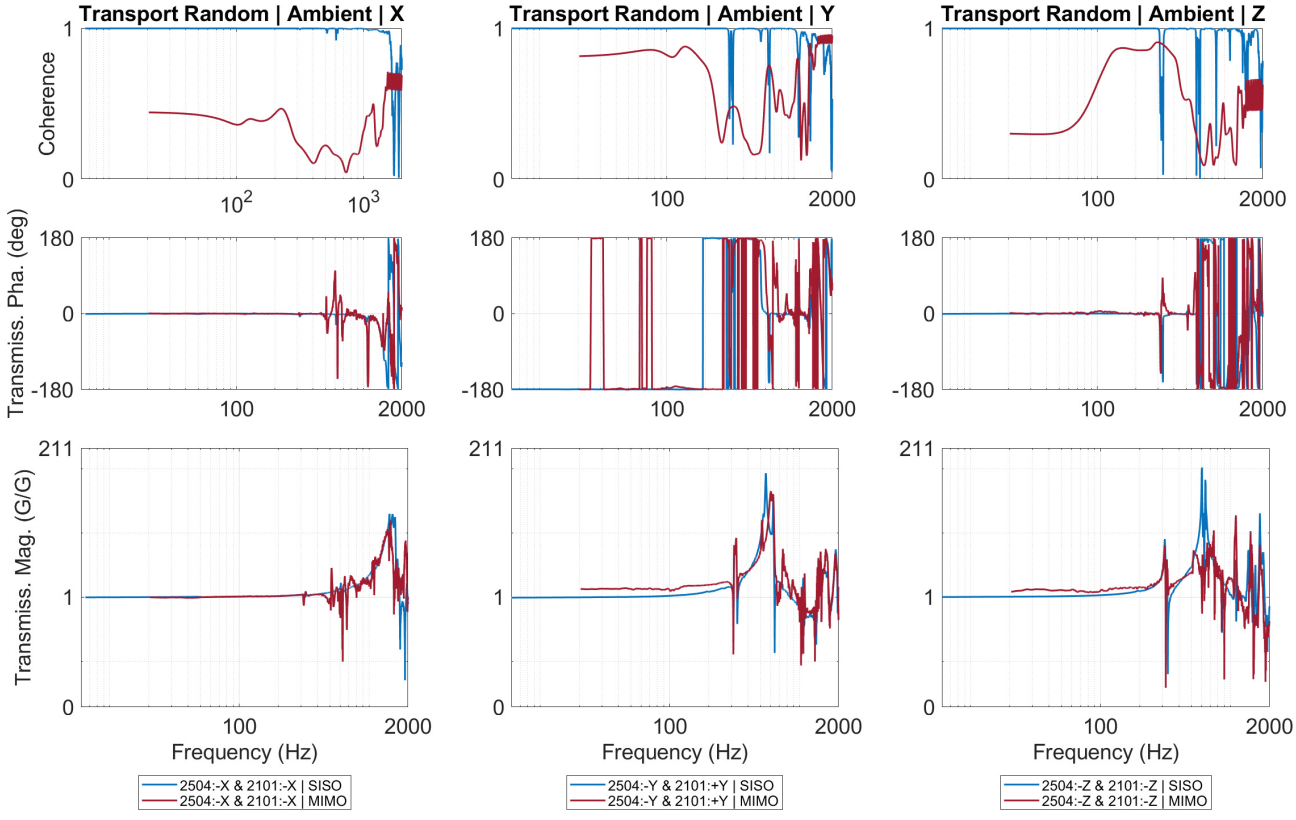

Fig. 12 FRF plots between Points 2101 and 2504 for the Transport Random environment

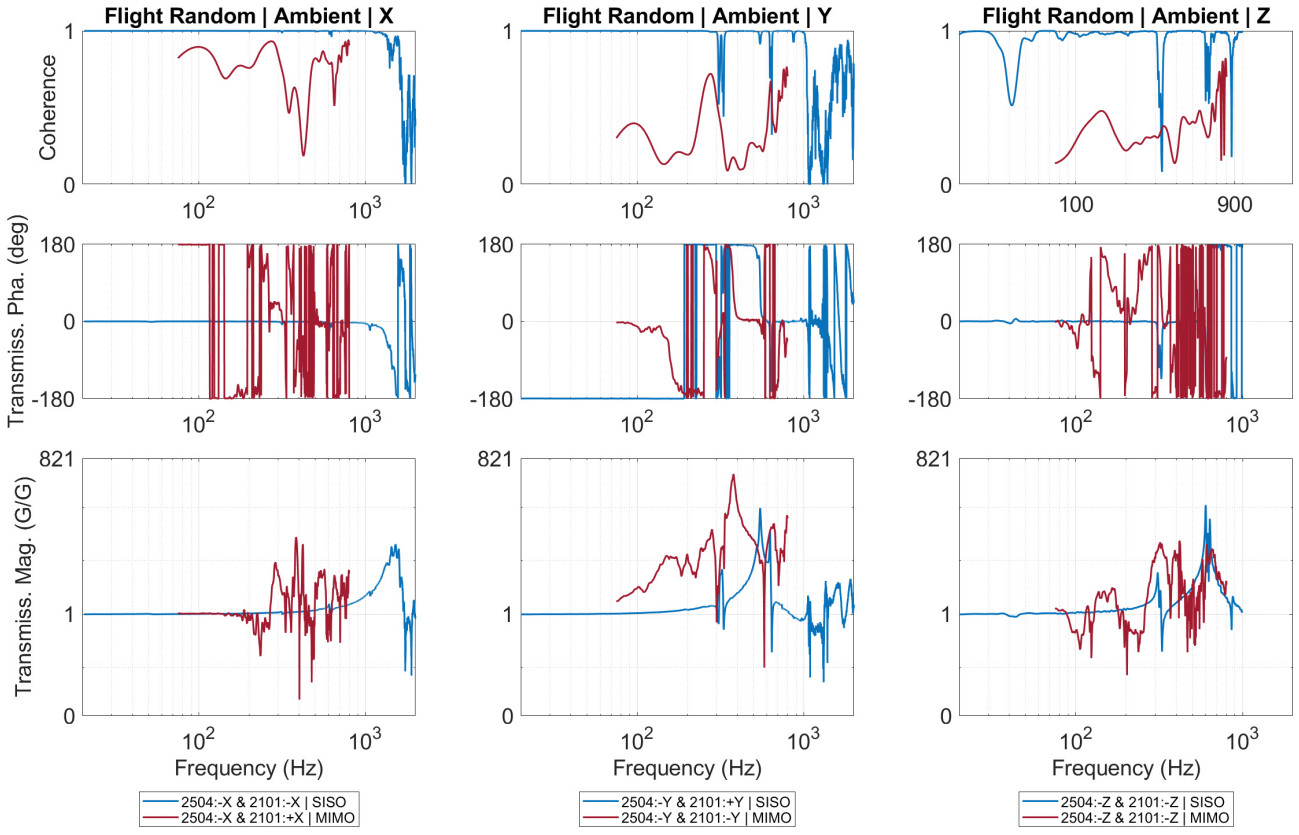

Fig. 13 FRF plots between Points 2101 and 2504 for the Flight Random environment

location (Point 2101) and the location of interest (Point 2504) for the Transport Random and Flight Random environments, respectively.

Discussion

By the G_{RMS} metric used in this study, the SISO tests produced lower control error than MIMO tests for both random vibration environments in all three axes. Interestingly, the SISO configuration resulted in under-tests at all control DoFs for both Transport Random and Flight Random environments, and the MIMO configuration resulted in over-tests. Excitation in other principal axes during each SISO test, also known as cross-axis excitation, may contribute additional energy to the system beyond the specification and lead to an over-test, but this phenomenon was not analyzed during this exploration of the MIMO test method. While it is expected that MIMO tests result in higher control error because of the added complexity of multiple control DoFs, the control performance for the MIMO Transport Random environment was unsatisfactory from 500 Hz–2000 Hz. The control challenges could be a result of many factors such as system resonance, shaker misalignments, shaker attachment locations, or shaker-frame interaction. Because of the limited testing window that we had for this study, we were unable to troubleshoot the poor control accuracy, but we will investigate methods for improvement in future work. Additionally, we plan to investigate strategies for increasing the MIMO frequency range to capture the full qualification environment, as well as analyzing cross-axis response from the SISO testing to better compare the test methods.

The Flight Shock environment had shortcomings in both SISO and MIMO testing. Consulting the shock time waveforms in Figure 11, we notice excessive high frequency content in the SISO X-axis shock pulse, included in the zero-padded signal before the pulse starts and during the ringdown. At first, we suspected an issue with the noise floor of our sensor, but further investigation revealed that the X-axis shock pulse magnitude, although the smallest of all three axes, was not near the noise floor of our control sensor. Next, we investigated whether the Point 2101 X sensor channel was broken. However, investigations revealed that the sensor and data acquisition channel were performing as expected during random vibration testing. Additionally, we replaced the Point 2101 triaxial accelerometer and attempted the shock pulse again; the same issues

remained present. One other source of poor performance could be the Simcenter Testlab shock controller. Unfortunately, the software is proprietary, so we are unable to explore what strategy the controller was using to create this shock pulse. We are interested in exploring the SISO shock control challenges further in future work, because the quality of SISO shocks is important for qualification testing.

As shown in Figure 11, the MIMO shock (maroon line) produced much larger acceleration levels than intended by the shock specification (black line). This over-test would not be acceptable for qualification tests, and future work should investigate whether control for MIMO shock with modal shakers can be improved to levels sufficient for qualification testing. Many factors, such as frame setup, shaker-frame interaction, shaker alignment and/or attachment, shaker location, and control software, could have played a role in the poor control accuracy. Perhaps with commercial MIMO setups, such as the Team Tensor 6 DoF platform, the hardware shortcomings could be less of an issue.

The SRS from both SISO and MIMO shock testing is shown in Figure 10. Comparing the poor performance in the time domain (Figure 11) to the SRS profiles in Figure 10, we note that the SRS alone does not provide enough information about control performance and data quality. For example, the X-axis SISO SRS visually matches the reference profile, with only a slight alarm excursion at 2000 Hz. However, as discussed earlier, the time waveform for the X-axis SISO test exhibited troubling high frequency content and was not considered a success. Likewise, although the MIMO SRS profiles from 700 Hz–2000 Hz exceed the specification, the excursions are visibly less extreme than the accelerations in the time waveform plots in Figure 11. The SRS is the common specification provided by customers for LANL qualification tests, but these findings hint that a different evaluation method should be explored.

The transmissibility magnitude remained similar between SISO and MIMO setups for the Transport Random environment (Figure 12), aside from a missing peak around 500 Hz–600 Hz in the Z axis. Recall that in Section 6.0, we attached the supplemental shakers to the rigid Part B for the Transport Random environment test. Because of this rigidity, it appears that the system dynamics remained similar between SISO and MIMO testing, and the relationship between Points 2101 and 2504 followed the same visual profile. Conversely, the transmissibility magnitude differed greatly between SISO and MIMO setups during the Flight Random environment test (Figure 13). Although we cannot compare dynamics for the full frequency range because of the truncation, within the 75 Hz–800 Hz range, we see many more peaks in transmissibility magnitude (i.e., resonances) for the MIMO test case. These additional resonances could be a result of change in the boundary conditions of the system when the supplemental shakers were mounted to Part A, the comparatively compliant location, for the Flight Random environment. Future work to optimize supplemental shaker attachment locations and better replicate boundary conditions will assist in evaluating the supplemental shaker method.

The transmissibility phase is difficult to evaluate because of sharp jumps between -180° and 180°, but it follows similar trends to transmissibility magnitude. There is less variation between SISO and MIMO for the Transport Random environment test (Figure 12), whereas for the Flight Random environment test (Figure 13), the phase changes occur at lower frequency values for the MIMO test than the SISO test. As we observed with transmissibility magnitude, the addition of shakers to the compliant Part A resulted in more resonances within 75 Hz–800 Hz, so the corresponding phase changes are reasonable.

The coherence between control signals and the response at Point 2504 is significantly lower in the MIMO configuration for both random vibration environments (Figures 12 and 13). Because we computed multiple coherence for the multi-axis tests, this lower value indicates that a large portion of the X-, Y-, and Z-axis response signals cannot be explained by the X-, Y-, and Z-axis control signals. We have not analyzed the coherence of the in-axis control and response signals (known as partial coherence), but it would be an interesting comparison for future work. Furthermore, the supplemental shakers and test frame may have introduced nonlinearities that contributed to the unexplained response signal.

Conclusion

This study aimed to extend previous work in supplemental shaker testing to all three principal axes, performing higher random vibration levels and MIMO shock environments with the assistance of an aluminum test frame. Our previous implementations showed promise for this test method, but area limitations resulted in only achieving two axes of excitation at levels lower than flight environments. In this paper, we present the GOBLET test assembly and relevant shock and vibration environments, describe our supplemental test frame design, conduct SISO tests for three environments to provide a comparison to traditional LANL shock and vibration test methods, and complete an initial three-axis MIMO test series with the supplemental shaker frame.

We learned valuable lessons about test setup during our first supplemental shaker test series. First, if shakers are to be rigidly attached to the test frame there must be other measures taken, such as isolating the shakers with rubber material or using stingers with ball joints to create compliance. Otherwise, the coupling between the frame, shaker, and test article produces too much frame movement and misaligns the shakers. Second, the print material and orientation of the additively

manufactured drive blocks are important for reaching test levels, especially for the Flight Random vibration. Third, the location of supplemental shaker attachment influences the frequency range and acceleration levels that can be achieved, as well as potentially modifying system dynamics. During shock implementation, we encountered some challenges with the Simcenter Testlab control software that may cause issues for future work.

The results presented here represent the first implementation of the new supplemental shaker test frame over a two-week test period. In future work, we aim to increase the tested frequency ranges of random vibration environments, investigate the poor control performance and low coherence during multi-axis tests, use optimization algorithms to inform supplemental shaker attachment locations, explore SISO cross-axis excitation, and develop a consistent MIMO test methodology to move this test method from the research and development (R&D) setting to the qualification setting.

Acknowledgments We would like to thank Lorenzo Placencia for assistance with the GOBLET design, Kirk Webber for strain gauge application on the GOBLET, Thomas Thompson and Kevin Craft for environmental specification development, and Alex Rose for help with supplemental shaker test implementation. This research is funded by the National Nuclear Security Administration (NNSA) Delivery Environments Program.

References

1. P. Daborn, “Smarter Dynamic Testing of Critical Structures,” Ph.D. dissertation, Aerospace Department, University of Bristol (2014).
2. D. Rohe, G. Nelson, and R. Schultz, “Strategies for Shaker Placement for Impedance-Matched Multi-Axis Testing,” in Sensors and Instrumentation, Aircraft/Aerospace, Energy Harvesting & Dynamic Environments Testing, Volume 7, C. Walber, P. Walter, and S. Seidlitz, Eds., pp. 195–212 (2020).
3. S. M. Danforth, S. M. Johnson, K. F. Fenstermacher, A. J. Ramirez, H. R. Sedillo, J. F. Schultze, and E. W. Ferguson, “Developing methods for single-axis base excitation vibration testing with additional distributed shakers,” in ISMA Conference on Noise and Vibration Engineering, pp. 860–871 (2024).
4. C. M. Harris and A. G. Piersol, Harris’ Shock and Vibration Handbook, 5th ed. (McGraw Hill, New York, New York, 2002), pp. 26.19–26.20.
5. H. R. Kramer, J. F. Schulze, S. M. Danforth, and B. P. Mann, “Dynamic Analysis of a Modular Test Stand for Multi-Axis Vibration Testing,” 43rd SEM International Modal Analysis Conference, Orlando, Florida, February 10–13, 2025, Los Alamos National Laboratory document LA-UR-24-30436.

Chapter 4
Smart Dynamic Testing of Aero Engine Externals: Challenges and Directions

Simon Euler, Ibrahim Sever, and Bernd Beirow

Abstract Aero engines are complex systems with stringent safety and performance requirements. These requirements apply to all engine parts, including a large number of control units, pipes, pumps, brackets etc. that sit outside gas path of a jet engine and are collectively referred to as externals. As with other parts in engines, manufacturers must demonstrate compliance with safety standards to regulatory authorities for the externals too. The said compliance evidence is mainly generated through rigorous qualification tests which are often based on specifications such as RTCA DO-160. However, such standardized tests may not accurately reflect real-world operating conditions, leading to over- or under-testing and potential in-service failures. Smart Dynamic Testing (SDT) is an evolving research domain aimed at addressing these limitations, encompassing Impedance-Matched Multi-Axis Testing (IMMAT), field environment characterization, control specification, test integration, and optimization. Among these, IMMAT has emerged as a promising methodology in experimental structural dynamics, aiming to replicate the in-field dynamic environment of the Unit Under Test (UUT) within a controlled laboratory setting. By replacing sequentially performed multiple single-axis tests with a single multi-axis test, IMMAT offers significant advantages in terms of cost and time savings, potentially eliminating the need for full-scale field trials. Despite its potential, IMMAT remains an open and complex research area, presenting several challenges. One key issue lies in the accurate definition of the target function, often hindered by incomplete sensor data from field measurements or the reliance on unvalidated numerical models. These limitations complicate the formulation of the Cross-Power Spectral Density (CPSD) matrix, which is essential for laboratory test replication. Furthermore, the placement of actuators (shakers) and control sensors is frequently based on engineering intuition, as systematic methodologies for their optimal configuration, and for the design of impedance-matched test fixtures, are currently lacking or underdeveloped. This paper exposes the challenges around SDT and provides an overview of the current methodologies and research areas approaching the underlying problems.

Introduction

The aerospace industry is a sector that depends heavily on the safety and reliability of its technical products. Aircraft manufacturers, engine producers, and component suppliers share the responsibility of demonstrating the functionality of their products under all operational conditions and throughout the product's lifecycle. This is achieved by providing evidence of functionality, mechanical integrity, and airworthiness to regulatory authorities, primarily through a combination of simulations and physical testing. The ultimate objective is to obtain product certification.

One critical area in which product robustness must be demonstrated is the field of aerodynamic and structure-borne vibration, which is the primary focus of this article.

For aero-engine manufacturers, components located outside the gas path – such as control units, pipes, pumps, and brackets (collectively referred to as externals) – are typically qualified through laboratory-based vibration testing. Depending on the application, this testing is carried out in accordance with standards such as RTCA DO-160G [1] for civil aviation or

Simon Euler · Bernd Beirow
Brandenburg University of Technology, Chair of Structural Mechanics and Vehicle Vibrational Technology, Cottbus, Germany
e-mail: Simon.Euler@Rolls-Royce.com; beirow@b-tu.de

Ibrahim Sever
Rolls–Royce plc., Derby, England, United Kingdom
e-mail: ibrahim.sever@rolls-royce.com

© The Author(s), under exclusive license to River Publishers 2026

Kristin B. Zimmerman, PhD (eds.), *Dynamic Evironments and Durability Testing, 2026, Vol. 7*, Conference Proceedings of the Society for Experimental Mechanics Series, https://doi.org/10.13052/rp-9788743814184

MIL-STD-810H [2] for defence applications. Although MIL-STD-810H permits multi-axis testing (see Method 527), most vibration testing continues to rely on traditional uniaxial methods developed in the 1960s and 1970s. These methods simulate a multi-directional vibration environment by sequentially applying excitation along the x-, y-, and z-axes using standardized test profiles and procedures [5, 6]. A typical vibration testing application in aero-engine development involves replicating a failure mode observed either on a development engine or in the operational fleet. Accurate replication in the lab requires environmental measurements from the system. However, due to the limited number of sensors installed on an engine, these measurements often do not coincide precisely with the failure location. As a result, the acceleration data used for base excitation is typically estimated from the closest available sensor.

Vibration Testing of Aero Engine Components

For this study, a simplified test setup was developed to represent a system environment. The setup consists of a pipe (e.g., a fuel line, representing the Unit Under Test – UUT) mounted on a steel beam (representing the Next-Level Assembly – NLA), and excited by a constant random drive signal form a $1kN$ shaker. The experimental setup is illustrated in figure 1a. Acceleration and force sensors were placed in-plane with the structure, aligned along the x-axis as shown in the figure. The measured power spectral density (PSD) spectra from selected sensors are presented in figure 1b. Notably, sensors $Acc12$ and $Acc17$ exhibit a peak at approximately $135Hz$. At this frequency, the PSD value at the coupling point between the beam and the vertical connection – measured by $Acc03$ – is approximately $0.008g^2/Hz$.

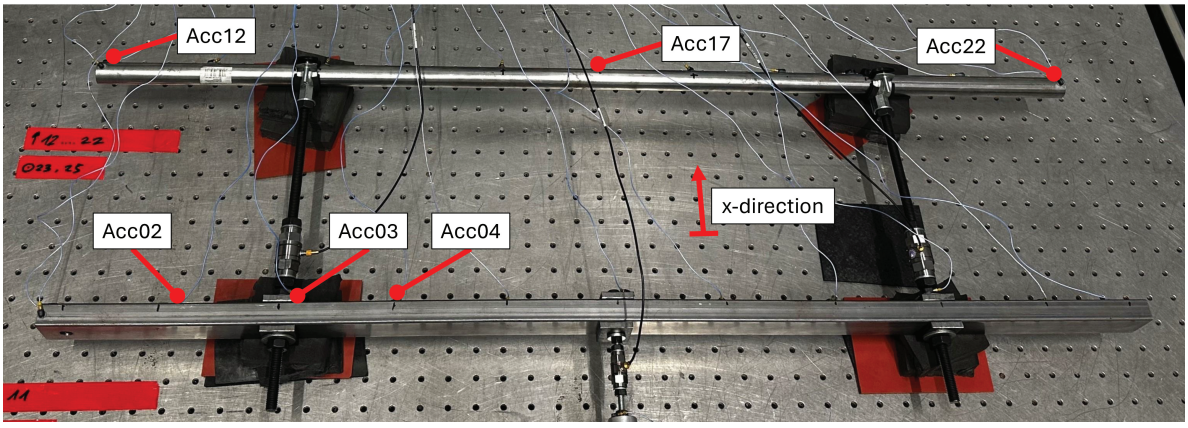

(a) UUT in System Environment

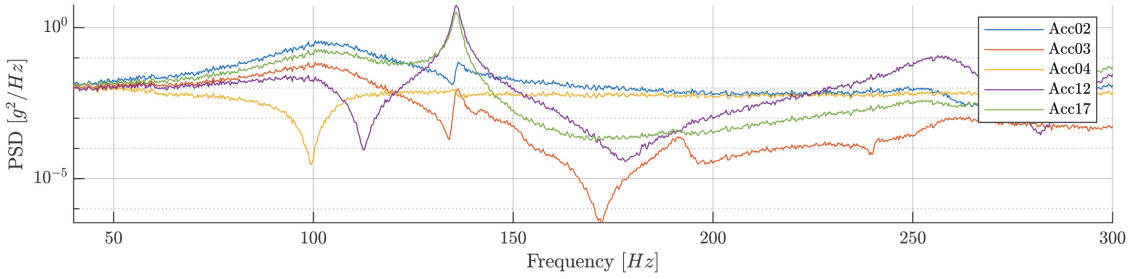

(b) PSD of selected sensors from system environment (with NLA)

Fig. 1 Simplified experimental set-up for pipe testing

A typical objective in a laboratory vibration test is to reproduce this peak excitation on the UUT through base excitation – commonly for high cycle fatigue (HCF) or qualification testing – using a defined acceleration input. The set-up for the laboratory configuration is shown in figure 2a. To investigate the influence of differences in mechanical impedance between the field and laboratory systems, an initial test was performed by directly applying the same PSD value ($0.008g^2/Hz$) measured by $Acc03$ in the system environment. This excitation was applied across a frequency range from $100Hz$ to $300Hz$. The resulting PSD spectra are shown in figure 2b.

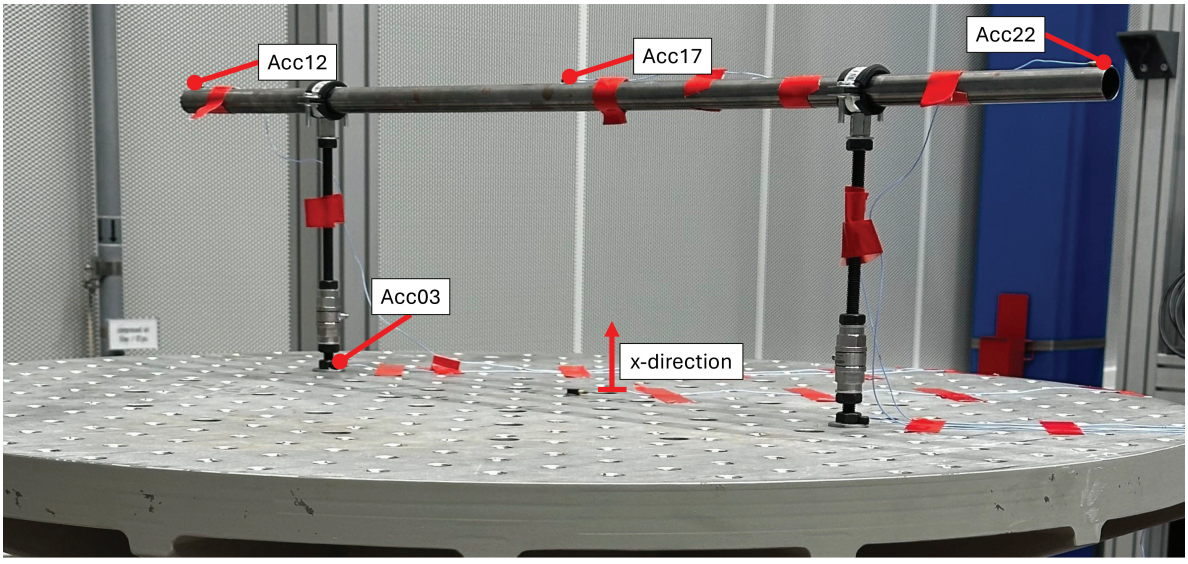

(a) UUT base excitation

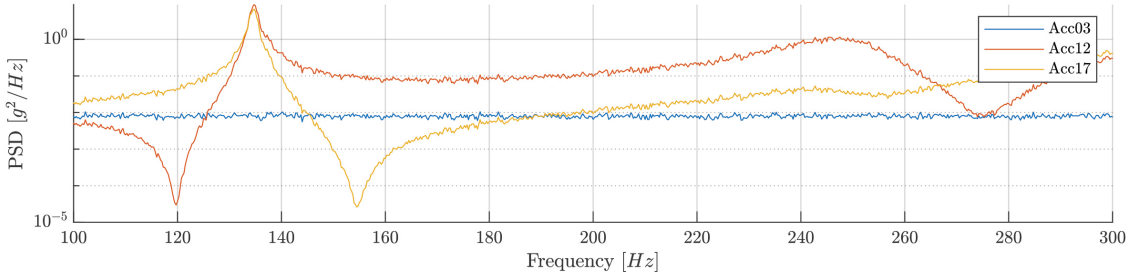

(b) PSD of $Acc03$, $Acc12$ and $Acc17$ from base excitation (Headexpander)

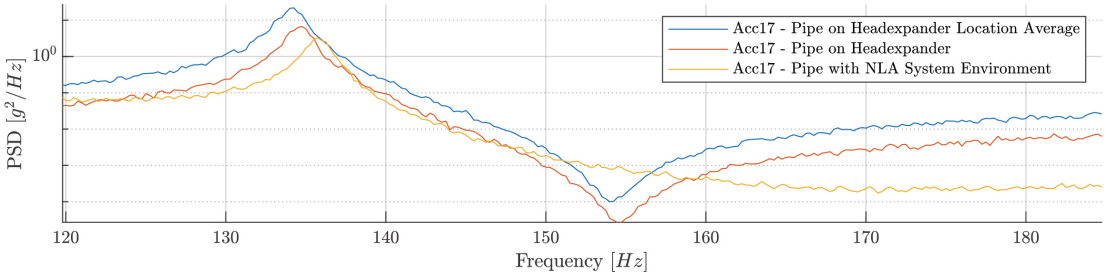

(c) $Acc17$ of system environment and base excitation

Fig. 2 Simplified experimental set-up for pipe testing

Often, the test engineer does not have access to measurements taken directly at the component interface. In such cases, nearby sensor data is typically used to estimate the base acceleration. For instance, if data from sensor $Acc03$ (located at the interface) is unavailable, one might use the PSD values from nearest sensors – such as $Acc02$ and $Acc04$ – and compute their average to define the base excitation. Based on this approach, the second test with the laboratory set-up was done with a base excitation of $0.0258 g^2/Hz$.

The resulting PSD spectra for sensor $Acc17$ of the different set-ups are shown in figure 2c. When compared to the system environment data, it becomes evident that even when using the exact interface acceleration, the Unit Under Test (UUT) experienced an over-test of approximately twice the amplitude due to differences in the mechanical coupling impedance between the field and lab set-ups. When instead using the average of neighbouring sensors, the over-test increased by a factor of six. This result highlights a key issue: base-controlled vibration tests can lead to significant over- or under-testing

depending on the mechanical impedance mismatch between the laboratory setup and the actual system environment. To address this, it becomes reasonable to consider response-controlled testing as an alternative.[1]

The first response-controlled test was carried out using the laboratory setup on the head expander (figure 2a), with the PSD of sensor $Acc17$ from the system environment serving as the reference. Figure 3a compares the controlled response at $Acc17$ to the target PSD from the system environment. The results show a good match at the control point. However, examining the uncontrolled response at $Acc12$ reveals that the component was under-tested at $135Hz$ and over-tested around $160Hz$, relative to the field data (figure 3b). This highlights a fundamental challenge: controlling a single response point is often insufficient to accurately reproduce the entire system dynamic.

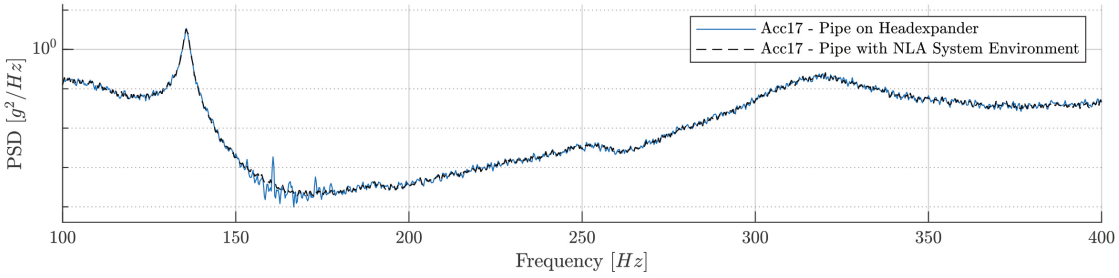

(a) Sensor $Acc17$ (Controlled) – Target PSD from System Environment and measured PSD

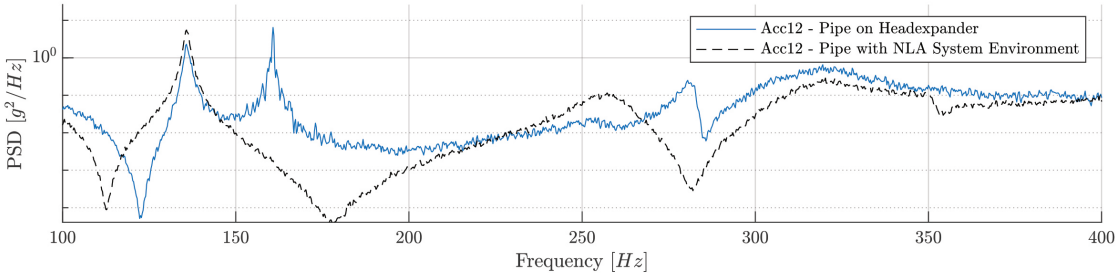

(b) Sensor $Acc12$ (Not Controlled) – Target PSD from System Environment and measured PSD

Fig. 3 Response-controlled at $Acc17$ on headexpander

To better replicate the dynamic environment, a rudimentary Multi-Exciter Single-Axis (MESA) setup was build by placing the UUT on two shakers (figure 4). The reference Cross-Power Spectral Density (CPSD) matrix for this random test was formulated using the PSD and phase data from the system environment (similar to the approach from Daborn et al. [5]). A coherence value of 1.0 was assumed across the frequency range.[2] The obtained PSD for the control points $Acc17$ and $Acc12$ can be found in figure 5a and figure 5b. It can be seen, that there are still control issues around a certain bandwidth of the anti-resonances, but in general showing a significant improvement in the response of the now controlled position $Acc12$.

Nevertheless, even by adding an additional control point to the UUT, the majority of the component is still uncontrolled during the test. For example, sensor $Acc22$ – located at the far right of the UUT – remains uncontrolled across all tests. Comparing its response from the test on the headexpander (figure 6a) and the dual shaker setup (figure 6b) shows that the response does not only differ significantly from the system environment, but switching to dual control can sometimes worsen the correlation. These results demonstrate a critical point: simply adding more exciters or control points may not be sufficient. There is a growing need for impedance-matched fixtures or a higher number of control points to better replicate the system environment dynamics.

The test series presented in this section underscores the uncertainties introduced by standard base-controlled vibration testing, which often lead to over- or under-testing. In practice, such uncertainties are typically addressed by applying conservative safety factors or broad acceleration envelopes, which can result in severe over-testing.[3] Response-controlled testing

[1] It is worth mentioning, that at least the RTCA DO-160 does not intend to carry out response-controlled testing.

[2] The MIL-STD-810H Method 527.2 Annex D recommends to use a coherence between 0.95 to 0.98 in the CPSD formulation, if not available from field measurements, to account for the always present noise in the measurement. This will be considered in future measurements.

[3] Daborn et al. [5] showed, that using "enveloping" over-tests the UUT by magnitudes.

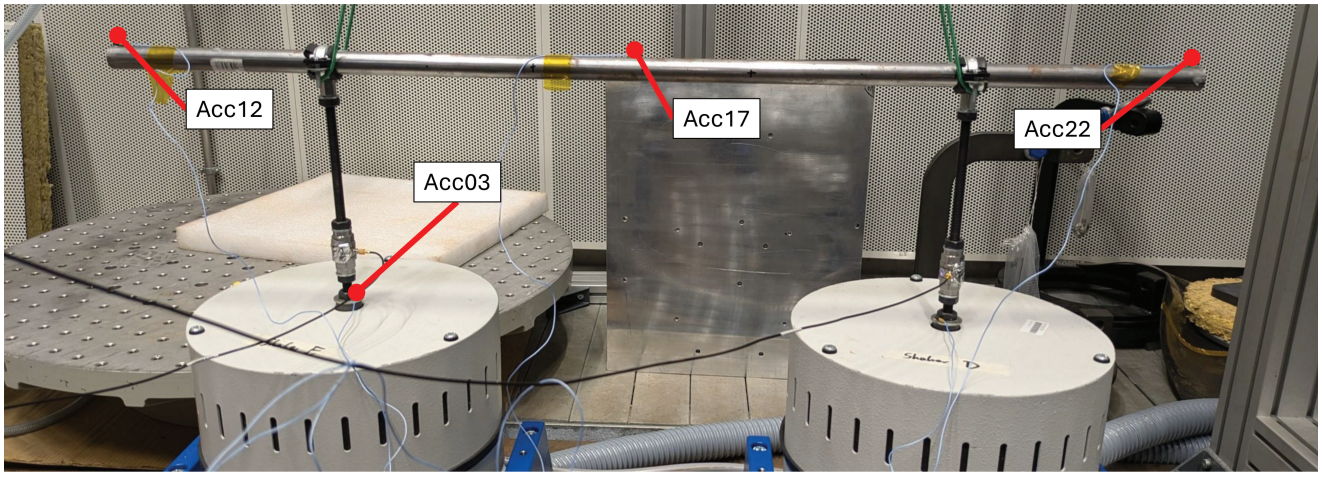

Fig. 4 UUT on Dual Shaker Set-Up

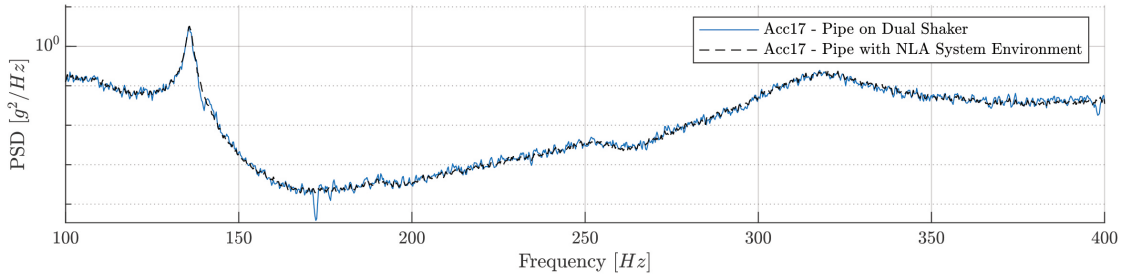

(a) Sensor $Acc17$ (Controlled) – Target PSD from System Environment and measured PSD

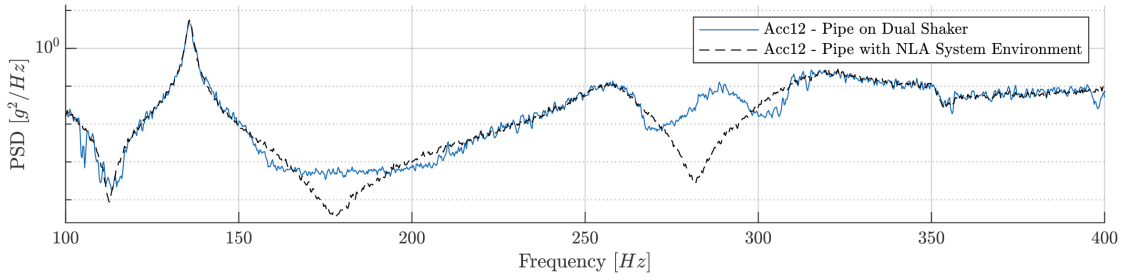

(b) Sensor $Acc12$ (Controlled) – Target PSD from System Environment and measured PSD

Fig. 5 Response-controlled at $Acc12$ and $Acc17$ on dual shaker

offers a more targeted approach, particularly when transitioning from single- to multi-exciter setups. However, even with increased control points, unmeasured positions may still exhibit significant deviations from their reference responses, as demonstrated in the final experiment.

Smart Dynamic Testing

Smart dynamic testing is an emerging research area aimed at addressing the limitations outlined in section . It provides the foundation for advanced techniques such as Impedance-Matched Multi-Axis Testing (IMMAT). Additional challenges not captured by the test series – such as field environment characterization, reference signal formulation, fixture design, and sensor/exciter placement – must also be considered.

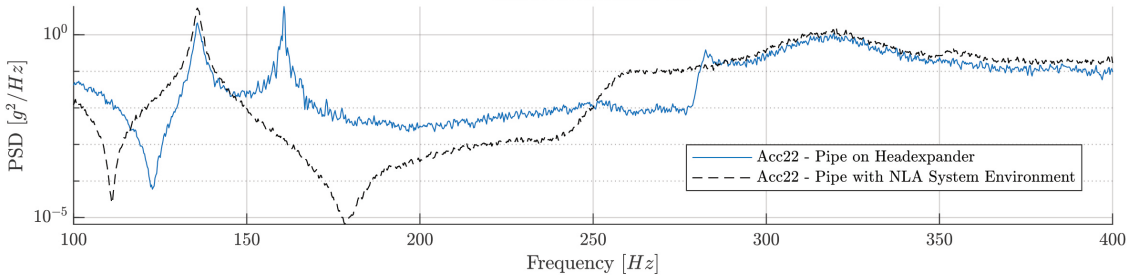

(a) Sensor *Acc*22 (Not Controlled) – Target PSD from System Environment and measured PSD

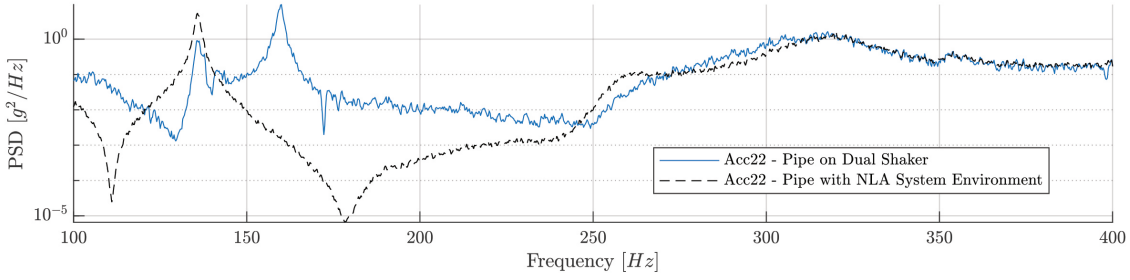

(b) Sensor *Acc*22 (Not Controlled) – Target PSD from System Environment and measured PSD

Fig. 6 *Acc*22 of response-controlled at headexpander on dual shaker test

The overarching goal is to enable accurate replication of the system environment in the laboratory, without requiring the full physical system, by virtually planning and optimizing the IMMAT approach in advance. Several key developments are summarized below.[4]

Field Characterization and Test Specifications

Daborn et al. [5] presented a method to replicate the system dynamics of a free-flying missile in a multiple-input multiple-output (MIMO) vibration test. They also showed, that a MIMO test is operating with lower force levels compared to traditional vibration testing, indicating an inherent problem with traditional test set-ups. The authors pointed out, that there is need for research in the area of test specification, as cross spectra many not always be available from direct measurements.

Mayes [8] introduced a method combining Modal Craig-Bampton (MCB) substructuring with a Transmission Simulator (TS) to decompose the system into the elastic response of the fixture/NLA and the fixed-base motion of the component. This technique enables quantification of mechanical impedance mismatches between lab and field environments and supports the selection of appropriate control parameters. Schultz and Nelson [13] proposed strategies to address differences between field and lab setups using spatial and frequency averaging, as well as frequency axis warping.

Shaker and Sensor Placement

Rohe et al. [9] developed a shaker placement method for IMMAT and highlighted the dependency of results on control strategy. Their method used the frequency response matrix obtained from modal impact tests to predict responses across different exciter combinations.

Beale and Schultz [3] developed and demonstrated [4] a sensor selection method for multi-exciter test, based on an error metric that quantifies the difference between the reference CPSD and the predicted response of a preselected set of sensors. To apply this method, one needs the frequency response functions of the laboratory system to calculate the laboratory response. Mayes et al. [7] presented a shaker placement strategy that uses substructured models and amplifier constraints to ensure target responses are met without exceeding operational limits.

[4]This is not meant to be a full literature review and only shows exemplary work in the areas.

Impedance-Matched Multi-Axis Testing

As early as the 1960's Klein and Piersol [6] pointed out, that an impedance-mismatch leads to a severe difference between the laboratory test and the coupling impedance in field. Scharton [10] showed, that using multimodal fixture to replicate the mounting point impedance, leading to a significant improvement of the structural response and developed a design guidelines for multimodal fixtures, including dimensions, measured point impedance, modal density and damping of the fixture. These fixtures enabled smaller shakers to achieve target vibration levels and provided a more triaxial excitation environment.

Schoenherr et al. [11] used an objective function that is based on matching the frequency response matrix of the laboratory and field configuration. Due to the amount of local minima the solution did not convert towards the global minium. Latest research of Schoenherr et al. [12] shows, that using an optimization approach with an objective function, based on the modal projection error is converging best towards an impedance-matched design, but also mentions, that the gradient based algorithm is struggling to follow the decreasing slope in the solution space. Tuman et al. [15] proposed the Transmission Simulator IMMAT (TS-IMMAT) approach, wherein only the control points on an impedance-matched fixture are excited. Although promising, challenges remain – e.g., reproducing radial responses in rocket vibration environments.

Conclusion and Planned work

This paper highlights the key differences between standard base-controlled vibration testing – such as that used for component qualification – and more advanced Multi-Exciter Single-Axis (MESA) configurations. The tests showed that coupling impedance plays a crucial role in determining the actual dynamic loading experienced by the UUT. While transitioning from base-controlled to response-controlled testing can reduce over-testing, the limited number of control points in conventional setups restricts test accuracy. Even MESA configurations only partially address this issue. Future work will focus on:

- Topology optimization for the design of impedance-matched fixtures, that replicates the field dynamics over a predefined frequency range.
- Incorporation of real aero-engine structures, including larger components and higher response magnitudes.

These efforts aim to move closer toward accurate, efficient, and reliable dynamic testing that truly reflects the operational environment, enabling better qualification of aerospace components.

Acknowledgments The authors gratefully acknowledge financial support from the State of Brandenburg (Germany), the EU and Rolls-Royce Deutschland Ltd & Co KG (Rolls-Royce). The authors also thank Rolls-Royce for granting permission to publish the results in this work.

References

1. *RTCA DO-160G*. Radio Technical Commission for Aeronautics, USA, 2010. URL https://www.rtca.org/do-160/.
2. *MIL-STD-810H*. Department of Defence, USA, 2019.
3. C. Beale and R. Schultz. Sensor Selection for MIMO Vibration. Technical report, Sandia National Laboratories (SNL-NM), Albuquerque, NM, 2020. URL https://www.osti.gov/biblio/1836906.
4. C. Beale, R. Schultz, C. Smith, and T. Walsh. Degree of Freedom Selection Approaches for MIMO Vibration Test Design. In *Proceedings of the 40rd IMAC*, volume 5, pages 81–90. Society for Experimental Mechanics, Springer Nature Switzerland AG, 2022. URL https://doi.org/10.1007/978-3-031-05405-1_10.
5. P. M. Daborn, P. R. Ind, and D. J. Ewins. *Enhanced ground-based vibration testing for aerodynamic environments*, volume 49, pages 165–180. Elsevier Ltd., 2014. URL https://doi.org/10.1016/j.ymssp.2014.04.010.
6. G. H. Klein and A. G. Piersol. *The development of vibration test specifications for spacecraft applications*, volume 4, pages 88–115. Elsevier Ltd., 1966. URL https://doi.org/10.1016/0022-460X(66)90156-8.
7. R. Mayes, L. Ankers, P. Daborn, T. Moulder, and P. Ind. *Optimization of Shaker Locations for Multiple Shaker Environmental Testing*, volume 44. Springer Nature Switzerland AG, 2019. URL https://doi.org/10.1007/s40799-019-00347-7.
8. R. L. Mayes. A Modal Craig-Bampton Substructure for Experiments, Analysis, Control and Specifications. In *Proceedings of the 33rd IMAC*, volume 4, pages 93–98. Society for Experimental Mechanics, Springer Nature Switzerland AG, 2015. URL https://doi.org/10.1007/978-3-319-15209-7_9.
9. D. P. Rohe, G. D. Nelson, and R. A. Schultz. Strategies for Shaker Placement for Impedance-Matched Multi-Axis Testing. In *Proceedings of the 37th IMAC* Soc [14], pages 195–212. URL https://doi.org/10.1007/978-3-030-12676-6_18.
10. T. D. Scharton. *Development of impedance simulation fixtures for spacecraft vibration test*. Aeronautics and Space Administration, 1969. URL https://ntrs.nasa.gov/api/citations/19690016937/downloads/19690016937.pdf.
11. T. Schoenherr, P. Coffin, and B. Clark. Use of Topology Optimization to Design Shock and Vibration Test Fixtures. In *Proceedings of the 37th IMAC* Soc [14], pages 77–92. URL https://doi.org/10.1007/978-3-030-12676-6_18.

12. T. Schoenherr, B. Zwink, and R. Schultz. *Optimization of an Impedance-Matched Test Fixture with the Modal Projection Error*, volume 49. Springer Nature Switzerland AG, 2025. URL https://doi.org/10.1007/s40799-025-00794-5.
13. R. Schultz and G. Nelson. Techniques for Modifying MIMO Random Vibration Specifications. Technical report, Sandia National Laboratories (SNL-NM), Albuquerque, NM, 2021. URL https://www.osti.gov/biblio/1892146.
14. *Sensors and Instrumentation, Aircraft/Aerospace, Energy Harvesting & Dynamic Environments Testing*, volume 7, 2019. Society for Experimental Mechanics, Springer Nature Switzerland AG. URL https://doi.org/10.1007/978-3-030-12676-6_18.
15. M. J. Tuman, M. Behling, M. S. Allen, W. J. DeLima, J. Hower, and R. L. Mayes. *Balancing Impedance and Controllability in Response Reconstruction with TS-IMMAT*, volume 48. Springer Nature Switzerland AG, 2023. URL https://doi.org/10.1007/s40799-023-00645-1.

Chapter 5
Correlating Damage in Vibration Environments Using Fixed-Base Modal Responses

Marcus Behling, Matthew S. Allen, Randy Mayes, and Washington DeLima

Abstract A significant challenge in dynamic environment testing is understanding how accurately the in-flight stress is recreated in the lab test. The RMS dB error metric is often used to gauge test success, and while it accurately quantifies the spectral differences between the flight and lab responses at various DOF, its correlation with stress is poorly understood. This study proposes an alternative metric and compares it to RMS dB error by simulating SDOF, 3DOF, 6DOF, and IMMAT tests using a finite element model case study. The proposed metric is shown to be better correlated with RMS Von Mises stress than RMS dB error in these simulated tests. It is observed to be best correlated to stress when modal responses are accurately reconstructed, though it marks an improvement over RMS dB error even when this is not the case.

Keywords Random vibration · Error metric · Fixed-base modes · Multi-axis testing · finite element modeling

Introduction

Vibration qualification tests are performed to verify a component's durability in its intended operating environment. The original military standard for these tests [1] specified enveloped acceleration power spectral densities (PSDs) to be controlled near the base of the device under test (DUT) in a single axis. Multi-axis testing methods, such as 6DOF [2] and Impedance Matched Multi-Axis Testing (IMMAT) [3], have grown in popularity in the past decade and have demonstrated the potential to improve environment reconstruction [4]. The preferred control target for these tests is an acceleration PSD matrix that is defined across various degrees of freedom (DOF) on the DUT. In single-axis and multi-axis tests, the controller replicates the environment as closely as possible. The RMS dB error metric, described in [5], is commonly used to quantify how accurately the flight environment is reconstructed. It is a measure of the area, in dB, between the flight and lab environments and thus is closely correlated with a visual comparison of the two environments plotted in dB. If the RMS dB error is low and the DUT functions properly during the test, it is deemed ready for flight.

Even though this metric is commonly used, the correlation between RMS dB error and stress is poorly understood. A test with a low RMS dB error might recreate stress inaccurately, in other words; a DUT that passes the test could fail in flight, and one that fails the test might have been flight-ready but would be redesigned and retested unnecessarily. One study suggested that RMS dB error is better correlated to stress than a variety of other metrics [6], though the two were found to have an

Marcus Behling
Graduate Research Assistant, Brigham Young University, Department of Mechanical Engineering
e-mail: mebehlin@byu.edu

Matthew S. Allen
Professor, Brigham Young University, Department of Mechanical Engineering
e-mail: matt.allen@byu.edu

Randy Mayes
Mayes Consulting
e-mail: rajnd75@msn.com

Washington DeLima
Honeywell Federal Manufacturing and Technologies
e-mail: wdelima@kcnsc.doe.gov

© The Author(s), under exclusive license to River Publishers 2026

Kristin B. Zimmerman, PhD (eds.), *Dynamic Evironments and Durability Testing, 2026, Vol. 7*, Conference Proceedings of the Society for Experimental Mechanics Series, https://doi.org/10.13052/rp-9788743814184

average Pearson correlation magnitude of only 0.11 across 100 simulated tests. This value increased to 0.26 when modal rather than physical acceleration responses were used, suggesting that modal responses are better correlated to stress. Others have similarly investigated modal metrics: Harvie [7] and Schoenherr [8] used fixed-base and free-free modes, respectively, to compare flight and test environments. Harvie's study showed that modal responses provide valuable insight that physical responses lack, and Schoenherr proposed comparing RMS free modal responses.

RMS dB error can also pose logistical problems to a testing program as the test environment often has to meet error requirements. A common requirement is that all spectral lines lie within 3 or 6 dB of the specification, and a similar requirement could be placed on the RMS dB error. If the error exceeds the maximum acceptable value, the test setup or environment must be modified, though doing so is not necessarily trivial; Schultz proposed a method for modifying a given environment to be more controllable in the lab [9], though it does not seem to have been extensively tested at this point. One could also use Daborn's buzz test method [10] to redefine the cross-PSDs, though the environment may remain challenging to recreate in the lab, and this procedure is likely to modify the reconstructed stress in ways that are poorly understood.

This study proposes using a DUT's RMS fixed-base modal responses to compare flight and lab environments. The concepts behind fixed-base modal responses are elaborated in the section that follows. As suggested by Beale [6], this metric may be better correlated to stress than methods based on physical responses. Additionally, it could help improve test program efficiency, as a pre-test could be performed, the RMS fixed-base modal responses calculated, and the control PSD matrix scaled up or down to reach equivalent RMS fixed-base responses in flight and lab. The test could be easily modified to meet the specification, in other words. The test workflow changes from a potentially iterative, costly procedure to a straightforward, linear one that yields more confidence that stress has been accurately reconstructed as shown in Figure 1.

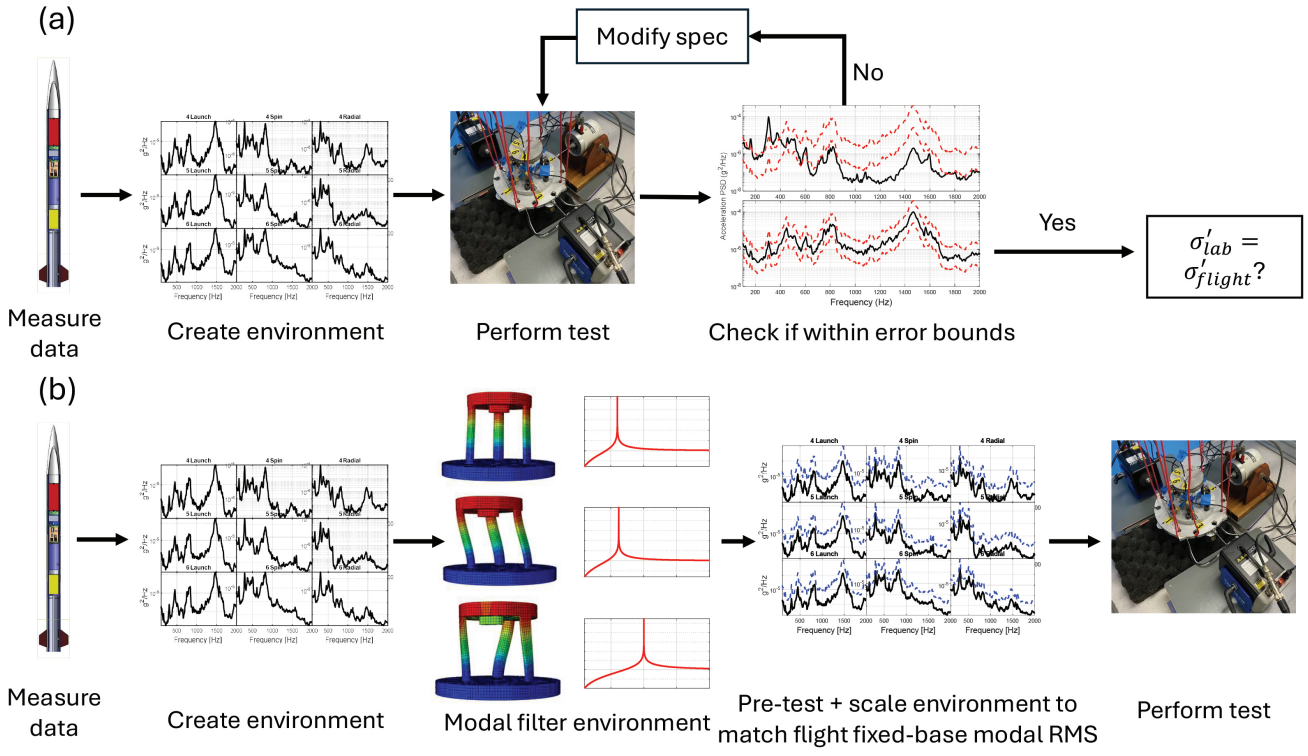

Fig. 1 Traditional test workflow (a) vs. proposed RMS fixed-base modal response workflow (b)

Damage Metric Calculation

The procedures for calculating the RMS dB error and RMS fixed-base modal response metrics are briefly described in the sections that follow.

RMS dB Error Metric

The calculation of the RMS dB error is described in [5] and reproduced here for convenience. A single error value is obtained at each frequency line by taking the RMS of the dB differences at each channel according to

$$e_{\text{PSD}}(\omega_i) = \sqrt{\frac{1}{n_{\text{accels}}} \sum_{k=1}^{n_{\text{accels}}} \left[\text{dB}\left(\mathbf{S}^r_{x_k x_k,\text{fl}}(\omega_i) \right) - \text{dB}\left(\mathbf{S}^r_{x_k x_k,\text{lab}}(\omega_i) \right) \right]^2}, \tag{1}$$

where $\mathbf{S}_{xx}$ is the acceleration PSD matrix, r denotes a set of reference DOF over which error is calculated, and fl denotes the flight environment. Ideally, the reference DOF contain flight measurements at uncontrolled DOF on the DUT, though in practice, measurements may be sparse, and error may be calculated at the control DOF on the DUT and / or test fixture. The RMS is then taken across frequency lines f to yield a single error value for the test,

$$e_{\text{PSD}} = \sqrt{\frac{1}{n_f} \sum_{i=1}^{n_f} \left(e_{\text{PSD}}(\omega_i) \right)^2}. \tag{2}$$

RMS Fixed-Base Modal Response Metric

The Hurty / Craig-Bampton method, developed in [11, 12], divides a system into boundary and interior DOF. For qualification tests, the interior DOF can be defined as those on the DUT, and the boundary DOF contain all other DOF of the system, e.g., those of the test fixture. The responses of the interior DOF are calculated according to

$$\mathbf{x}_i = \mathbf{\Phi}_i^{\text{FB}} \mathbf{p} + \mathbf{\Psi}_i \mathbf{x}_b, \tag{3}$$

where i and b are the interior and boundary DOF, respectively, $\mathbf{\Phi}_i^{\text{FB}}$ is the mode shape matrix of the DUT with a fixed-base boundary condition, $\mathbf{p}$ is the vector of fixed-base modal responses, and $\mathbf{\Psi}_i$ is the constraint shape matrix which relates the displacements of the boundary DOF to those of the interior DOF. This equation separates the rigid body and elastic portions of the DUT's response into $\mathbf{\Psi}_i \mathbf{x}_b$ and $\mathbf{\Phi}_i^{\text{FB}} \mathbf{p}$, respectively. Since the DUT's stress is caused by its elastic deformation, comparing $\mathbf{p}$ in the flight and lab should better reflect how accurately stress is recreated than comparing physical responses.

In this study, the modal responses are calculated using

$$\begin{bmatrix} \mathbf{s} \\ \mathbf{p} \end{bmatrix} = \begin{bmatrix} \mathbf{\Phi}_d^{\text{RB}} & \mathbf{\Phi}_d^{\text{FB}} \end{bmatrix}^+ \mathbf{x}_d, \tag{4}$$

where $\mathbf{s}$ is the vector of rigid body modal responses, $\mathbf{\Phi}_d^{\text{RB}}$ are the rigid body mode shapes at a set of DUT measurement DOF d, $\mathbf{\Phi}_d^{\text{FB}}$ are the fixed-base mode shapes at the same DOF, $+$ denotes the pseudoinverse, and $\mathbf{x}_d$ is the vector of measured accelerations on the DUT. One could also use a combination of DUT and next assembly measurements, though this requires including the next assembly's mode shapes and following a slightly different procedure such as that outlined in [13].

There must be at least as many measurements as the total number of modes to accurately estimate modal responses, and even more accelerometers might be needed in practice; they must also be placed so that $\mathbf{\Phi} = \begin{bmatrix} \mathbf{\Phi}_d^{\text{RB}} & \mathbf{\Phi}_d^{\text{FB}} \end{bmatrix}$ is well conditioned. $\mathbf{\Phi}$ should include the modes that are needed to describe the system's motion in the frequency band of interest, and it is common to include all modes below 1.5 times the highest frequency of interest to account for residual effects.

Each fixed-base modal response can be described by a single RMS value calculated according to

$$\mathbf{p}_{k_{\text{RMS}}} = \sqrt{\delta f \sum_{i=1}^{n_f} \mathbf{S}_{p_k p_k}(\omega_i)}, \tag{5}$$

where δf is the frequency spacing and $\mathbf{S}_{p_k p_k}$ is $(k,k)^{th}$ element of the fixed-base modal acceleration PSD matrix. The RMS of the resulting values can then be taken according to

$$\mathbf{p}_{\text{RMS}} = \sqrt{\frac{1}{n_{FB}} \sum_{k=1}^{n_{FB}} \mathbf{p}^2_{k_{\text{RMS}}}}, \tag{6}$$

yielding a single fixed-base RMS modal acceleration value. Dividing this value in the lab and flight configurations provides a ratio which is the desired metric. If this ratio equals one, then the RMS accelerations are equal, and one might assume

that stress is accurately recreated; conversely, stress reconstruction is expected to be overly severe when greater than one and not severe enough when less than one. The primary goal of this study is to understand if the fixed-base modal response metric accurately reflects the stress imparted in a test, i.e., to understand if $\mathbf{p}^{\text{lab}}_{\text{RMS}}/\mathbf{p}^{\text{fl}}_{\text{RMS}} = \sigma'^{\text{lab}}_{\text{RMS}_{\text{max}}}/\sigma'^{\text{fl}}_{\text{RMS}_{\text{max}}}$, where $\sigma'_{\text{RMS}_{\text{max}}}$ is the maximum RMS Von Mises stress on the DUT. To this end, a set of tests is simulated, and the correlation between this metric and maximum RMS Von Mises stress is studied in section . The maximum RMS Von Mises stress is calculated using Segalman's method [14] which is reviewed in appendix .

Advantages of Fixed-Base Modal Response Metric

The RMS fixed-base modal response value provides a few significant advantages as an error metric:

- **Fixed-base modes define how the DUT elastically deforms.** When responses are compared in physical coordinates, it is difficult to tell how significant differences between environments are. Harvie simulated a test that seemed to be conservative from the observed physical response [7]. In reality, one of the elastic modal responses was reconstructed conservatively while the other was under-excited. Fixed-base modes provided this crucial insight that physical responses could not.
- **Fixed-base modes do not change between the flight and lab setups** when the DUT has the same connection DOF in both cases. This means that fixed-base modal responses can be compared between the flight and lab setups. The free modes of the DUT and transmission simulator (attached to each other) are usually different in flight and in the lab and cannot generally be compared. An accurate comparison would require that the free modes happen to be similar as Schoenherr noted [8]. Even if the next assembly elastically deforms while the fixture remains rigid, the fixed-base modes stay the same.
- **The DUT's elastic motion can often be described with only a few fixed-base modal responses.** In addition, there are typically fewer fixed-base modes than free modes of the DUT and transmission simulator. A flight vehicle may have hundreds of modes, and it would be challenging to estimate their responses. In contrast, a DUT might have a few fixed-base modes which are easier to estimate and analyze. Fixed-base modes provide an effective way to separate the DUT's motion from the rest of the flight vehicle and reduce the complexity of the analysis.
- **Accurate RMS response reconstruction is easier than accurate spectral reconstruction.** The RMS of a signal weights peaks more heavily than the rest of the signal. This means that errors in reconstructing the environment at low response levels do not significantly affect the RMS; if only the peaks of the environment are matched, the RMS will be matched reasonably well. This could reveal that requirements for an accurate test are less stringent than previously thought; perhaps fewer shakers are required to accurately capture the RMS of the fixed-base modal responses, for example. The ability to meet test specifications more consistently would also improve test program efficiency as previously mentioned.

Estimating fixed-base modal responses generally requires accurate response spectra at various locations on the DUT. When this data is not available, this metric cannot be accurately used. In addition, rigid body motion causes damage to some components. The solder joints on a PCB might not have resonances in the frequency band of interest, though they may still experience high stresses due to the inertial forces caused by the rigid body motion. Since the rigid body modes must be included in the modal filtering process, the RMS rigid body modal responses can be readily calculated and analyzed if needed without much additional effort.

Method for Evaluating the Metrics

To understand the relationship between the damage metrics and stress, qualification tests are simulated using a finite element model case study. The RMS dB error, RMS fixed-base modal response, and maximum RMS Von Mises stress are calculated for each test case and compared. In the sections that follow, the finite element model case study is introduced, and the steps of the simulated experiment are described in further detail.

Flight and Lab Configurations

The "flight vehicle" of interest is shown in Figure 2(a), where the DUT is the stool at the top of the vehicle. This vehicle, which will be referred to as the wedding cake, has 13 free modes below 2000 Hz, corresponding to six rigid body modes, three fixed-base modes of the DUT, and four elastic modes of the next assembly. The four columns near the bottom of the

wedding cake induce elasticity into the plates above them, though these plates appear to be rigid when the columns are absent. This boundary condition mismatch between configurations makes the case study relevant to real hardware, while the relative simplicity of the FEM also makes it a useful testbed for verifying the damage metrics.

A flight environment was created by applying a 1 N^2/Hz force PSD at 14 different DOF on the wedding cake simultaneously, and a random value between $\pm$ 10 percent of the PSD magnitude was added at each frequency line to simulate sensor noise. Four simulated tests were performed to capture a variety of qualification testing methods that are currently practiced, namely SDOF, 3DOF, 6DOF, and IMMAT. These test setups are shown in Fig. 2(b) with shakers shown in blue and accelerometers in red. One percent modal damping was assumed for each mode in the flight and lab configurations. In the SDOF test, rigid body motion is fixed in all but the translational direction of interest, and all rigid body rotation modes are constrained in the 3DOF test. A condition number threshold of 0.01 was applied to the control FRF in each of the tests to reduce the shaker forces to levels that could feasibly be reached in an actual test. The condition number threshold sets all FRF singular values that are less than one percent of the largest singular value to zero at each frequency line, eliminating the ill-conditioned portions of the FRF matrix. This procedure is further described in [15].

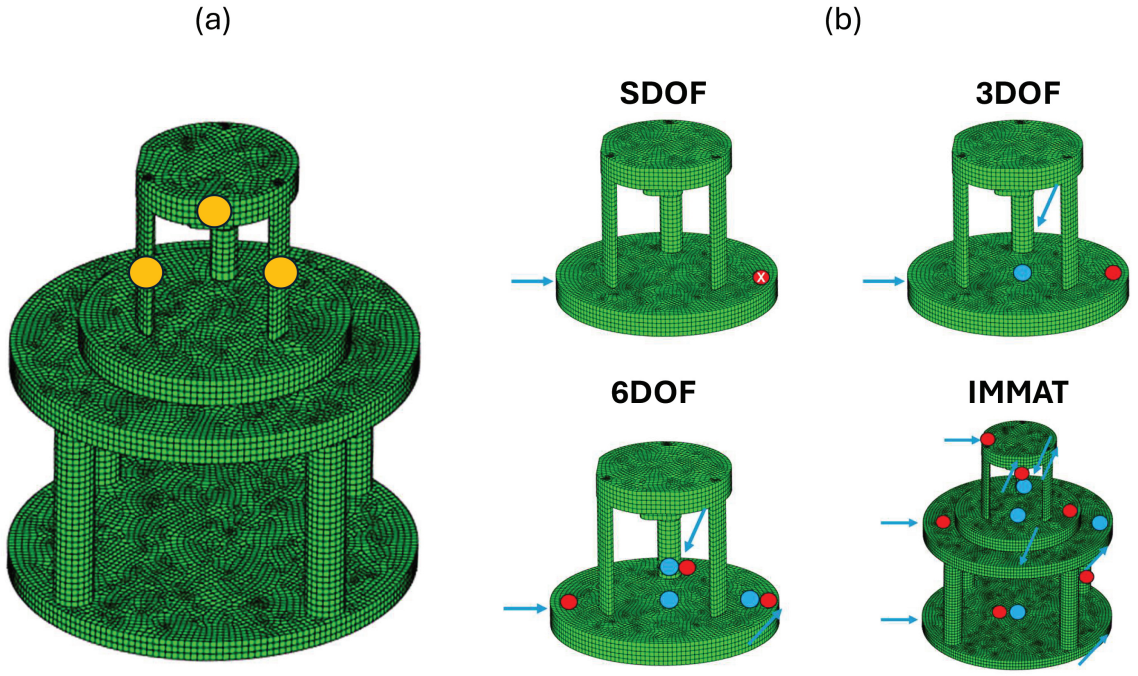

Fig. 2 Flight vehicle (a) with reference triaxial accelerometers in orange and lab test setups (b), where blue arrows represent shakers, blue circles represent shakers that apply force in the launch direction, and red circles represent triaxial control accelerometers

Comparing the Metrics to Stress

The RMS dB error for each test is calculated over the 3 orange triaxial accelerometers in Fig. 2. These locations are spread across the DUT to observe its dynamics and global response. They are not controlled in the test, but are rather reference DOF at which the environment is known. To calculate the RMS modal responses, a modal filter must first be applied to the test results. There are 9 modes to be filtered - six rigid body modes, and three fixed-base modes which are shown in Fig. 3 - so there must be at least 9 accelerometer channels on the DUT to observe these modes. 24 channels at various locations on the DUT are used in the filtering process to ensure that its dynamics are observed.

Fixed-base modal responses can be accurately estimated when the transmission simulator elastically deforms, though doing so requires including the transmission simulator modes and measurements on the transmission simulator in the filtering process. In this study, only DUT measurements are used to estimate the fixed-base modal responses, so only the rigid body modes and fixed-base modes are included. Accurate modal filtering requires that the rigid body and fixed-base modes fully span the response space of the DUT below 2000 Hz in each test configuration. This is expected to be the case since the plate directly below the stool appears to remain rigid in each of the test configurations, but Schoenherr's modal projection error

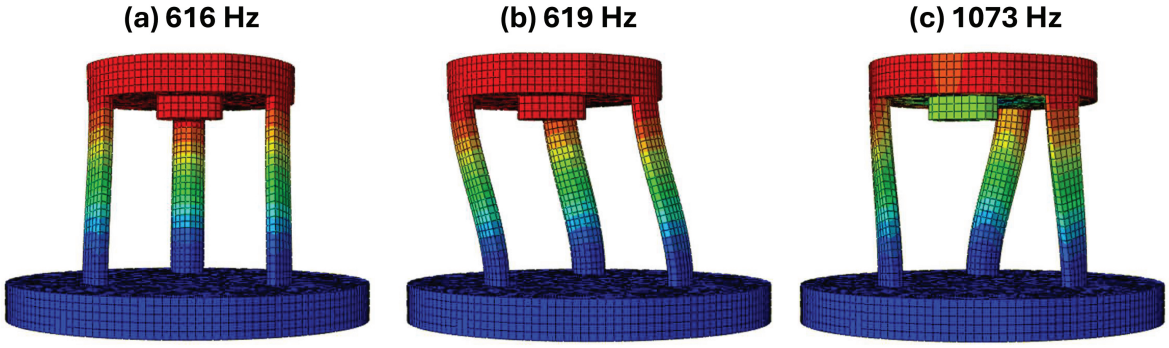

Fig. 3 616 Hz bending, 619 Hz bending, and 1073 Hz torsion fixed-base modes

metric [16] can be used to verify the quality of modal filtering more rigorously. This metric is not directly computed here, but similar insight is gained by expanding the estimated modal responses back to physical DOF and comparing them to the original environment.

The most significant modal projection error is expected in the wedding cake configuration as the plate experiences a slight bubbling motion in its 13th mode at 1882 Hz; this could cause the plate to dynamically interact with the DUT, potentially introducing new motion into the DUT that is not spanned by the rigid body and fixed-base modes. The flight modal responses are estimated using 21 of the aforementioned filtering channels and are then expanded to physical DOF and compared to the flight environment on the three DUT channels not used in the filtering process. As seen in Fig. 4, there is generally close agreement between the flight and filtered environment, suggesting that the fixed-base modes span the DUT's motion in the wedding cake assembly fairly well. This process was repeated for the other test setups and even less error was observed. Visually, the most significant errors occur below 600 Hz and above 1800 Hz, where there is a plate bubble mode that causes the DUT to deform in a shape not spanned by the fixed-base modes. These errors are unlikely to have a significant effect on the RMS of the fixed-base modal responses since the response magnitude is much smaller at these frequencies than between 600 and 1200 Hz, where most of the fixed-base modal energy is concentrated. In this frequency band, the radial response is conservative around 900 Hz, and that likely affects the RMS somewhat. Most of the energy in this band is captured well, though, so the fixed-base modes appear to be a good basis for the elastic motion of the DUT in the three configurations.

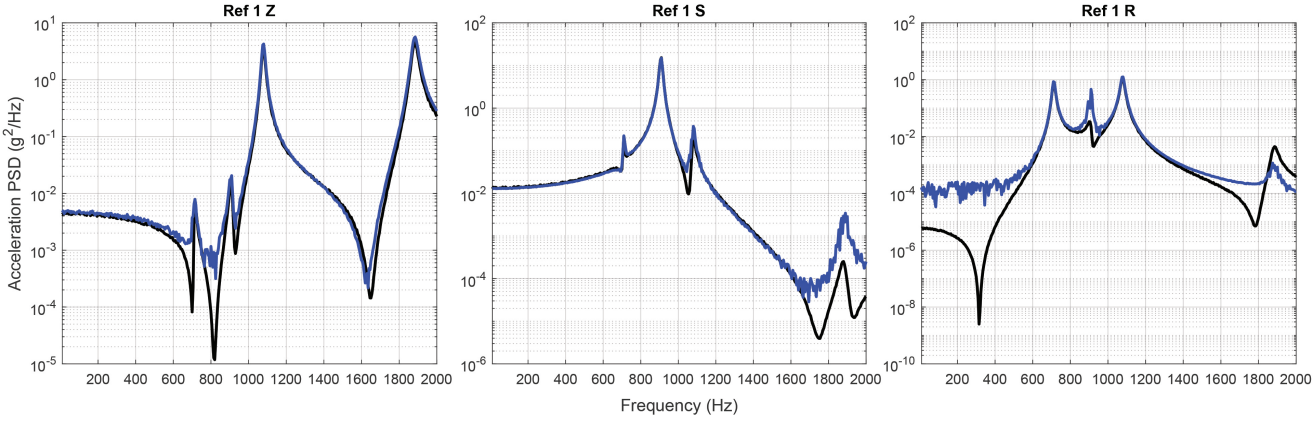

Fig. 4 Flight (black) and modal filtered (blue) environments for first 3 DUT reference channels

In this study, the RMS Von Mises stress is calculated at various points of interest on the DUT. Observation of the stress modes reveals that the top of the stool and the plate both appear to remain rigid below 2000 Hz, suggesting that the most significant stresses occur in the stool legs. The RMS Von Mises stress is calculated at the 36 candidate locations in Figure 5 to capture these areas of most probable failure. These same stress locations are used for each model with negligible variation because each model has the same mesh seed size. The final values reported are the maximum of the RMS Von Mises stresses across these locations, as that is where failure would first occur in flight.

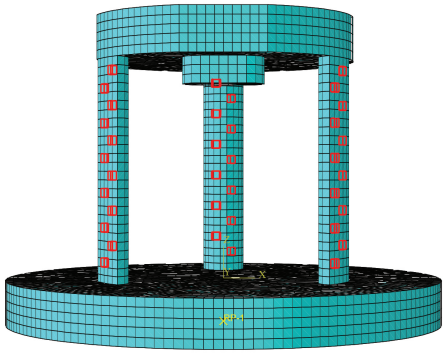

Fig. 5 Locations where RMS Von Mises stress was calculated (red)

To summarize, tests are simulated using the finite element model case study. The RMS dB error and RMS fixed-base modal response values are then calculated and compared to the maximum RMS Von Mises stress values to understand how closely each of these metrics correlates to stress.

Results

The maximum RMS Von Mises stress ratios, RMS dB errors, and RMS fixed-base modal response ratios for the simulated tests are shown in Table 1. In each case, the ratio is the lab value divided by the flight value, so a stress ratio lower than one denotes an under-test. Similarly, a fixed-base response ratio of less than one predicts that a test is not severe enough. All fixed-base modal response ratios are reported, though the analysis will primarily focus on the combined ratios which were calculated using Eq. (6).

Table 1 Comparison of stress and error metrics in SDOF, 3DOF, 6DOF, and IMMAT Tests, where all ratios are the lab value divided by the flight value

Type of test	Max RMS VM Stress Ratio	RMS dB Error	RMS FB 1 Ratio	RMS FB 2 Ratio	RMS FB 3 Ratio	RMS FB Combined Ratio
SDOF	0.81	38.7	0.02	0.85	0.01	0.38
3DOF	3.0	15.2	1.46	0.83	0.02	1.17
6DOF	1.69	6.6	0.91	0.93	2.53	1.44
IMMAT	1.07	4.5	0.99	0.93	0.98	0.97

Discussion of RMS dB Error

It is often desired that each spectral line lie within 3 or 6 dB of the specified environment, and the same criterion could be applied to the RMS dB error metric. Looking at the stress ratios and RMS dB errors, it becomes apparent that the RMS dB

error metric does not predict stress reconstruction very accurately. It is most accurate in the 6DOF test, where the RMS dB error is 6.6 and the stress ratio is 1.69, and the IMMAT, where the RMS dB error is 4.5 and the stress ratio is 1.07. This suggests that the error in the IMMAT may be acceptable while that of the 6DOF test would not be. In reality, both tests recreate stress conservatively and could be acceptable depending on the desired level of margin in the test. Hence, the RMS dB error metric could result in a reasonable test being rejected, redesigned, and repeated unnecessarily.

In the SDOF and 3DOF cases, the RMS dB error metric is far less accurate. The SDOF test results in a stress ratio of 0.81 and an RMS dB error of 38.7, while the 3DOF test results in a stress ratio of 3.0 and an RMS dB error of 15.2. The SDOF test RMS dB error suggests that it is inaccurate by almost four orders of magnitude when, in reality, it is only a slight under-test. The 3DOF test error value similarly predicts that the test is off by more than an order of magnitude though it is actually just three times as severe as it ought to be.

In summary, the RMS dB error metric seems to over-predict test error, and this might cause accurate tests to be needlessly redone. Significant resources could be dedicated to modify the environment to be more replicable in the lab, though this is challenging and still might not meet the error requirements. This metric likely overestimates error because it calculates the difference between response magnitudes at each frequency line. It is difficult to accurately recreate a set of response spectra in general, so it makes sense that this value would often be large. Error at lower response levels is likely not important, though, as most of the stress is caused by the peaks in the environment. In short, the RMS dB error metric weights errors at low response magnitudes equally to high ones, and this is part of the reason that it is poorly correlated to stress.

It is worth repeating that the RMS dB error was calculated over a set of 9 uncontrolled reference accelerometer channels. In practice, these channels may not be available and the metric could be calculated over the control accelerometer responses instead. This would reduce the RMS dB error values which would make them closer to the stress ratios in this case, though the correlation with stress would still be poor as accurate reconstruction of the control responses does not necessarily mean that the rest of the structure's response is accurately recreated. In the 3DOF test, for example, the RMS dB error on the control channels is zero even though stress reconstruction is very inaccurate.

Discussion of Fixed-Base Modal Response Metric

The RMS fixed-base modal response ratios match the maximum stress ratios much more closely than RMS dB error does. Like RMS dB error, this metric is most accurate in the 6DOF and IMMAT cases. In the 6DOF case, the maximum stress ratio is 1.69 and the fixed-base ratio is 1.44, while the stress ratio is 1.07 and the fixed-base ratio is 0.97 in the IMMAT case. This agreement is excellent, particularly compared to the RMS dB error predictions. The RMS fixed-base response ratio is less accurate in the SDOF and 3DOF cases, however. In the SDOF case, the max stress ratio is 0.81 and the fixed-base response ratio is 0.38, while the 3DOF max stress ratio is 3.0 and the fixed-base response ratio is 1.17. While still more accurate than the RMS dB error predictions, the level of disagreement between the proposed metric and stress reconstruction is significant in these cases.

It should also be noted that the fixed-base metric would result in a conservative test in both the SDOF and 3DOF cases since the max stress ratios are larger than the combined RMS fixed-base response ratios. Scaling environment magnitude to make the fixed-base response ratio equal one would result in a stress ratio greater than one, in other words. This is not expected to be the case in general, though.

To understand why the RMS fixed-base modal response metric is accurate in some cases but not others, it is helpful to consider the criterion $\mathbf{p}^{lab}/\mathbf{p}^{fl} = \sigma'^{lab}_{max}/\sigma'^{fl}_{max}$ for a system with two fixed-base stress modes ψ_1 and ψ_2:

$$\frac{{p_1^l}^2 + {p_2^l}^2}{{p_1^{fl}}^2 + {p_2^{fl}}^2} = \frac{(\psi_1 {p_1}^l + \psi_2 {p_2}^l)^{\mathrm{T}} \mathbf{A} (\psi_1 {p_1}^l + \psi_2 {p_2}^l)}{(\psi_1 {p_1}^{fl} + \psi_2 {p_2}^{fl})^{\mathrm{T}} \mathbf{A} (\psi_1 {p_1}^{fl} + \psi_2 {p_2}^{fl})} \tag{7}$$

Note that the free modes of the lab and flight configurations were actually used to compute stress to eliminate modal projection error, but the right side of this equation is accurate when fixed-base modal responses are perfectly known and when fixed-base modes span the free modes of the flight and lab configurations. Making those assumptions, it is apparent that both sides of this equation will equal one if the flight fixed-base modal responses $\mathbf{p}$ are reconstructed perfectly. When there is significant error in response reconstruction, the two sides of the equation are no longer guaranteed to be equal and can be quite different due to the stress modes and interaction terms - e.g., $\psi_1\psi_2 p_1 p_2$ - on the right side. The two sides of the equation might happen to be similar when the fixed-base modal responses are recreated with error, though they are only guaranteed to be equal with accurate modal response reconstruction.

Conclusion

In this study, qualification tests were simulated to attempt to accurately recreate in-flight stress due to vibration. The RMS dB error metric, which is often used to compare environments across multiple accelerometers, was calculated for each case. The RMS fixed-base modal response ratio metric was proposed as an alternative and was also calculated for each test. These were compared to the maximum RMS Von Mises stress ratios to understand how accurately the two metrics captured stress.

The RMS dB error metric was shown to over-estimate the error in tests because it accounts for every spectral difference between environments, some of which can be large in magnitude while not significantly contributing to the stress state of the DUT. The fixed-base modal response ratio metric was shown to represent stress far more accurately in the simulated tests. It was shown to be particularly accurate when modal response spectra were closely matched in the lab. When fewer shakers and / or accelerometers were used, the modal responses were less accurate, and the complex relationship between the modal responses and Von Mises stress resulted in an increased discrepancy between the two. Even with this discrepancy, the proposed metric marked a significant improvement over the RMS dB error metric in every case observed in this study.

Appendix: RMS Von Mises Stress Calculation

RMS Von Mises stress is calculated using the method presented in [14]. While the Von Mises stress mode shapes can be obtained directly from a finite element analysis, modal superposition cannot be applied using these shapes because Von Mises stress is a nonlinear function of the elements of the stress tensor. Because the elements of the stress tensor, $\boldsymbol{\sigma} = \left[\sigma_{xx}\ \sigma_{yy}\ \sigma_{zz}\ \sigma_{xy}\ \sigma_{xz}\ \sigma_{yz}\right]^{\mathrm{T}}$, are linearly related to strain - which is linearly related to derivatives of displacement - modal superposition can be applied to the stress tensor mode shapes, so these are the desired output of the FEM. The RMS Von Mises stress at a single point z on the structure is computed according to

$$\sigma'_{\mathrm{RMS},z} = \sqrt{\delta f \sum_{k=1}^{n_f} \sum_{i=1}^{m} \sum_{j=1}^{n} \mathbf{S}_{\sigma_i \sigma_j, z}(\omega_k) \mathbf{A}_{i,j}}, \tag{8}$$

where $\mathbf{S}_{\sigma_i \sigma_j, z}(\omega)$ is the i, j^{th} element of the stress tensor PSD matrix at some location z. The elements of the stress tensor are related to Von Mises stress according to $\sigma'(\omega) = \sigma(\omega)^{\mathrm{T}} \mathbf{A} \sigma(\omega)$ where

$$\mathbf{A} = \begin{bmatrix} 1 & -0.5 & -0.5 & 0 & 0 & 0 \\ -0.5 & 1 & -0.5 & 0 & 0 & 0 \\ -0.5 & -0.5 & 1 & 0 & 0 & 0 \\ 0 & 0 & 0 & 3 & 0 & 0 \\ 0 & 0 & 0 & 0 & 3 & 0 \\ 0 & 0 & 0 & 0 & 0 & 3 \end{bmatrix}. \tag{9}$$

The stress tensor PSD matrix at point z is calculated according to

$$\mathbf{S}_{\sigma\sigma,z}(\omega) = \mathbf{H}_{\sigma f}(\omega) \mathbf{S}_{ff}(\omega) \mathbf{H}_{\sigma f}(\omega)^*, \tag{10}$$

where $\mathbf{H}_{\sigma f}(\omega)$ is a $(6, n_{\mathrm{forces}})$ matrix relating applied force to the elements of the stress tensor and $\mathbf{S}_{ff}(\omega)$ is the force PSD matrix. In flight, the force PSD matrix contains the forces applied to the vehicle, while it contains shaker forces in the lab. $\mathbf{H}_{\sigma f}(\omega)$ can be computed using modal analysis theory based on the free displacement mode shapes at the shaker DOF and the free stress tensor mode shapes at the response point of interest. The maximum RMS Von Mises stress of the structure is obtained by calculating the RMS Von Mises stress at various points on the DUT and retaining the largest of them. Accurately calculating the maximum value requires that the point of highest stress is included in the set of points at which stress is evaluated. This may be challenging to identify, though intuition for potential failure points can be gained by looking at the stress mode shapes, and it also helps to use a large set of candidate locations.

Acknowledgments Notice: this manuscript has been authored by Honeywell Federal Manufacturing & Technologies, LLC under Contract No. DE-NA-0002839 with the U.S. Department of Energy / National Nuclear Security Administration. The United States Government retains and the publisher, by accepting the article for publication, acknowledges that the United States Government retains a nonexclusive, paid-up, irrevocable, world-wide license to publish or reproduce the published form of this manuscript, or allow others to do so, for United States Government purposes.

References

1. Military Standard Environmental Test Methods for Aerospace and Ground Equipment. Technical Report MIL-STD-810, United States Air Force, June 1962.
2. J. Paripovic and R. L. Mayes. Reproducing a Component Field Environment on a Six Degree-of-Freedom Shaker. In *Dynamic Substructures, Volume 4*, pages 73–78. Springer International Publishing, Cham, 2021. Series Title: Conference Proceedings of the Society for Experimental Mechanics Series.
3. P. Daborn, P. Ind, and D. Ewins. Enhanced ground-based vibration testing for aerodynamic environments. *Mechanical Systems and Signal Processing*, 49(1):165–180, December 2014.
4. C. Roberts and D. Ewins. Multi-axis vibration testing of an aerodynamically excited structure. *Journal of Vibration and Control*, 24(2):427–437, January 2018. Publisher: SAGE Publications Ltd STM.
5. D. P. Rohe, G. D. Nelson, and R. A. Schultz. Strategies for Shaker Placement for Impedance-Matched Multi-Axis Testing. In *Sensors and Instrumentation, Aircraft/Aerospace, Energy Harvesting & Dynamic Environments Testing, Volume 7*, Conference Proceedings of the Society for Experimental Mechanics Series, pages 195–212, Cham, 2020. Springer International Publishing.
6. D. Beale, W. Larsen, and P. Coffin. Assessment of Metrics Between Acceleration Power Spectral Density Metrics and Failure Criteria. In *Sensors and Instrumentation, Aircraft/Aerospace, Energy Harvesting & Dynamic Environments Testing, Volume 7*, Conference Proceedings of the Society for Experimental Mechanics Series, pages 85–102, Cham, 2022. Springer International Publishing.
7. J. Harvie. Using Modal Substructuring to Improve Shock & Vibration Qualification. In *Topics in Modal Analysis & Testing, Volume 9*, Conference Proceedings of the Society for Experimental Mechanics Series, pages 227–239, Cham, 2019. Springer International Publishing.
8. T.F. Schoenherr and M. Khan. Using Modal Acceleration to Compare Two Environments of an Aerospace Component. In *Proceedings of the 41st International Modal Analysis Conference*, Austin, TX, February 2023.
9. R. Schultz and G. Nelson. Towards Generalized MIMO Random Vibration Specifications. In *Proceedings of the 43rd International Modal Analysis Conference*, Orlando, FL, February 2025.
10. P. Daborn. *Smarter dynamic testing of critical structures*. Ph.D., University of Bristol, 2014. Accepted: 2014.
11. W. Hurty. Dynamic Analysis of Structural Systems Using Component Modes. *AIAA Journal*, 3(4), April 1965.
12. R. Craig and M. Bampton. Coupling of Substructures for Dynamic Analyses. *AIAA Journal*, 6(7):1313–1319, July 1968.
13. R. Mayes. A Craig-Bampton Experimental Dynamic Substructure Using the Transmission Simulator Method. In *Dynamics of Coupled Structures, Volume 4*, pages 139–148. Springer International Publishing, Cham, 2015. Series Title: Conference Proceedings of the Society for Experimental Mechanics Series.
14. D. J. Segalman, C. W. G. Fulcher, G. M. Reese, and R. Field Jr. An efficient method for calculating RMS von Mises stress in a random vibration environment. Technical Report SAND-98-0260, Sandia National Lab. (SNL-NM), Albuquerque, NM (United States), February 1998.
15. R. Schultz and P. Avitabile. Shape-constrained Input Estimation for Efficient Multi-shaker Vibration Testing. *Experimental Techniques*, 44(4):409–423, August 2020.
16. T. Schoenherr and J. Rouse. Characterizing Dynamic Test Fixtures Through the Modal Projection Error. *Mechanical Systems and Signal Processing*, 204, September 2023.

Chapter 6
A Multivariate Specification Development Approach Using Principal Component Analysis

Colin M. Haynes and Sean T. Kelly

Abstract The concept of a conservative, bounding environment for multiple-input, multiple-output (MIMO) vibration testing is inherently multivariate. However, some multivariate statistical methods proposed for MIMO specification development are very computationally expensive. This computational burden has motivated work to reduce the computational complexity of a specification with many control degrees of freedom (or variates). In this paper, a new method based on principal component analysis is presented that decomposes the multivariate specification problem into a univariate one while still accounting for the underlying correlation structure of the data. Numerical studies are used to illustrate the benefits of the new approach.

Keywords Multivariate · Specifications · MIMO · Environmental Testing · Conservatism · Principal Component Analysis

List of Notations and Abbreviations
Mahalanobis distance (MD)
multiple-input, multiple-output (MIMO)
principal component (PC)
principal component analysis (PCA)
probability density function (PDF)

Introduction

To ensure that structures can perform their functions as intended under uncertain loading conditions, it is necessary to characterize the loading they are expected to undergo. These estimates of the service environment can then be used to develop a statistically-conservative bounding environment to test one or more structures to and qualify them for service. This sort of environmental specification development and testing is common for shock and vibration environments.

Historically, such testing has been done on single-axis electrodynamic shakers by applying the bounding environment to one axis at a time. As test equipment and control software have improved, new multi-axis approaches have been considered for more environmental testing applications to produce responses more representative of the true service environment [1, 2].

Traditional univariate approaches to specification development cannot account for the correlations between variates, which in the case of multiple-input, multiple-output (MIMO) testing are assumed to be different channels (locations and directions) used for control of an environmental test. Previous work has demonstrated that these correlations exist and that naive approaches, such as applying univariate one-sided normal tolerance bounds to each variate separately, often result in either: 1) impossibly unlikely specifications with respect to the service environment, or 2) likely specifications which are not sufficiently conservative [3]. For the former, to ignore the correlations is to attempt a test that distorts the way the structure would respond in service.

Previous proposals for multivariate specifications have accounted for the correlation structure of the data, but often the computational cost at higher dimensions (e.g., up to 24 dimensions) is prohibitive [4]. This paper proposes an approach

Colin M. Haynes · Sean T. Kelly
Mail Stop C932, Los Alamos National Laboratory, Los Alamos, NM 87545
e-mail: cmhaynes@lanl.gov; stkelly@lanl.gov

*Colin M. Haynes and Sean T. Kelly contributed equally to this work.

© The Author(s), under exclusive license to River Publishers 2026

Kristin B. Zimmerman, PhD (eds.), *Dynamic Evironments and Durability Testing, 2026, Vol. 7*, Conference Proceedings of the Society for Experimental Mechanics Series, https://doi.org/10.13052/rp-9788743814184

based on transforming the data using principal component analysis (PCA), which enables much more efficient calculation of the maximum predicted environment by using univariate calculations on individual principal coordinates rather than on variates directly.

Properties of PCA as Applied to Specification Development

PCA Overview

PCA is a common data reduction and decomposition technique based on the singular value decomposition. It can be shown that the left singular vectors of the mean-centered data matrix identified for this linear operation are the orthogonal directions that successively maximize the explained variance [5]. A detailed description of the mathematics behind PCA is out of the scope of this paper. Instead, only the properties particularly useful for the proposed specification development approach will be highlighted.

Assumption of Lognormality

In line with common practice in the field, we assume that environments data (usually power spectral densities and shock response spectra) are lognormally distributed [6]. However, each variate at each frequency line has some correlation to (relationship with) the other variates based on the dynamics (modes) of the structure. Such data can often be easily transformed into data following a multivariate normal distribution by simply taking the logarithm.

One convenient property of PCA is that the resulting principal coordinates are uncorrelated [5]. However, it can also be shown that in the situation of uncorrelated multivariate normal data, the variates are also independent [7]. Thus, applying PCA to log-transformed spectra may reasonably be assumed to produce fully independent coordinates. Furthermore, data scaling is performed such that the resulting principal coordinates all have equal sample standard deviation $\overline{\sigma}_{\mathrm{pca}}$.

The original probability density function (PDF) isocontours of representative bivariate synthetic data with a correlation ρ of -0.6719 at a given frequency line are shown on the left side of Figure 1. Note that the correlation structure between variates causes these isocontours to appear as ellipses in the two-dimensional case and generalize to hyperellipsoids in higher dimensionalities. Once transformed through PCA, because of the properties just mentioned, the PDF isocontours become circles in two dimensions and hyperspheres in higher dimensions. The right side of Figure 1 illustrates the result of this data standardization in the PCA space when the data are projected onto both principal components (PCs).

Note that Figure 1 includes more information than just the PDF isocontours in illustrating the effect of the workflow that is outlined in the following section. Also plotted are the 95/50 (i.e., 95% coverage and 50% confidence) one-sided univariate tolerance limits for each variate independently, expressed as purple lines. As shown in Figure 1 and discussed in the Introduction, the intersection of these lines (purple dot) is significantly unlikely to occur based on its proximity to the data distribution. This intersection is also shown when projected in the PCA space, further demonstrating its distance from the data population when viewed in independent principal coordinates with equal sample standard deviation. PC 1 and PC 2 are also depicted with scaling added for ease of visualization, as well as the point selected by calculating the one-sided univariate tolerance limit for each principal coordinate in the PCA space (this intersection point is denoted $\mathbf{x}_{\mathrm{pca,s}}$), as described in the following section.

Proposed PCA Specification Development Workflow

PCA Factorization

The first step of the proposed derivation approach is to form the data matrix $\mathbf{A}$ (dimension m variates by n samples) and perform PCA factorization. This factorization is given by $\mathbf{A}{=}\mathbf{W}_{\mathrm{pca}}\mathbf{X}_{\mathrm{pca}}$, where $\mathbf{W}_{\mathrm{pca}}$ contains the left singular vectors scaled by their respective singular values as columns (both calculated from the mean-centered data matrix), and the rows of $\mathbf{X}_{\mathrm{pca}}$ are the principal coordinates (accounting for if $\mathbf{A}$ is not mean-centered by default). Note that for this work we consider a PC to refer to a column of $\mathbf{W}_{\mathrm{pca}}$, rather than a left singular vector alone.

Here we assume that n is greater than m—that is, there are more samples of the intended service environment than intended control channels to estimate—as this is the situation that tends to produce reasonable variance estimates when calculating estimates of bounding environments. However, this approach is not limited to this situation and does not inherently impose a constraint on whether $n > m$ or $n \leq m$.

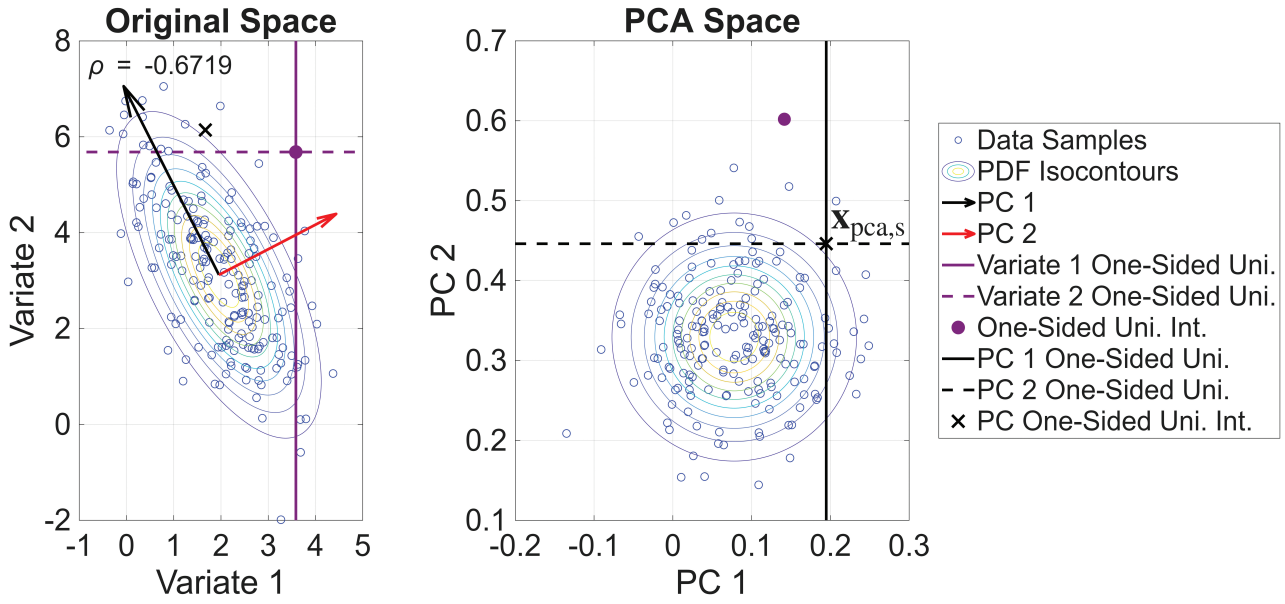

Fig. 1 Comparison of data samples and ellipses (PDF isocontours) in (left) original space (i.e., physical coordinates) vs. (right) PCA space to show the standardization. Variate 1 and 2 one-sided univariate upper tolerance limits and their intersection are shown as purple lines and a dot, respectively. Principle coordinate 1 and 2 one-sided univariate upper tolerance limits and their intersection are shown as black lines and an $\times$, respectively, with intersection denoted $\mathbf{x}_{\mathrm{pca,s}}$.

Because PCA is often used for data reduction and reconstruction, it is common in many applications to use fewer principal components p than the number of dimensions (i.e., $p < m$). However, for the sake of brevity, in this paper we only consider the case where all principal components are retained (i.e., $p = m$)

Compute Univariate Intersection of Principal Coordinates

As mentioned previously, once the data are transformed into PCA space, each principal coordinate becomes independent. Statistical independence allows the principal coordinates to be treated separately in computing a one-sided upper tolerance bound. In fact, here, because the data are standardized in the PCA space to have the same sample standard deviation $\overline{\sigma}_{\mathrm{pca}}$, only one calculation is necessary for a given coverage-confidence level. The mathematical form of this operation is shown in Eq. 1.

$$\mathbf{x}_{\mathrm{pca,s}} = \begin{bmatrix} x_{\mathrm{pca,s},1} \\ x_{\mathrm{pca,s},2} \\ \vdots \\ x_{\mathrm{pca,s},m} \end{bmatrix} = \begin{bmatrix} \overline{\mu}_{\mathrm{pca},1} \\ \overline{\mu}_{\mathrm{pca},2} \\ \vdots \\ \overline{\mu}_{\mathrm{pca},m} \end{bmatrix} + k\,(n,\ \beta, \gamma)\,\overline{\sigma}_{\mathrm{pca}}\mathbf{1} \tag{1}$$

In Eq. 1, $\mathbf{x}_{\mathrm{pca,s}} \in \mathbb{R}^m$ is a column vector containing the univariate one-sided upper tolerance bounds for each principal coordinate (i.e., the intersection of the univariate bounds shown in the right plot in Figure 1), $x_{\mathrm{pca,s},i}$ is the upper bound for principal coordinate i, $\overline{\mu}_{\mathrm{pca},i}$ is the sample mean of principal coordinate i (stored in the principal coordinate sample mean vector $\overline{\boldsymbol{\mu}}_{\mathrm{pca}}$), $k\,(n,\ \beta, \gamma)$ is the one-sided k-factor (or tolerance factor [8]) for number of samples n and prescribed coverage β and confidence γ, $\overline{\sigma}_{\mathrm{pca}}$ is the sample standard deviation of each principal coordinate (equal due to data scaling) as mentioned previously, and $\mathbf{1}$ is an m-dimensional column vector of ones. Note that if one selects $p < m$, additional modifications to Equation 3.1 are needed to account for selected vs. unselected principal components. While the case of $p < m$ is not considered here, this case is permissible with this approach and is to be included as part of future work.

Mahalanobis Distance as Severity Surrogate

In the univariate specification development case, "severity" is usually taken simply as the higher value of the spectrum being considered. The fact that all values reside on a number line implies the ordering of different values very clearly. However, ordering is not so simple in the multivariate case, requiring the definition of some metric that represents increasing severity

across multiple variates. Note that only considering univariate specification development does not alleviate this problem. Instead, such an approach means deciding that only one variate needs to be considered while allowing responses at all other locations and directions to vary arbitrarily.

In this paper, we propose using Mahalanobis distance (MD) as a severity surrogate for defining an environment specification. To the authors' knowledge, while the MD and Mahalanobis-squared distance have been commonly used as part of damage detection methodologies for structural health monitoring [9, 10], MD has not been explicitly used for assessing severity when defining, comparing, and evaluating environment specifications.

For the multivariate lognormal data considered here, the MD, denoted d_M, quantifies the distance between a point $\mathbf{a}$ and a distribution specified by a mean $\boldsymbol{\mu}_\mathrm{a}$ and covariance matrix $\boldsymbol{\Sigma}_\mathrm{a}$ as:

$$d_M(\mathbf{a};\ \boldsymbol{\mu}_\mathrm{a},\ \boldsymbol{\Sigma}_\mathrm{a}) = \sqrt{(\mathbf{a}-\boldsymbol{\mu}_\mathrm{a})^T \boldsymbol{\Sigma}_\mathrm{a}^{-1} (\mathbf{a}-\boldsymbol{\mu}_\mathrm{a})} \tag{2}$$

This formulation allows for a simple way to represent the ordering of different potential multivariate points, with larger d_M values being more "severe" relative to smaller values. However, any ordering will not necessarily be unique—that is, multiple points may have the same MD. Also note that this metric is agnostic to any damage mechanisms, just as the corresponding univariate approach does not imply any particular failure model or damage metric.

Notably, MD is invariant under the PCA transformation (and affine transformations in general), meaning a selected point or contour in the PCA space represents the same distance (or severity) as the point transformed back to physical coordinates.

Project Result Back to Physical Coordinates

Once the univariate calculation has been performed in the PCA space at the chosen level of coverage and confidence, the hypersurface of points with the same MD can be determined. The selected specification point (here, $\mathbf{x}_{\mathrm{pca,s}}$) may then simply be transformed back to physical coordinates to produce the multivariate environmental specification.

Note that any point on the hypersphere in PCA space is equally valid according to this approach, though clearly some will be more damaging than others in practice. Metrics are currently in development which aim to select the point on the hypersphere that represents the most severe environment. These metrics are omitted for brevity and will be a subject of future work.

This approach has been described to this point assuming a given data matrix $\mathbf{A}$ at a single frequency line ω. However, to define an environment specification over a frequency range, one simply needs to repeat this process for all frequency lines of interest.

Figure 2 shows an overview of the process presented so far.

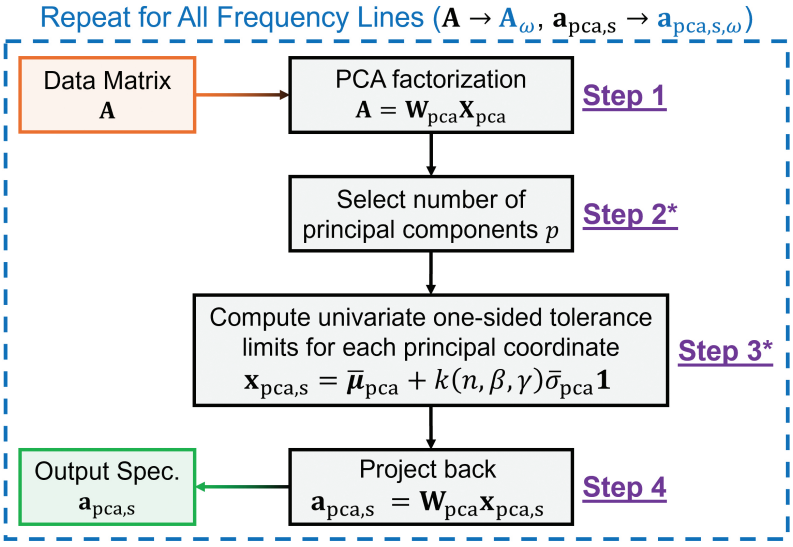

Fig. 2 Flowchart illustrating the proposed specification development process. *It is important to note that, as shown, the equation for $\mathbf{x}_{\mathrm{pca,s}}$ in Step 3 assumes $p = m$ (i.e., all principal components are used). However, for completeness, we include Step 2 where one may select $p < m$. If one selects $p < m$, Step 3 requires a minor modification to the equation for $\mathbf{x}_{\mathrm{pca,s}}$. This modification is a subject of future work, and we confine discussion here to the case of $p = m$.

Lastly, the PCA specification development approach outlined here is compatible with other specification development techniques. Notably, it can be combined with both frequency smoothing and spatial averaging schemes [11].

Conclusion

This paper proposes a novel approach to multivariate environmental specifications that retains the correlation structure of the underlying data while also retaining the computational simplicity of existing methods based on the univariate one-sided tolerance bound. This approach is enabled by the observation that projecting jointly normal source data onto principal components results in independent coordinates. In addition, data scaling results in the principal coordinates being standardized—that is, $\overline{\sigma}_{\mathrm{pca}}$ and $k(n, \beta, \gamma)$ each only needs to be computed once for given $\mathbf{A}$ at a given frequency line.

MD is proposed as a surrogate for assessing environment severity in the absence of information on damage modes when defining environment specifications. Notably, MD is invariant under the PCA transformation and therefore can be computed in either physical space or PCA space.

Future work is planned to extend this method into the selection of different points on the PCA hypersphere that may be of practical interest in testing or may better target damage modes of interest.

References

1. G. D'Elia, U. Musella, E. Mucchi et al., "Analyses of drives power reduction techniques for multi-axis random vibration control tests," Mechanical Systems and Signal Processing, vol. 135, pp. 106395, 2020. https://doi.org/10.1016/j.ymssp.2019.106395
2. P. M. Daborn, P. Ind, and D. Ewins, "Enhanced ground-based vibration testing for aerodynamic environments," Mechanical Systems and Signal Processing, vol. 49, no. 1-2, pp. 165-180, 2014. https://doi.org/10.1016/j.ymssp.2014.04.010
3. C. Haynes, T. Thompson, and A. Watts (2025), "Motivating Multivariate Specifications for Multiple-Input, Multiple-Output Vibration Testing." Proc. In International Modal Analysis Conference, Orlando, FL, Feb. 2025.
4. A. Watts, T. Thompson, and D. Harvey, "Confidence Intervals on Multivariate Normal Quantiles for Environmental Specification Development in Multi-axis Shock and Vibration Testing," arXiv preprint arXiv:2404.06565, 2024. https://doi.org/10.48550/arXiv.2404.06565
5. M. Greenacre, P. J. Groenen, T. Hastie et al., "Principal component analysis," Nature Reviews Methods Primers, vol. 2, no. 1, pp. 100, 2022. https://doi.org/10.1038/s43586-022-00184-w
6. MIL-STD-810H "Environmental Engineering Considerations and Laboratory Tests", Method 514.8, ANNEX F, APPENDIX B, pg. 4, January 2019.
7. D. Bertsekas and J. N. Tsitsiklis, *Introduction to Probability*, 1 ed.: Athena Scientific, 2002.
8. K. Krishnamoorthy and T. Mathew, *Statistical Tolerance Regions: Theory, Applications, and Computation*, 1 ed. John Wiley & Sons, Ltd, 2009. https://doi.org/10.1002/9780470473900
9. H. Sarmadi and A. Karamodin, "A novel anomaly detection method based on adaptive Mahalanobis-squared distance and one-class kNN rule for structural health monitoring under environmental effects," Mechanical Systems and Signal Processing, vol. 140, pp. 106495, 2020. https://doi.org/10.1016/j.ymssp.2019.106495
10. Y. L. Zhou, E. Figueiredo, N. Maia et al., "Damage detection in structures using a transmissibility-based Mahalanobis distance," Structural Control and Health Monitoring, vol. 22, no. 10, pp. 1209-1222, 2015. https://doi.org/10.1002/stc.1743
11. R. Schultz and G. Nelson, "Techniques for Modifying MIMO Random Vibration Specifications," Sensors and Instrumentation, Aircraft/Aerospace and Dynamic Environments Testing, Volume 7: Proceedings of the 40th IMAC, A Conference and Exposition on Structural Dynamics, pp. 71-83, 2022. Cham: Springer International Publishing, 2022. https://doi.org/10.1007/978-3-031-05415-0_7

Chapter 7
NASA Armstrong's Thermal Vibration Test System (TVTS) Pathfinder Capability

Jessica J. De la Cruz, Keerti K. Bhamidipati, Chris B. Kostyk, Jackson T. Winter, Natalie D. Spivey, Phillip C. Nguyen, and Samson S. Truong

Abstract The National Aeronautics and Space Administration Armstrong Flight Research Center Flight Loads Laboratory is developing a new capability for combined vibration and thermal load testing called the Thermal Vibration Test System. A pathfinder capability has been demonstrated and consisted of a radiant quartz lamp heater installed above a 500-lbf electrodynamic shaker. This passively cooled test fixture was designed to test up to five accelerometers simultaneously at temperatures up to 1000 °F, for durations of up to 75 min. The fixture was used to evaluate accelerometer performance up to 3 grms over a 5 – 300 Hz frequency range for multiple sensors subjected to single-sided heating at temperatures between room temperature and 1000 °F. The shaker was controlled using the Sandia National Laboratory (Albuquerque, New Mexico) "Rattlesnake" vibration controller, programed to trigger vibration test profiles during constant temperature holds. Vibration test data was acquired using the Hottinger Brüel & Kjær LAN-XI data acquisition hardware and BK Connect® software. Separate thermal data acquisition and control systems were used for single thermocouple thermal control and to gather test data from thermocouples installed on the accelerometers and fixture. This combined load test served as a pathfinder to investigate high-temperature sensor measurements and develop larger scale Thermal Vibration Test System capability.

Keywords Testing · Environmental · Durability · Thermal · Vibration

Introduction

The National Aeronautics and Space Administration (NASA) Armstrong Flight Research Center (AFRC) (Edwards, California) has completed a series of test runs to develop a new thermal vibration-combined load testing capability in the Flight Loads Laboratory (FLL). This pathfinder Thermal Vibration Test System (TVTS) served as a platform to work through known challenges of thermal vibration testing (such as accelerometer piezoelectric resistance loss at higher temperatures [1], protecting shaker equipment from heat, and simultaneous thermal and dynamic control of a multi-environment test setup [2]-[6] at a smaller scale and less severe thermal environment than an envisioned full operating capability. In the future, the FLL plans to mature this TVTS capability to larger scale environmental qualification testing for high-temperature sensors.

The pathfinder test setup consisted of a test fixture assembly with a two-story stainless-steel heatsink bolted to a magnesium fixture atop a 500-lbf shaker. The setup was designed to generate a combined thermal-vibration environment on the top of the heat-sink. A quartz lamp radiative heater was installed above this region, and reflective alumina "fences" served both to direct heat to the region and prevent heat spillover to low-temperature hardware. Independent vibration and thermal data acquisition systems were run simultaneously and time synchronized. A central control thermocouple provided feedback to drive closed-loop control, and various additional thermocouple sensors were placed on the top surface of the heatsink to measure the thermal loads. A low-temperature control accelerometer was placed on top of the shaker armature to provide closed-loop control to the vibration fixture. During pathfinder testing, the performance of commercially available accelerometers in a combined thermal-mechanical environment was evaluated. A maximum target test temperature limit of

Jessica J. De la Cruz · Keerti K. Bhamidipati · Chris B. Kostyk · Jackson T. Winter · Natalie D. Spivey · Phillip C. Nguyen · Samson S. Truong
National Aeronautics and Space Administration, Armstrong Flight Research Center, 4800 Lilly Ave, Edwards, CA 93523, USA
e-mail: jessica.j.delacruz@nasa.gov; keerti.k.bhamidipati@nasa.gov; chris.b.kostyk@nasa.gov; jackson.t.winter@nasa.gov; natalie.d.spivey@nasa.gov; phillip.c.nguyen@nasa.gov; samson.s.truong@nasa.gov

© The Author(s), under exclusive license to River Publishers 2026

Kristin B. Zimmerman, PhD (eds.), *Dynamic Evironments and Durability Testing, 2026, Vol. 7*, Conference Proceedings of the Society for Experimental Mechanics Series, https://doi.org/10.13052/rp-9788743814184

1000 °F was selected based on the temperature ratings of candidate accelerometers available within the testing time-window. A target shaker level of 3 grms was also identified based on the capabilities of the FLL 500-lbf shaker and weight of the passively cooled test fixture. Five accelerometers and three signal conditioning hardware configurations that were considered promising candidates were evaluated to measure noise in accelerometer signals at elevated temperature, and the ability of the signal conditioning hardware to mitigate that noise. The data obtained from multiple test cases was used to validate the application of the combined loads and the performance of each accelerometer with signal conditioning hardware.

Test Objectives

The purpose of this new pathfinder TVTS capability was to apply combined thermal and vibrational loads and to measure accelerometer characterization vibration data at high temperatures (∼1000 °F). The primary objectives included the following:

- Verify the Thermal Vibrational Test System (TVTS) methodology and analysis for combined load environmental testing.
- Evaluate the performance of commercially available high-temperature (HT) accelerometers under a radiant quartz lamp environment.
- Test ability of various configurations of signal conditioning hardware to mitigate effects of HT piezoelectric resistance loss [1] in accelerometers.

Test Fixture

The test fixture consisted of a stainless-steel two-story heatsink top plate designed to hold high-temperature accelerometers on the top surface under a radiant quartz lamp heat input. The two-story design provided a thermal brake between the high-temperature test environment and low-temperature shaker hardware while maintaining adequate stiffness to transfer dynamic loads in the frequency range of interest. This two-story plate was bolted to a magnesium vibration fixture that attached to an Unholtz Dickie (Unholtz Dickie Corporation, Wallingford, Connecticut) T100 500-lbf shaker. A thermal and electrical barrier of flame retardant (FR5) G-11 sheet was placed between the test fixture and the magnesium fixture, as shown in Fig. 1**(a)**. A summary of the test fixture components, shown in Fig. 1**(a),** is listed in **Table 1**. The dimensions of the test fixture is shown in **Fig. 1(b)**. The total testable area on top of the heatsink was approximately 6- by 6-in.

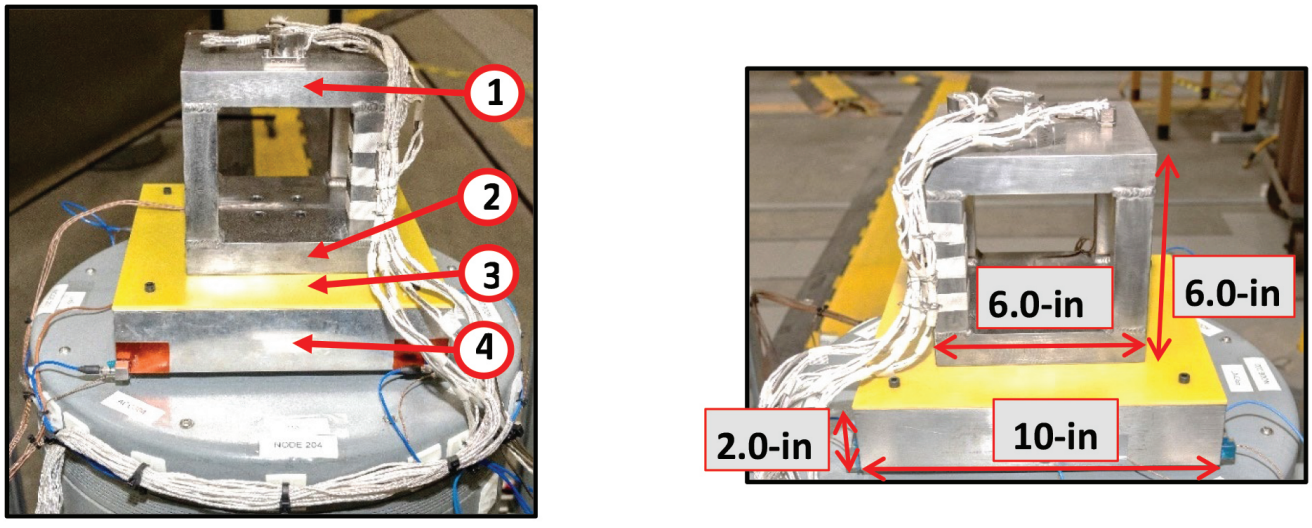

(a) (b)

Fig. 1 **(a)** TVTS pathfinder, test fixture heatsink and magnesium fixture mounted on top of Unholtz Dickie T100 shaker, and **(b)** TVTS test fixture heatsink and fixture dimensions

Table 1 TVTS test fixture and magnesium fixture material details

Number	Component	Material	Weight [lbs]
1	Test fixture heatsink top plate and supporting bars	Stainless Steel 304	25.0
2	Test fixture heatsink bottom plate	Steel A36	
3	Thermal electrical insulating barrier	Garolite G-11/FR5	0.9
4	Magnesium fixture	Magnesium AZ31B	12.5
Total weight			38.4

Material Selection

A material design space considered constraints such as material melting temperatures, thermal heatsink performance, shaker operational temperature limit and dynamic transmissibility. The target test temperature requirement was 1000 °F to be applied on high-temperature accelerometers. A heatsink was designed to dissipate thermal energy so that the maximum temperature of the fixture was less than the shaker operational temperature limit of 100 °F. Simultaneously, the stiffness-to-weight ratio had to be evaluated to make maximum use of the fixture mass [2]. Resonance is determined primarily by stiffness and mass (weight), a relationship characterized by the ratio of the modulus of elasticity, E, and density, ρ, (**Eq.** (1))**:**

$$\frac{E}{\rho} \tag{1}$$

This ratio is approximately 10^8 for metals that are suited for vibration fixtures such as steel, aluminum, and magnesium. The natural frequency of the test fixture had to rest outside of the test frequency range. The natural frequency was evaluated initially by considering a uniform cantilevered rod with the cantilevered rod vibrating in the vertical direction (**Eq.** (2)), with the moment of inertia of the rod cross-section (**Eq.** (3)):

$$f_n = \frac{1.76}{\pi}\left(\frac{EIg}{WL^3}\right)^{1/2} \tag{2}$$

$$I = \frac{bh^3}{12} \tag{3}$$

$$\frac{f}{f_n} \leq 0.8 \tag{4}$$

Where g is acceleration of gravity, W is the weight, L is the length of the rod, b is the base, h is the height, f is the forcing frequency, and f_n is the natural frequency. The fixture was kept as small as possible to reduce mass and keep effective spring rates high [7]. Dynamic transmissibility was addressed by keeping an acceptable forcing frequency to natural frequency ratio (**Eq.** (4)) of less than 0.8 since resonant amplification occurs when the frequency ratio is very near one [8]. The material selection in the material design space was confirmed by the analytical modeling found in **section 5**.

Test Setup

The thermal vibration test was conducted in the FLL High Bay area during the spring of 2025 [9], [10]. A primary frame was placed above the shaker to hold a single 36-kW quartz lamp heater with perimeter-surrounding insulating alumina fences, as shown in **Fig. 2**. A secondary inner, shorter frame was placed horizontally above the shaker to hold additional horizontal alumina sheets, providing a 6- by 6-sq in aperture for the heatsink test fixture. The alumina fences served as an insulating boundary around the quartz lamp heater to trap thermal radiation. The quartz lamp heater provided the thermal load into the thermal control region (the area within the alumina fences) via radiation, as shown in **Fig. 3**. The quartz lamp operated at 480 V with air cooling. Insulated blankets were placed around the test setup to reduce convective currents and to protect hardware and personnel. The candidate high-temperature accelerometers were mechanically fastened to the top surface of the heatsink test fixture and were exposed to radiant heat. The primary and secondary frames were bolted into the lab floor. A fan was placed over a lift table and aligned to the height of the heatsink to cool down the test fixture more rapidly after test completion. A shaker amplifier and cooling blower were placed in the vicinity for shaker cooling during operation.

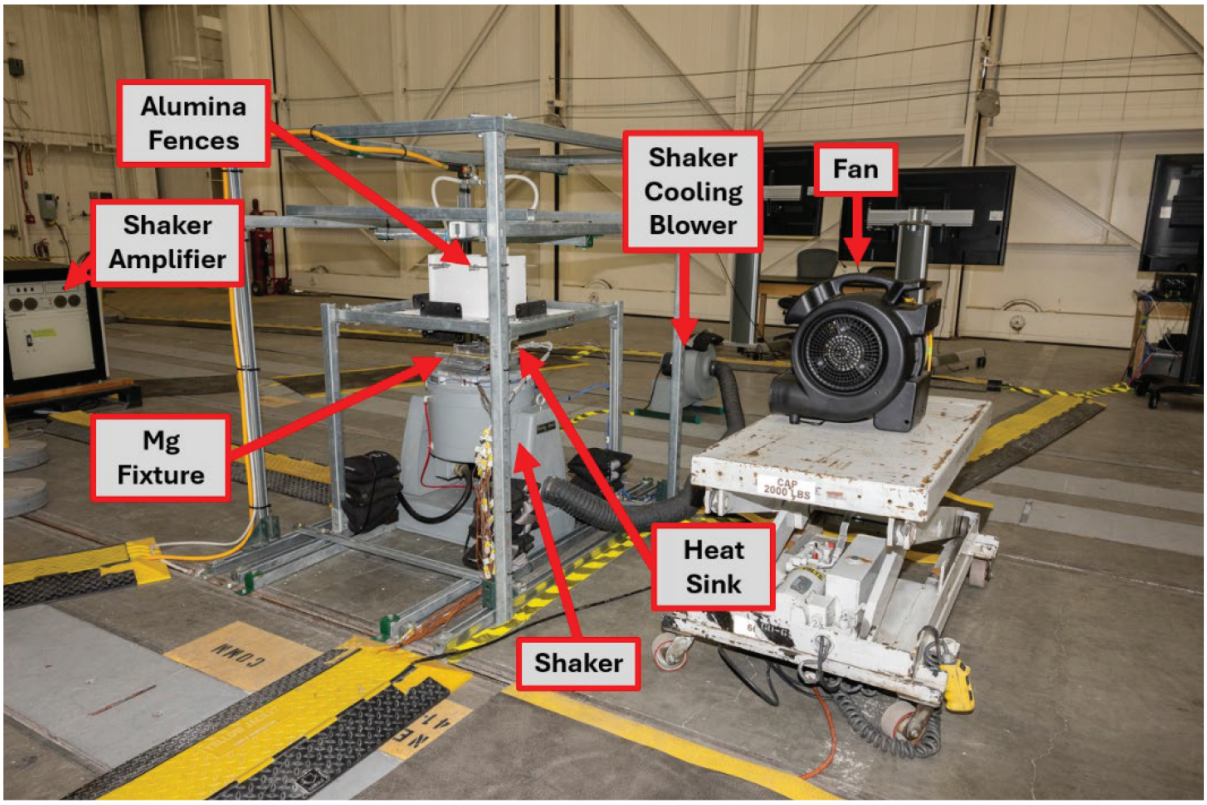

Fig. 2 TVTS test fixture heatsink and fixture mounted over shaker under quartz lamp heater

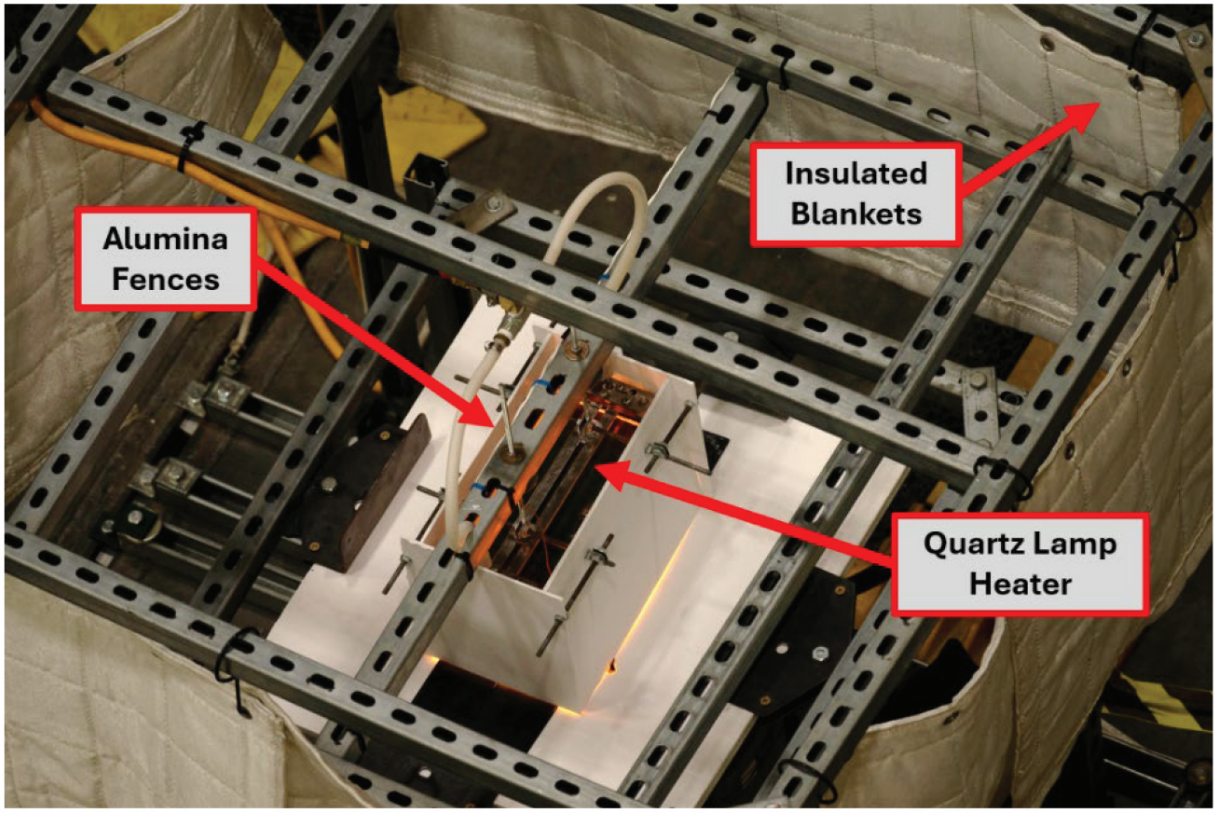

Fig. 3 TVTS test fixture heatsink and fixture mounted over shaker under quartz lamp heater

Pre-Test Design Analysis

Analytical modeling and analyses were completed to ensure that the heating system could achieve desired ramp rates and that the low-temperature hardware would not overheat. In addition, a modal analysis was conducted to ensure test fixture natural frequencies were outside of the testing frequency range to avoid resonance. For the pathfinder test series, a stepped quasi-constant temperature profile was developed. This profile included eight-minute thermal soaks at 200 °F, 500 °F, 700 °F, 900 °F, and 1000 °F. These soak durations were designed such that an incrementally stepped-vibration profile sequence (up to 3 grms) could be executed at quasi-constant temperature. An initial thermal screening was planned to assess the test setup heat transfer performance prior to the stepped quasi-constant temperature profile. This thermal screening subjected the accelerometer sensors and the test fixture to a maximum heat soak at 1000 °F for eight minutes plus an additional ramp-up time.

Thermal Soak Analysis

A conservative thermal heat soak at 1000 °F for the entire duration of the thermal screening profile of 38 minutes was modeled using COMSOL® Multiphysics simulation software. A simple and conservative transient thermal model was built to ensure that all low-temperature test hardware remained within temperature limits during the planned holds at high temperatures. A 1000 °F temperature boundary condition was applied to the top surface of the heatsink fixture, and room temperature convection was applied to the exposed lower surfaces of the fixture. The analytical results for a thermal soak at 1000 °F for 38 minutes are shown in **Fig. 4**. Most of the heat was found to dissipate via the temperature rise of the steel.

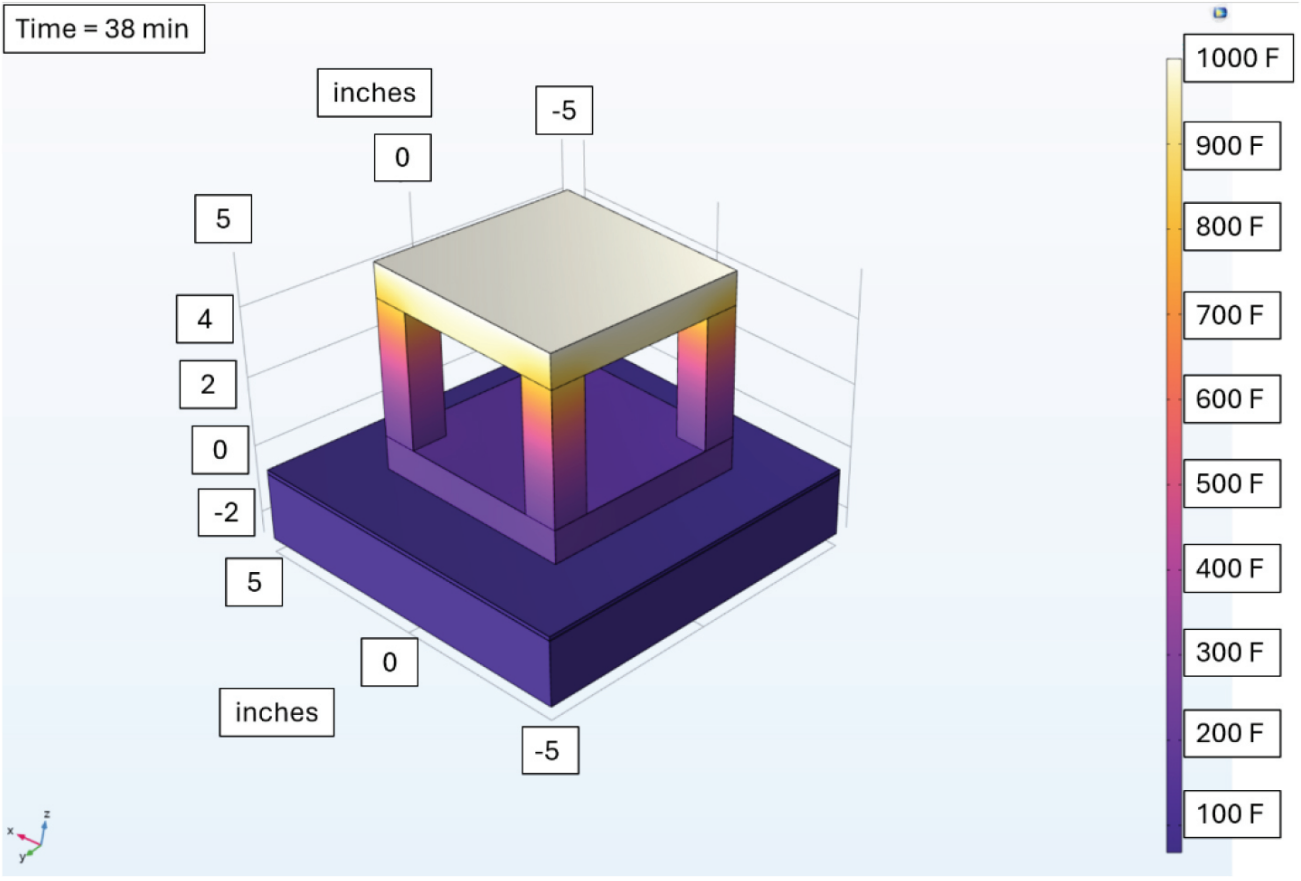

Fig. 4 Heat transfer from a 1000 °F heat soak for 38 minutes

Thermal Ramp Rate Analysis

A benchmark heater ramp rate of 80 °F/min was identified for transient temperature simulations. To ensure that the planned heater configuration could achieve this ramp rate, a second transient COMSOL® Multiphysics analysis was performed. The radiation from the quartz lamp was modeled at maximum power, as shown in **Fig. 5**. The ramp rate at maximum power was found to be 229 °F/min. Note that during testing, a ramp rate of 20 °F/min was used to achieve desired thermal gradients within the accelerometer bodies and thermal system controllability.

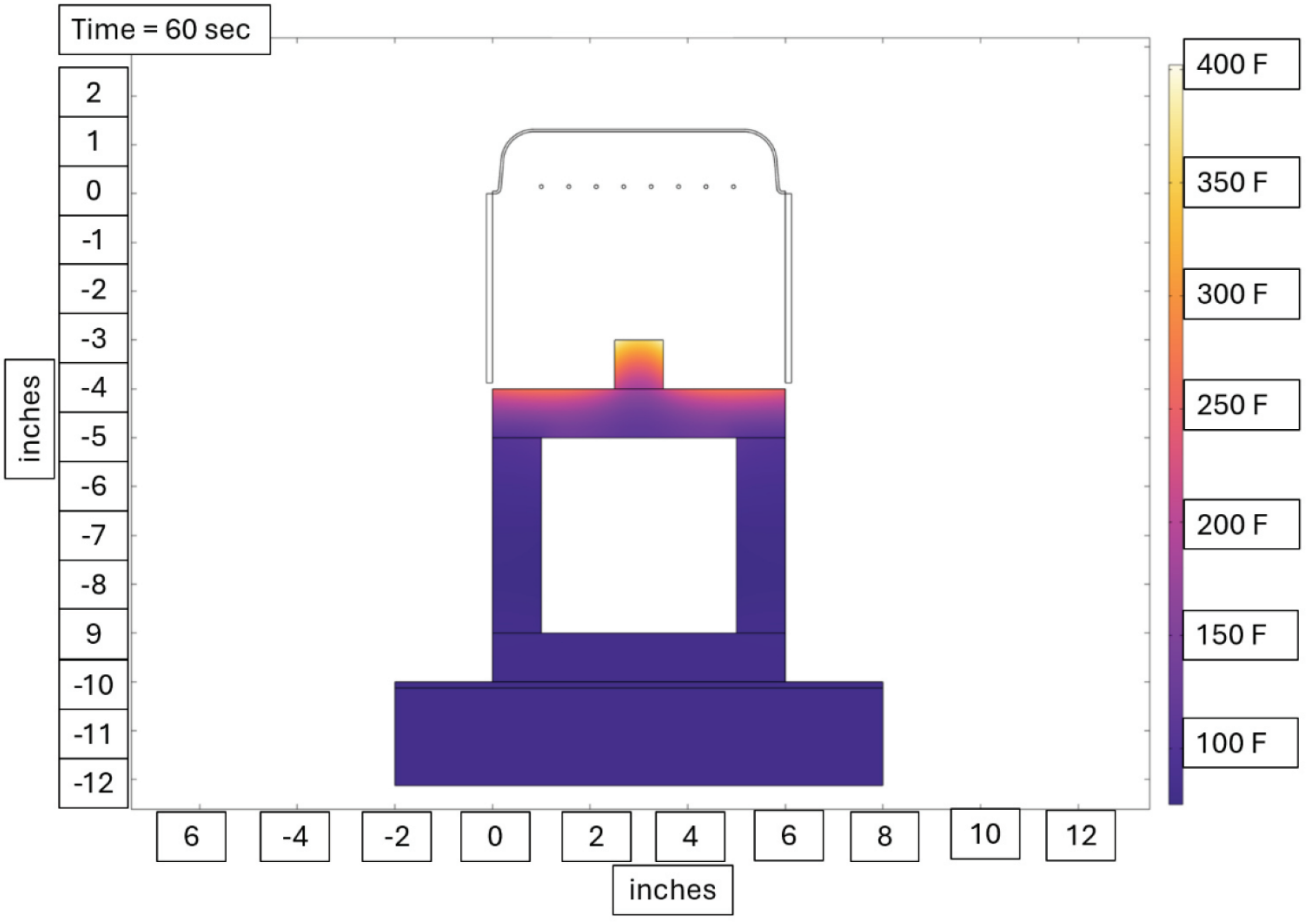

Fig. 5 Quartz lamp bulbs radiating at maximum power over the control accelerometer

Modal Analysis

For the pathfinder test series, the natural frequencies of the test fixture had to rest outside of the test frequency range to avoid amplification of dynamic loads and damage to test equipment [6]. The heatsink test fixture was set to be exposed to vertical excitation using random vibration test specifications at a maximum of 3 grms over a 5 – 300 Hz frequency range. An analytical model was built in Creo Parametric (now "Creo") 3D modeling software prior to testing to find the mode shapes, as shown in **Fig. 6**. A modal analysis at room temperature was executed with six degrees of freedom, and fixed boundary conditions at the shaker armature bolt circle pattern attachments. The material properties for each component were evaluated at 1000 °F to ensure the test fixture could transfer the dynamic loads at high temperature with **Eq.** (1).

Vibration Test Equipment

The vibration equipment utilized in this test includes high-temperature single-ended and differential charge accelerometers (rated to at least 1000 °F) from PCB Piezotronics (Depew, New York) and Dytran (Dytran by HBK, Chatsworth, California,

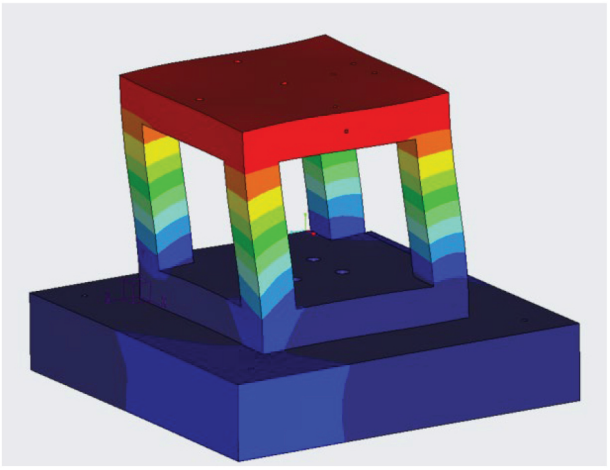

(a) [720 Hz] Heatsink in-plane sway with symmetric magnesium fixture in-plane sway

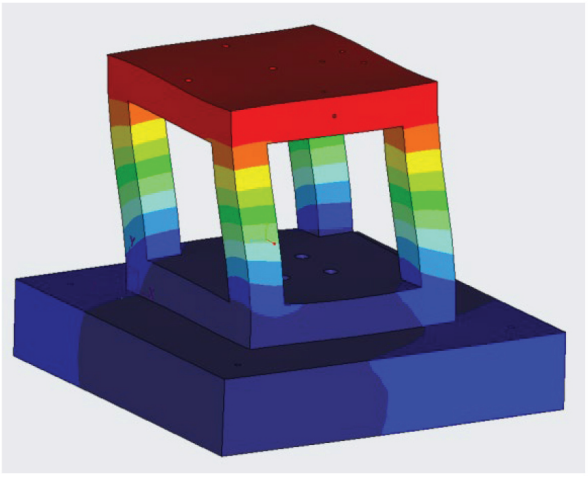

(b) [721 Hz] Heatsink out-of-plane sway with symmetric magnesium fixture out-of-plane sway

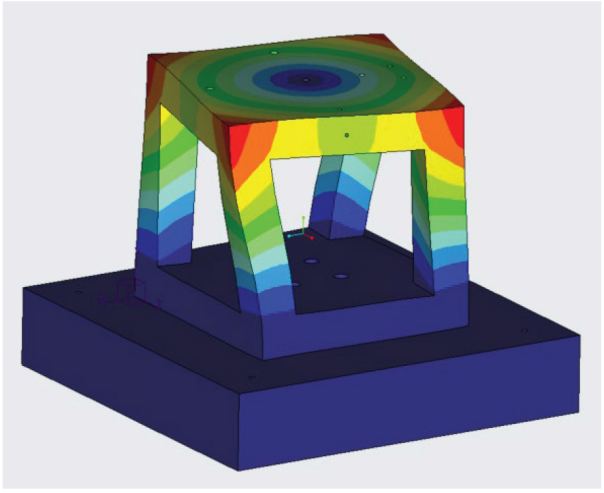

(c) [1,145] Heatsink table twist

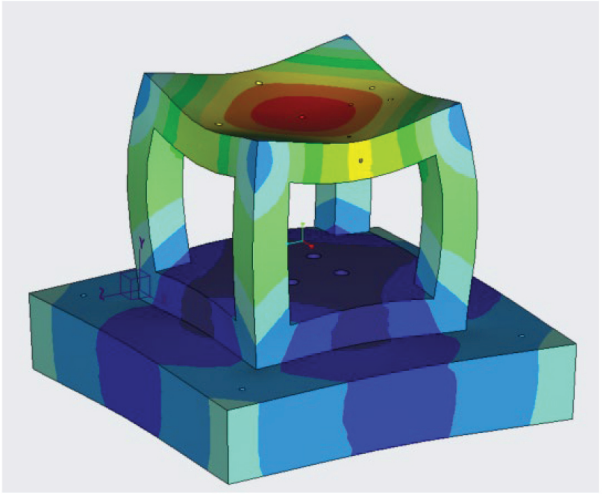

(d) [2,382] Heatsink 1st bending with symmetric magnesium fixture slight 1st bending

Fig. 6 Test fixture heatsink and magnesium fixture first four analytical mode shapes: **(a)** 720 Hz, **(b)** 721 Hz, **(c)** 1,145 Hz and **(d)** 2,382 Hz

formerly Dytran Instruments, Inc.), uniaxial standard Integrated Circuit Piezoelectric (ICP) accelerometers from PCB® and Dytran, Unholtz Dickie T100 shaker (500 lbf). Software consisted of the Sandia National Laboratory "Rattlesnake" vibration controller [11], and Hottinger Brüel & Kjær (HBK) (Darmstadt, Germany) BK Connect® vibration test software. Data acquisition and signal conditioning hardware consisted of an HBK LAN-XI 4-channel input plus 2-channel output 3160 module, a LAN-XI 6-channel 3050 module, one LAN-XI 5-slot mainframe, LAN-XI front panels 6-channel Charge UA-2120, 6-channel Differential (UA-2119, UA-2100, UA-2113), PCB®, and Dytran in-line charge amplifiers and the Precision Filters, Inc. (PFI) (Ithaca, New York) 28000 signal conditioning system.

Thermal Test Equipment

The thermal test equipment includes a 36-kW radiant-quartz lamp gold-coated heater, K-type thermocouples, a Pacific Instruments (PI) (Concord, California) 6000 data acquisition system, an Interactive Analysis and Display System (IADS) display software, the Power Control Cabinet (PCC) power system, the Thermal Controller System (TCS), and a fan.

Accelerometer Layout

High-temperature single-ended and differential charge uniaxial accelerometers were evaluated within the thermal control region. Uniaxial standard ICP accelerometers were used for vibration control and monitoring in areas where temperatures were under 250 °F. The HT accelerometers were located at the top plate of the heatsink test fixture (within the thermal control region surrounded by alumina fences). The majority of the ICP accelerometers were placed at the edges of the magnesium fixture to monitor plate-bending frequencies. The control ICP accelerometer was located directly underneath the magnesium fixture and on top of the shaker armature. This control accelerometer was used to drive the shaker armature vibration with the Sandia National Lab "Rattlesnake" vibration controller. The remaining accelerometer time histories were gathered with the HBK BK Connect® software. **Table 2** shows the accelerometer numbering scheme, number of locations, and number of channels for this test. A total number of 10 accelerometers were used with a total number of 10 channels. Accelerometer locations are shown in **Fig. 7**.

Table 2 Accelerometer Summary

Node series	Description	Accelerometer type	No. of locations	No. of channels
100	Control accelerometer	ICP	1	1
200	Top plate	HT single-ended and differential charge	5	5
300	magnesium fixture	ICP	4	4
Total accelerometers			**10**	**10**

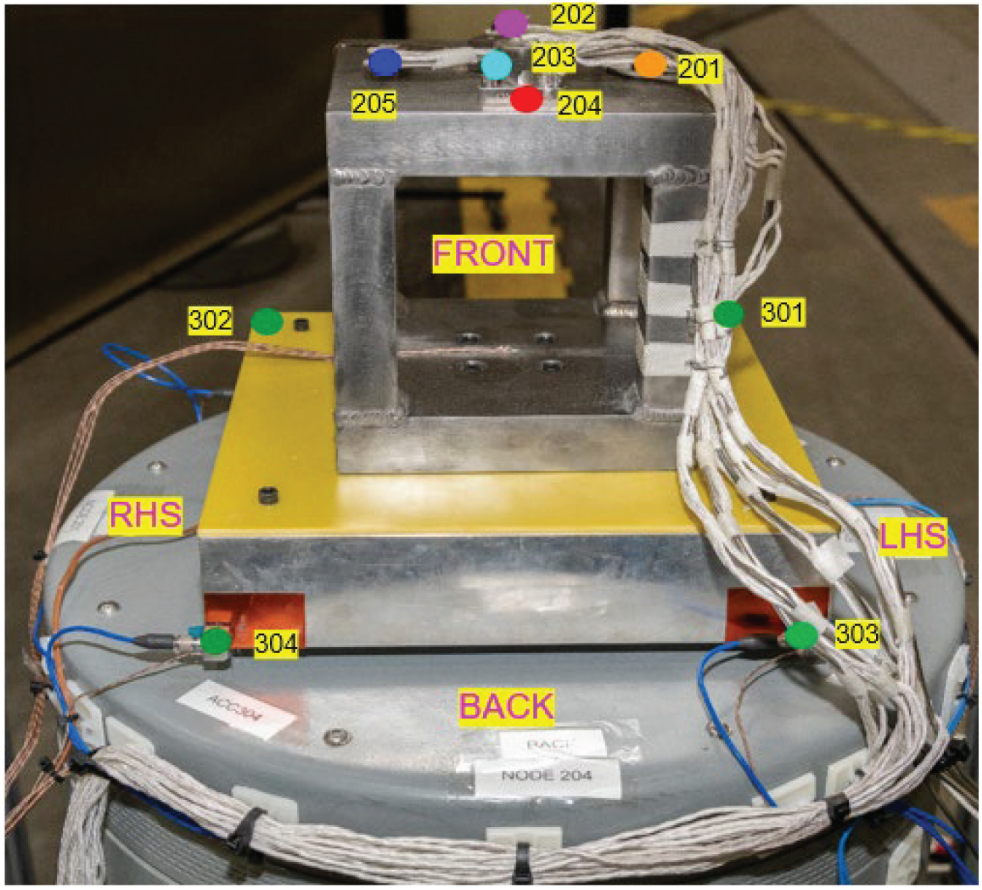

Fig. 7 Accelerometer locations

Thermocouple Layout

Each HT accelerometer was instrumented on the sensor housing with two thermocouples (TCs), with one on the top surface and the other on a side near the accelerometer base. A total of 25 thermocouples were used for this test, as shown in **Table 3.** The test fixture heatsink and the fixture were instrumented with Type-K thermocouples with high-temperature Nextel^{TM} (Newtex Industries, Victor, New York) heat-resistant braided rope. These thermocouples were installed with strain relief and formed via spot welding. Two thermocouples were used to monitor the magnesium fixture temperatures, as shown in **Fig. 8(a)**. A total of six thermocouples were placed at target heat transfer locations and are shown in red (**Fig. 8(b)**). **Fig. 9** shows an additional thermocouple that was installed on the quartz lamp heater to monitor quartz lamp reflector temperature as well as another thermocouple on the shaker.

Table 3 Thermocouple summary

Thermocouple channel name	Location description
ACC201_TOP	Accelerometer 201, top surface
ACC202_TOP	Accelerometer 202, top surface
ACC203_TOP	Accelerometer 203, top surface
ACC204_TOP	Accelerometer 204, top surface
ACC205_TOP	Accelerometer 205, top surface
ACC201_BOT	Accelerometer 201, bottom surface
ACC202_BOT	Accelerometer 202, bottom surface
ACC203_BOT	Accelerometer 203, bottom surface
ACC204_BOT	Accelerometer 204, bottom surface
ACC205_BOT	Accelerometer 205, bottom surface
TAHT1	Test fixture top-surface thermocouple, center, top
TAHT2	Test fixture top-surface thermocouple, center, bottom
TAHT3	Test fixture bar top-edge thermocouple
TAHT4	Test fixture bottom-edge thermocouple
TAHT5	Test fixture bottom-surface thermocouple, center
TAHT6	Test fixture surface thermocouple, region of interest
MGHT1	Cavity of magnesium fixture thermocouple
MGHT2	Magnesium fixture edge thermocouple
SHAKHT	Shaker thermocouple
ACC301_TOP	Accelerometer 301 left-hand-side front thermocouple, top
ACC302_TOP	Accelerometer 302 right-hand-side front thermocouple, top
ACC303_TOP	Accelerometer 303 right-hand-side back thermocouple, top
ACC304_TOP	Accelerometer 304 left-hand-side back thermocouple, top
ACC100_TOP	Control accelerometer top-surface thermocouple
QLAMP	Quartz lamp reflector temperature thermocouple
Total thermocouples	**25**

Test Configurations

The test described in this paper evaluated various accelerometers with various signal conditioning hardware to mitigate charge accelerometer signal noise due to impedance drop at elevated temperatures [1]. The five high-temperature accelerometers were conditioned in separate tests with three different signal conditioning configurations:

- **Configuration A:** Hottinger Brüel & Kjær (HBK) prototype front panels.
- **Configuration B:** PCB and Dytran in-line charge amplifiers.
- **Configuration C:** Precision Filter, Inc. (PFI) signal conditioning filter.

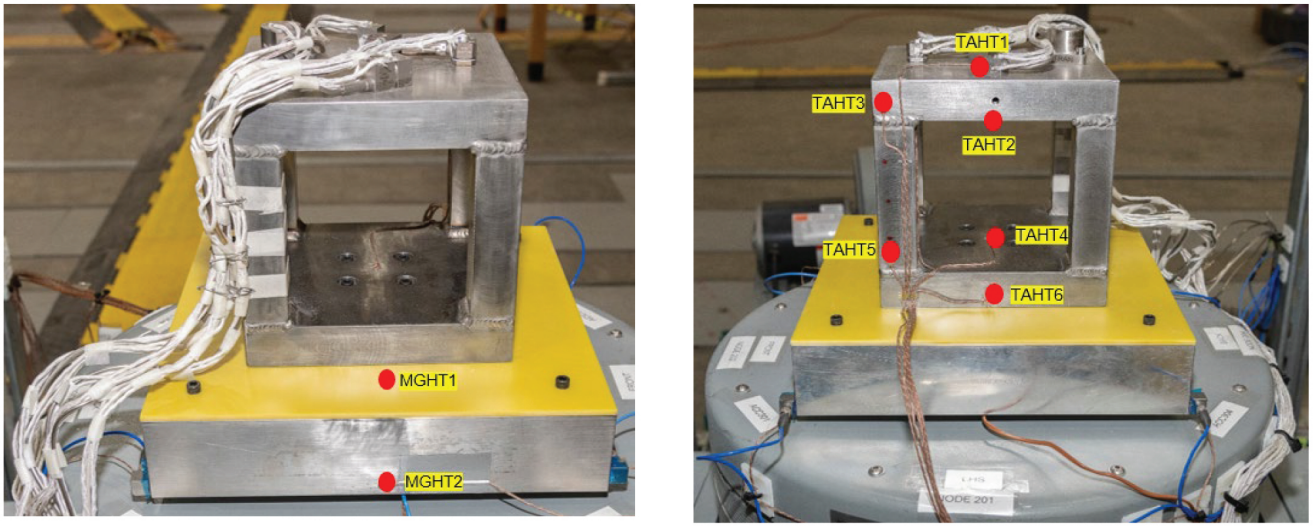

(a) (b)

Fig. 8 **(a)** Thermocouples installed on magnesium fixture and **(b)** Heatsink fixture

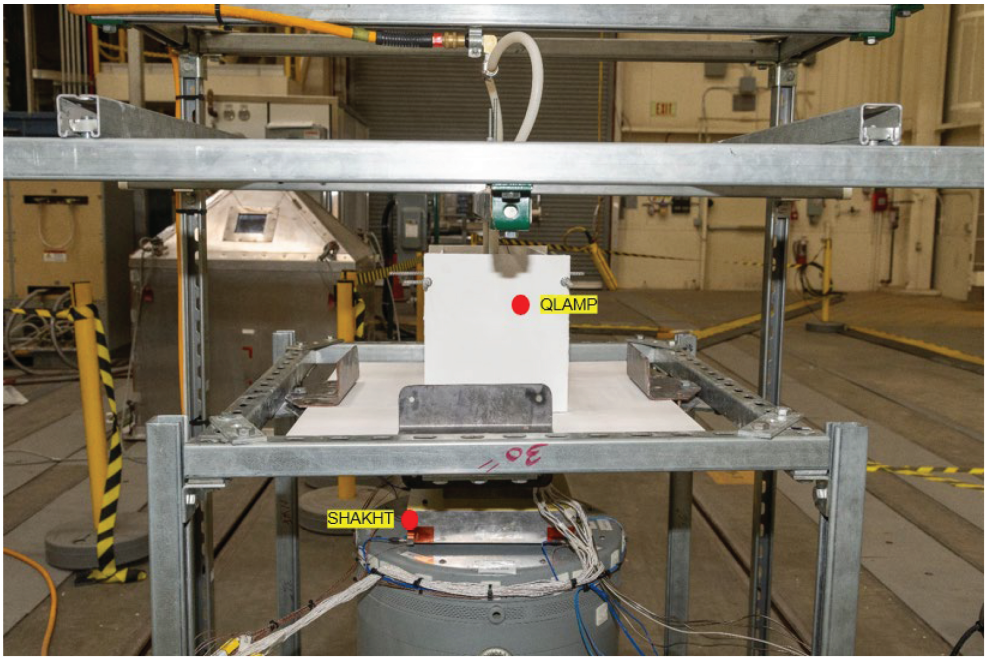

Fig. 9 Thermocouple locations on shaker and quartz lamp

The first test run cases were room-temperature vibration-only test cases with vibe profiles up to 3 grms for all three test configurations. A thermal load-only screening was executed to evaluate the survival of the sensors with a continuous ramp from room temperature to 1000 °F at 20 °F/min. Then, the combined thermal and vibration test cases (A3, B3, and C3) were executed for all test configurations with a vibration profile up to 3 grms and a thermal profile with temperature holds at 200 °F, 500 °F, 700 °F, 900 °F, and 1000 °F. Results for these three test cases will be discussed in the next section. **Table 4** shows the total number of tests runs for the test series. The separate vibration and thermal test runs helped identification and troubleshooting of any challenges before attempting the combined load test cases. The vibration-only test cases were executed to make sure the shaker had no operating issues and that the random vibration specification was being outputted correctly. The thermal screening test case was utilized to ensure that safety of test temperatures was within bounds as well as to refine the thermal controller gain and time constant for closed-loop control. The temperatures and random vibration outputs were monitored real time with IADS during testing on multiple thermal and vibration displays.

Table 4 Test configuration matrix for TVTS shakeout test

Test case	Config.	Hardware	Test case no.	Vibe profile [grms]	Thermal profile	Max temperature [°F]	Duration [min]	Number of runs
Random vibration	A	HBK front panels	A1	0.6, 1.5 & 3	-	68 - 74	10	1
	B	In-line charge amplifiers	B1	0.6, 1.5 & 3	-	68 - 74	10	1
	C	PFI signal conditioner	C1	0.6, 1.5 & 3	-	68 - 74	10	1
Thermal load	A	HBK front panels	A2	-	Screening	1000	51	1
	B	In-line charge amplifiers	B2	-	Screening	1000	51	1
	C	PFI signal conditioner	C2	-	Screening	1000	51	1
Combined thermal & vibrational loads	A	HBK front panels	A3	0.6, 1.5 & 3	Step profile	1000	75	1
	B	In-line charge amplifiers	B3	0.6, 1.5 & 3	Step profile	1000	75	1
	C	PFI signal conditioner	C3	0.6, 1.5 & 3	Step profile	1000	75	1
Total number of runs								**9**

Results

The random vibration test cases (A1 to C1) and then the thermal load test cases (A2 to C2) were executed independently in a buildup approach to verify the controllers and data acquisition systems were working properly. The thermocouples and accelerometers were examined independently to troubleshoot any issues before confirming the thermal- and vibration-profile load outputs against the controller inputs. After successfully completing the random vibration test cases (A1 to C1) and the thermal load test cases (A2 to C2), the combined load test cases (A3 to C3) were executed by simultaneously running both controllers and data acquisition systems.

The time histories and thermal profiles of the five different high-temperature accelerometers (**Table 2** and **Fig. 7**) for test cases A3 to C3 are shown in **Figs. 10** to **12**. The HT single-ended charge accelerometers are nodes 201, 202, and 203, whereas the HT differential charge accelerometers are nodes 204 and 205. The thermal profiles are plotted over the time histories for the top- and bottom-surface thermocouples on the high-temperature accelerometers in nodes 201 to 205. The accelerometer mass and location under the footprint of the quartz lamp influences the actual thermal profile applied to each individual accelerometer. The HT accelerometer at node 204 had the greatest mass and size and therefore showed the greatest temperature difference between the top and bottom surface, as shown in the different test cases (**Figs. 10(d)** to **12(d)**). The maximum temperature difference recorded between the top and bottom surface of the accelerometer at node 204 was 121 °F when the accelerometer top surface went above a 1000 °F (test case C3), as shown in **Fig. 12(d)**.

The control accelerometer shows the vibration output of the shaker and is plotted against the high-temperature accelerometer for nodes 201 to 205, as shown in **Figs. 10** to **12**. The differential charge accelerometers at nodes 204 and 205 show an increase in noise in test case A3 when compared to the single-ended charge accelerometers in nodes 201 to 203, as shown in **Figs. 10** and **12** (except for node 202)**.** The differential charge accelerometers nodes 204 and 205, however, show lower noise levels in test case B3, as shown in **Fig. 11**.

The accelerometer at node 203 shows more acceleration in all configurations when compared to the control accelerometer due to a believed calibration coefficient issue, as shown in **Figs. 10** to **12**. The same result for accelerometer 203 was observed in a different stationary heating oven test setup(results not included in this paper).

For test case C3, the differential charge accelerometers at nodes 204 and 205 show an increase in noise at higher temperatures, as shown in **Figs. 12(d)** and **(e)**. The single-ended charge accelerometer at node 202 shows unreasonably high levels of noise for test case C3 which is believed to be due to a ground isolation issue.

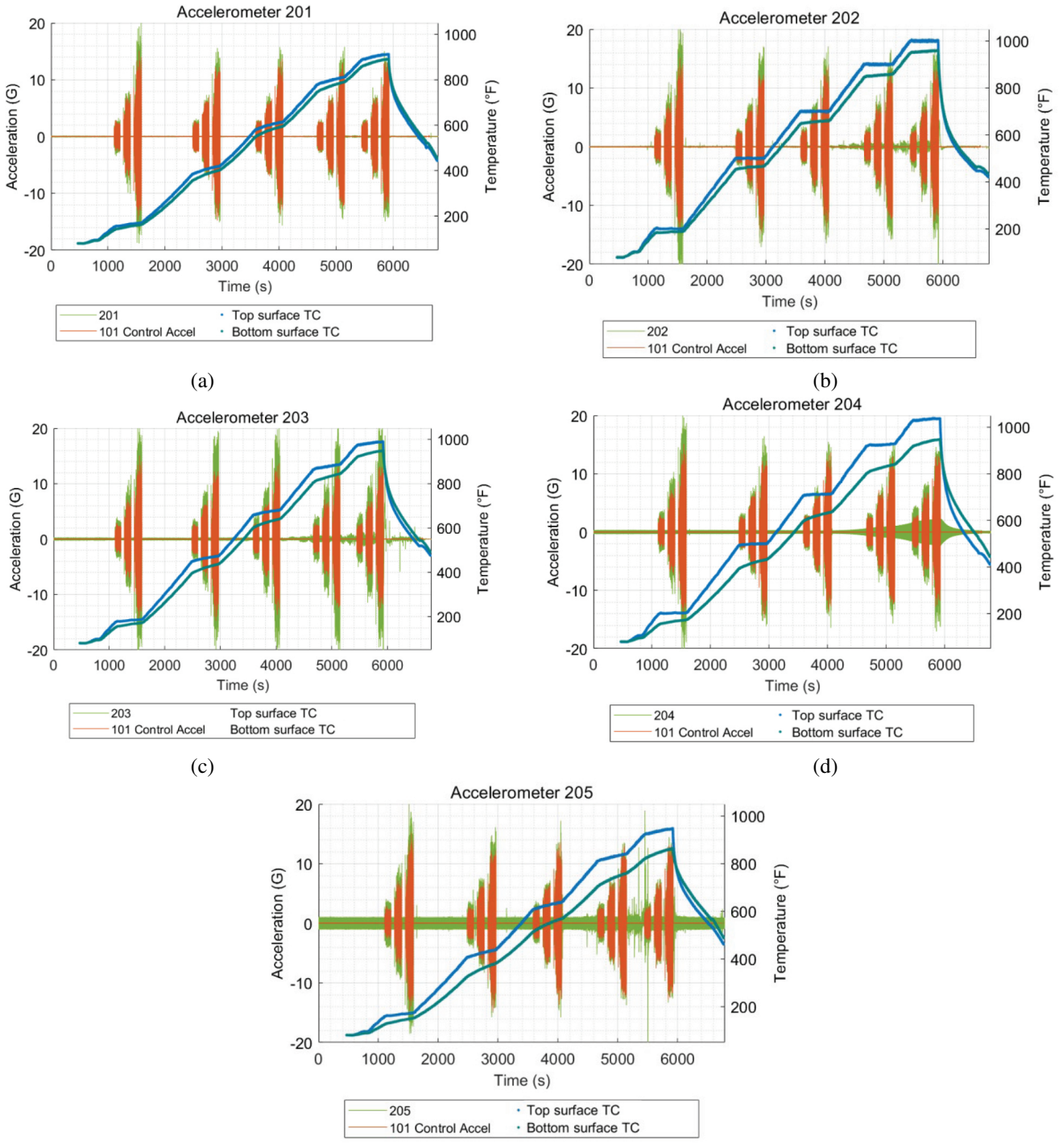

Fig. 10 Time histories for test case A3 (combined thermal and vibration loads with HBK front panels) for HT accelerometers at nodes **(a)** 201 **(b)** 202 **(c)** 203 **(d)** 204 and **(e)** 205

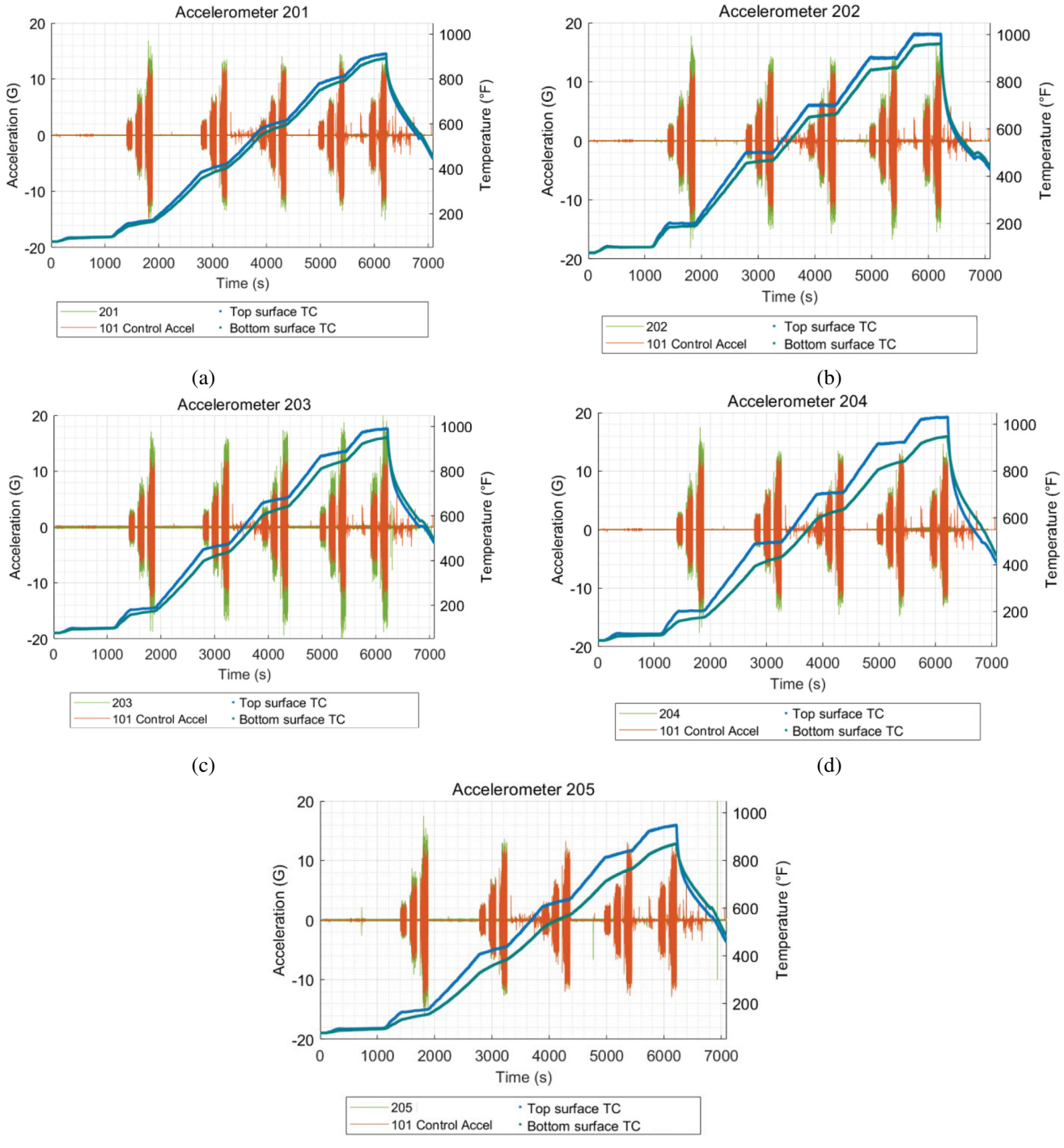

Fig. 11 Time histories for test case B3 (combined thermal and vibration loads with in-line charge amplifiers) for HT accelerometers at nodes **(a)** 201 **(b)** 202 **(c)** 203 **(d)** 204 and **(e)** 205

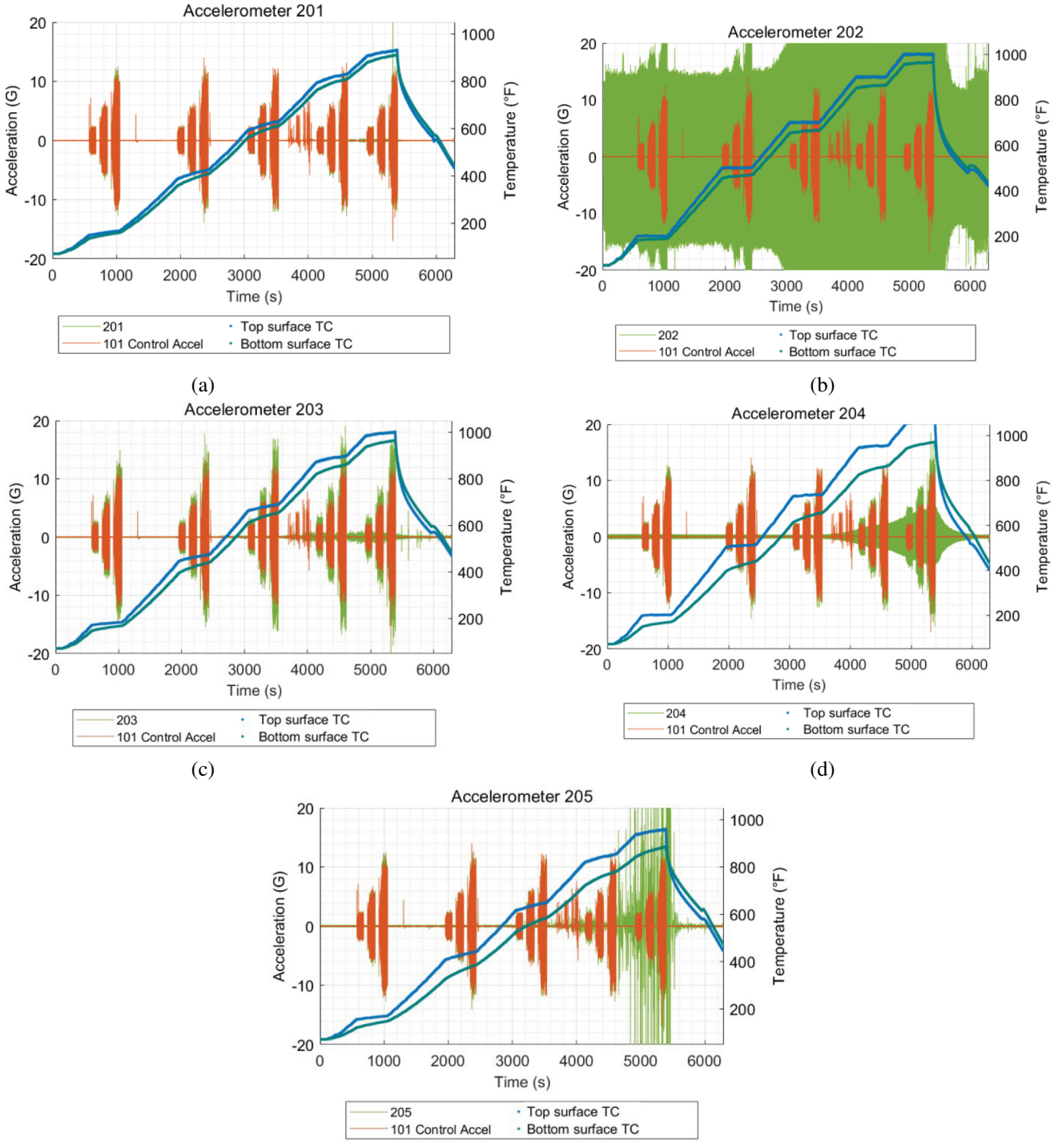

Fig. 12 Time histories for test case C3 (combined thermal and vibration loads with PFI signal conditioner) for HT accelerometers at nodes **(a)** 201 **(b)** 202 **(c)** 203 **(d)** 204 and **(e)** 205

The power spectral density (PSD) for the 3 grms vibe profile is plotted for each nominal thermal soak temperature for single-ended charge and differential charge accelerometers in nodes 201 to 205 (**Figs.** 13 to 17). Electrical noise valleys are seen at 60 and 180 Hz for all nodes and test configurations from either an unknown heater or setup isolation issue. Test cases A3 and B3 PSD curves showed a peak near 250 Hz due to the presence of loose bolts, as shown in **Fig.** 13**(b)**. The bolts were observed to loosen after every thermal shake due to a coefficient of thermal expansion mismatch between the bolts and the test fixture. A requirement to torque the bolts was enforced prior to running test case C3. This behavior was also observed for all accelerometers from nodes 201 to 205 for test cases A3 and B3, as shown in **(a)** and **(b)** for **Figs.** 13 to 17.

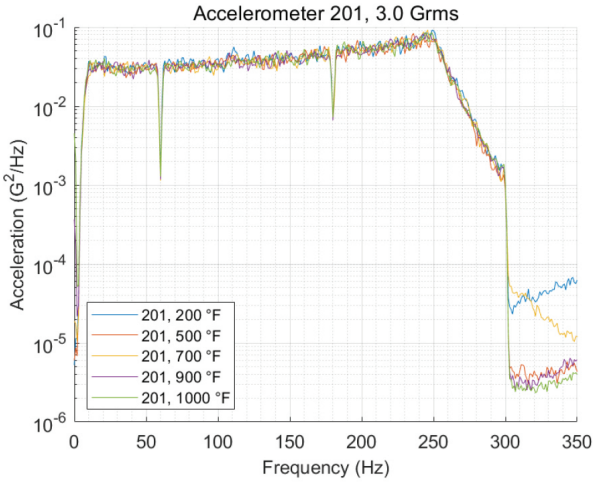

(a) Test case A3 (combined thermal and vibration loads with HBK front panels)

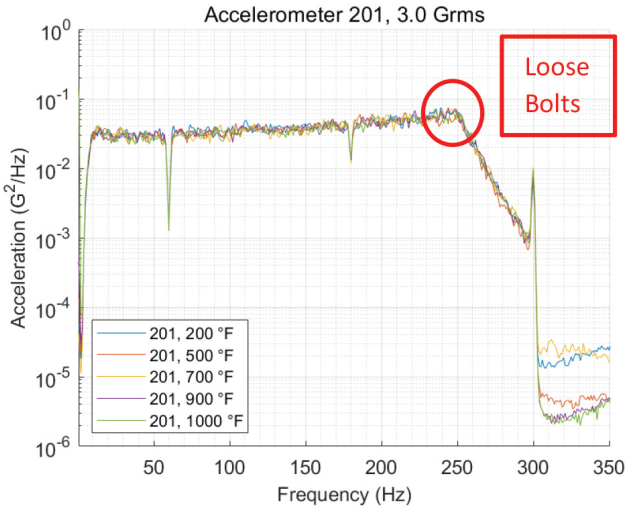

(b) Test case B3 (combined thermal and vibration loads with in-line charge amplifiers)

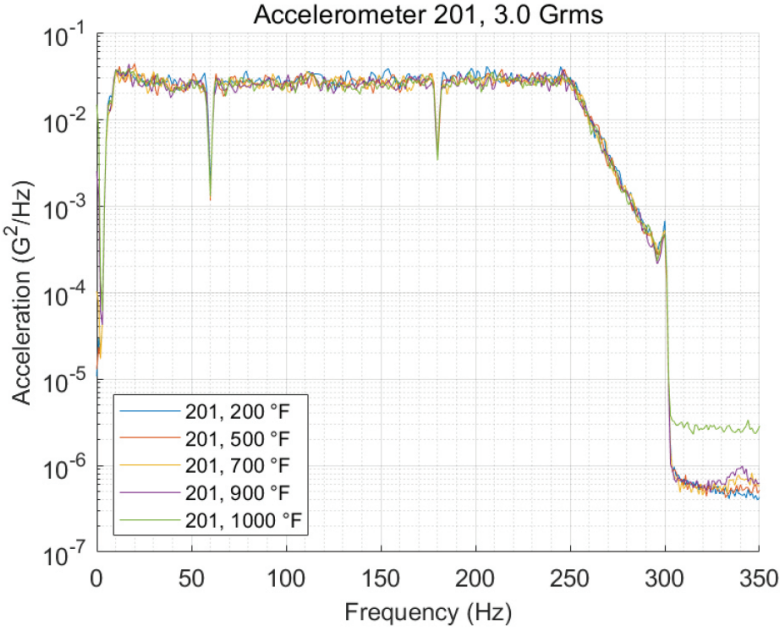

(c) Test case C3 (combined thermal and vibration loads with PFI signal conditioner)

Fig. 13 Output PSD for HT accelerometer at node 201 at different temperatures for **(a)** Test case A3 (combined thermal and vibration loads with HBK front panels), **(b)** test case B3 (combined thermal and vibration loads with in-line charge amplifiers) and **(c)** test case C3 (combined thermal and vibration loads with PFI signal conditioner)

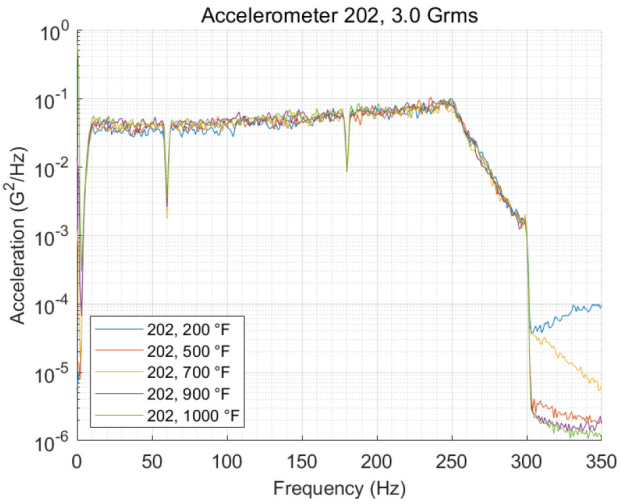

(a) Test case A3 (combined thermal and vibration loads with HBK front panels)

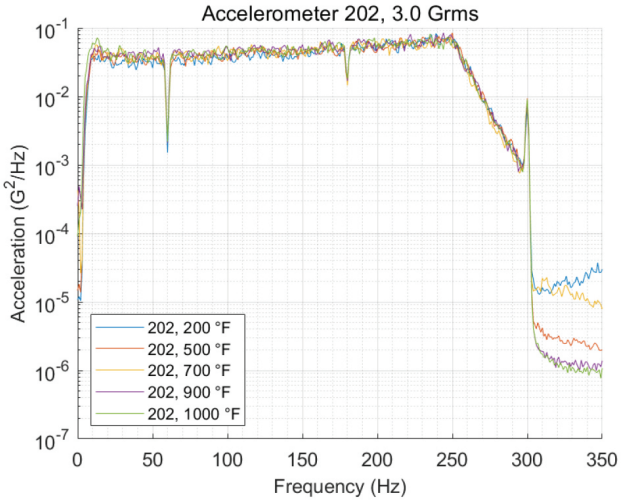

(b) Test case B3 (combined thermal and vibration loads with in-line charge amplifiers)

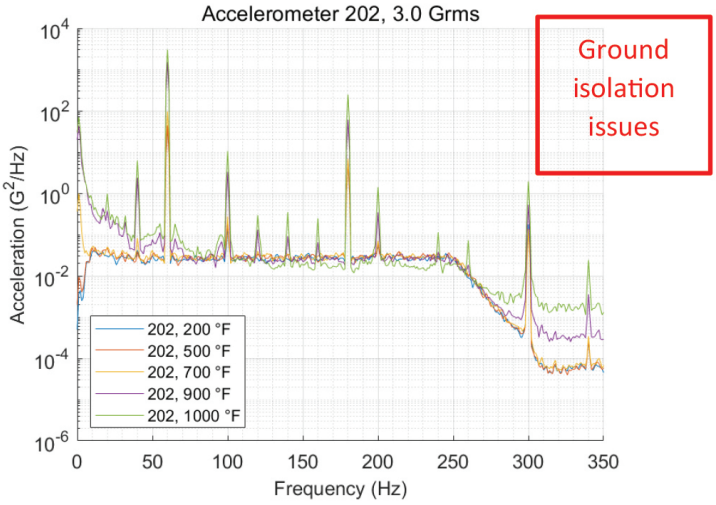

(c) Test case C3 (combined thermal and vibration loads with PFI signal conditioner)

Fig. 14 Output PSD for HT accelerometer at node 202 at different temperatures for **(a)** test case A3 (combined thermal and vibration loads with HBK front panels) **(b)** test case B3 (combined thermal and vibration loads with in-line charge amplifiers) and **(c)** test case C3 (combined thermal and vibration loads with PFI signal conditioner)

The high-temperature accelerometer in node 202 is believed to have an incidental ground isolation issue for test case C3, as shown in **Figs. 14(c)** and **12(b)**. Electrical noise and ground loops are seen to alter the vibration data and introduce unreasonable unwanted noise peaks in the output PSD frequency range. The differential accelerometer in node 204 shows significant noise level peaks at the electrical noise frequencies 60 and 180 Hz for test cases B3 and C3, as shown in **Figs. 16(b)** and **(c)**.

The change of temperature did not affect the 3 grms output PSD drastically within the specification frequency range for accelerometers in nodes 201 to 205, as shown in **Figs. 13** to **17**. The highest temperature recorded for the top plate of the two-story heatsink from TAHT1 was 880 °F, which was less than the 38-minute thermal soak analytical screening prediction of 1000 °F. The highest temperature recorded for TAHT6 (near the mounting boundary of the test fixture heatsink to the magnesium fixture) was 175 °F, which was nowhere near the 329 °F predicted by the 38-minute thermal soak analytical screening. The highest temperature recorded for SHAKHT was 85 °F. The heat transfer into the shaker did not exceed the

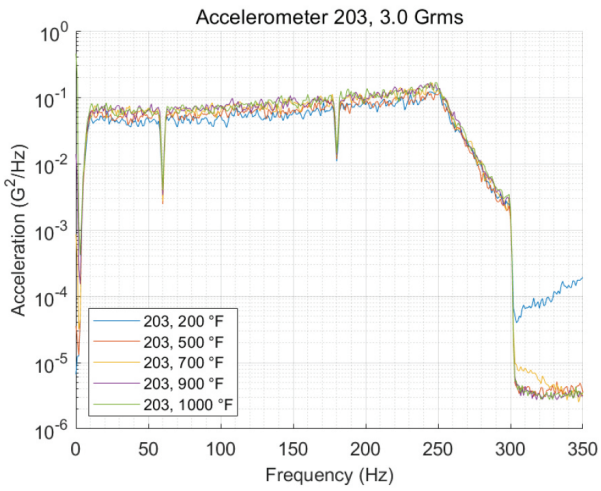

(a) Test case A3 (combined thermal and vibration loads with HBK front panels)

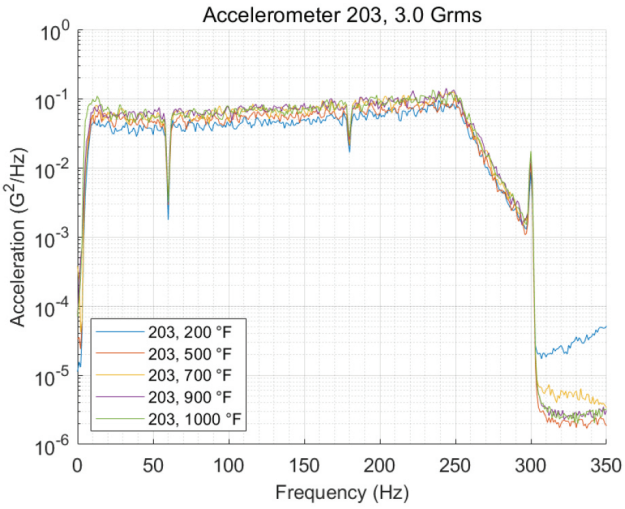

(b) Test case B3 (combined thermal and vibration loads with in-line charge amplifiers)

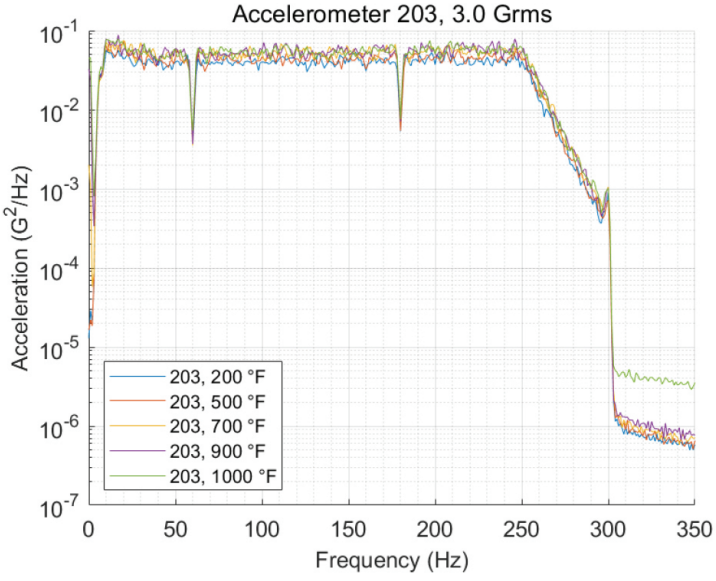

(c) Test case C3 (combined thermal and vibration loads with PFI signal conditioner)

Fig. 15 Output PSD for HT Accelerometer at node 203 at different temperatures for **(a)** test case A3 (combined thermal and vibration loads with HBK front panels) **(b)** test case B3 (combined thermal and vibration loads with in-line charge amplifiers) and **(c)** test case C3 (combined thermal and vibration loads with PFI signal conditioner)

low-operational shaker temperature limit of a 100 °F. No amplification of resonant frequencies was found within the testing range of 5 – 300 Hz.

Conclusions

The signal quality of the power spectral densities (PSDs) from each accelerometer with signal conditioning hardware combination was unique. The influence of the thermal and vibration environment was found to loosen test fixture bolts, and it is recommended to check torque periodically prior to testing. Electrical noise valleys were observed at 60 and 180 Hz for

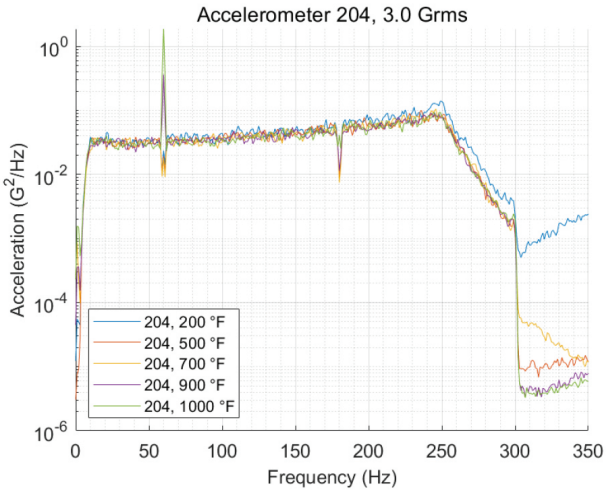

(a) Test case A3 (combined thermal and vibration loads with HBK front panels)

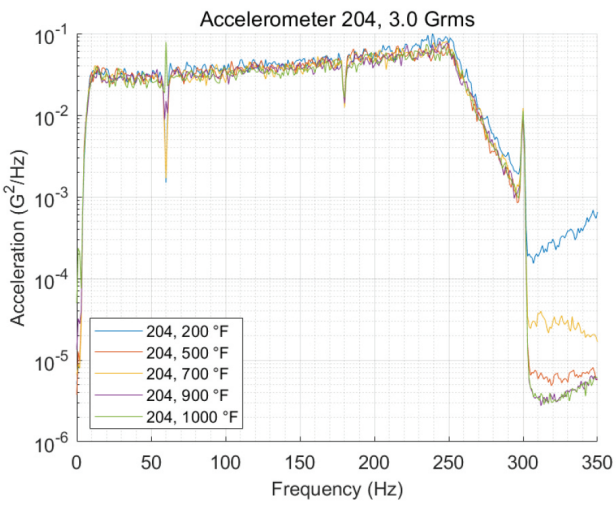

(b) Test case B3 (combined thermal and vibration loads with in-line charge amplifiers)

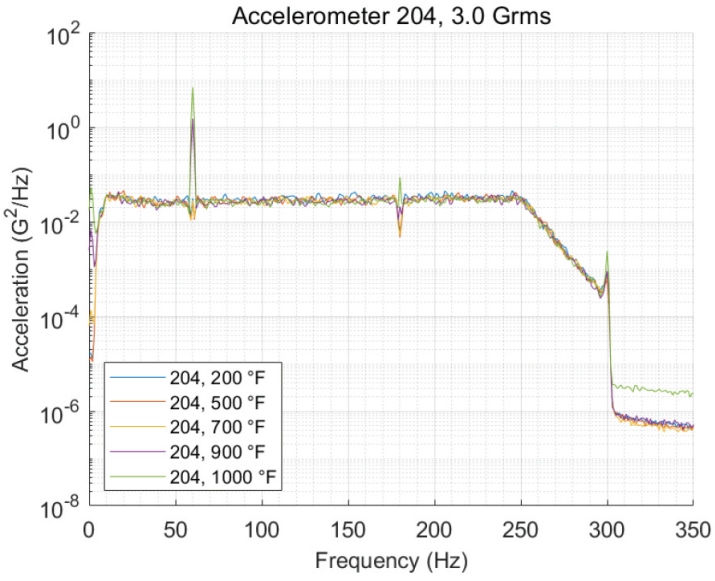

(c) Test case C3 (combined thermal and vibration loads with PFI signal conditioner)

Fig. 16 Output PSD for HT accelerometer at node 204, at different temperatures for **(a)** test case A3 (combined thermal and vibration loads with HBK front panels) **(b)** test case B3 (combined thermal and vibration loads with in-line charge amplifiers) and **(c)** test case C3 (combined thermal and vibration loads with PFI signal conditioner)

all nodes and test configurations. The change of temperature did not affect the 3 grms output PSD drastically within the specification frequency range for nodes 201 to 205. Further testing will confirm if this result is consistent for higher grms vibration profiles with different test fixture weights and thermal cooling properties. The accelerometer and thermal time histories along with the output PSDs show that the NASA Armstrong new testing capability can apply the random vibration test specification and the thermal load, simultaneously.

The single-ended and differential charge accelerometers performed similarly in the radiant quartz lamp environment used during this pathfinder test. The single-ended charge accelerometers in nodes 201 to 203 required commercially available 10-32 connector cables, whereas the differential accelerometers required unique cable connectors that were not as readily commercially available. The higher price of the differential accelerometers is a tradeoff to assess since they did not

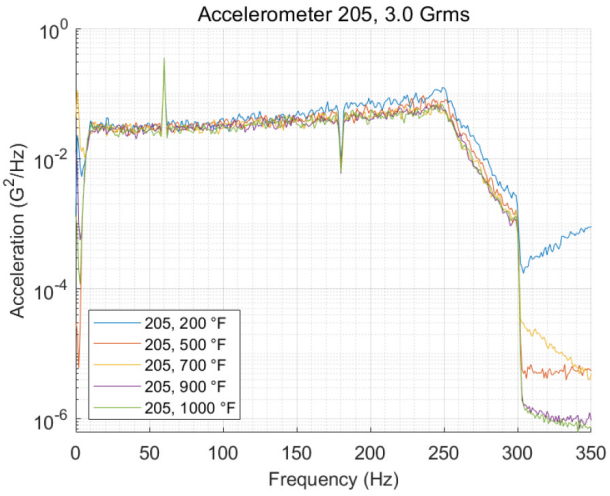

(a) Test case A3 (combined thermal and vibration loads with HBK front panels)

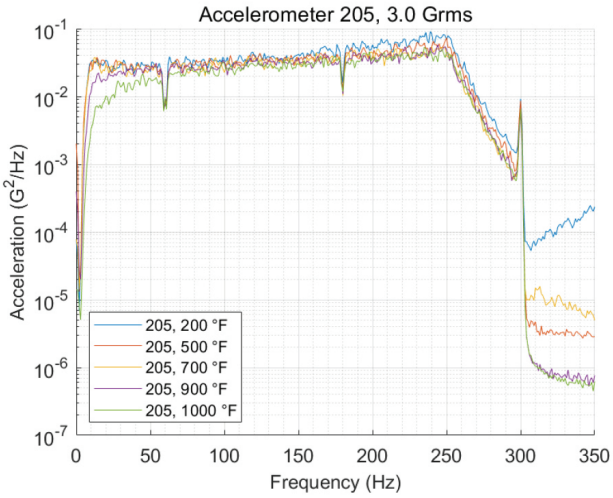

(b) Test case B3 (combined thermal and vibration loads with in-line charge amplifiers)

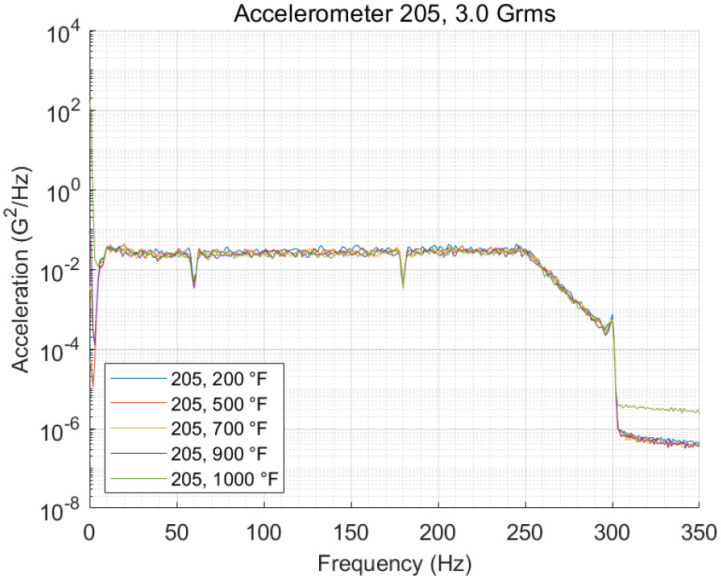

(c) Test case C3 (combined thermal and vibration loads with PFI signal conditioner)

Fig. 17 Output PSD for HT accelerometer at node 205, at different temperatures for **(a)** test case A3 (combined thermal and vibration loads with HBK front panels) , **(b)** test case B3 (combined thermal and vibration loads with in-line charge amplifiers) and **(c)** test case C3 (combined thermal and vibration loads with PFI signal conditioner)

improve the signal quality greatly for this application. Size, mass, price, and connector cable availability are influencing factors to consider when selecting a high-temperature accelerometer for combined load testing. For the single air-cooled lamp quartz lamp setup used in the FLL, differential charge accelerometers were not needed to mitigate test environment noise.

The pathfinder Thermal Vibrational Test System (TVTS) test results show additional combined thermal vibration tests could be developed by following the analysis methodology and setup described in this paper. The Flight Loads Laboratory (FLL) plans to mature TVTS to a larger-scale environmental qualification capability for new high-temperature sensors. Several opportunities to evolve TVTS for larger scale testing include active cooling arrangements to thermally isolate fixtures, larger shakers, and vacuum chamber integration.

Acknowledgments The authors thank the AFRC FLL and the AFRC Code 560 Aerostructures personnel who supported planning and operations to test in the lab. The authors also thank Kevin Westhora from Dytran, Mike Powell from FLW, Inc., Doug Lovelace and Melissa Hall from HBK, Nicholas Schultz, Bob Metz and Roger Kenyon from PCB, and Alan Szary from PFI for providing hardware knowledge, purchase assistance, loaners and support.

References

1. Mayo, Scott, "Considerations For Using Charge Amplifiers With High Temperature Piezoelectric Accelerometers," Technical Paper 339, Endevco.
2. Hudson, Larry, and Stephens, Craig, "X-37 C/SiC Ruddervator Subcomponent Test Program," 2009 Annual Meeting, NASA Dryden Flight Research Center, Edwards CA, September 29, 2009.
3. Kehoe, Michael W., and Deaton, Vivian, "Correlation of Analytical and Experimental Hot Structure Vibration Results," NASA Technical Memorandum 104269, 1993.
4. Kehoe, Michael W., and Snyder, Todd H., "Thermoelastic Vibration Test Techniques," NASA Technical Memorandum 101742, April 1991.
5. Snyder, Todd H., and Kehoe, Michael W., "Determination of the Effects of Heating on Modal Characteristics of an Aluminum Plate with Application to Hypersonic Vehicles," NASA Technical Memorandum 4274, 1991.
6. Spivey, Natalie, "High-Temperature Modal Survey of a Hot-Structure Control Surface," 27th International Congress of the Aeronautical Sciences (ICAS), 2010, Nice, France.
7. Steinberg, Dave S., "Vibration Analysis for Electronic Equipment," 3rd Ed., John Wiley & Sons, 2000.
8. Irvine, Tom, "An Introduction to Shock and Vibration Response Spectra," Revision E, August 23, 2023.
9. De la Cruz, Jessica, "NASA Armstrong's New Thermal Vibration Test System (TVTS) Capability," Conference Presentation, Structures, Loads & Dynamics, Materials, and Mechanical Systems (SLAMMS) 2025, July 8, 2025, Merritt Island, FL. Available from J. De la Cruz, Armstrong Flight Research Center, Edwards, CA 93523.
10. De la Cruz, Jessica, "NASA Armstrong's Thermal Vibration Test System (TVTS)," Conference Presentation, Structures, Loads & Dynamics, Materials, and Mechanical Systems (SLAMMS) 2024, July 23, 2024, Las Cruces, NM 88012. Available from J. De la Cruz, Armstrong Flight Research Center, Edwards, CA 93523.
11. Rohe, Daniel P., Schultz, Ryan, and Hunter, Norman, "Rattlesnake User's Manual," Version 3, Sandia National Laboratories, Printed: Oct. 2024, SAND2024-14378, Albuquerque, NM and Livermore, CA. doi.org/10.2172/2480206

Chapter 8
A Recommended Procedure and Best Practices for MIMO Vibration Testing

Ryan Schultz and Steven Carter

Abstract Test teams must follow several steps to meet vibration test objectives, such as matching the desired specification and delivering quality data. These steps include test setup, pre-test troubleshooting and verification, test execution, data analysis, and documentation. With multiple-input/multiple-output (MIMO) vibration testing growing in popularity, a MIMO-specific testing procedure and recommended best practices is needed to help test teams and their customers set expectations and ensure high-quality, reliable test outcomes. Though vibration testing is well established with good recommended best practices available in standards and procedures from various test laboratories, there is less available for MIMO vibration and what is available may not be in common use.

Sandia National Laboratories (SNL) is pushing to develop and adopt a MIMO vibration testing procedure and disseminate best practices as the use of MIMO grows for both research and customer-facing test work. This paper aims to be a supplement to existing MIMO testing guidance in MIL810 Method 527 based our own needs and experience [1]. We present a procedure that is applicable to random vibration and transient vibration test methods. Example test setups and procedures will be given along with recommended best practices.

Keywords MIMO · Random vibration · Transient vibration · Vibration testing · Procedure · best practices

Introduction

A test procedure is useful for many reasons, including standardizing work, improving quality, and making it easier for test engineers and operators to complete test programs. Even though MIMO vibration testing is still in the research and development phase for some uses or test laboratories, a MIMO-specific testing procedure is still useful. At SNL, we are developing new MIMO test techniques and putting them to work in a rapid research-development-application sequence. On the one hand, this makes it difficult to have a standard procedure or workflow as almost no test is the same as the last. On the other hand, the demand for MIMO tests is increasing, requiring more tests and more staff to run those tests. Having some procedure to use to train these staff and standardize aspects of the MIMO testing workflow is valuable, even at this stage of MIMO test adoption.

Brief Overview of MIMO Vibration Testing

The purpose of vibration testing is to subject test hardware to vibration environments that may be encountered in-service to verify the adequacy of the design or test functional performance. Vibration testing is also used to generate test-based structural dynamics models and generate model validation data in relevant vibration conditions. MIMO vibration tests provide various benefits for each of these use cases, but the main benefit is that in-service environments are typically multi-axial and as a result a MIMO test is needed to accurately recreate the in-service environment. Outputs of a MIMO vibration test are dynamic response data, often in the form of acceleration responses from gauges installed on the test hardware, and functional performance or survivability during and after the vibration test. As a result, obtaining high-quality vibration response data and performing a test that is within specifications is critical.

Ryan Schultz · Steven Carter
Sandia National Laboratories, P.O. Box 5800, MS0346, Albuquerque, NM, 87185
e-mail: rschult@sandia.gov; spcarte@sandia.gov

© The Author(s), under exclusive license to River Publishers 2026

Kristin B. Zimmerman, PhD (eds.), *Dynamic Evironments and Durability Testing, 2026, Vol. 7*, Conference Proceedings of the Society for Experimental Mechanics Series, https://doi.org/10.13052/rp-9788743814184

Types of MIMO Vibration Tests

There are two main classes of MIMO vibration tests: base excitation and multi-shaker excitation. In a base excitation test, commonly called a 6DOF test, the test hardware is mounted to the table of a 6DOF vibration test machine via fixturing and shakers excite the table to create a multi-axial vibration environment for the table and attached parts. Fig. 1 shows an example 6DOF setup with a test article mounted to a large 6DOF test machine via a fixture.

In a multi-shaker test, sometimes called an impedance-matched multi-axis test (IMMAT test), the test hardware is directly connected to several small shakers which work together to excite the system [2, 3]. Fig. 2 shows an example multi-shaker or IMMAT test setup where several small modal shakers are directly attached to a large test article. A fixture is attached to the test article to simulate the in-service attachment impedance and boundary condition.



Fig. 1 Example 6DOF test setup

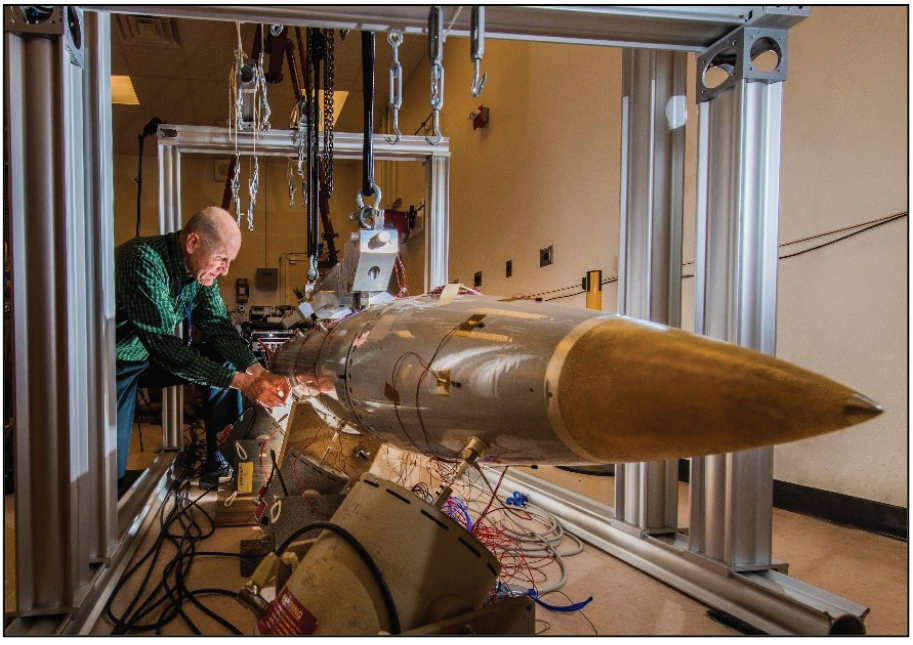

Fig. 2 Example multi-shaker or IMMAT test setup

For either setup, a MIMO vibration control system reads the accelerometer response of the 6DOF table or test hardware and determines how the shakers need to be driven to create a response which matches the test specifications. MIMO vibration specifications are typically written at multiple locations and/or directions, defining the complicated, multi-axial vibration conditions that are observed in-service.

General Testing Process

The basic test process is as follows:

1. The test provider receives a test request from the customer. All stakeholders meet to define the MIMO test type and test article configuration.
2. Perform the initial test set-up and troubleshooting to install the test article on the 6DOF machine or in the IMMAT test set-up.
3. Perform system identification testing and standard data quality evaluations (coherence, kurtosis, etc.).
4. Perform pre-test predictions to determine the optimal controller settings.
5. Perform the vibration test and process the resulting data.
6. Review the test data and report the test results to the stakeholders.
7. Archive the all the test data and reports to close-out the test.

The Need for a Procedure

While each test is different in terms of test hardware, setup, instrumentation, environments, and goals, much of what makes for a good test is common. This includes thorough and thoughtful test planning and design, work planning and review, test execution, data post-processing and test close out. This MIMO vibration testing procedure lists out these steps in moderate detail, including what should be done at each step to ensure a test is well planned, thoroughly documented, properly executed, and provides reliable data. When completed per the procedure, the test should meet the customer's goals.

This process was developed with the acknowledgement that MIMO is relatively new, so techniques and best practices will change as the field matures. However, it is important to have a standard procedure we can follow for each test to ensure consistent practices and quality outcomes.

The procedure begins with initial test definition, which is used to roughly define the goals and approach that should be used for the test. This is then refined in a thorough test design phase, where all the details of the test process and physical setup are defined. The hands-on portion of testing begins with the test setup phase, which includes hardware and data acquisition setup, instrumentation, and documenting the test setup. Next, the test can be run, which follows the test plan and entails troubleshooting, system characterization, and the actual vibration tests. Checkpoints are inserted between runs to verify data quality, check test results, and make controller or setup changes. The last step is to close-out the test by completing documentation and archiving data. This document is written in roughly chronological order, so the readers can follow it step by step as they progress through the MIMO testing workflow. That said, much like following a recipe, it is important to read then entire procedure and understand each step before beginning. A selection of recommended best practices is included at the end.

Initial Test Definition

Test activities begin with initial conversations between the customers (hardware owners needing a test) and the test engineers (those designing and performing the test) and any other stakeholders. These conversations should begin to define the test in terms of budget, schedule, hardware, test method, specifications, requirements and data products. The goals of these initial consultation meetings are to understand customer needs, requirements, desired outcomes, and how that may (or may not) connect to what a MIMO test can provide.

With test goals and requirements understood, the test team should meet to begin preliminary test definition. The following questions should be addressed in preliminary test definition:

- Is MIMO a good test methodology for this customer's test goals?
- What setup and test approach is appropriate? 6DOF machine, frame-based 6DOF, IMMAT, etc.?
- Resources: are there staff available to support this? Is there lab space and test equipment available?

- Are there pre-existing specifications or are data available to derive specifications available?
- Is modeling and simulation support needed for pre-test design?
- What custom hardware or additional equipment is needed?
- Who should be on the test team and what are the roles and responsibilities for all the members of the team. It is critical that a test lead be identified in this step.

With those questions answered, the test team should write up the proposed test definition and review it with the customer, making any necessary changes.

Resource Allocation

Next, the test lead should meet with lab owners, the test team, and other support personnel to discuss the schedule, budget, lab space, and equipment to ensure there are the resources needed, at the right time, to complete the test activities. It is the test lead's job to manage risks, including schedule, budget, space and equipment, to ensure the test is completed in the desired time frame and meets customer goals.

Test Requirements

Test requirements must be discussed and negotiated between the test lead and the customer as all test design and test execution activities are done to meet test requirements. Though not all requirements are top of mind for all customers, each of these should be discussed so the test lead and customer agree on the purpose of the test, the expected outcomes, and the reports and data products.

Requirements will vary from test-to-test but may include:

- The high-level goals of the test and how those connect to test data products (e.g., the test is for functional performance of a component in a vibration environment, so the goal of the test is to accurately create the vibration environment and function the component during vibration)
- Test hardware and boundary conditions (e.g., test a mass mock using a 6DOF base input)
- Test levels and durations (e.g., test to 0 dB of a P95/50 reentry random vibration specification for 60 seconds)
- Test specifications and tolerances (e.g., multi-axis random vibration profiles from 30 to 4000 Hz with a +/- 6dB tolerance on the specification PSD)
- Do not over-test in terms of duration or level (e.g., one run at full level)
- Collect time history data for all accelerometer channels for all full-level runs and select low-level and system ID runs
- Perform system ID tests pre- and post-full level runs
- Process test data into relevant QOIs and verify data quality for all runs
- Compare test results vs. specifications to verify the test is within tolerance and document any channels or frequency bands out of tolerance
- Document test activities including a complete test geometry, channel table, run log, photos and quick look report

Note that even though the test requirements are defined by a small subset of the stakeholders, everyone involved in the test should have a general familiarity with the test requirements.

Test Design

With the initial test definition completed and agreed upon by the test team and stakeholders, the next step is the development of a detailed test design. Test design encompasses several aspects of testing: test requirements, the list of tests to be run, test specifications, the physical test setup (fixtures, boundary conditions, shaker and accelerometer locations) and pre-test predictions (if possible). Thoughtful and thorough test design is necessary to ensure test objectives can be met within test equipment limitations and the test series can be completed as quickly and smoothly as possible.

Create the Test Matrix and Test Plan

The test matrix and test plan are critical to ensuring that the right tests are run to meet customer needs and to ensure the test hardware isn't over- or under-tested. Typically, the test plan is a document detailing the test hardware, test method, specifications and requirements. The test matrix is the list of tests or runs which are required to meet test requirements and should be created by the test lead and agreed upon by the test team and customer.

A typical MIMO test matrix includes setup and troubleshooting runs (like noise floor and rigid body checks), system ID runs at various levels, low-level tests, full-level tests, and a post-test system ID run. The test matrix should include each test to be run, in the expected order, and include details such as the test level, frequency range, specification, and other useful information such as settings or control methods to use. Any run where data is collected should be planned and put in the test matrix. Deviations from the test matrix should be documented.

The test matrix should also include gates or stopping points to ensure that the group is ready to move forward (i.e., after the system ID and rigid body checks). These may involve thorough data quality reviews or test vs. specification comparisons after key runs. An example test matrix is provided in Appendix A.

Potential Anomalies and Go/No-Go Parameters

In the test plan, list out what could go wrong in the test and develop a procedure about how the expected anomalies should be handled. Attempt to define go and no-go parameters so the test facility can operate as efficiently as possible. Example anomalies could include poor data quality, degraded coherence, failures of critical gauges, test control issues, notable audible responses like rattles or bangs, clear system dynamic changes, or problems with the test article.

Define and Derive Test Specifications

Test specifications are essential to connecting the test results to in-service environments and should be carefully considered during pre-test planning. The test lead should work with the customer and environments engineers to define appropriate, MIMO-compatible specifications for each test. This should be done as early as possible as it may take time to obtain the source data and perform data processing needed to derive specifications. In addition to specifications, test tolerances, limits, and quantities of interest should be defined and derived by this team.

The specification derivation varies in complexity, depending on the MIMO approach that is being used for the test. A simple example of MIMO is simultaneously running an X, Y, and Z direction single axis test, where typical "straight line" PSD specifications can be used for each direction. A complex example of MIMO would be simultaneously controlling the three-dimensional motion at many response DOFs, where the specification includes the phase and coherence between the DOFs in addition to the PSD response at each DOF. Note that, in general, specifications for a MIMO test are not available in standards like MIL810 and need to be derived test-by-test, so this should not be minimized or left to the last minute.

Design the Test Configuration and Setup: Boundary Conditions, Load Paths, Inputs and Outputs

Aspects of the test setup, including fixtures, boundary conditions, shaker locations and sensor locations, all affect test results. With MIMO tests, especially multi-shaker or frame-based tests, there is a lot of design flexibility and therefore a lot to design. The test team should consider and design each aspect of the test setup, ideally with the help of structural dynamics models. Several aspects of the test setup design can be counterintuitive, at least at this point in our collective experience, so basic engineering judgement may not suffice.

For all forms of MIMO tests, the control sensor set must be carefully chosen as the control sensors will affect the response of the rest of the body. In some cases, sensor locations are predetermined based on specification data or pre-existing hardware. General guidance is to have at least as many control DOFs as input DOFs and to have control DOFs well distributed at various locations and directions to cover or observe the entire test article. Having large regions without a control DOF, especially if they have high modal mass, may lead to control problems. In general, more control DOFs lead to more robust vibration control, assuming that the additional control DOFs are not redundant.

For 6DOF tests on the small or large 6DOF machines with built-in tables, a fixture plate and adapters may be needed to go between the 6DOF table and the test article. The fixture plate and adapters should be short, stiff, and light to avoid adding unwanted mass or dynamics to the 6DOF table and to translate the 6DOF motion as completely as possible to the test article.

Frame based tests generally require more elaborate designs and the test team will need to consider the following:

- The general test frame configuration to support the shakers and test article.

- The position, orientation, and quantities of shakers to achieve the desired excitation. It is important to consider the amount of force that is required from each shaker to avoid over-taxing or under-utilizing a specific shaker.
- The test article fixturing and necessary supports.
- How the test stand and fixture dynamics might interact with the test article and influence the control accuracy

For IMMAT setups, use pre-test predictions to determine the number, location, and orientation of shakers needed to meet test requirements. Try to equally load each shaker to avoid over-taxing some shakers and under-utilizing others. Design drive pads which connect the shaker stinger to test article, keeping the drive pads small and light. IMMAT setups also need the test article suspension and boundary conditions to be designed. As the name suggests, the interface impedance should be approximated with a fixture. Dynamic fixture design is notoriously fickle, so again utilize structural dynamics models and predictions in the fixture and general setup design phase.

Custom hardware, including fixtures, adapters, and support structures, should be designed and procured well ahead of the scheduled test date to allow for manufacturing time, dry-fits, and any necessary modifications.

Perform Pre-test Predictions

Early pre-test predictions are useful in test planning for two reasons. First, predictions using structural dynamics models can be used to design the test setup, including fixtures, sensor locations, and shaker locations. Second, once the test configuration is determined, predictions with a structural dynamics model can be used to determine control settings and methods to best balance equipment capabilities (e.g., shaker force) with test outcomes (e.g., meeting accuracy requirements or test levels). These predictions significantly de-risk the test program as changes can easily be made to a model to change fixtures or shaker configurations to design a test that will meet requirements, whereas making these changes later in hardware is often difficult or impossible. If possible, source a model and perform pre-test predictions to make informed test design decisions and understand test performance before any hardware is procured. These models and predictions do not need to be perfect or validated to be useful for test design purposes; use what is available but do not skip this step unless there is known margin in the test setup or a history of adequate performance.

Conduct Test Design Reviews

Once the test design is complete, the test team should conduct design reviews with the customer and peer reviewers to ensure the proposed design will meet test objectives. This review should cover the physical test setup as well as specifications and control approaches. The general test approach should be reviewed as well to ensure the high-level test definition is appropriate.

Test Setup

Test setup begins when test hardware is in-hand and includes building the test frame and test fitting fixtures, gathering instrumentation, data acquisition, and other supplies, installing gauges, and mounting the test article and shakers. Next, the data acquisition system is set up and the data gathering, converting, and archiving methodology is established. Then, photos and notes should be taken to completely document the setup. Once test setup is complete, testing can begin. Note that there is natural overlap with test setup and troubleshooting, so it is reasonable to expect some changes to the test setup after testing begins as the data may indicate something needs to change.

Apply Instrumentation

Instrumentation locations, directions, and labels should be pre-determined in the Test Design phase. Physically installing the instrumentation must be done per the planned instrumentation design and any deviations to gauge locations or directions, as well as any additions or removals must be documented and communicated to the test team and customer. Gauge installation should follow lab best practices to ensure each gauge is securely attached, appropriately isolated, and its cables are cleanly routed. It is important to label each sensor with an ID number and mark the local or global test axes near the sensor to make documenting the sensor's measurement axes as simple as possible.

Once all sensors are installed, document the as-instrumented gauge configuration in the channel table and by building a test geometry, which allow for visualization of each sensor's location and measurement directions. The sensor locations and directions should be compared to specification to ensure that the test setup is compatible with the specification. Subtle errors (such as a polarity flip) in the specification and test setup compatibility can lead to significant control issues in the test.

Install the Test Article

This step varies depending on the test type, but generally entails installing the test article into the test frame or onto the test machine. Specific installation details will be omitted here, but some best practices are to:

- Ensure fixtures or other hardware are securely attached and won't rattle
- Bundle and route cables to strain-relieve gauges and keep the workspace clear
- Label shaker drive cables to ensure the correct drive signal is going to each shaker
- For IMMAT setups, ensure shaker stinger attachments are installed properly and well aligned
- For free-free test setups, check the rigid body mode frequencies to ensure they are sufficiently low
- Document the shaker locations and directions in the channel table and test geometry once test setup is complete

Set up the Data Acquisition and Control System

Carefully connect the gauges and shaker drives to the data acquisition system, following the channel table. Using a two-person team is recommended, with one person plugging in and one person checking or correcting the channel table to match the as-installed sensor configuration. Have both people verify the sensors are plugged into the correct channels before proceeding. Once cable installation is complete, bundle and organize cables to organize the setup and reduce chances of snags or trips.

Define File Naming and Organization Conventions

Data from many tests will be saved during a test series so a simple, common data file naming and file organization convention should be established before testing. A recommended naming convention is to sequentially number the runs and append a short description of the test type, for example:

- run001_noise_floor for a noise floor run at the start of testing (run 1)
- run002_system_id for a system ID test
- run003_random_vibe for a random vibration test after the initial noise floor and system ID runs are complete
- run004_transient for a transient vibration test

Experience has shown that it is not possible to capture all the relevant information for test run in the file name. Consequently, details of each run, including levels, settings, and specifications used would be captured in the run log.

A file structure should be established to organize and store test data files. This may include one or more folders (e.g., organized by day or test type). However it is done, it should be clear and obvious to ensure data is easy to find and access.

The test lead should communicate this naming convention and folder structure to the test team and ensure it is being followed throughout testing.

Document the Test Setup with Photos and Notes

Once the setup is complete, document setup details with photos and notes in the test log. Photos should include the following:

- Several shots of the entire setup taken from various angles and perspectives around the setup (show the entire setup all the way around)
- Several shots zoomed in to show key details in context such as the system axes, shaker arrangements, cable routing and external instrumentation
- At least one well-posed photo which is taken to showcase the test and be used in slides and reports. This photo should have strong visual impact and be free from visual clutter such as tools, supplies or things in the background

Verify that all photos are clear and in focus. Ensure the entire setup is documented before proceeding.

Notes of the setup should supplement the photos and include details such as the location of shakers and sensors, orientation of the system on the test setup (e.g., system axes) and hardware used such as fixturing and suspension. Notes and photos should be complete enough to allow the test to be recreated in the future.

Test Execution

Test execution begins after test setup is complete and the test team and customer agree testing can proceed. Specific runs will vary test to test, but will generally include the following steps:

- Troubleshooting where the test setup is checked and changed until everything is working properly
- System identification and rigid body tests where low-level inputs are used to characterize the system dynamics and transfer functions and verify the sensor orientations
- Low-level and full-level tests for each environment
- Post-test checks to verify the system state of health after testing is complete

Successful testing is often the product of thorough planning and proper execution, so care must be taken to methodically complete each test in the test matrix, document the results, and verify data quality and test results along the way.

Pre-test Brief

The test lead should coordinate a pre-test brief with the test team, customer, and other stakeholders. This brief should review the test goals, test plan and test matrix, any hazards, and roles during test. The test lead should document when the pre-test brief occurred, who attended, and what was covered.

Follow the Test Matrix and Complete the Run Log

Testing should follow the test matrix step by step. After each test is complete, note the details of the test in the run log and complete the necessary data quality and test comparison checks before proceeding. Tests should not be run in batches (e.g., multiple runs back-to-back) as details from each test can get missed or problems may go unnoticed until the end. Before proceeding to the next test, ensure the test data is properly saved, the run log is complete, and the data and test results are adequate.

At times, there may be additional tests beyond what was planned in the test matrix or test plan. For example, during troubleshooting, there may be a dead sensor which needs to be replaced and verified or during low-level testing some controller settings may need to be modified. These are expected changes and are generally acceptable deviations, though the test lead should oversee and verify any deviations from the test matrix. Additional tests at high or full levels must be approved by the customer and other stakeholders as additional high-level tests may induce damage to the test article. Any deviations from the test matrix should be documented and treated as an informal “change order” to the test.

In many cases, the test run log is the single source of truth for what testing was done, the test settings, and what (if any) anomalies were encountered during the test. As such, it is imperative that the test run log is complete and contains the details of how each test was run, any anomalies that occurred, along with the data and specification file names. The run log should include key controller settings such as control channels, regularization settings, and transformations. All post-processing relies on connecting the data files to the metadata in the run log, so the run log must be complete, clear, and useful. The run log must be filled out after each individual run. At the end of each test day, the test lead should verify the run log is complete and save an archived copy.

Troubleshoot the Test Setup

The first step in testing is troubleshooting the setup, which includes verifying each sensor is reading and each shaker is running. Utilize noise floor and system ID tests to troubleshoot the system and identify and fix problematic sensors or shakers. During troubleshooting and all phases of testing (system ID, low level and full level vibration testing) it is important to listen for rattles or other sources of nonlinearity and identify these issues in the data, for example by checking coherence. Poor coherence in control gauges will result in poor test results, so rattles or loose joints which cause poor coherence should be addressed during troubleshooting and throughout the test.

Run Rigid Body Checks to Verify Instrumentation and Test Geometry

Verify sensor orientation by running rigid body checks on the system. This entails shaking the system in 3 translation and 3 rotation directions (e.g., X, Y, Z, RX, RY, RZ) using a low level, low frequency sinusoidal excitation. With a MIMO setup, specific drives need to be used in phase or out of phase (or set to zero) to create this uniaxial motion. The goal is to move

the test article in a simple, prescribed way well below its first elastic modes so the responses of in-axis gauges can easily be compared to verify the local sensor orientation is correct. Correct any gauge orientation issues in the channel table and test geometry then complete a final set of rigid body checks to verify everything is correct before proceeding.

Note that most test setups will not have pure rigid body modes in the test coordinate system. For example, it is common to see a rigid body mode with some rotation motion that is superimposed on the primary translating motion. It is easy to identify this kind of motion as rigid when evaluating the operating deflection shapes from the rigid body check but can be very difficult to identify when just evaluating the time data or frequency spectra. As such it is suggested that the rigid body checks be done through inspection of the operating deflection shapes or metrics based on the operating deflection shapes.

Run System Identification Tests

System ID tests should be run at multiple levels to characterize the test system's dynamics and linearity. Start at a very low level, then use predictions to determine appropriate drive levels to achieve reasonable system ID test levels. At SNL, it is common to run system ID tests at low, medium, and high levels that are spread 6 dB apart. Ensure the high-level system ID test responses are between -12 and -6 dB below the test specification levels so the system ID data is similar to, but not above, the desired full test level. Process the responses after each system ID test and check data quality metrics.

Sometimes it is necessary to use shaped spectra to ensure good data quality (high SNR, linearity, coherence) while keeping levels below the test specification. This may require tailoring drive signals to be more low-frequency or high-frequency dominant.

When running a 6DOF test or any test using drive transformations in the control, it may be useful to perform system ID checks with untransformed drives as well as transformed drives. The transformations will produce different results as the drives are working together differently with or without a drive transformation. The resulting FRFs will be different as well. In general, if a drive transformation will be used in the test, use the same drive transformation in the system ID tests.

In addition to data quality checks, it is useful to plot example FRFs and condition numbers to understand system mode frequencies and system rank. Verify and document data quality for every system ID test. We recommend locking in an appropriate system ID test level for the duration of testing (determine it during pre-testing, then use the exact same method for all subsequent system ID tests to help with state of health and system change assessments).

Run Low Level Tests

It is recommended to run tests at multiple levels from low level to full level at increments of 3 or 6 dB to verify control accuracy and test quality. For example, low-level tests may be run at -12 dB and -6 dB prior to running at full level (0 dB). Run each test one at a time, checking data quality and test vs. specification comparisons for each test before proceeding to the next. Adjust controller settings as needed between tests and document how each test was run in the run log. Ensure there is ample headroom in the drives, amplifiers, and shakers to achieve the full test level; adjust settings as needed. Note that the low-level tests should be prescribed in the test matrix and agreed upon by the test stakeholders, since additional test time may be unacceptable in some scenarios.

Run the Full Level Test

With settings determined by low level tests, run the full level test. Process the full level test data and do data quality checks. Do initial test vs. specification comparisons and determine if adequate control accuracy was achieved. Do not re-run the full level test unless allowed by the test lead (undue hardware damage could occur from running at high levels for additional durations).

Post-test System Identification

At the end of the test series, run a post-test system ID test to verify the system state of health and compare vs. prior system ID tests. Document any changes in the system pre- vs. post-test in the test documentation and inform stakeholders. Ensure the run log is fully completed, with no empty spaces, and reflects what was done and how each test was performed. Note any changes or omissions to the test matrix.

Test Anomalies

All the test stakeholders should be consulted in the case of a test anomaly (poor control, something breaks, etc.). The test lead and customer should determine how to proceed.

End of Day and End of Test: Compile Data Packages and Document Progress

At the end of each test day, take time to compile data packages and document test progress for the day. Doing this regularly will ensure details do not get missed or forgotten. Update test notes and the test run log to ensure they are accurate and reflect what was done and how each test was performed. Note any anomalies or issues.

After all tests are complete, organize test data files, ensuring a consistent naming convention was used. If test data files are compiled with other data (for example photos, test geometries, processed data, etc.) into test data packages, ensure those are consistent and complete. Archive the run log, channel table, test matrix, and test data files/packages to ensure there is a backup copy of each. Share data with stakeholders as needed.

Post-Processing and Close Out

After testing is complete, move on to the post-processing phase where in-depth data analysis and documentation can occur. Initial results were obtained and reviewed during testing, but further analysis may be needed to more completely understand the test results. Analyses and QOIs should be agreed to during test planning.

One option is to compare various runs to understand the effects of controller settings or test levels on results. This would entail plotting data from multiple tests together and comparing vs. themselves or the test specification. Document observations from these comparisons and try to assess how controller or test settings affected results.

Create the final data analysis report, which is a comprehensive collection of processed test data. Often, this includes data quality checks and test vs. spec comparisons for each test. It may also include test vs. test and test vs. prediction comparisons, as well as other QOIs that are impractical to implement during day-of or quick look data analysis.

The final test setup should also be compared to the initial test setup (from Section 4.5). It is common to make small changes during a test, such as fixing a sensor orientation, and these changes should be properly documented.

Best Practices

The previous sections outlined a comprehensive MIMO testing procedure which, while thorough and time consuming, should result in high-quality test results. Following each step in the procedure is useful, but it is helpful to highlight some key focus areas which often make or break a MIMO test.

Instrumentation and Test Geometry

Getting instrumentation exactly right and documenting the as-instrumented test geometry is critical for MIMO to work properly and to make an accurate test record. Bookkeeping and consistent practices play a big role in reducing instrumentation errors. First, choose a convention for global (system), local, and gauge coordinate systems. Understand how to transform between each of these coordinate systems. Typical practice is to have the local and gauge coordinate system transformation handled by simply re-labeling the gauge axis to the local coordinate system in the channel table (e.g., the gauge axis is X+ but that is pointing in local Y-, so call that measurement Y-). Then, a transformation matrix can be used to convert from the local to the global systems (or vice versa). Next, to minimize bookkeeping, keep consistent with how gauges are installed (e.g., gauge Z+ is up, away from the mounting surface) and how channels are ordered in the channel table (e.g., each triax is plugged in in X, Y, Z gauge order).

Whenever possible, make an accurate test geometry which captures the location and direction of the as-measured channels. This test geometry can be used to determine if gauges are installed correctly using rigid body checks and is useful for understanding system motion using operational deflection shape analysis. Most importantly, the test geometry is a visual record of the test configuration. If exact locations or directions are not known, approximations can still be useful.

Understanding System FRFs, Conditioning and Rank

System ID measurements are used throughout MIMO test series to estimate the system output/input transfer functions (or FRFs) for use in MIMO control, but the same data and FRFs are very helpful for understanding the system dynamics, conditioning and effective rank. The condition number and rank of the FRF matrix is critical for determining appropriate transformations and regularization schemes to use in MIMO control. Always compute and plot the condition numbers (ratio of the biggest to smallest singular values) to determine the system rank as a function of frequency as this will tell you the

number of active modes and how to appropriately regularize the system. It can also be useful to explicitly review the singular values of the FRF matrix to understand the number of "independent" inputs that are acting on the system.

Optimizing Controller Settings

Many MIMO tests are sensitive to controller settings. The test operators should be familiar with various controller settings and methods such as: closed-loop control methods, input and output transformations, regularization, and weighting. Each of these settings affects test behavior for both inputs and outputs and should be chosen thoughtfully and carefully. Consider which settings to choose based on the test type, and then refine those settings based on low-level tests and pre-test predictions. For example, a 6DOF test will often utilize an input (drive) transformation, which may then be augmented with regularization. To dial-in control accuracy at DOFs of interest, a weighting scheme could be used.

Day-of Data Analysis and Data Quality Checks

It is imperative that test operators analyze test results and understand what has happened in each run. This is for two reasons: first, to verify data quality (do I trust this measurement?) and second, to understand the test results (did this test meet objectives?). If test data is not examined in near real time, it is not possible to optimize settings or determine if test objectives are being met; you are flying blind. Tools and workflows to analyze data and perform test and data quality checks should be developed and available to support day-of data analyses.

Documentation

Thorough notes and documentation are critical to keeping track of various methods, settings and results. With each MIMO test, there can be dozens of parameters to document so the test operators must capture all this important information in a comprehensive run log. While many of these settings may be captured in data files, the operators should interpret this information and record it in the run log, so it is human readable and actionable for future runs or future tests.

Keep up with documentation, recording information about each run immediately and noting test performance, anomalies, and settings. It can be helpful to document the test two ways: first, the run log which captures each run and its settings and second, with a set of notes which is the "story" of the test day, focused more on what and why than a specific set of details.

Two-person Test Execution

MIMO vibration test execution is a complicated activity and can be overwhelming activity for a single person to undertake. Consequently, a two-person framework with clear roles and responsibilities is suggested to maximize test efficiency and quality. An example of the roles in a two-person framework is:

- Test Operator: The test operator is responsible for the activities related to running the test, such as: operating the control and data acquisition software, monitoring shaker performance, etc.
- Test Documenter: The test documenter is responsible for ensuring that the test matrix is being followed and that the appropriate information is entered into the run log.

Note that the roles in the two-person testing framework can change depending on the skillsets of performing the test. However, each person show have a clear role that covers the different tasks for the activities that were described in Section 5. Ideally, the roles should be defined such that each person can focus on a single task at any one-time during test execution. A secondary benefit of two-person testing is that it ensures a second person is always available for peer review and consultation during test execution.

Conclusions

Proliferation of MIMO vibration tests for research, development, and qualification activities requires test labs demonstrate a history of consistent, high-quality tests. An important step in that direction is formalizing and documenting processes, and this paper aims to be a useful starting point for MIMO testing procedures for various laboratories. This procedure is written and organized to ensure that test activities meet customer goals: run the required tests using an appropriate test setup and guarantee the data is reliable. Each step is designed to guarantee that a test is carefully planned, comprehensively

documented, correctly executed, and yields dependable data. When carried out according to the procedure, the test should fulfill the customer's objectives.

Acknowledgments This procedure is the result of more than a decade of MIMO R&D and applied work from many contributors across Sandia National Laboratories, in addition to many more years of experience in single-axis vibration testing, modal testing, and related structural dynamics work.

Sandia National Laboratories is a multimission laboratory managed and operated by National Technology and Engineering Solutions of Sandia, LLC, a wholly owned subsidiary of Honeywell International, Inc., for the U.S. Department of Energy's National Nuclear Security Administration under contract DE-NA0003525.

This article has been authored by an employee of National Technology & Engineering Solutions of Sandia, LLC under Contract No. DE-NA0003525 with the U.S. Department of Energy (DOE). The employee owns all right, title and interest in and to the article and is solely responsible for its contents. The United States Government retains and the publisher, by accepting the article for publication, acknowledges that the United States Government retains a non-exclusive, paid-up, irrevocable, world-wide license to publish or reproduce the published form of this article or allow others to do so, for United States Government purposes. The DOE will provide public access to these results of federally sponsored research in accordance with the DOE Public Access Plan https://www.energy.gov/downloads/doe-public-access-plan

References

1. U.S. Department of Defense, "MIL-STD-810H, Environmental engineering considerations and laboratory tests," Department of Defense Test Method Standard, 2019.W309W9360
2. P. M. Daborn, C. Roberts, D. J. Ewins and P. R. Ind, "Next-generation random vibration tests," in Proceedings of IMAC XXXII, the 32nd International Modal Analysis Conference, Orlando, FL, 2014. W309W9360
3. P. M. Daborn, "Scaling up of the Impedance-Matched Multi-Axis Test (IMMAT) Technique," in Proceedings of IMAC XXXV, the 35th International Modal Analysis Conference, Garden Grove, CA, 2017. W309W9360

Appendix A

Below is an example test matrix for a random vibration 6DOF test which includes various runs in the setup and troubleshooting phase, two runs in the low-level test phase, one full-level test and a post-test system identification run. The test series is divided into different phases with checkpoints (highlighted blue) to instruct the test team to pause and check specific data or results before proceeding. The test matrix can also serve as the basis for a run log by including fields to note test anomalies, file names, and other relevant information.

Table 1 Example test matrix

Phase	Complete ?	Date	File Name	Test Description	Spec Description	Test Level (dB)	Frequency Range (Hz)	Duration (s)	MIMO Control Settings & Transformations
Setup & Trouble-shooting			run001_pretest	Check amp to shaker connection: run each shaker one at a time	N/A	N/A	N/A	30	N/A
			run002_noise_floor	Preliminary noise floor	N/A	N/A	N/A	30	N/A
			Pause: Verify shaker drives, note noise issues and fix bad channels						
			run003_rigid_body	Rigid body check: X	N/A	0.10 V-pk	20 Hz	10	6DOF kinematic drive transformation
			run004_rigid_body	Rigid body check: Y	N/A	0.10 V-pk	20 Hz	10	6DOF kinematic drive transformation
			run005_rigid_body	Rigid body check: Z	N/A	0.10 V-pk	20 Hz	10	6DOF kinematic drive transformation
			run006_rigid_body	Rigid body check: RX	N/A	0.10 V-pk	20 Hz	10	6DOF kinematic drive transformation
			run007_rigid_body	Rigid body check: RY	N/A	0.10 V-pk	20 Hz	10	6DOF kinematic drive transformation
			run008_rigid_body	Rigid body check: RZ	N/A	0.10 V-pk	20 Hz	10	6DOF kinematic drive transformation
			Pause: Check rigidy body test results and verify gauge orientations. Fix test geometry and re-run as needed						
			run009_system_id	Preliminary system ID, low level	N/A	0.10 V-RMS	20-4000 Hz	60	6DOF kinematic drive transformation
			run010_system_id	Preliminary system ID, medium level	N/A	0.20 V-RMS	20-4000 Hz	60	6DOF kinematic drive transformation
			run011_system_id	Preliminary system ID, high level	N/A	0.40 V-RMS	20-4000 Hz	60	6DOF kinematic drive transformation
			Pause: Compare system ID results to understand linearity, necessary amplifier gain, and required system ID levels. Run additional system ID at desired system ID level						
Low Level Tests			run012_system_id	System ID before random vibe tests	N/A	0.20 V-RMS	20-4000 Hz	60	6DOF kinematic drive transformation
			run013_random_vibe	Low level test, -12 dB	6DOF virtual point translated to table gauges	-12 dB	50-2000 Hz	30	condition number threshold of 500. 6DOF kinematic drive transformation
			run014_random_vibe	Low level test, -6 dB	6DOF virtual point translated to table gauges	-6 dB	50-2000 Hz	30	condition number threshold of 500. 6DOF kinematic drive transformation
			Pause: Check control accuracy, adjust control settings and re-run as needed						
Full Level Test			run015_random_vibe	Full level test, 0 dB	6DOF virtual point translated to table gauges	0 dB	50-2000 Hz	30	condition number threshold of 500. 6DOF kinematic drive transformation
			Pause: Check control accuracy and note test performance						
Post Test			run016_noise_floor	Post-test noise floor	N/A	N/A	N/A	30	N/A
			run017_system_id	System ID before random vibe tests	N/A	0.20 V-RMS	20-4000 Hz	60	6DOF kinematic drive transformation
			Pause: Compare pre- and post-test noise floor and system ID results to verify the system did not change and sensors are healthy						

Chapter 9
Test-to-Failure Characterization and Acceleration Signal Feature Analysis of Electronic Systems Under Repeated Shock Loading

Trotter Roberts, Hugo Luck, Joud N. Satme, Mohsen Gol Zardian, Sina Navidi, Ryan Yount, Austin R.J. Downey, and Chao Hu

Abstract Electronic systems operating in high-rate dynamic environments are susceptible to mechanical and electrical failure due to extreme shock loading. Understanding how shock response correlates with physical degradation in electronic components is critical for predicting failure and designing more resilient hardware or active control solutions. This study presents a repeatable testing framework for evaluating damage accumulation in printed circuit boards (PCBs) subjected to high-energy shock events. In this work, a PCB with an onboard resistor is mounted as a fixed-fixed beam and exposed to a test-to-failure sequence under a constant shock energy profile. High-resolution electrical resistance is monitored in situ over the course of each test to track the initiation and evolution of damage. Simultaneously, high-speed acceleration data is collected via PCB-mounted sensors, enabling detailed analysis of dynamic system behavior under repeated mechanical loading. By applying this protocol across multiple boards of identical configuration, the study generates a consistent and controlled dataset for assessing how dynamic response features relate to damage progression in electronics subjected to shock events. A series of time- and frequency-domain features (e.g., root-mean-square amplitudes, crest factors, and spectral centroids) are extracted from the acceleration signals. These features are then analyzed alongside resistance trends to identify consistent markers that precede or coincide with failure. While no online learning algorithms are implemented in this study, the framework is explicitly designed to support the development and evaluation of real-time machine learning-based classifiers for electronic condition assessment in high-rate environments, including potential applications in onboard sensing, autonomous fault detection, and predictive maintenance of mission-critical systems. All data is shared through a public repository.

Keywords Structural health monitoring · Damage detection · Feature extraction · Shock testing · Reliability

Introduction

In many high-performance applications, electronic hardware is subjected to intense shock events that can rapidly degrade structural and electrical integrity. Shock events are high-energy impulses occurring within microseconds to milliseconds, generate enormous stress gradients and abrupt deformations that threaten the integrity of mission-critical electronics. Conventional structural health monitoring and fatigue assessment techniques struggle to operate within these severe time constraints, where damage can accumulate before diagnostic systems can react [1]. Passive design techniques, like shock-

Trotter Roberts · Hugo Luck · Joud N. Satme · Mohsen Gol Zardian · Ryan Yount · Austin R.J. Downey
Department of Mechanical Engineering, University of South Carolina, Columbia, SC 29208
e-mail: tjr7@email.sc.edu; golzardm@email.sc.edu; jsatme@email.sc.edu; golzardm@email.sc.edu; rjyount@email.sc.edu; austindowney@sc.edu

Sina Navidi · Chao Hu
School of Mechanical, Aerospace, and Manufacturing, University of Connecticut, Storrs, CT 06269
e-mail: sina.navidi@uconn.edu; chao.hu@uconn.edu

Austin R.J. Downey
Department of Civil and Environmental Engineering, University of South Carolina, Columbia, SC 29208
e-mail: austindowney@sc.edu

© The Author(s), under exclusive license to River Publishers 2026

Kristin B. Zimmerman, PhD (eds.), *Dynamic Evironments and Durability Testing, 2026, Vol. 7*, Conference Proceedings of the Society for Experimental Mechanics Series, https://doi.org/10.13052/rp-9788743814184

absorbing mounts or ruggedized enclosures, offer some protection but are unable to completely reduce failure risks when repeated shock loads cause progressive damage to delicate components [2].

To address the reliability limitations of electronics subjected to shock, there is an increasing need for high-fidelity testing and monitoring frameworks that link dynamic shock response features to physical damage evolution in electronic hardware. Prior studies have demonstrated the value of vibration and shock testing for mechanical assemblies [3], but electronic systems introduce additional complexities arising from the coupled mechanical–electrical failure modes of printed circuit boards. printed circuit boards (PCBs) damage frequently starts as trace delamination or microcracking in solder joints, which can show up as minor variations in electrical resistance prior to catastrophic failure [4]. Understanding how particular loading conditions accelerate damage requires robust analysis of time- and frequency-domain dynamic features in conjunction with in situ sensing at high temporal resolution in order to capture these early-stage signatures [5].

Active monitoring during controlled laboratory shock experiments provides a pathway to generate repeatable, high-rate datasets that reveal the interplay between mechanical response and electronic degradation. By mounting PCBs as structural elements, such as fixed-fixed beams, test configurations can reproduce realistic boundary conditions and load transfer pathways seen in embedded electronic assemblies [6]. When paired with high-speed acceleration sensing, this approach enables simultaneous observation of both the system's dynamic behavior and the onset of electrical performance degradation. Extracting statistical and spectral features from the shock response, such as root-mean-square amplitudes, crest factors, and spectral centroids, can yield early indicators of cumulative damage prior to failure [7].

This study introduces a repeatable shock testing framework to evaluate damage accumulation in PCBs subjected to controlled high-energy impact sequences. All data is shared through a public repository [8]. Electrical resistance is monitored in situ throughout the test-to-failure process, while high-speed acceleration data is simultaneously recorded to capture the dynamic response. By applying an identical test protocol across multiple boards, the framework produces a consistent dataset that links time- and frequency-domain shock response features to progressive electrical degradation. Although no learning algorithms are implemented here, the experimental design explicitly supports future integration of machine learning-based classifiers for real-time fault detection and predictive maintenance in high-rate operational environments. The primary contributions of this work are twofold. First, it provides a controlled experimental platform for quantifying the relationship between high-rate shock response features and progressive electrical failure in PCBs. Second, it establishes a feature extraction methodology and cumulative damage framework that lays the groundwork for future real-time, learning-enabled monitoring of electronic systems in extreme dynamic environments.

Background

Controlled laboratory shock environments are commonly used to replicate the transient loading conditions found in operational platforms to study these effects. Drop towers, pneumatic impactors, and similar setups allow researchers to apply repeatable, high-energy impulses to test specimens while controlling boundary conditions and impact energy. Fixed–fixed or cantilever mounting arrangements are frequently used because they reproduce realistic load transfer paths and constraint conditions seen in embedded assemblies [9]. Such controlled test environments have been shown to isolate specific failure mechanisms, making it possible to correlate the PCB's structural response with progressive electrical damage [10]. Time-domain features such as root-mean-square (RMS) acceleration, crest factor, and signal energy ratios can capture changes in amplitude and impulse response. Likewise, frequency-domain features, including spectral centroid shifts and energy redistribution across frequency bands, can reveal subtle structural softening or nonlinear effects that occur as damage accumulates [11]. In our specific application, these features provide a way to quantify subtle changes in response behavior that may correlate with solder joint fatigue or progressive micro-cracking.

Methodology

PCBs fabricated from FR4 were prepared as test specimens. Each board measured 25.40 mm $\times$ 76.20 mm $\times$ 1.60 mm and contained a single 100 mΩ, 1 W surface-mount resistor soldered at midspan using a controlled stencil process to reduce variability. The boards were mounted as fixed–fixed beams in a custom aluminum fixture (Figure 1), providing rigid boundary conditions representative of embedded electronic assemblies.

Shock loading was applied using a drop tower system (Figure 2), where a guided mass was released from a height of 12 inches (0.305 m), producing repeatable shock pulses of approximately 5000 g. The drop height and mass were held constant across all tests to ensure consistent impact energy. Dynamic response was measured using Endevco 727 piezoresis-

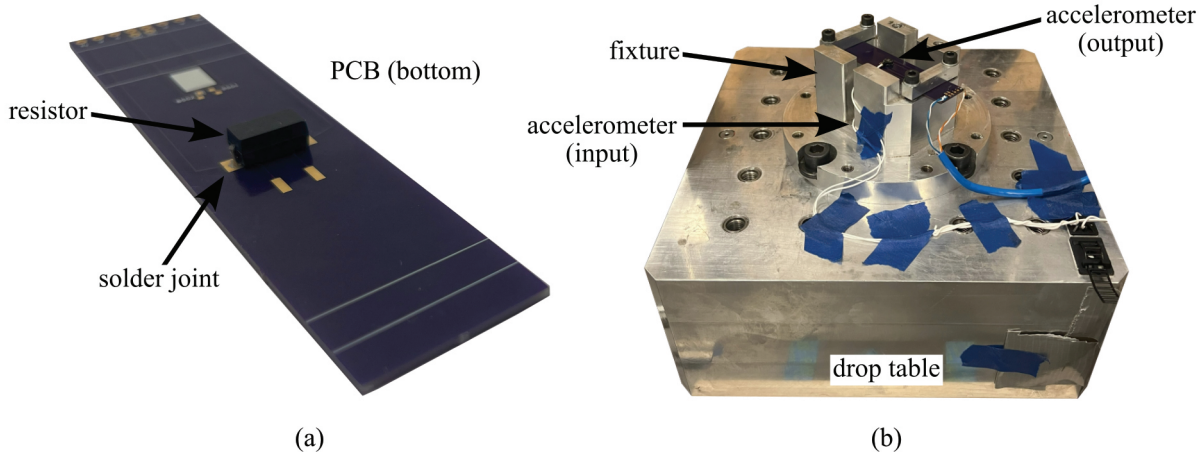

Fig. 1 The considered test setup, showing: (a) PCBs specimen with a surface-mount resistor attached at midspan (bottom side up), and (b) PCB mounted in the aluminum fixture in a fixed–fixed configuration.

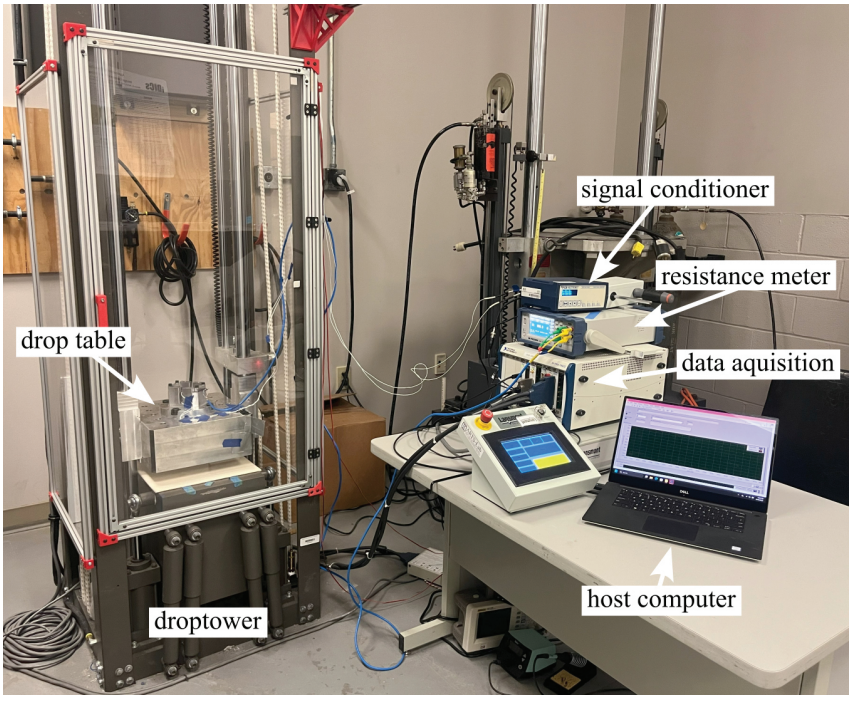

Fig. 2 The experimental setup for repeated shock testing.

tive accelerometers (20k g range, DC–50 kHz bandwidth). One accelerometer was mounted on the fixture beneath the PCB midspan to capture input excitation, while another was placed at the PCB surface at midspan to record local response. Acceleration signals were conditioned with a PCB 482C unit (gain 100×) and digitized using a PXIe-4483 module at 200 kHz, yielding 20,000 samples over a 0.1 s window per shock event. A representative excitation–response time history is shown in Figure 3.

Electrical resistance was monitored in situ with a BK Precision 2841 micro-ohmmeter (0.1 $\mu\Omega$ resolution, 0.01% accuracy) in a four-wire configuration to minimize lead effects. After each impact, ten consecutive resistance readings were recorded and averaged to provide one value per event. Acceleration and resistance data were acquired simultaneously, enabling direct correlation between mechanical response and electrical degradation. A total of ten boards were tested under identical conditions. Each was subjected to repeated shocks until failure, defined as an irreversible increase in resistance

beyond baseline variability. All boards were tested to failure, and three representative cases are reported here for clarity and consistency.

Following data collection, acceleration and resistance signals were processed to extract features representative of system dynamics and progressive damage. Time-domain features included maximum amplitude, root-mean-square (RMS) value, absolute mean, skewness, kurtosis, crest factor, shape factor, and impulse factor. Frequency-domain features such as spectral centroid and bandwidth were also calculated. To allow direct comparison across boards and impact histories, all features were normalized with respect to their initial values.

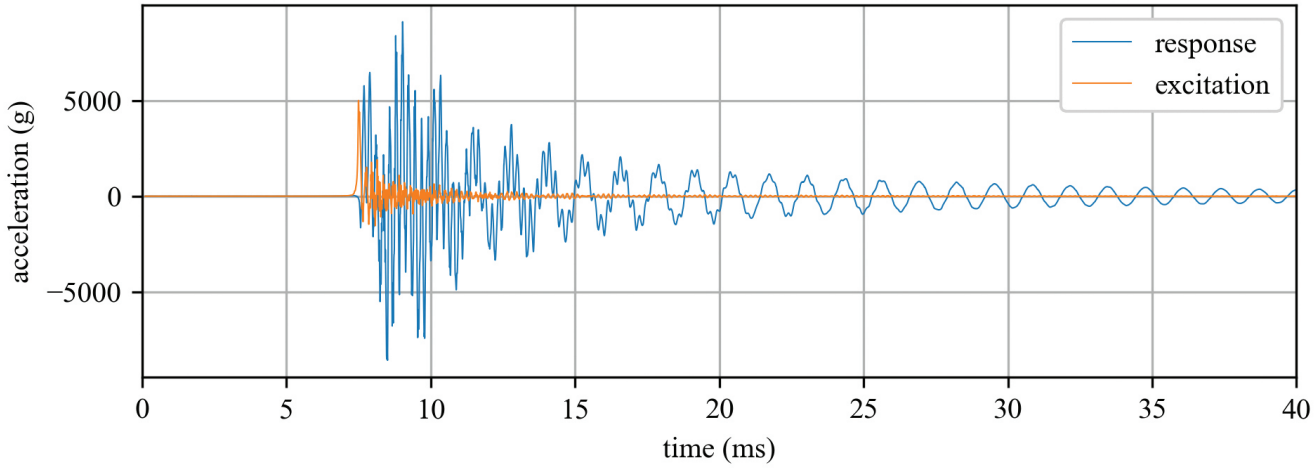

Fig. 3 Excitation and response acceleration time series under repeated impact.

Results and Analysis

The resistance histories of all three representative test boards are presented in Figure 4. These plots show the evolution of electrical resistance over the course of repeated impacts, providing a direct view of how each board progressed to failure. Although the number of shocks sustained and the absolute resistance values at failure varied between boards, a common pattern emerged. After an initial break-in period, resistance typically increased sharply, then transitioned to a slower, more gradual rise before the onset of failure. Outliers were observed where resistance deviated from this general progression, highlighting the inherent variability in solder joint and trace degradation.

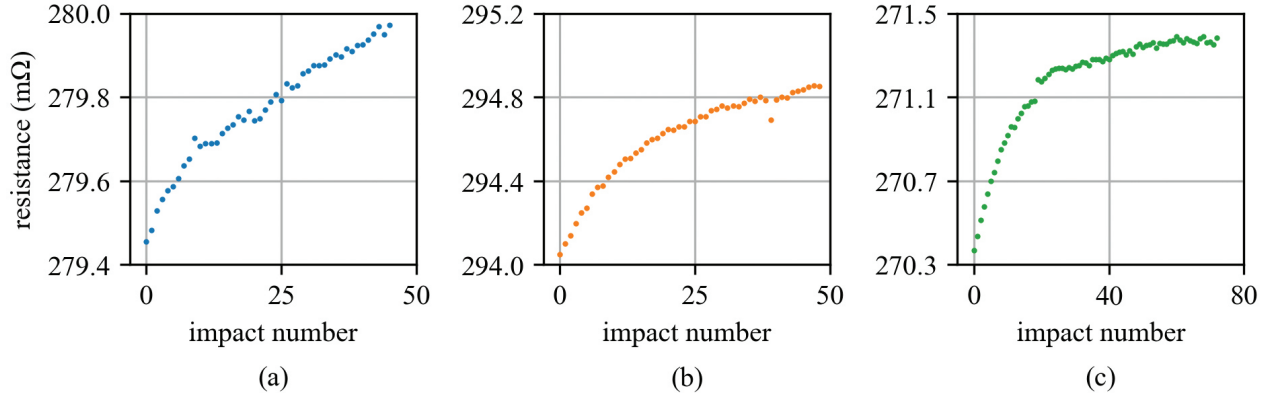

Fig. 4 Raw resistance versus impact number for (a) board 1, (b) board 2, and (c) board 3.

To better illustrate consistent resistance degradation trends, Figure 5 presents resistance histories after manual preprocessing. Outliers were first removed, followed by trimming the initial break-in period and the final few impacts where failure

was imminent. While these segments are excluded here for clarity, the complete datasets remain available in the shared repository for future analysis [8]. As shown, the processed resistance measurements reveal a common progression across boards: gradual drift followed by abrupt increases approaching failure. Figure 5 also includes fitted exponential trend-lines of the form

$$y(x) = \frac{100\left(1 - e^{-bx}\right)}{1 - e^{-100b}}, \tag{1}$$

where x is the normalized impact number (0–100), y is the normalized resistance (0–100), and b is a fitted growth-rate parameter. The anchoring ensures that all curves pass exactly through $(0, 0)$ and $(100, 100)$, enabling direct comparison between boards. The fitting was performed using nonlinear least-squares optimization via the `curve_fit` function from the `SciPy` library [12].

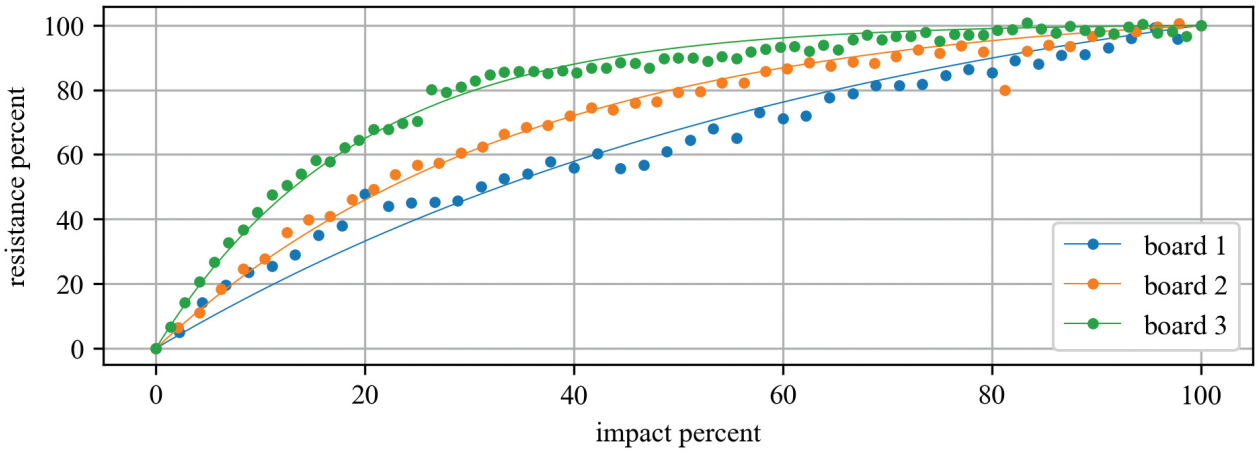

Fig. 5 Normalized resistance versus impact number with superimposed exponential trendline fits for selected boards.

Dynamic response features derived from acceleration data were analyzed in the time domain. Figures 6–8 illustrate the evolution of normalized features across repeated impacts for three representative boards. For Board 1, shape factor, RMS,

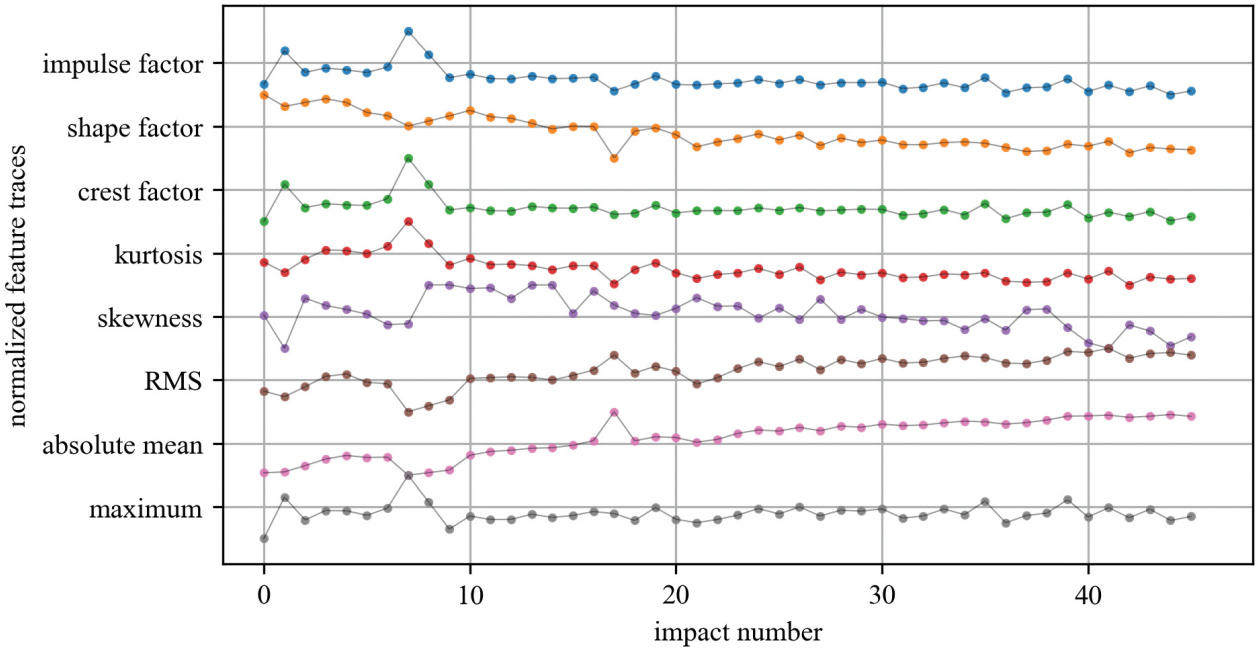

Fig. 6 Normalized time-domain features extracted from excitation and response signals for Board 1.

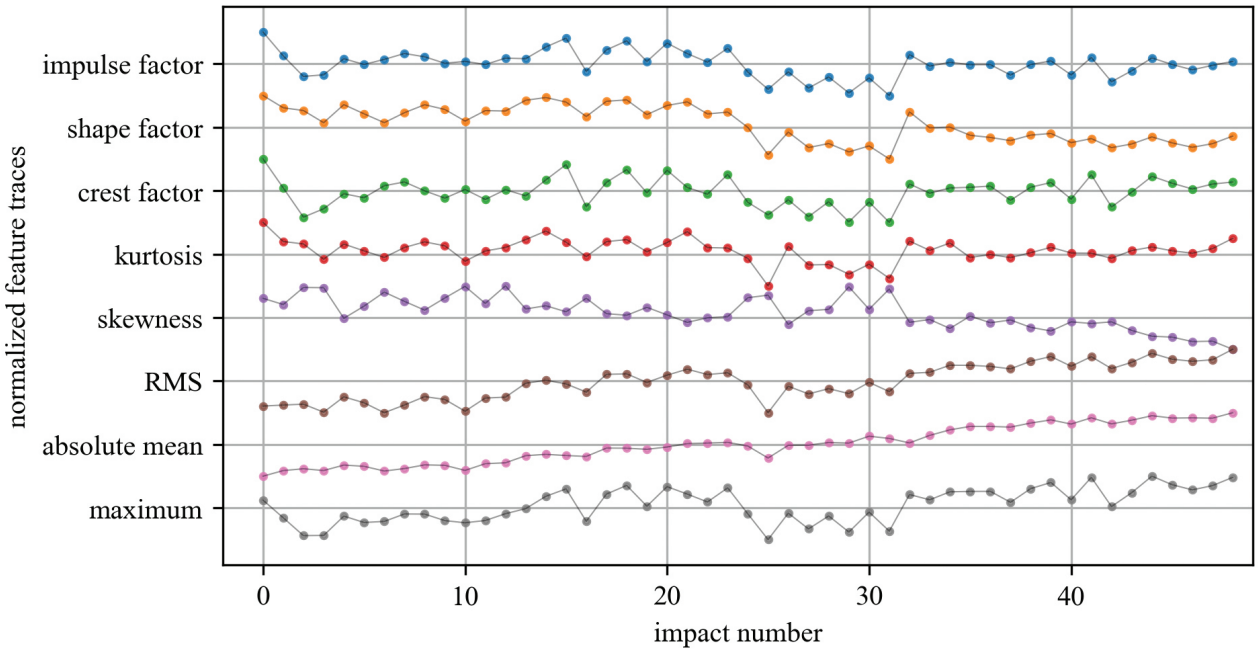

Fig. 7 Normalized time-domain features extracted from excitation and response signals for Board 2.

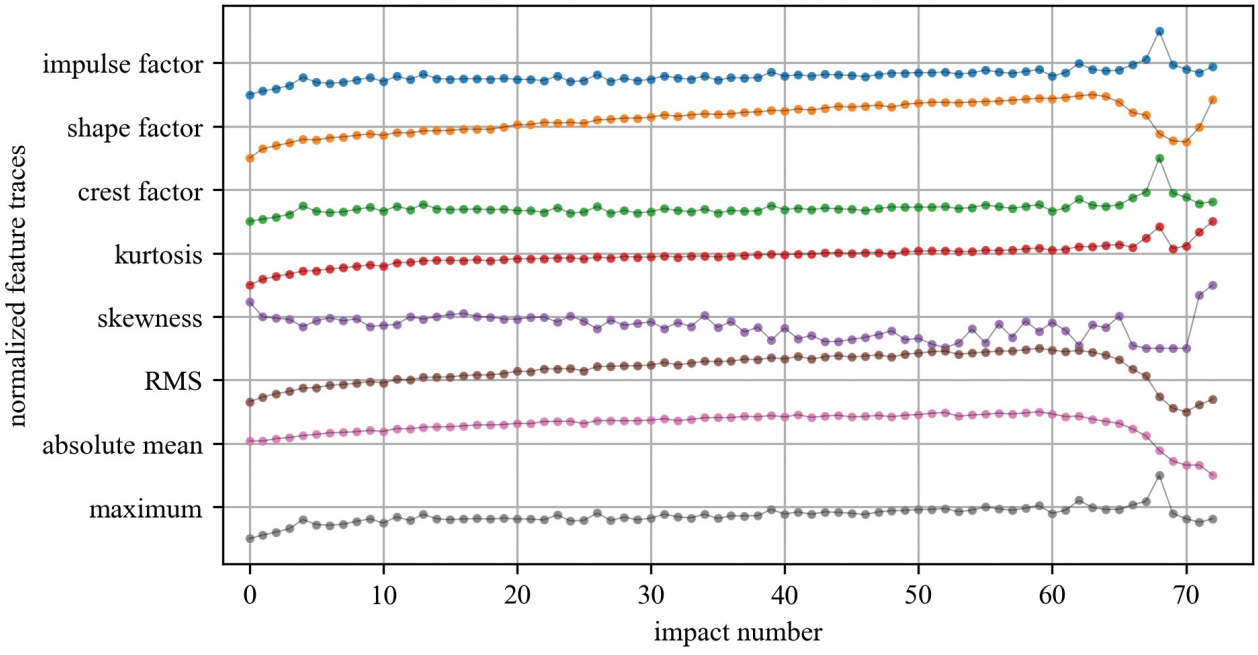

Fig. 8 Normalized time-domain features extracted from excitation and response signals for Board 3.

and absolute mean showed gradual upward trends, while the other features remained relatively stable throughout most of the sequence. Board 2 exhibited similar behavior, with RMS and absolute mean sharing consistent visible trends, while crest factor and kurtosis remained essentially flat; this board also displayed the highest variability in individual data points, suggesting greater issues in data collection, something expected as measuring high-rate impact events is experimentally challenging to do without noise. Board 3 displayed the clearest late-stage excursions: although all features followed steady trends through most of the test, shape factor, RMS, and absolute mean dropped sharply during the last 10–15 impacts

following steady climbs, coinciding with the abrupt resistance increase near failure. These observations indicate that while some features provide gradual indicators of cumulative degradation, others remain stable until close to failure, where rapid excursions reveal the onset of irreversible damage.

The Pearson correlation coefficient r quantifies the strength and direction of a linear relationship between the fitted resistance degradation trendline and each feature trajectory [13]. Values of r range from -1 (perfect negative correlation) to $+1$ (perfect positive correlation), with values near zero indicating little to no linear association. The associated p-value tests the null hypothesis of no correlation, with $p < 0.05$ taken as statistically significant. Because Pearson correlation is limited to linear trends, the Spearman rank correlation coefficient ρ was also evaluated. Spearman correlation measures monotonic associations, making it more robust in cases where feature trajectories evolve nonlinearly with degradation [14, 15]. Tables 1 and 2 summarize both correlation metrics across the three boards, with the final column reporting the mean $\pm$ standard deviation.

The results show clear differences between the two measures. Features such as *absolute mean* and *RMS* yielded moderate Pearson correlations ($r \approx 0.5$) but much higher Spearman values ($\rho > 0.75$), suggesting strong but nonlinear monotonic relationships with resistance. Conversely, *kurtosis* and *skewness* displayed inconsistent Pearson values, including negative correlations, yet ranked among the strongest features under Spearman analysis, reflecting late-stage nonlinear excursions near failure. In contrast, features like *crest factor* and *shape factor* remained weak under both measures. Overall, *absolute mean*, *RMS*, and *kurtosis* emerged as the most reliable indicators of cumulative degradation across boards. These results are visualized in Figure 9, where features are ranked by mean absolute importance to emphasize the most informative indicators of cumulative damage progression.

Table 1 Pearson correlation results for boards 1–3, with mean correlation across boards.

	board 1		board 2		board 3		mean $\pm$ std
feature	r	p-value	r	p-value	r	p-value	r
impulse factor	-0.272	6.77×10^{-2}	-0.329	2.09×10^{-2}	0.263	2.44×10^{-2}	-0.113 ± 0.327
shape factor	-0.397	6.29×10^{-3}	-0.673	1.20×10^{-7}	0.198	9.39×10^{-2}	-0.291 ± 0.445
crest factor	-0.265	7.51×10^{-2}	-0.041	7.82×10^{-1}	0.174	1.41×10^{-1}	-0.044 ± 0.220
kurtosis	-0.222	1.38×10^{-1}	-0.322	2.39×10^{-2}	0.579	7.85×10^{-8}	0.012 ± 0.494
skewness	-0.182	2.27×10^{-1}	-0.634	1.02×10^{-6}	-0.309	7.82×10^{-3}	-0.375 ± 0.233
RMS	0.529	1.56×10^{-4}	0.801	4.98×10^{-12}	0.207	7.96×10^{-2}	0.512 ± 0.297
absolute mean	0.555	6.19×10^{-5}	0.907	3.17×10^{-19}	0.103	3.85×10^{-1}	0.522 ± 0.403
maximum	-0.137	3.65×10^{-1}	0.525	1.08×10^{-4}	0.634	1.72×10^{-9}	0.341 ± 0.417

Table 2 Spearman correlation results for boards 1–3, with mean correlation across boards.

	board 1		board 2		board 3		mean $\pm$ std
feature	ρ	p-value	ρ	p-value	ρ	p-value	ρ
impulse factor	-0.771	3.58×10^{-10}	-0.353	1.28×10^{-2}	0.820	7.04×10^{-19}	-0.101 ± 0.825
shape factor	-0.883	4.79×10^{-16}	-0.728	3.16×10^{-9}	0.684	2.67×10^{-11}	-0.309 ± 0.863
crest factor	-0.554	6.55×10^{-5}	0.072	6.23×10^{-1}	0.609	1.11×10^{-8}	0.042 ± 0.582
kurtosis	-0.786	1.02×10^{-10}	-0.266	6.50×10^{-2}	0.940	6.63×10^{-35}	-0.037 ± 0.885
skewness	-0.555	6.23×10^{-5}	-0.758	2.86×10^{-10}	-0.571	1.33×10^{-7}	-0.628 ± 0.113
RMS	0.873	2.56×10^{-15}	0.868	7.21×10^{-16}	0.530	1.39×10^{-6}	0.757 ± 0.196
absolute mean	0.929	1.37×10^{-20}	0.974	6.52×10^{-32}	0.416	2.55×10^{-4}	0.773 ± 0.310
maximum	0.020	8.95×10^{-1}	0.612	2.97×10^{-6}	0.729	2.50×10^{-13}	0.454 ± 0.380

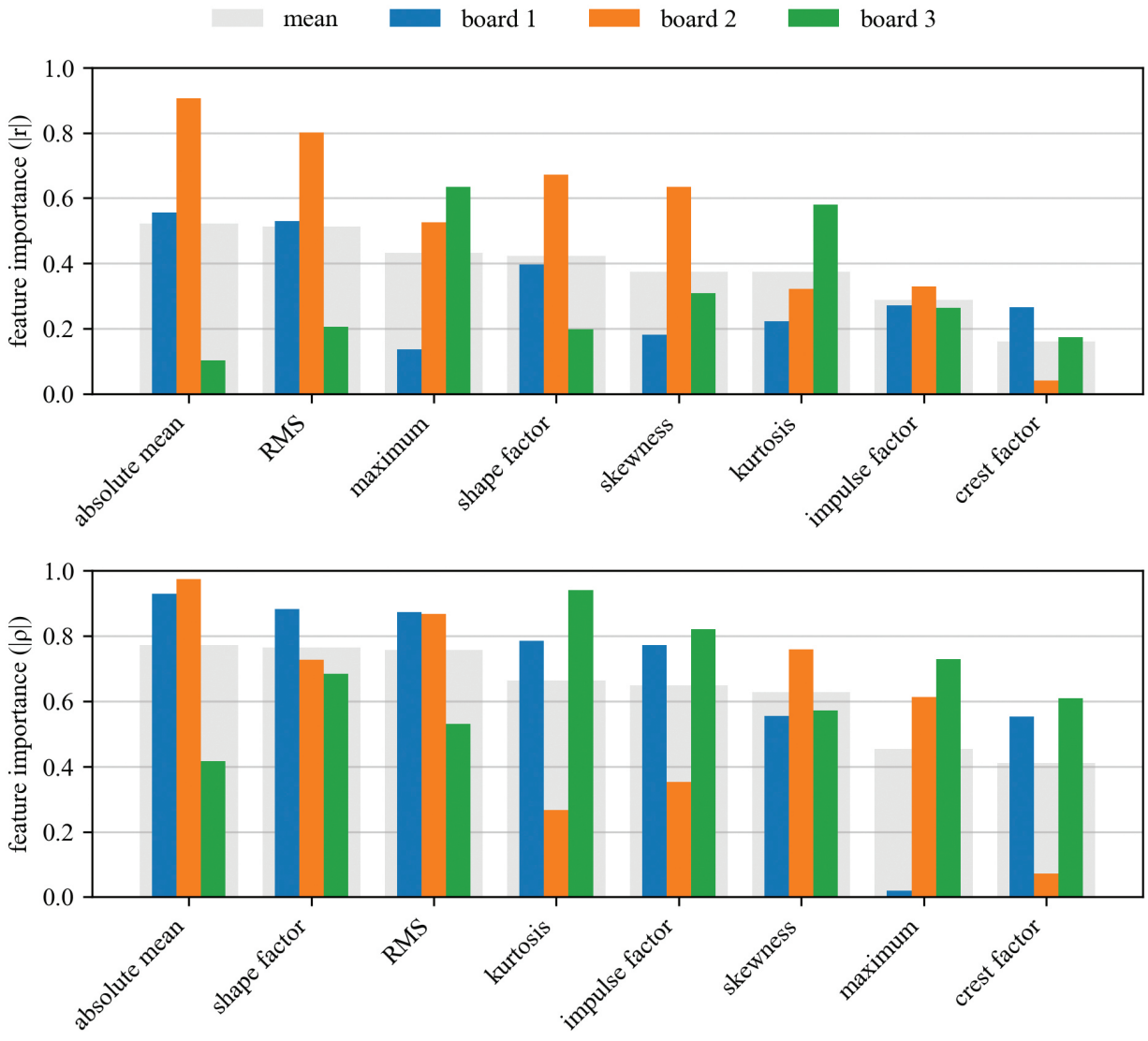

Fig. 9 Feature importance based on absolute mean correlation across boards, shown for both Pearson (top) and Spearman (bottom).

Conclusion

This study introduced a repeatable experimental framework for evaluating cumulative damage in PCBs subjected to repeated high-g shock events. The framework created a controlled dataset that connected dynamic response features to progressive electrical degradation by fusing high-rate acceleration measurements along with resistance monitoring. Resistance histories consistently exhibited gradual drift followed by abrupt increases prior to failure, while feature trajectories revealed both steady long-term trends and late-stage excursions. Correlation analysis identified maximum, kurtosis, and skewness as the most reliable indicators of degradation, highlighting their potential value for monitoring cumulative damage in high-rate environments. Overall, the results establish initial links between mechanical shock response and electrical degradation in PCBs.

By quantifying feature–damage correlations and demonstrating the reproducibility of the experimental protocol, this study establishes the foundation for condition indicators that can aid in real-time failure diagnosis. In the future, the framework will be expanded to include more PCB shapes and loading scenarios, incorporate cumulative damage data more clearly, and use machine learning techniques for predictive maintenance and categorization. When combined, these advancements

will make it possible to use more reliable, data-driven methods to guarantee the dependability of electronics used in extremely dynamic settings.

Acknowledgments This material is based upon work supported by the National Science Foundation grant numbers CCF - 1956071, CCF-2234921, and CPS - 2237696. Additional support was provided from the Air Force Office of Scientific Research (AFOSR) through award no. FA9550-21-1-0083. Any opinions, findings conclusions, or recommendations expressed in this material are those of the authors and do not necessarily reflect the views of the National Science Foundation or the United States Air Force.

References

1. Dodson, J., Downey, A., Laflamme, S., Todd, M.D., Moura, A.G., Wang, Y., Mao, Z., Avitabile, P., and Blasch, E. "High-rate structural health monitoring and prognostics: An overview". In *Data Science in Engineering, Volume 9*, pages 213–217. Springer International Publishing (2021)ifnextchar.gobble.
2. Fisco, N. and Adeli, H. "Smart structures: Part i—active and semi-active control". *Scientia Iranica*, 18(3):275–284 (2011)ifnextchar.gobble.
3. Roberts, T., Yount, R., Dodson, J., Moura, A., and Downey, A.R. "Towards active structural control strategies for electronic assemblies in high-rate dynamic environments.". SAVE, 94th Shock and Vibration Symposium (2024)ifnextchar.gobble.
4. Hu, B., Sun, Y., and Wu, S. "Vibration characteristics and lead stress optimization for printed circuit board with pqfp under random loads". *Microelectronics Reliability*, 171:115817 (2025)ifnextchar.gobble.
5. Buckley, T., Ghosh, B., and Pakrashi, V. "A feature extraction & selection benchmark for structural health monitoring". *Structural Health Monitoring*, 22(3):2082–2127 (2022)ifnextchar.gobble.
6. Yount, R., Roberts, T., Dodson, J., Moura, A., and Downey, A.R. "Experimental analysis to enable low-latency structural health monitoring for electronics in high-rate dynamic environments". Springer Nature Switzerland (2025)ifnextchar.gobble.
7. Satme, J.N., Coble, D., and Downey, A.R.J. "Online health monitoring of electronic components subjected to repeated high-energy shock". In *ASME 2024 Conference on Smart Materials, Adaptive Structures and Intelligent Systems*, SMASIS2024. American Society of Mechanical Engineers (2024)ifnextchar.gobble.
8. ARTS-Lab. "Paper-2026-test-to-failure-characterization". GitHub (2026)ifnextchar.gobble. https://github.com/ARTS-Laboratory/Paper-2026-Test-to-Failure-Characterization.
9. Roberts, T., Gol Zardian, M., Satme, J.N., and Downey, A.R.J. "Finite element modeling of fixed-fixed beams under shock excitation with active control". IMECE, American Society of Mechanical Engineers (2025)ifnextchar.gobble.
10. Muthuram, N. and Saravanan, S. "Fatigue life based study of electronic package mounting locations on printed circuit boards subjected to random vibration loads". *Journal of Electronic Testing*, 40(6):761–776 (2024)ifnextchar.gobble.
11. Liu, F., Gong, R., Duan, Z., Wang, Z., and Zhou, J. "Research on vibration reliability of solder joint based on modal experiment of pcba". *Journal of Materials Science: Materials in Electronics*, 36(1) (2024)ifnextchar.gobble.
12. Virtanen, P., Gommers, R., Oliphant, T.E., and et al. "Scipy 1.0: fundamental algorithms for scientific computing in python". *Nature Methods*, 17(3):261–272 (2020)ifnextchar.gobble.
13. Pearson, K. "Vii. note on regression and inheritance in the case of two parents". *Proceedings of the Royal Society of London*, 58(347–352):240–242 (1895)ifnextchar.gobble.
14. Spearman, C. "The proof and measurement of association between two things". *The American Journal of Psychology*, 100(3/4):441 (1987)ifnextchar.gobble.
15. Hauke, J. and Kossowski, T. "Comparison of values of pearson's and spearman's correlation coefficients on the same sets of data". *QUAGEO*, 30(2):87–93 (2011)ifnextchar.gobble.

Chapter 10
Structural Response Characterization under Multi-Axis Excitation via Video Motion Magnification

Davide Mastrodicasa, Alberto Garcia de Miguel, Andrea Cavagnolo, Ruben Araujo, Umberto Musella, Emilio di Lorenzo, and Enrico Zappino

Abstract Vibration control testing aims at reproducing the dynamic environments that a component is expected to withstand in operation. These tests, typically conducted on shaker platforms, allow engineers to validate the survivability of hardware against severe vibration conditions. Recent advances enable excitation of components in multiple directions simultaneously using multi-axis shaker platforms controlled by advanced multiple-input multiple-output (MIMO) algorithms, thus simulating realistic dynamic environments. Pre-test activities are always conducted to ensure the feasibility of the test and optimize the setup and control parameters. However, the limited availability of sensors, coupled with time constraints, often leads to insufficient pre-test structural analysis. Such analyses could help identify critical responses or couplings with the shaker platform. This work proposes the use of Video Motion Magnification (VMM), a non-intrusive optical method based on video post-processing, to characterize structural responses. A novel aspect is the integration of synthetic image generation in Blender to anticipate the performance of the available cameras, whose noise floor is usually much higher than that of accelerometers. By replicating the setup in Blender, the feasibility of displacement retrieval through VMM can be verified before real testing. This two-step workflow is then applied in a laboratory pre-test, validating its capability to identify critical structural responses on a 3D printed CubeSat model.

Keywords Video motion magnification · Modal analysis · Pre-test · Vibration control · Optical methods

Introduction

Vibration qualification tests play a critical role in aerospace and mechanical engineering, ensuring that components survive harsh launch and operational environments. Traditionally, tests have been performed with sequential single-axis excitations, but the introduction of multi-axis shakers and MIMO control allows simultaneous excitation, offering a more realistic reproduction of in-service conditions [1].

Pre-test analyses are intended to optimize setup, refine control parameters, and anticipate dangerous resonances. In practice, though, they are often limited due to short campaign times and the difficulty of instrumenting small or inaccessible components with accelerometers. Non-contact optical methods provide a potential solution: Video Motion Magnification (VMM) can reveal otherwise invisible deformations by amplifying small motions in video recordings [2–4]. Despite its promise, the adoption of VMM in pre-tests is hampered by the relatively high noise floor of cameras compared to traditional sensors. This raises the question: can structural displacements expected in multi-axis tests actually be resolved with available imaging equipment?

Davide Mastrodicasa · Alberto Garcia de Miguel · Andrea Cavagnolo · Ruben Araujo · Umberto Musella · Emilio di Lorenzo
Siemens Industry Software NV, Interleuvenlaan 68, Leuven, 3001, Belgium
e-mail: davide.mastrodicasa@siemens.com; alberto.garcia_de_miguel@siemens.com; andrea.cavagnolo.ext@siemens.com; ruben.araujo@siemens.com; umberto.musella@siemens.com; emilio.dilorenzo@siemens.com

Andrea Cavagnolo · Enrico Zappino
Politecnico di Torino, Corso Duca degli Abruzzi 24, 10129 Turin, Italy
e-mail: andrea.cavagnolo.ext@siemens.com; enrico.zappino@polito.it

© The Author(s), under exclusive license to River Publishers 2026

Kristin B. Zimmerman, PhD (eds.), *Dynamic Evironments and Durability Testing, 2026, Vol. 7*, Conference Proceedings of the Society for Experimental Mechanics Series, https://doi.org/10.13052/rp-9788743814184

To address this challenge, we propose a two-step framework. The first step introduces synthetic image generation in Blender, a rendering and simulation tool, to act as a proof of concept. By replicating the test setup in a virtual environment, animating structural responses from numerical simulations, and applying VMM to the rendered videos, it is possible to determine in advance whether the chosen camera configuration is theoretically capable of resolving the displacements of interest. In this paper, this stage does not serve as direct validation against the physical experiment, but rather as a feasibility study to demonstrate the potential of the approach.

The second step applies the same optical configuration in the real laboratory pre-test, where low-level multi-axis excitation is introduced, and VMM is used to extract modal parameters and operational deflection shapes. Together, the virtual feasibility study and the real pre-test establish a practical pathway for incorporating optical methods into vibration campaigns, strengthening pre-test reliability and reducing the risk of unsuccessful measurement campaigns.

The proposed workflow is demonstrated through a vibration test campaign conducted on a multi-axis testing platform available in the Siemens facilities at Leuven, Belgium. The device under test (DUT) was a composite CubeSat made of PEEK material, manufactured by Politecnico di Torino, Italy, using 3D-printing techniques.

Methodology

The proposed methodology integrates numerical simulation, virtual imaging, and physical experimentation into a unified pre-test framework:

1. **Numerical Predictions:** Structural responses are estimated via finite element (FE) models under representative aerospace vibration profiles, which are generated in the software Simcenter 3D. The displacement fields are exported to provide input for the virtual stage.
2. **Virtual Pre-test in Blender:** The CubeSat model, fixture, and camera setup are replicated in Blender. The FE displacements are animated, and synthetic videos are rendered under realistic optical and lighting conditions.
3. **VMM on Synthetic Videos:** The rendered sequences are processed using phase-based VMM. This stage serves as a proof of concept to determine whether the expected displacements can be resolved above the simulated camera noise floor, guiding camera placement and acquisition parameters.
4. **Experimental Pre-test:** The validated configuration is transferred to the laboratory. The CubeSat demonstrator is mounted on a multi-axis shaker, excited under low-level broadband input using the control software Simcenter Testlab MIMO Random Control, and recorded using the high-speed camera. The videos are processed with the same VMM pipeline to extract modal parameters and operational deflection shapes.

This two-step framework ensures that optical measurements are not only theoretically feasible but also practically applicable in real test environments, reducing uncertainty and de-risking vibration campaigns.

Synthetic Image Generation and Virtual Test

Blender was employed to perform a virtual pre-test replicating both the specimen and the test environment. The geometry of the CubeSat demonstrator was modeled and imported into Blender, where the dynamic response obtained from FE simulations was animated. This enabled direct visualization of the expected mode shapes and displacement fields under low-level excitation.

Figure 1 illustrates the FE model of the structure mounted on the multi-axis platform, including the actuators that provide excitation along different directions. In the numerical campaign, the structure was excited using a power spectral density (PSD) profile representative of typical aerospace vibration environments, based on the VEGA C specifications, ensuring realistic loading conditions. The transient dynamic analysis provided the time histories of nodal displacements across the component. These displacement fields were then exported in a format suitable for post-processing and subsequently imported into Blender, where they served as the basis for generating synthetic video sequences of the vibrating structure.

To replicate laboratory conditions, the geometry was textured and rendered, as shown in Figure 2. The texturing step was not only meant to provide a more realistic appearance of the CubeSat structure, but also to introduce visual contrast features that enhance the detectability of small displacements during Video Motion Magnification. Smooth, uniform surfaces can often limit the sensitivity of optical methods, whereas patterns, grey scale variations, or surface textures allow the algorithm to track the displacement field. The resulting rendered model, therefore, supported both the aesthetic realism of synthetic videos and the technical requirement of making subtle vibrations visible once magnified.

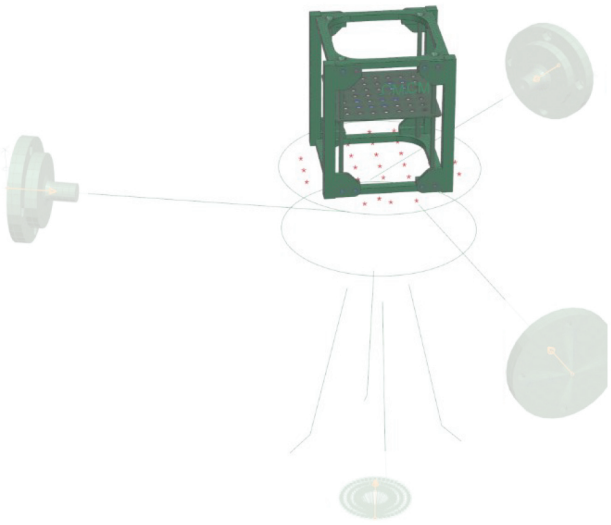

Fig. 1 Finite element model of the CubeSat demonstrator mounted on the multi-axis shaker platform, showing the actuators used for excitation

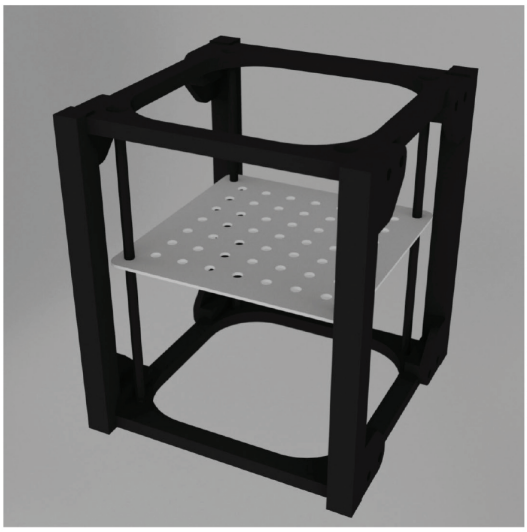

Fig. 2 Rendered CubeSat model with texture applied, used for generating synthetic video sequences

The rendered videos were subsequently processed using the phase-based Video Motion Magnification pipeline. The virtual test revealed whether the expected displacements could be resolved above the camera noise floor. This virtual pre-test therefore acted as a risk-free proof of concept, guiding the choice of optical parameters and acquisition settings for the real campaign. The virtual test was then carried out by exciting the structure up to 400 Hz. Synthetic cameras operating at a sampling rate of 800 Hz were used to record the response. The motion magnified videos were post-processed to extract the modal parameters of the structure. Using the Polymax algorithm [5], the natural frequencies and damping ratios were identified directly from the optical data. Subsequently, Operational Deflection Shapes (ODSs) corresponding to the identified natural frequencies were reconstructed, providing a clear visualization of the dominant vibration patterns. The first ODS, reported in Figure 3, corresponds to the first plate bending mode of the CubeSat panel, while Figure 4 shows the ODS associated with the second plate bending mode. These results confirm that the synthetic videos generated in Blender, once processed with VMM, can resolve structural responses with sufficient clarity to support optical measurements in vibration testing.

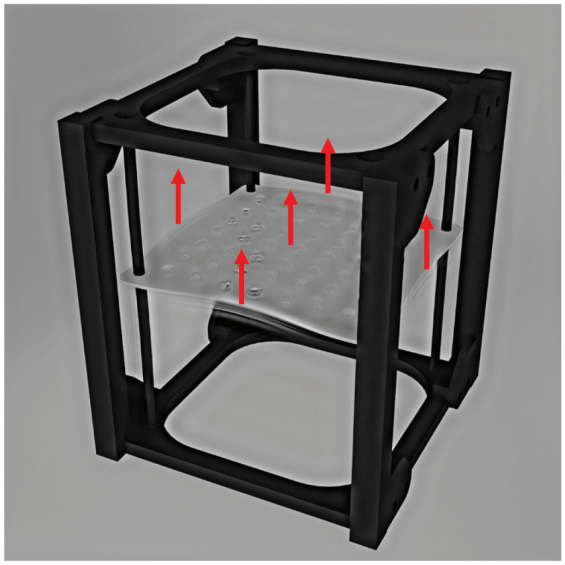

Fig. 3 ODS related to the first plate bending mode

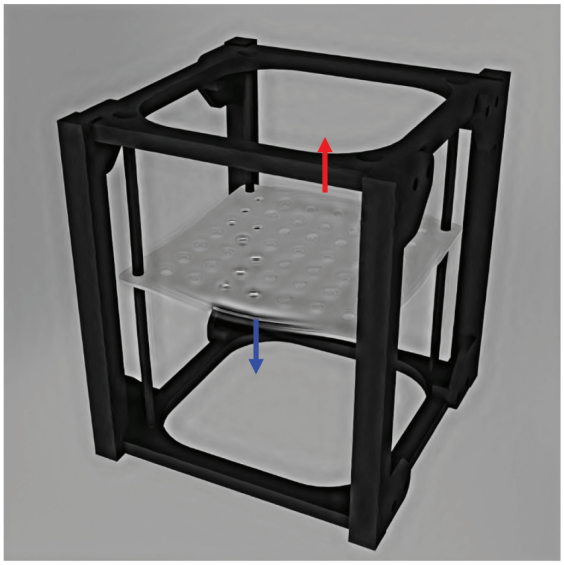

Fig. 4 ODS related to the second plate bending mode

Experimental Pre-test

The feasibility study carried out in the virtual environment was followed by a laboratory pre-test, designed to acquire real optical data of the CubeSat demonstrator under controlled excitation. The specimen was mounted on the multi-axis shaker platform and subjected to a broadband random excitation defined by the same PSD profiles in the 3 directions, consistent with qualification standards. Figure 5 shows the responses at the control locations against the reference profiles, indicating that the MIMO control test was successful.

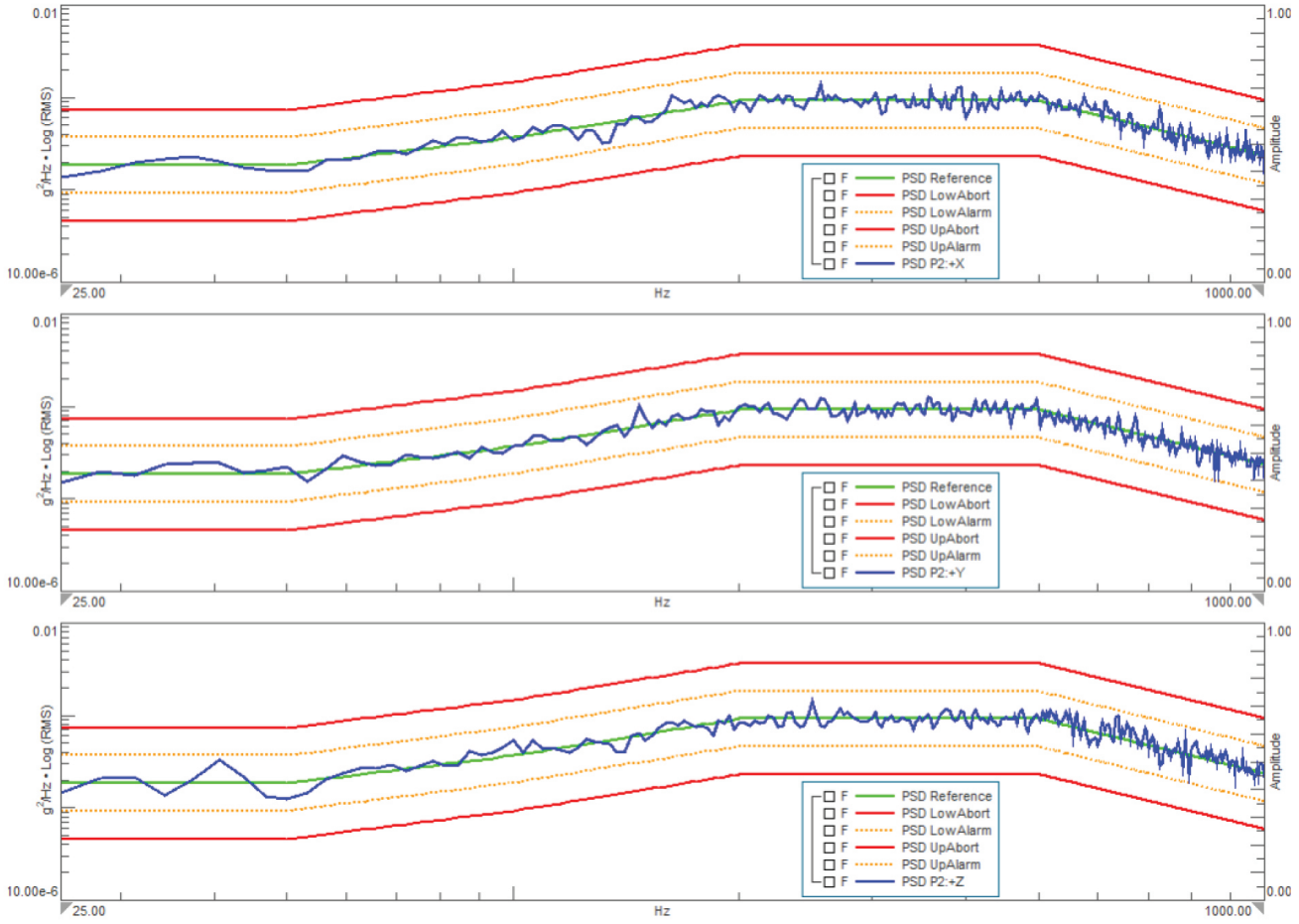

Fig. 5 PSD profiles used in the multi-axis shaker platform at the Siemens facilities in Leuven, Belgium. The blue lines are the acceleration PSD measured at the control sensors

A single high-speed 2 MPx iX i-SPEED 5 Series camera was positioned to reproduce the same point of view adopted in the synthetic image generation part. The camera operated at a sampling frequency of 1600 Hz, ensuring that vibration content up to 800 Hz could be resolved with adequate fidelity. Lighting conditions were optimized to minimize noise and enhance surface contrast, thereby improving the effectiveness of the Video Motion Magnification pipeline. An example of the recorded footage is shown in Figure 6.

The acquired sequences were processed using the same phase-based VMM algorithm employed in the virtual test. From the magnified motions, cross-power spectra were estimated, and the modal parameters, natural frequencies and damping ratios, were extracted using the Polymax method. The Cross Power Sum (CPS), reported in Figure 7, provides a frequency-domain overview of the global vibrational energy. The peaks in the CPS clearly indicate the locations of the main resonances.

Finally, the ODSs reconstructed at the identified resonances are shown in Figures 7 and Figure 8, corresponding respectively to the first and second plate bending modes of the CubeSat structure. These ODSs demonstrate that, even with the inherent noise floor of the optical acquisition, the structural dynamics of the component can be successfully resolved through video-based analysis.

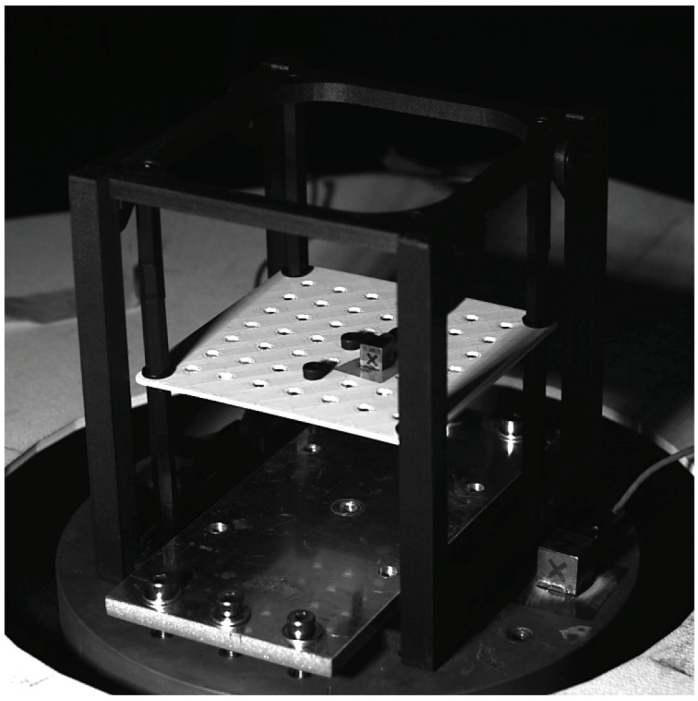

Fig. 6 Real footage

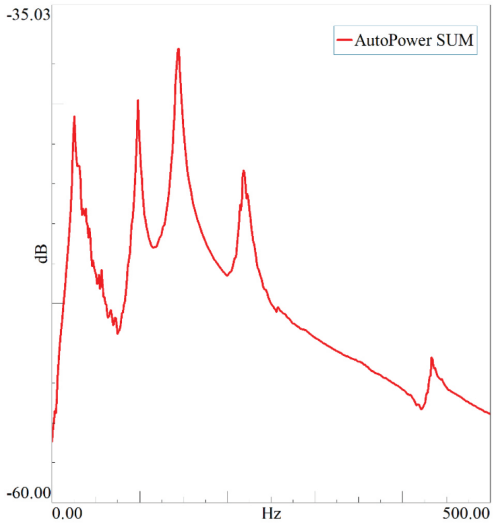

Fig. 7 Cross Power Sum

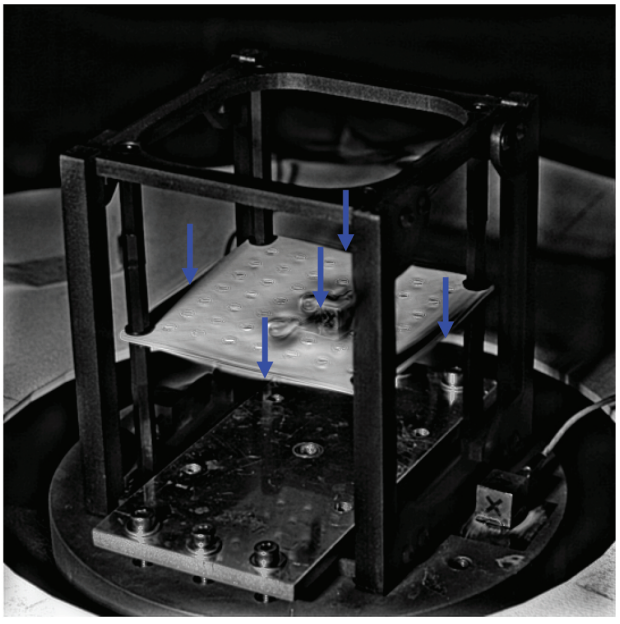

Fig. 8 ODS corresponding to the first plate bending mode, obtained from VMM-processed videos

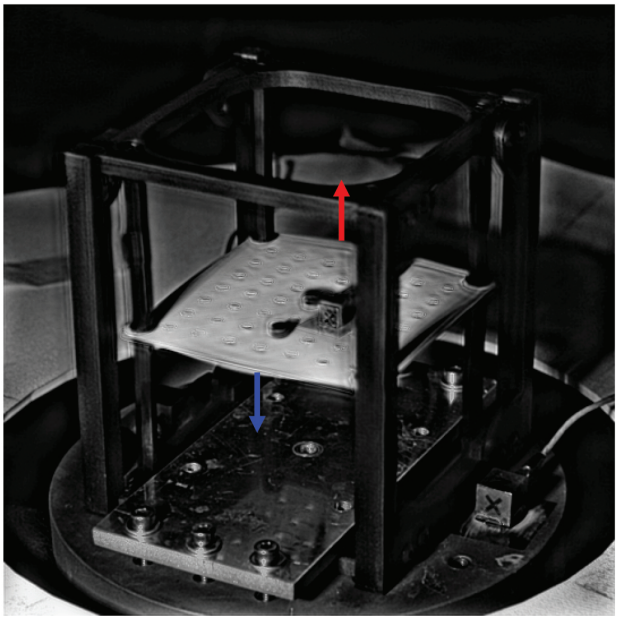

Fig. 9 ODS corresponding to the second plate bending mode, obtained from VMM-processed videos

Conclusion

This work presented a two-step methodology for structural response characterization for vibration control using video motion magnification. The first stage introduced a synthetic image generation workflow in Blender, where finite element displacements were animated and processed through VMM. This step served as a feasibility study to optimize camera placement and

acquisition parameters, ensuring that the expected structural responses could be made optically detectable despite the higher noise floor of cameras compared to conventional sensors.

The second stage applied the methodology in a laboratory pre-test, where a CubeSat demonstrator was subjected to a controlled vertical excitation. High-speed video acquisition, followed by VMM processing, enabled the extraction of modal parameters and the reconstruction of operational deflection shapes. The results confirmed that optical methods can provide valuable insight into structural dynamics in a non-intrusive manner.

Together, these two stages establish a practical pathway for the use of video-based techniques in vibration test campaigns. The synthetic stage reduces risk by guiding the optical configuration and verifying feasibility in advance, while the experimental stage provides real-world confirmation of the method's applicability. This combined approach supports safer, more efficient test campaigns and offers a complementary tool to conventional sensor-based measurements.

Future work will aim at extending the methodology to more complex assemblies, improving displacement quantification, and further automating the integration between numerical simulations, synthetic video generation, and experimental testing.

References

1. B. Peeters, J. Debille, "Multiple-input-multiple-output random vibration control: theory and practice," in: Proc. of the International Conference on Noise and Vibration Engineering, 2002.
2. F. Cosco, J. Cuenca, W. Desmet, K. Janssens, and D. Mundo, "Towards phase-based defect detection: A feasibility study in vibrating panels," J Sound Vib, vol. 537, Oct. 2022, doi: 10.1016/j.jsv.2022.117196.
3. N. Wadhwa, M. Rubinstein, F. Durand, and W. T. Freeman, "Phase-based video motion processing," ACM Trans Graph, vol. 32, no. 4, Jul. 2013, doi: 10.1145/2461912.2461966.
4. J. G. Chen, N. Wadhwa, Y.-J. J. Cha, F. Durand, W. T. Freeman, and O. Buyukozturk, "Modal identification of simple structures with high-speed video using motion magnification," J Sound Vib, vol. 345, pp. 58–71, Jun. 2015, doi: 10.1016/j.jsv.2015.01.024.
5. Peeters, Bart & Van der Auweraer, Herman. (2005). PolyMax: a revolution in operational modal analysis. 1st International Operational Modal Analysis Conference.

Chapter 11
Shaker Testing of a Fuel Cell Stack: Modal Survey, FE Model Updating, and Fixture Coupling Neutralization

Giancarlo Kosova, Vittoria D'Alessio, Emilio Di Lorenzo, Lorenzo Dozio, Simone Gallas, Hervé Denayer, Giovanni Fasulo, Mattia Barbarino, and Oskar Ekblad

Abstract This paper presents a comprehensive study of a fuel cell stack's dynamic behavior through shaker testing, focusing on experimental characterization and numerical model validation. The investigation was conducted as part of a design campaign to ensure structural integrity under operational conditions.

The study pursued four main objectives: (1) conducting preliminary environmental tests on single and multi-axis shaker platforms to assess structural durability, (2) performing experimental modal analysis to extract mode shapes and frequencies, (3) updating and validating a finite element model (FEM) for structural integrity predictions, and (4) developing decoupling procedures to neutralize the dynamic interaction between the test structure and the fixture/slip table assembly.

The investigation yielded several key results. The preliminary environmental tests successfully validated control-loop stability across different stack configurations. The modal survey, using table acceleration as a reference, revealed amplitude-dependent behavior indicative of structural nonlinearities. Despite having detailed design information, the initial finite element model showed significant discrepancies compared to experimental data. Through model updating based on the experimental modal model, these differences were substantially reduced, achieving excellent correlation in natural frequencies and mode shapes, while transmissibility functions showed good but not perfect agreement. Various substructuring methods were implemented to extract the fixed-base characteristics of the fuel cell stack, and while they partially corrected both natural frequencies and mode shapes, their effectiveness demonstrated considerable sensitivity to the specific approach and parameters employed.

The results illustrate the fundamental importance of shaker testing in the design process of fuel cell stacks, providing crucial insights into their dynamic behavior and enabling the development of reliable numerical models for durability predictions.

Keywords Shaker testing · EMA · FEM · Decoupling

Giancarlo Kosova · Vittoria D'Alessio · Emilio Di Lorenzo
Siemens Digital Industries Software, Leuven, Belgium
e-mail: giancarlokosova@siemens.com; dalessiovittoria1@gmail.com; emilio.dilorenzo@siemens.com

Vittoria D'Alessio · Lorenzo Dozio
Politecnico di Milano, Milan, Italy
e-mail: dalessiovittoria1@gmail.com; lorenzo.dozio@mail.polimi.it

Simone Gallas · Hervé Denayer
KU Leuven, Department of Mechanical Engineering, Heverlee, Belgium
e-mail: simone.gallas@kuleuven.be; herve.denayer@kuleuven.be

Simone Gallas · Hervé Denayer
Flanders Make, Flanders Make@KU Leuven, Belgium
e-mail: simone.gallas@kuleuven.be; herve.denayer@kuleuven.be

Giovanni Fasulo · Mattia Barbarino
Italian Aerospace Research Centre (CIRA), Capua, Italy
e-mail: g.fasulo@cira.it; m.barbarino@cira.it

Oskar Ekblad
PowerCell Group, Gothenburg, Sweden
e-mail: oskar.ekblad@powercellgroup.com

© The Author(s), under exclusive license to River Publishers 2026

Kristin B. Zimmerman, PhD (eds.), *Dynamic Evironments and Durability Testing, 2026, Vol. 7*, Conference Proceedings of the Society for Experimental Mechanics Series, https://doi.org/10.13052/rp-9788743814184

Introduction

Hydrogen-Powered Aviation: Challenges and Opportunities

The aviation industry is undergoing a transformative shift toward sustainable propulsion systems, driven by the urgent need to reduce greenhouse gas emissions and achieve carbon neutrality. Among the emerging technologies, hydrogen-powered engines and fuel cell systems represent promising alternatives to conventional jet fuel propulsion. Hydrogen fuel cells offer several compelling advantages for aviation applications, including zero local emissions (producing only water vapor), high energy efficiency, and the potential for quiet operation. Additionally, hydrogen can be produced from renewable energy sources, making it a truly sustainable fuel option.

However, the integration of hydrogen fuel cell systems into aircraft presents significant technical challenges. These include the need for specialized storage systems to handle hydrogen's low volumetric energy density, thermal management requirements, and the necessity to ensure system reliability and safety under the demanding operational conditions of aviation environments. Furthermore, fuel cell stacks must demonstrate exceptional durability and vibration immunity to withstand the dynamic loads encountered during flight operations, including engine vibrations, turbulence, and landing impacts.

The NEWBORN Project Framework

The research presented in this paper was conducted within the framework of the NEWBORN project (NExt generation high poWer fuel cells for airBORNe applications) [1, 2], a European initiative aimed at developing hydrogen-electric propulsion systems for sustainable aviation. The NEWBORN project addresses the critical technological gaps in hydrogen fuel cell integration for aircraft applications, focusing on system optimization, safety, and certification requirements.

Paper Scope and Objectives

This paper describes the vibration analysis activities carried out as part of a specific task within the NEWBORN project, focusing on a fuel cell stack prototype developed by the PowerCell Group [3]. The stack tested and modeled in this work is not the NEWBORN 300-kW stack, but a previous model. The ultimate objective of this research is to conduct a comprehensive vibration immunity analysis of the fuel cell stack to ensure its compliance with aviation standards and operational requirements.

The vibration immunity assessment follows the rigorous requirements outlined in the RTCA document DO-160G "Environmental Conditions and Test Procedures for Airborne Equipment," Section 8 Vibration [4], which establishes the standard testing procedures for airborne equipment certification. Prior to conducting the full durability test procedure, a numerical immunity analysis must be performed to identify critical systems and components requiring detailed examination. This numerical analysis employs stress analysis methods for low to medium-frequency ranges and energy-based approaches for high-frequency evaluation.

The specific scope of the work presented in this paper encompasses preliminary experimental testing of the fuel cell stack, which is designed to address two primary objectives. First, the testing aims to identify potential criticalities in both the fuel cell components and the experimental testing setup at an early stage of the development process. Second, a comprehensive modal survey [5] is conducted to experimentally determine the natural frequencies, damping ratios, and mode shapes of the fuel cell stack. The results of this modal survey serve as the foundation for updating and validating the finite element model (FEM) of the stack, ensuring an accurate representation of its dynamic behavior.

A critical aspect of this work addresses the challenge of boundary condition representation in experimental modal analysis. While correlation between experimental and numerical results is typically performed under known and comparable boundary conditions, assuming a fixed-base condition (clamped at the base) for the fuel cell stack, this assumption may not accurately reflect the actual test conditions. The dynamic coupling between the shaker table and the device under test can significantly influence the measured response characteristics. Therefore, this paper also explores methodologies to correct the experimental data and extract the true fixed-base dynamic characteristics of the fuel cell stack, accounting for fixture coupling effects.

The paper is structured as follows: Section Shaker testing provides a detailed description of the experimental testing setups and procedures employed in this study. Section Experimental modal analysis presents the analysis of experimental data and the comprehensive modal analysis results. Section Finite element model updating introduces the finite element model of the fuel cell stack and describes the model updating process based on experimental findings. Section Fixture coupling neutralization addresses the decoupling analysis methodology for separating the fuel cell dynamics from the slip table effects. Finally, conclusions and recommendations for future work are presented in Section Conclusions.

Shaker testing

This section describes the two different experimental setups employed for the vibration testing of the PowerCell Group fuel cell stack. The testing was conducted using two distinct shaker configurations: the CUBE system and a slip table configuration, as illustrated in Figures 1a and 1b, respectively.

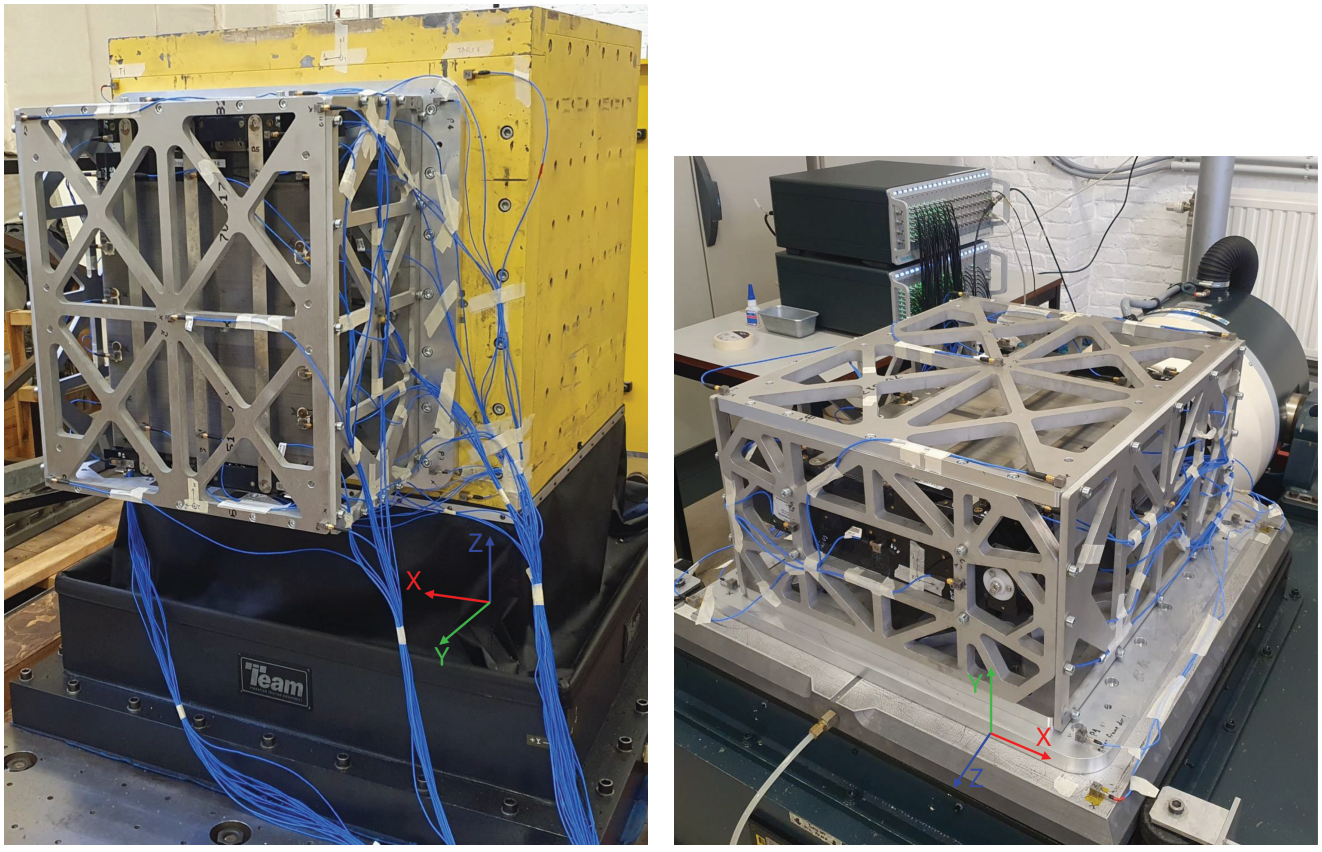

(a) The CUBE multi-axis shaker table [6].

(b) Single-axis slip table.

Fig. 1 Fuel-cell stack shaker table configurations.

In both configurations, the fuel cell stack is securely clamped to the respective testing table through an identical fixture plate. However, the bolt positions are adapted to accommodate the different hole patterns of each table, a consideration that will be further addressed in Section Fixture coupling neutralization. The structure surrounding the fuel cell stack serves as an additional fixture component, referred to as the "cage" throughout this paper. This cage is specifically designed to maintain the stack in boundary conditions that closely simulate operational conditions and can be considered rigid up to a certain frequency threshold.

The main differences between the CUBE and slip table configurations can be summarized as follows:

- **Excitation capabilities**: The CUBE system provides excitation along 6 independent axes, while the slip table is limited to single-axis excitation.
- **Frequency range**: The CUBE system operates up to 300 Hz, whereas the slip table extends the frequency range up to 1000 Hz.
- **Fixture clamping conditions**: Different mounting configurations are required to accommodate the specific interface requirements of each system.

All experimental tests were performed using two Simcenter SCADAS Lab hardware systems [7] configured in a main/secondary arrangement, coupled with Simcenter Testlab software [8] utilizing both structural dynamics and shock and vibration applications.

The instrumentation setup consists of approximately 54 PCB high-sensitivity triaxial accelerometers strategically mounted on the structure to record the dynamic response, resulting in a total of approximately 162 measurement channels. This extensive sensor array ensures excellent spatial discretization for two primary reasons: first, to capture the complex mode shapes of the fuel cell stack with sufficient detail, and second, to provide adequate data for robust finite element model updating and validation procedures. Figure 2 shows the geometry used in the data analysis, indicating accelerometer locations and labels. The orange plate represents the vibration table, the blue plate represents the fixture, the green component represents the fuel cell stack, and the cage is represented by grey lines.

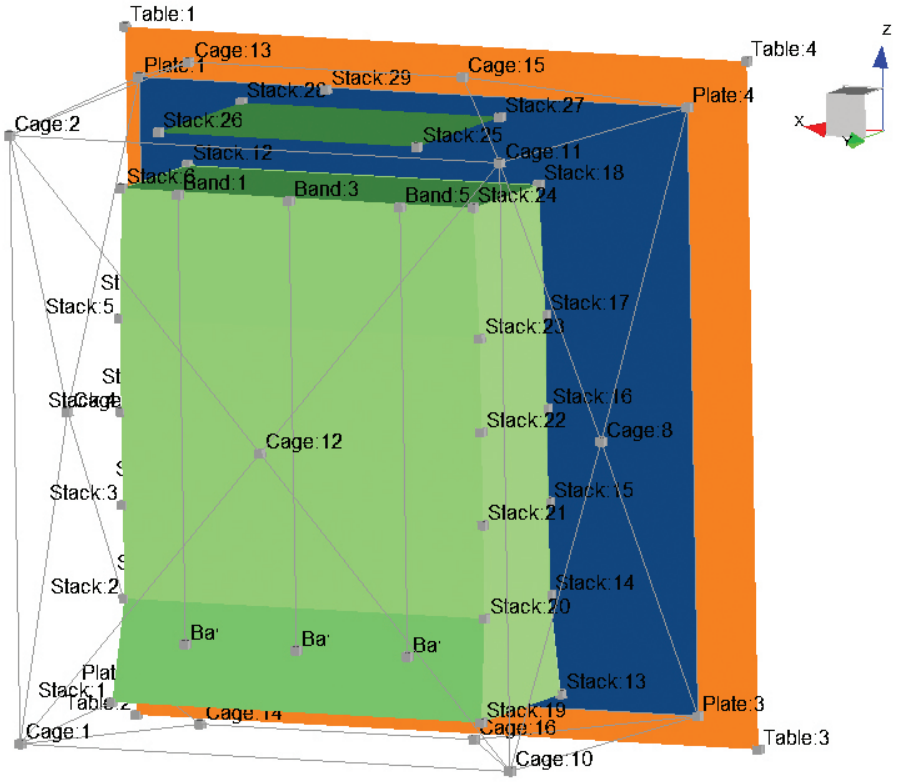

Fig. 2 Test-analysis geometry and sensor locations.

The comprehensive testing program performed on both configurations is summarized in Table 1, which details the various excitation signals, directions, frequency ranges, and excitation levels employed.

Table 1 Summary of vibration tests performed on both shaker configurations

Test	Excitation CUBE	Excitation Slip table	Freq. Range CUBE (Hz)	Freq. Range Slip table (Hz)	Excitation Level
Pseudorandom	X, Y, Z, RX, RY, RZ, XYZ, 6-axis	Z	10–300	10–1000	low, mid, high
Swept sine	X, Y, Z	Z	10–300	10–1000	0.7, 1, 2 (g)

The pseudorandom test refers to an open-loop test with a pseudorandom signal and periodic acquisition, with the parameters in Table 2, using the Simcenter Testlab MIMO FRF application. The Swept sine test refers to a closed-loop test with a logarithmic swept-sine signal with a sweep rate of 1 octave per minute, using the Simcenter Testlab Sine Control application.

Table 2 Open-loop pseudorandom test parameters

Sampling Frequency	Sampling Period	Number of Periods	Number of Realizations
3200Hz	5s	6	5

On the CUBE, for both Sine control and open-loop pseudorandom tests, the excitation level refers to an accelerometer at the top left of the table in Figure 1a, named *Table:1*. More specifically, for the Sine control runs, the defined excitation level of this accelerometer in each direction is controlled, i.e., the software controls the drive to ensure the acceleration follows the target amplitude spectrum; for the open-loop pseudorandom test, this is the resulting excitation level of *Table:1* in the excitation direction of the table. Instead, the accelerometer in *Table:5* placed at the joint between the shaker and table is used for the slip table.

Experimental modal analysis

Although a wide range of tests has been conducted, in this section, we focus only on data from the CUBE. Additionally, only the results in the Z direction are shown. These runs gave the best results in terms of modal excitation and stability in the mode identification.

In all the analyses, the frequency response functions (FRFs) are the transmissibility functions, using *Table:1:+Z* channel as reference.

Figure 3 shows a homogeneity test [9] to understand the degree of nonlinearity of the structure. Some of the most representative points are selected, which together highlight most of the peaks present in the different FRFs. The axis ticks and values are hidden due to confidentiality. Several mode peaks shift with the amplitude of excitation. In particular, most of the modes shift to lower frequency and amplitude with increasing excitation. This is a typical behavior of contact friction nonlinearity [9], which can be due to bolts and cell-to-cell contact. Only one mode, which corresponds to the first bending frequency of the compression bands, increases in amplitude with increasing excitation.

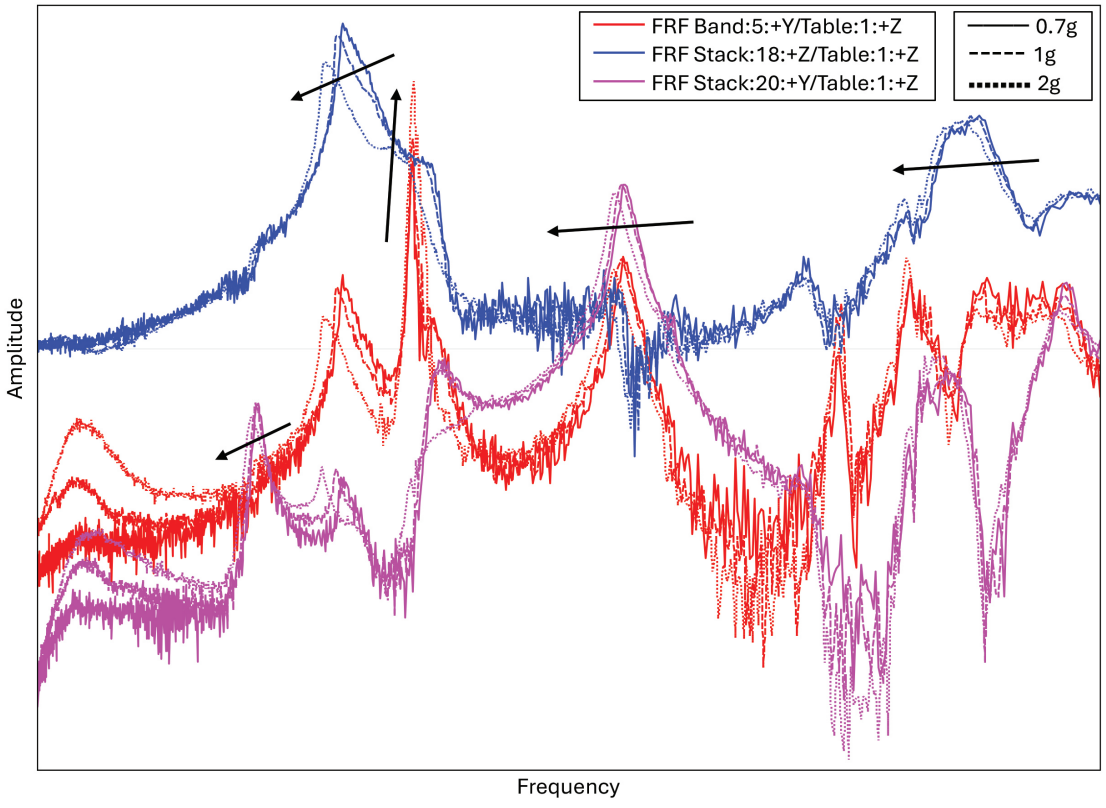

Fig. 3 Homogeneity test of controlled swept sine tests.

Since the goal of the experimental modal analysis is to identify the underlying linear system, open-loop pseudorandom runs are processed, as this type of signal injects less energy at each excited frequency line, and is therefore less prone to excite amplitude-dependent nonlinearities. Indeed, it can be shown that the homogeneity test at three different levels of pseudorandom excitation shows almost overlapping curves.

The data are processed using the Polymax modal parameter estimator [10]. The transfer functions of all the measured channels with respect to *Table:1:+Z* are included in the analysis. The modes are of different types: fuel cell stack body axial mode along Z, bending about X and Y, torsion about Z, and bending of the bands. Most of these modes are identified up to their second order (e.g., second bending, second torsion). Some of the identified mode shapes are plotted in Figure 4. The colored geometry represents the modal deformation, while the grey lines and grey node markers represent the undeformed geometry.

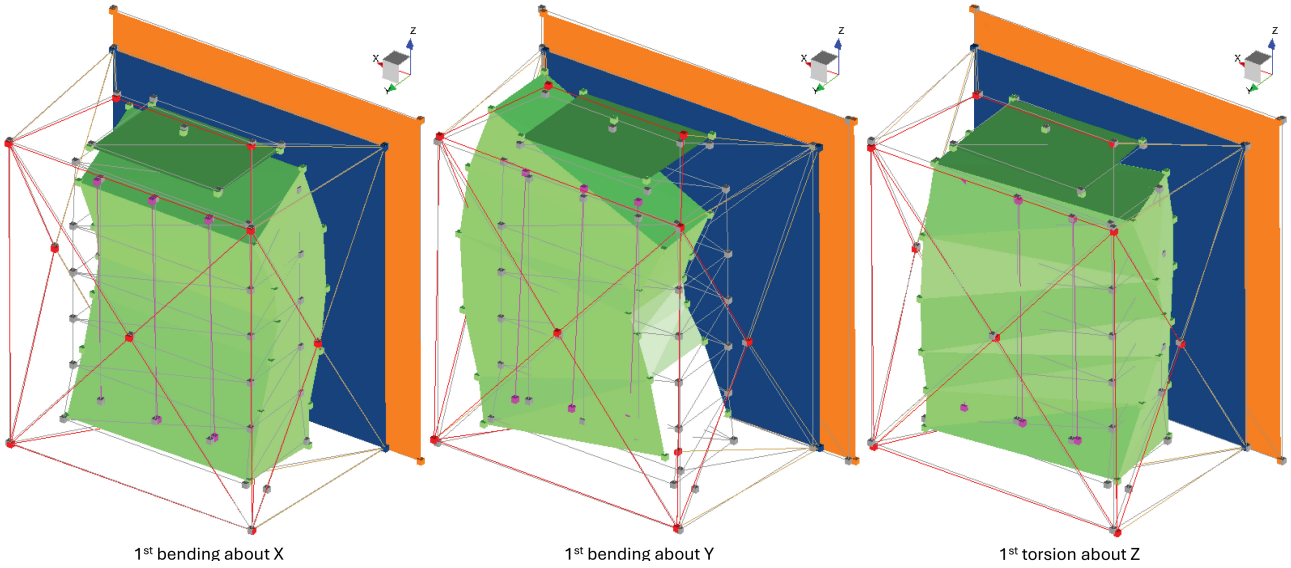

Fig. 4 Identified mode shapes.

The auto MAC (modal assurance criterion) [11] in Figure 5 shows a high degree of discretization between the different modes, as the out-of-diagonal values are very low. The modes increase in frequency from the top left to the bottom right of the matrix. The high values of out-of-diagonal auto MAC, up to 50%, are due to a correlation between flexible modes of the stack and modes due to coupling between the stack and the cage. Indeed, the cage is not rigid in the highest part of the excited frequency band. Instead, the first mode, which slightly correlates with two other modes, is a pseudo-rigid mode of the table, i.e., a rigid rotation of the entire structure, device under test (DUT), and table, about the X axis.

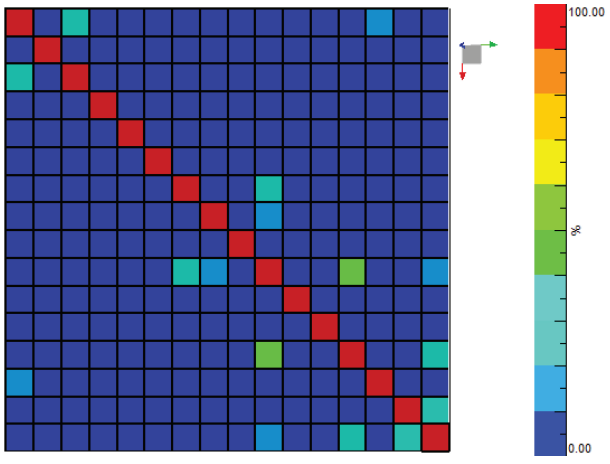

Fig. 5 Auto MAC matrix showing modal correlation.

Figure 6 shows, for three representative points, the modal synthesis of the identified modeset, i.e., a comparison between the measured FRFs and the FRFs synthesized using the modal model. A very accurate modal synthesis is proven, with a level of correlation above 90% for most of the relevant measurement channels.

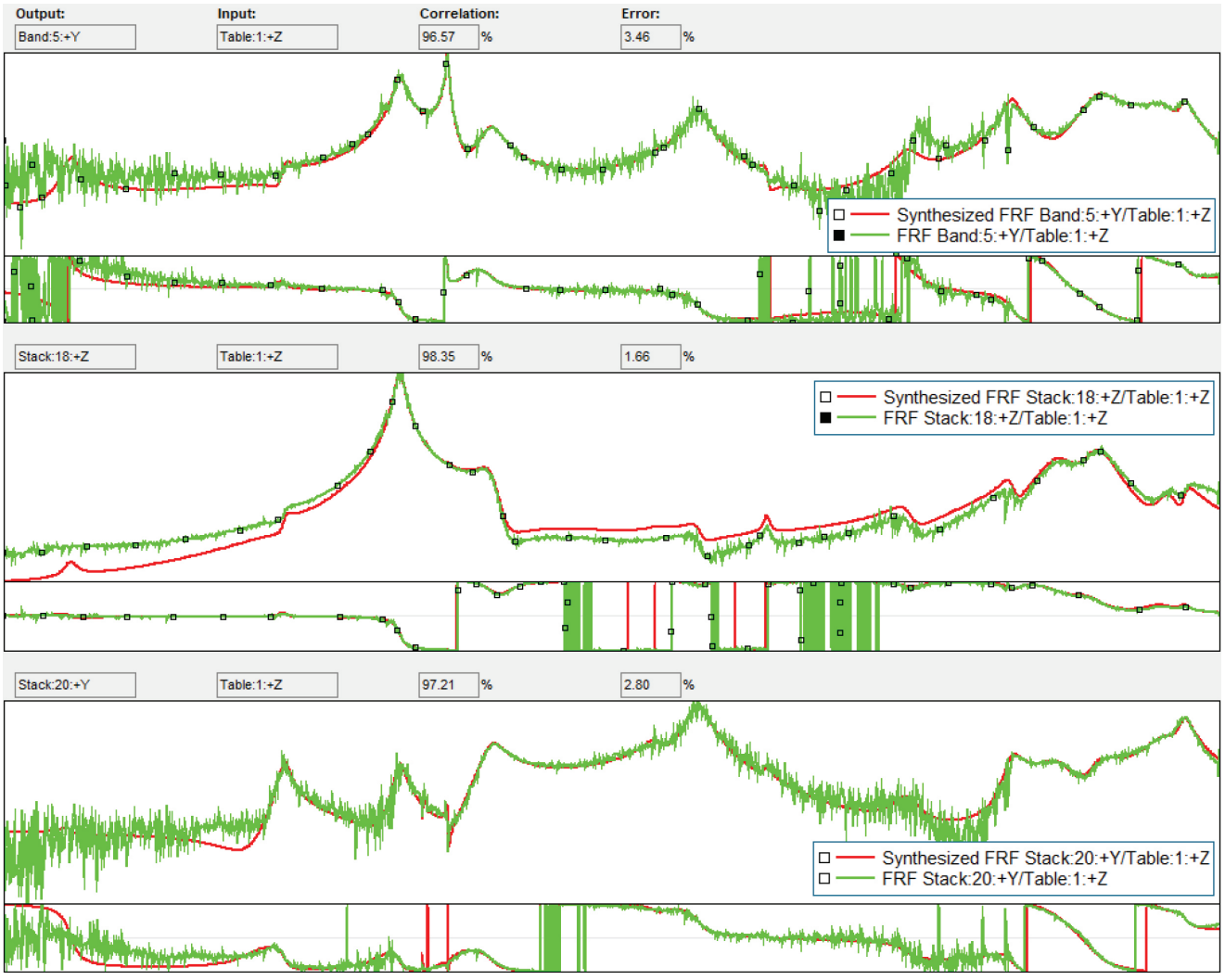

Fig. 6 Modal synthesis validation.

A low level of complexity of the modes is also verified, resulting in a mode phase collinearity above 90% for all the modes.

To summarize, auto MAC, modal synthesis, and mode complexity are the most important indicators for the validation of a modeset. Therefore, the identified modeset can be considered as an accurate test reference for finite element model updating.

Finite element model updating

The FE model of the stack must be used to perform a numerical immunity analysis. To retrieve meaningful information, the FEM must be well correlated with the structure [12]. The model, therefore, requires updating and validation using results from a test reference analysis. In this section, the model is briefly presented, and the results of the model updating are shown. A detailed description of the FEM, including the modeling of the different components in relation to the design inputs and correlation results, can be found in [13]. Instead, this section primarily focuses on the model update from experimental data.

The model updating is performed using Simcenter Nastran SOL200 [14, 15] in Simcenter 3D [16]. The advantage of using Simcenter 3D is that the test reference can be easily imported and correlated with the numerical solution. In particular, the test geometry can be easily aligned with the mesh, and the numerical and test modes are automatically paired based on their MAC and frequency distance. The correlation based on MAC and frequency error is calculated and used as a metric in the optimization function for model updating.

The procedure is as follows:

1. The design variables are defined. These can be either material or element properties. In this case, the assigned design variables are:
   - The Young's modulus of an isotropic material,
   - The six shear moduli of anisotropic materials,
   - The six stiffnesses of spring elements.
2. The design variable definition includes assigning lower and upper bounds. Smaller bounds are assigned to well-known materials, while larger bounds are given to equivalent elements representing a simplification of actual components.
3. The targets are assigned.
4. The errors are calculated.
5. The model update process is performed.
6. The optimized design variables are updated in the FEM.

The last three steps are iterative, as the sensitivities to the design variables are calculated around the initial values. For more details, see [14].

The FEM of the stack includes the cage but does not include the fixture or the shaker table. All the nodes of the face of the cage oriented toward the fixture are clamped.

Figure 7 shows the MAC between the experimentally identified modes and the numerical modes before and after the updating.

Figure 8 shows the test-numerical frequency error: each point represents a pair of numerical and test mode frequencies. The pairing between the modes is automatically computed as in the model update, selecting for each reference (test) mode the numerical mode with the highest MAC value (with a threshold of 0.5). The zero-error line is indicated together with the $\pm 5\%$ bounds, which represent a very acceptable error value.

Figure 8 should be analyzed in combination with Figure 7. The model before updating exhibits relatively low accuracy. Only the first mode pair achieves a frequency error below 5% and displays a comparatively high MAC of about 80%. The second mode pair also demonstrates acceptable correlation. However, all other mode pairs show poor correlation in either frequency or MAC, or both indicators. Additionally, several reference modes do not find a corresponding numerical mode.

In contrast, the model after updating shows excellent agreement in both frequency and mode shape. Most mode pairs achieve errors lower than, or very close to, 5%. All pairs except one present MAC values above 76%, with several exceeding 90%. This is a remarkable result given that 54 triaxial sensors were used for the MAC calculation. The third mode pair, with a MAC value of 63%, corresponds to one of the three bending modes of the compression bands; the other two are not displayed in the MAC matrix plot. In the FEM, these modes involve all three bands equally but with varying phase relationships. In the actual structure, due to asymmetries from band weldings, these modes are slightly split, and each is dominated by the motion of a different band. This structural feature explains the higher error observed in the MAC for this mode, and it is not modeled by choice. The reason for the absence of pairing between the seventh test mode in the MAC matrix and any numerical mode remains unclear. The last four modes are high-order modes with complex shapes that are not captured by the model, as is generally expected.

A comparison between the numerical and experimental calculations of the stack's first bending mode is shown in Figure 9, showing a perfect agreement and the absence of any point of critical discrepancy.

The springs whose stiffnesses were updated correspond to elements that simulate the connection between the compression plate and the top-end plate of the stack, which are located at the top in the representations of the stack. In the initial design, these components were considered to possess flexibility exclusively in the axial (Z) direction. However, experimental analysis revealed significant rotational motion, particularly about the X axis. By including the stiffness of these springs as parameters in the updating process, it was possible to achieve a substantial improvement in both quantitative (MAC) and qualitative (visual inspection) agreement between experimental and numerical mode shapes (Figure 9). This finding underscores the critical importance of validating and, if necessary, refining model assumptions using experimental data [12]. Figure 10 further substantiates this conclusion by visually illustrating the effect of updating the spring elements, through a comparison of the first bending mode before and after the model update.

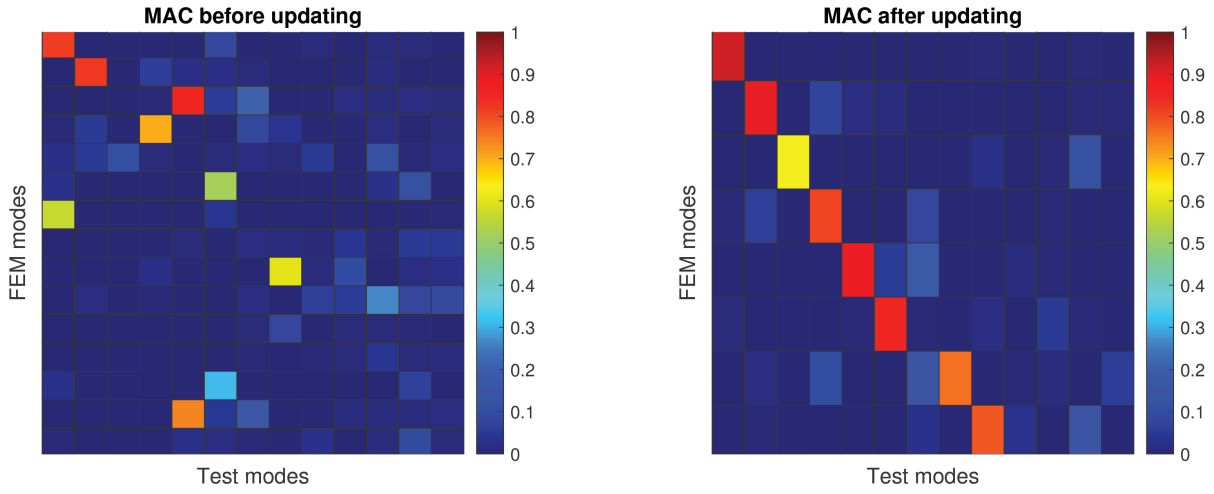

(a) MAC before updating

(b) MAC after updating

Fig. 7 Modal Assurance Criterion (MAC) before and after model updating

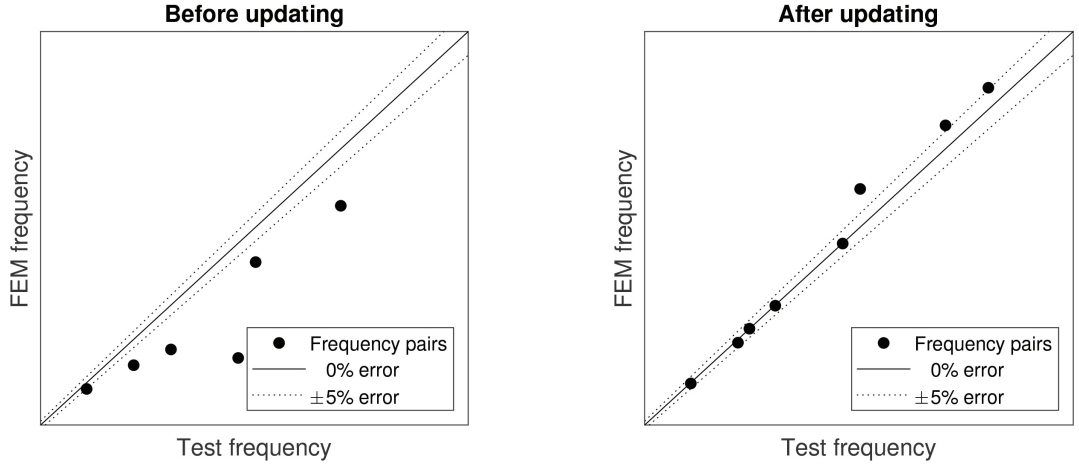

(a) Frequency error before updating

(b) Frequency error after updating

Fig. 8 Frequency error between experimental and numerical modes before and after model updating

Fixture coupling neutralization

Introduction to the problem

Aerospace structures are commonly tested on shaker tables for qualification. Typically, a modal survey is conducted separately from qualification tests. Extracting modal parameters directly from the data collected during shaker tests is highly desirable [17, 18, 19, 20], since it offers several advantages, such as:

- Time and cost savings.
- Good modal excitation, especially with multi-axial platforms.
- Increased safety, by reducing handling and transportation between different testing facilities, and avoiding local excitation methods such as modal hammer or secondary shakers.
- Avoidance of overtesting by notching resonances identified as caused by coupling. Indeed, if additional resonances originate from coupling, these can often be notched during qualification tests.

However, the interface between the structure and the shaker introduces fixture coupling effects, which can influence the identification of modal parameters [21, 22]. These effects often result in:

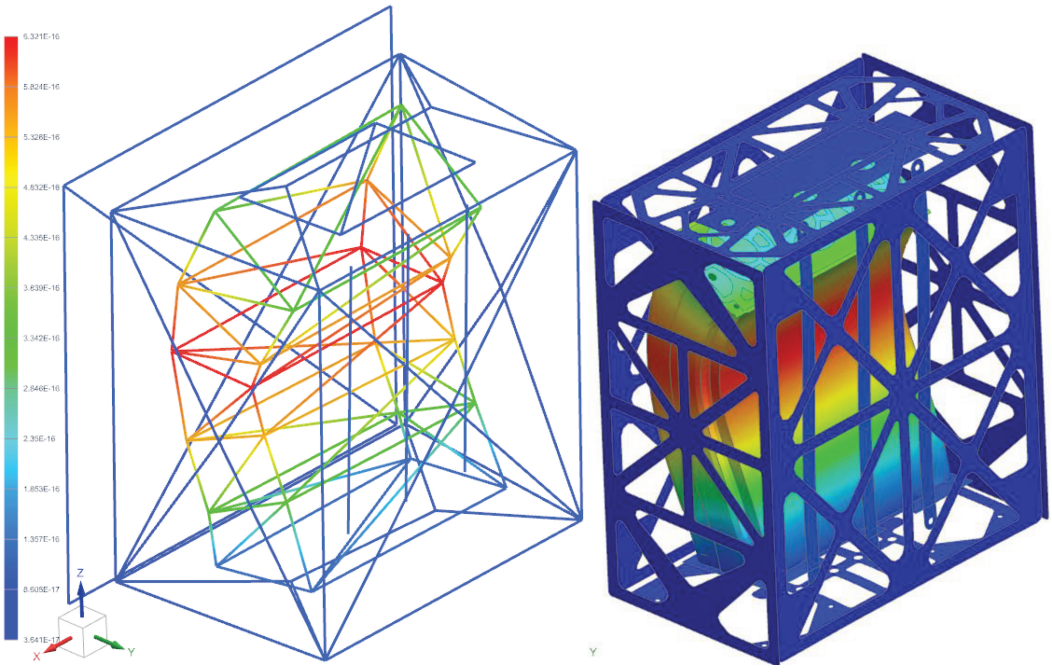

Fig. 9 Comparison of the first bending mode of the stack: numerical vs experimental

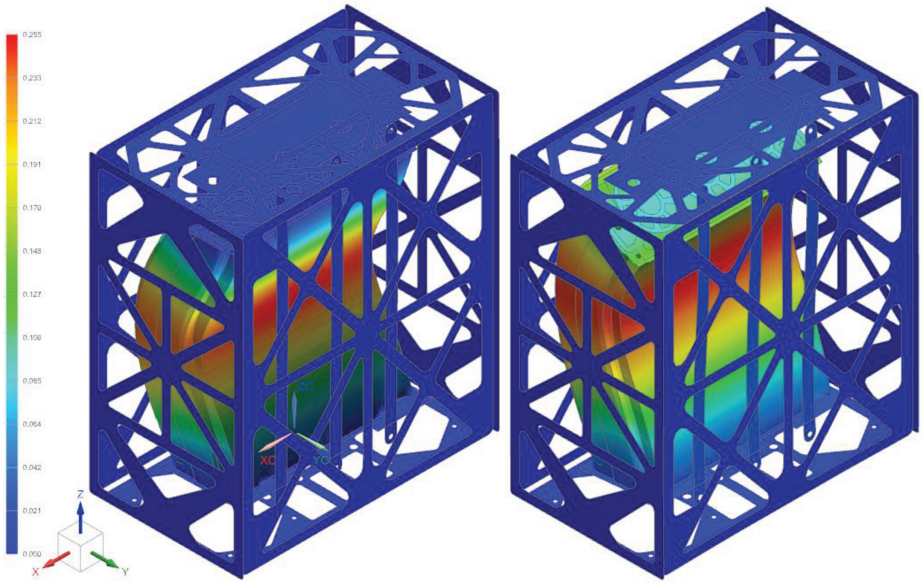

Fig. 10 Comparison of the first bending mode of the stack: before (left) and after (right) updating

- Additional resonances associated with the dynamics of the fixture.
- Modification of the structure's dynamics in terms of mode shapes, natural frequencies, and damping ratios.

The ability to accurately estimate fixed-base (FB) modal parameters is essential for model correlation, as shown in the previous section, as well as for structural response prediction and qualification processes. Constraining a model with non-trivial boundary conditions, such as fixed-base or free boundaries, introduces further challenges that should be avoided. The goal of fixture coupling neutralization is therefore to correct the coupled dynamics to recover the characteristics of the device under test (DUT).

Various decoupling methodologies have been developed in the literature. Early approaches utilize transmissibility-based methods [21, 22], while others employ multi-axial excitation and direct force measurements at the interface [17, 18, 19, 20].

More recent methods provide solutions for reconstructing FB modes from coupled data, such as [23, 24, 25, 26, 27] and [28, 29, 30, 31, 32, 33, 27]. These strategies allow for more accurate identification of the structure's inherent dynamic properties.

A schematic representing the coupling effects due to table flexibility or pseudo-rigid table modes is shown in Figure 11, together with the goal of decoupling.

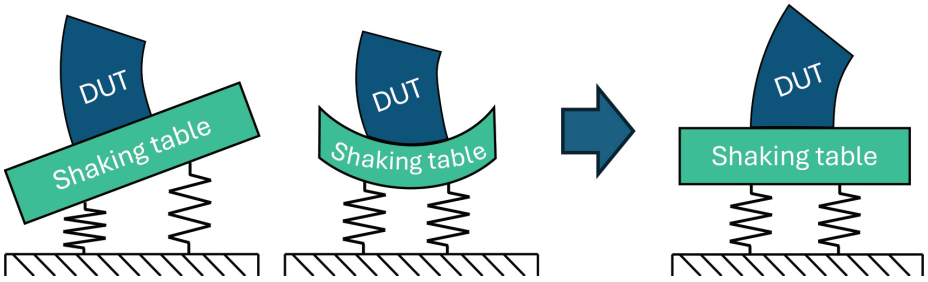

Fig. 11 Visual explanation of coupling and decoupling effects.

Employed methodologies

In this paper, the approaches presented in [23, 34, 35] by the same main author, Randy L. Mayes, are explored, namely the Frequency-based approach [23], the Modal-based approach [34], and the Singular value decomposition based approach [35]. The methods in [28, 36, 29, 30, 31, 32, 37, 33, 27] were not used, since only one direction of excitation was available, while several constraint modes were observed.

Frequency-based approach

To summarize this approach:

- The FB boundary conditions are mathematically constrained.
- An estimation of the shaker force is required.
- The full FRF matrix must be synthesized.
- The classical mathematical constraints used to produce FB conditions are modified to mitigate the ill-conditioning that typically arises when employing conventional constraint equations.

The mathematical basis, and the testing and analysis procedures in [23], are reported here for completeness. The input-output equation can be partitioned as follows:

$$\left\{ \begin{array}{c} \mathbf{a}_f \\ \mathbf{a}_c \end{array} \right\} = \left[\begin{array}{cc} \mathbf{H}_{ff} & \mathbf{H}_{fc} \\ \mathbf{H}_{cf} & \mathbf{H}_{cc} \end{array} \right] \left\{ \begin{array}{c} \mathbf{f}_f \\ \mathbf{f}_c \end{array} \right\}, \tag{1}$$

where $\mathbf{a}$ and $\mathbf{f}$ are vectors of acceleration and force, respectively, $\mathbf{H}$ is an FRF matrix, subscript c refers to the degrees of freedom (DOFs) to be constrained, and subscript f to the free ones. Only a few columns, or sometimes just one column, of this matrix are measured. Therefore, the first step is to reconstruct the entire matrix using the modal parameters extracted from the measured columns. By setting the corresponding constrained DOFs to zero (i.e., $\mathbf{a}_c = \mathbf{0}$), Equation 1 can be reformulated as shown in Equation 2.

$$\mathbf{a}_f = \left[\mathbf{H}_{ff} - \mathbf{H}_{fc} \mathbf{H}_{cc}^{-1} \mathbf{H}_{cf} \right] \mathbf{f}_f \tag{2}$$

As $\mathbf{H}_{cc}^{-1}$ is often poorly conditioned, the physically constrained DOFs are reduced to the modal coordinates of the table, using its modal matrix $\mathbf{\Phi}_c$, to enhance stability. The final form of the correction is given in Equation 3.

$$\mathbf{a}_f = \left[\mathbf{H}_{ff} - \mathbf{H}_{fc} \mathbf{\Phi}_c^{T+} \left(\mathbf{\Phi}_c^{+} \mathbf{H}_{cc} \mathbf{\Phi}_c^{T+} \right)^{-1} \mathbf{\Phi}_c^{+} \mathbf{H}_{cf} \right] \mathbf{f}_f \tag{3}$$

This modification significantly improves the robustness of the results. The procedure for obtaining FB FRFs can be summarized in the following steps:

1. The mode shapes of the bare table can be identified either by performing a modal shaker test or by using a modal hammer.
2. The Device Under Test is mounted on the shaker table, and two tests are performed:
   - An external shaker is attached to the tip of the table with a force gauge. The acceleration due to this force at the shaker location is measured. A modal hammer can also be used. The output of this test is $\mathbf{H}_{st}$.
   - The tip-shaker is removed and a shaker table test is performed to obtain the transmissibility to tip accelerations $\mathbf{a}_i/\mathbf{a}_t$.

   The additional shaker test is performed to estimate the shaker force using Maxwell's reciprocity principle. This estimation is necessary because the next step (synthesizing the FRF matrix) requires calculation of the modal mass, which requires a driving point FRF. However, the input force at the shaker is typically not measured. To circumvent this, the following procedure is applied:
   - The relationship between the FRFs is: $\mathbf{H}_{st} = \mathbf{H}_{ts}$
   - The acceleration at the tip of the table is: $\mathbf{a}_t = \mathbf{H}_{st}\mathbf{f}_s$
   - Rearranging for the shaker force: $\mathbf{f}_s = \mathbf{a}_t/\mathbf{H}_{ts}$
   - Substituting: $\mathbf{f}_s = \mathbf{a}_t/\mathbf{H}_{st}$
   - The FRF at any location of interest is then: $\mathbf{H}_{is} = \mathbf{a}_i/\mathbf{f}_s$
   - Finally, substituting the acceleration, the accelerance FRF is estimated as: $\mathbf{H}_{is} = \mathbf{H}_{st}\mathbf{a}_i/\mathbf{a}_t$
3. Extract modal parameters from the accelerance FRFs.
4. Synthesize the full FRF matrix using the modal parameters obtained in the previous step. This is a critical step, and can be quickly performed in Testlab [8] if a driving point FRF is available. However, the synthesis of FRFs for the additional input columns is not always accurate. The accuracy in this step plays an important role in the final estimation of the fixed-base characteristics.
5. Apply the constraint Equation 3 to the synthesized FRFs.

The fixed-base FRFs are therefore obtained and can be used for modal analysis.

Modal-based approach

The approach in [34] enables the structural system to be constrained solely through the modal shapes of the assembly, the structure under test, and the table, along with the modal shapes of the bare table. To ensure clarity, the following nomenclature is adopted:

- $\mathbf{\Phi}_c$: modes of the table alone,
- $\mathbf{\Psi}$: modes of the assembly (structure and table combined),
- $\mathbf{\Psi}_c$: assembly modes associated exclusively with the DOFs of the table.

Again, the theory in [34] is reported for completeness. The first step is to define the $\mathbf{B}$ matrix as the projection of $\mathbf{\Psi}_c$ onto $\mathbf{\Phi}_c$, as shown in Equation 4.

$$\mathbf{B} = \text{pinv}(\mathbf{\Phi_c}) \cdot \mathbf{\Psi}_c \tag{4}$$

The matrix $\mathbf{B}$ provides, through its coefficients, a measure of the contribution of each mode in $\mathbf{\Psi}_c$ to the modes of $\mathbf{\Phi}_c$. By exploiting orthogonality, the non-zero coefficients in Φ_c correspond to modes in $\mathbf{\Psi}_c$ that are similar to those in $\mathbf{\Phi}_c$. Thus, in essence, $\mathbf{B}$ defines the constraints that establish the clamping of the base. Subsequently, the null space of $\mathbf{B}$ can be computed as in Equation 5, and this gives the directions of $\mathbf{\Psi}_c$ not captured by $\mathbf{\Phi}_c$.

$$\mathbf{L} = \text{null}(\mathbf{B}) \tag{5}$$

This represents a coordinate transformation, which enables reducing the number of free modal coordinates to a smaller, constrained set. By applying $\mathbf{L}$ and solving the eigenvalue problem, the FB natural frequencies ω_{fix} and the corresponding

eigenvectors $\mathbf{\Gamma}$, which should be mass-normalised, are obtained. The eigenvalue problem to be solved is given in Equation 6, which is formulated under the assumption of unit-mass scaled modal shapes and with the damping matrix $\mathbf{C}$ neglected.

$$\left[\mathbf{L}^T \operatorname{diag}(\omega_{\text{ass}}^2)\mathbf{L} - \omega^2 \mathbf{L}^T \mathbf{I}\mathbf{L}\right] q = 0 \tag{6}$$

When accounting for damping, the formulation is modified as in Equation 7.

$$\left[\omega^2 \mathbf{L}^T I\mathbf{L} - \omega \mathbf{L}^T 2\,\zeta_{\text{ass}}\omega_{\text{ass}}\mathbf{L} + \mathbf{L}^T \operatorname{diag}(\omega_{ass}^2)\mathbf{L}\right] q = 0 \tag{7}$$

Finally, it is necessary to return to physical coordinates. The FB mode shapes are then computed as in Equation 8, following the formulation in [34].

$$\mathbf{\Psi}_{\text{fixed}} = \mathbf{\Psi}\mathbf{L}\mathbf{\Gamma} \tag{8}$$

Singular value decomposition based approach

A valid alternative to avoid characterizing the bare table is presented in [35]. Singular Value Decomposition (SVD) is applied to the assembly modal shapes, considering only the boundary DOFs as in Equation 9.

$$\mathbf{U}\mathbf{S}\mathbf{V}^H = \mathbf{\Psi_c} \tag{9}$$

Then $\mathbf{U}$ is used to modify $\mathbf{\Psi_c}$ as shown in Equation 10.

$$\mathbf{T_{ref}} = \mathbf{U}\mathbf{\Psi_c} \tag{10}$$

$\mathbf{T_{ref}}$ is then used in Equation 4 instead of $\mathbf{\Phi_c}$. However, only a few columns, i.e., a limited number of modes of $\mathbf{T_{ref}}$, should be included in the correction to avoid over-decoupling the dynamics.

This method has proven effective in constraining the boundary, removing the table modes, and correcting the FB frequencies and modal shapes. Additionally, no bare table characterization is required.

Comparison of approaches

Table 3 summarizes the differences among the methods, outlining their respective requirements and limitations.

Table 3 Comparison of method requirements and limitations.

Frequency based	**Modal based**	**SVD based**
$a_f = [H_{ff} - H_{fc}\Phi_c^{T+}(\Phi_c^+ H_{cc}\Phi_c^{T+})^{-1}\Phi_c^+ H_{cf}]f_f$	$\Psi_{\text{fixed}} = \Psi\mathbf{L}\Gamma$	$[U][S][V]^H = \Psi_c$
Synthesize full FRF matrix, and conduct a separate bare table test.	Separate bare table test for modal shapes.	No modal test for bare table required.
Sensitive to synthesized FRF accuracy.	Unit mass scaling needs driving point FRF.	Unit mass scaling needs driving point FRF.

To avoid constraining the test article modes but only constraining the table modes, a guiding rule for choosing the number of shapes in Φ_c exists [35]. Specifically, the number of modes dominated by the shaker table dynamics, when testing the test article on the table, must be at least equal to the number of constraint shapes in Φ_c.

Fixture decoupling results

Here, the case of the fuel cell stack is analyzed. First, in Evidences of coupling, the investigation shows qualitatively and quantitatively the coupling between the DUT (fuel cell stack and cage) and the shaking table (table and fixture). Secondly, the methodologies described in Employed methodologies are verified to mitigate the effect of the coupling and to extract the fixed-base modes.

Evidences of coupling

Summarizing what is described in Introduction to the problem, the main evidence of coupling is the appearance of additional resonances associated with the dynamics of the fixture and a modification of the modal parameters. This is, of course, due to FRFs not representing fixed-base characteristics. Placing sensors at the boundary conditions (i.e., on the fixture and on the table) allows identification of whether the mode shapes of the DUT involve motion of the boundary DOFs, thereby detecting coupling. If the boundary DOFs are accessible, this verification is always possible. However, a modification of the natural frequencies (for example) can only be detected when a fixed-base reference is available. This is the case for the fuel cell stack. As described in Shaker testing and shown in Figure 1, the stack was mounted and tested on two different shaker tables: the CUBE and a slip table. While the data acquired on the CUBE show relatively low motion of the boundary DOFs, the slip table data show all the aforementioned signs of coupling. The authors believe that this is mainly due to different methods of fixing the fixture. In particular, as shown in Figure 12, the fixture is bolted to the slip table only in the middle, due to alignment between holes. For the CUBE, holes close to the border were used for clamping, providing better clamping and lower fixture motion, which is assumed here to explain the difference in coupling between the two setups. Therefore, in this analysis, the CUBE's mode shapes and frequencies are assumed as the fixed-base reference.

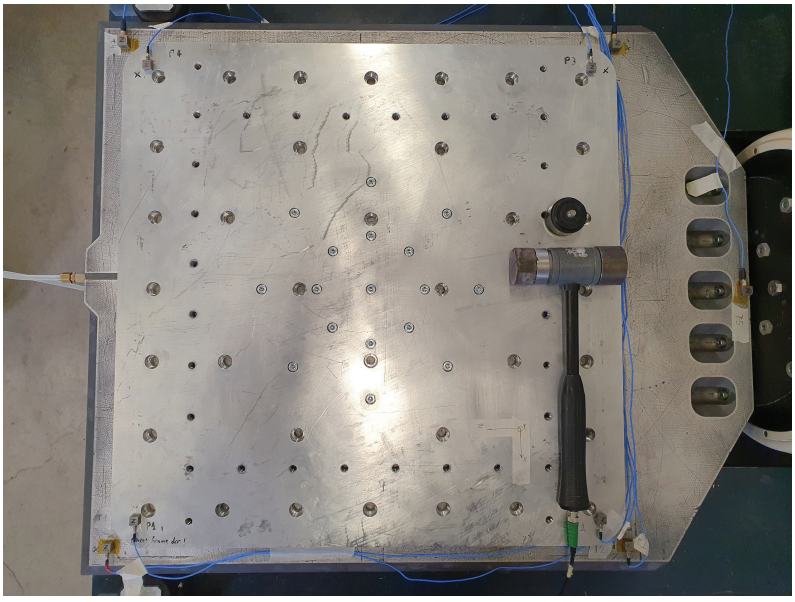

Fig. 12 Slip table to fixture fixing

Figure 13 presents the MAC between the CUBE and slip table modes. A few observations are listed below, together with information about frequencies.

- The slip table modeset has a few more modes in the bandwidth of the stack flexible modes. While CUBE mode 1 is pseudo-rigid, additional modes are present for the slip table, e.g., mode 7. The presented MAC matrix is from a selection of slip table modes that best correlate with the CUBE modes; several stable modes from the stabilization diagram were discarded during the modal validation.

- At lower frequencies, the correlation between the modesets is higher, while at higher frequencies it degrades. This is because:

  - At lower frequencies, the cage is rigid and the DUT couples mainly with fixture and table motion. At higher frequencies, the cage is more flexible and its dynamics couple with those of the fixture.
  - Modes 4, 5, and 6 of the CUBE, or 3, 4, and 5 of the slip table, are the compression band modes, which are local.

- Several slip table modes, even those with high MAC, are shifted down in frequency, indicating more flexible boundary conditions. Denoting CUBE modes as $C1$, $C2$, etc., and slip table modes as $ST1$, $ST2$, etc., some frequency relations are: $ST1$ is 96% of $C2$; $ST2 = 87\%\, C3$; $ST8 = 93\%\, C8$; $ST9 = 90\%\, C9$; $ST14 = 92\%\, C12$.

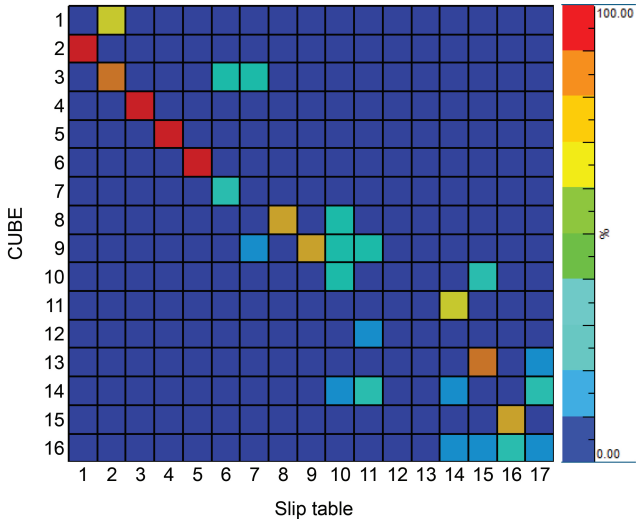

Fig. 13 MAC between CUBE and slip table modes

Figures 15, 16, and 14 present comparisons between pairs of modes shown to be impacted by coupling. In all cases, the eight boundary sensors for the CUBE are almost static, while there is significant motion—especially of the fixture—for the slip table.

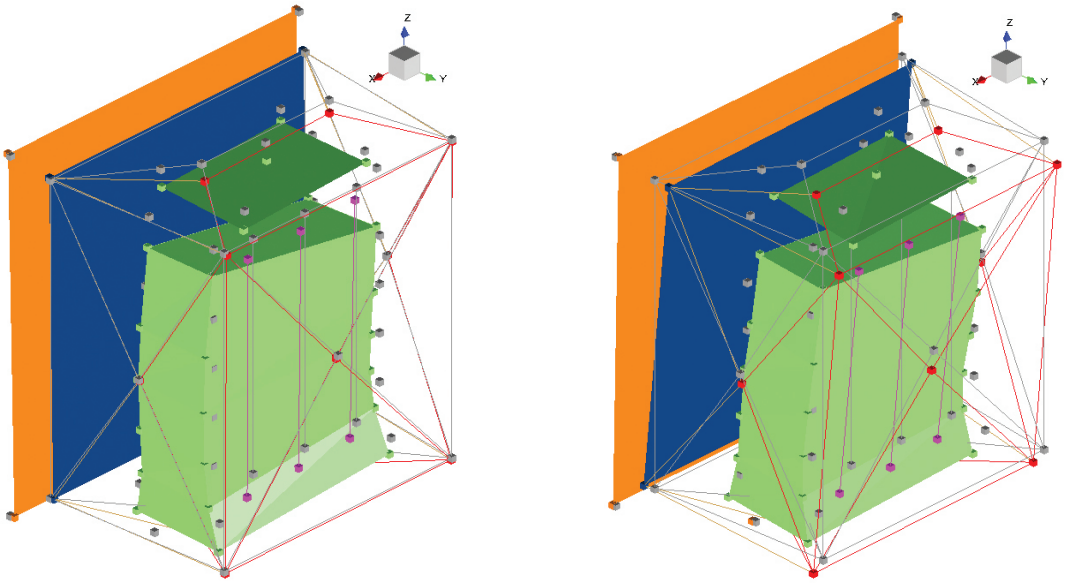

(a) CUBE ($C3$) (b) Slip table ($ST2$)

Fig. 14 Comparison of 1st longitudinal mode shapes along Z between shaker tables. $ST2 = 87\%C3$.

Decoupling of longitudinal mode

Here, the decoupling of the 1st longitudinal mode shape along Z is investigated, as it is one of the most affected by coupling. As previously reported, for the slip table, the longitudinal mode frequency ($ST2$) is 87% of that of the CUBE setup, and their mode shapes are compared in Figure 14, with a MAC value of 82%. All results are presented using the CUBE's $C3$ mode as reference.

The Frequency-based approach and Modal-based approach require identification of the table's modes, isolated from the DUT. To this end, slip table modes with only the fixture mounted were identified via hammer testing and Polymax postprocessing [10]. The setup is shown in Figure 12.

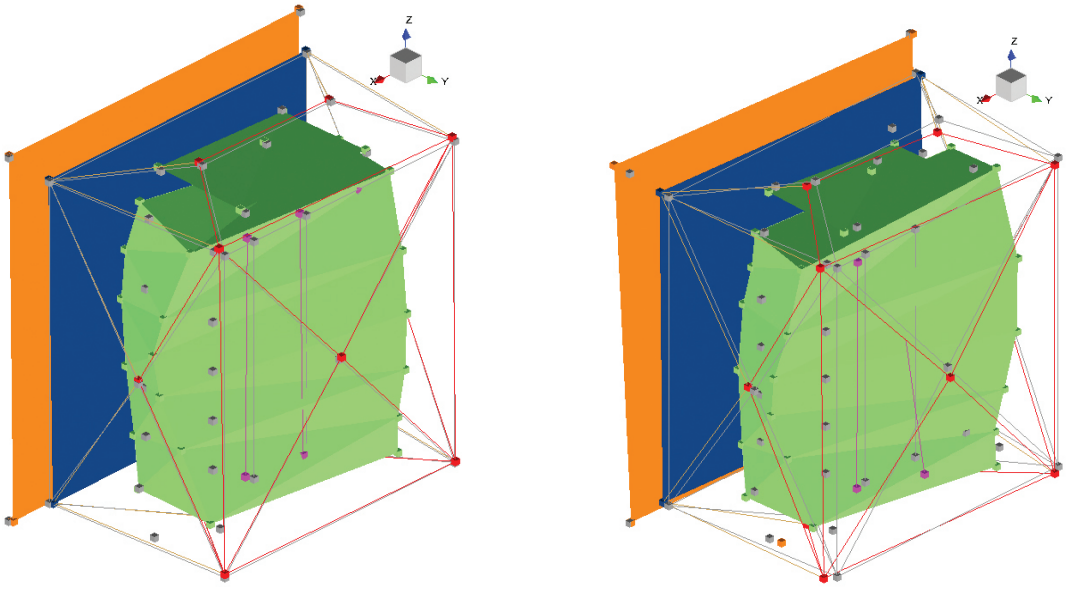

(a) CUBE ($C8$) (b) Slip table ($ST8$)

Fig. 15 Comparison of 1st torsional mode shapes between shaker tables. $ST8 = 93\%C8$.

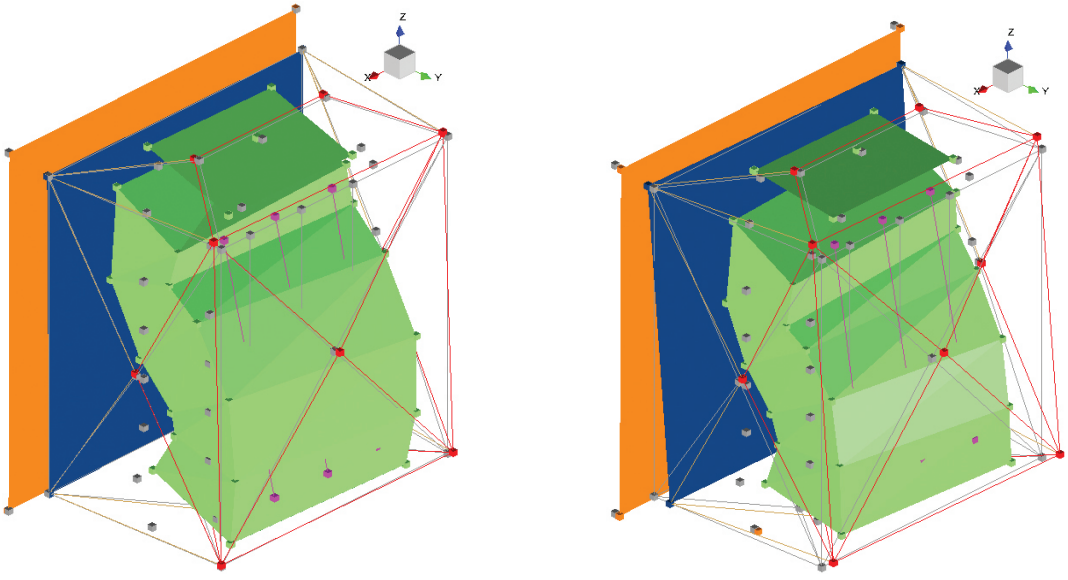

(a) CUBE ($C9$) (b) Slip table ($ST9$)

Fig. 16 Comparison of 2nd bending (about X axis) mode shapes between shaker tables. $ST9 = 90\%C9$.

Selecting all modes in the frequency band of interest would lead to incorrect correction. If the number of table modes used in the correction exceeds the actual number of modes coupled with the structure, the correction can compromise the structural modes themselves [23] because modes not coupled would also be incorrectly adjusted.

Thus, the main challenge in applying this method is accurately identifying the table modes. The mode selection was lengthy, mainly based on correlation with the assembly modes (considering only the table's DOFs) and on trial and error.

Figure 17 shows the selected bare table modes. The fuel cell stack geometry is included as a reference, but the stack was not mounted on the table when identifying those modes. The modes depict the motion of both the table and fixture, as well as their relative movement. This illustrates a complex scenario where different components contribute to the coupling.

The Frequency-based approach is then applied. Not all DOFs have been used for the correction; those related to the compression bands were excluded as they mostly contribute only to their associated modes. By omitting these components,

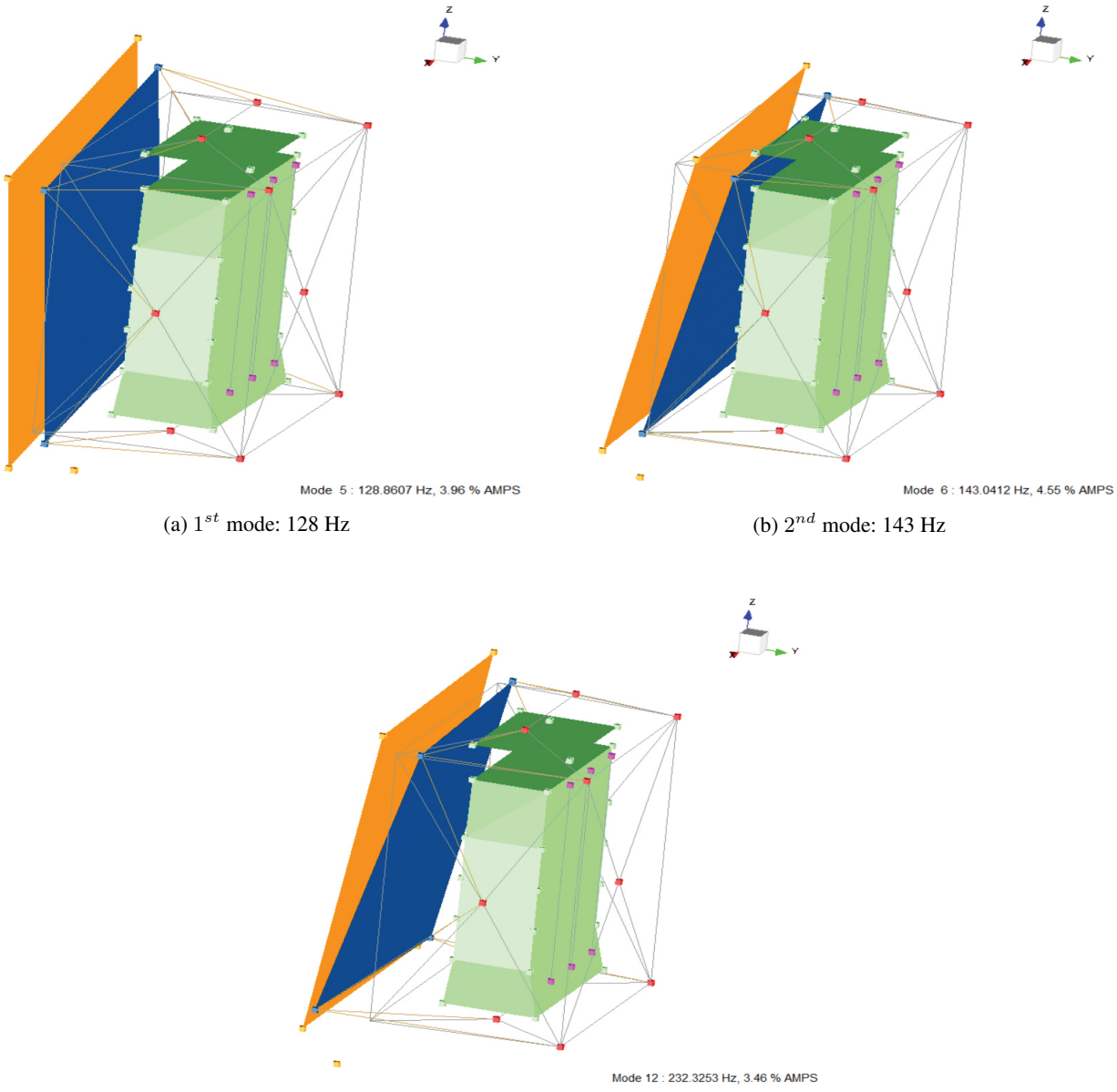

(a) 1st mode: 128 Hz

(b) 2nd mode: 143 Hz

(c) 3rd mode: 232 Hz

Fig. 17 Slip table and fixture modes (without fuel cell stack).

subsequent operations like FRF matrix synthesis—an important step—are simplified, and the correction can be focused on the actual coupled modes. Equation 3 is applied using the modes at 143 Hz and 232 Hz as the table mode matrix $\mathbf{\Phi}_c$. As a result, the additional modes originating from coupling are removed.

The corrected axial mode from the Mayes method is shown in Figure 18. There is still some cage movement, but it is significantly reduced. Despite this, the MAC remains above 80%. The corrected frequency is about 105% of that mode's natural frequency on the CUBE ($C3$), thus the correction changes the error from -13% to $+5\%$, i.e., from 87% to 105% of $C3$. The reason for this frequency overshoot requires further investigation.

The Modal-based approach has also been applied to the same mode. Results, shown in Figure 19, were obtained using three different datasets of table modes, and are summarized in Table 4. This method effectively eliminates the movement of both the fixture and the table. The cage remains stationary, resulting in a better modal shape outcome than that from the Frequency-based approach. All corrected modes show a MAC greater than 80% relative to the CUBE axial mode. However, the frequencies are substantially different from the CUBE reference.

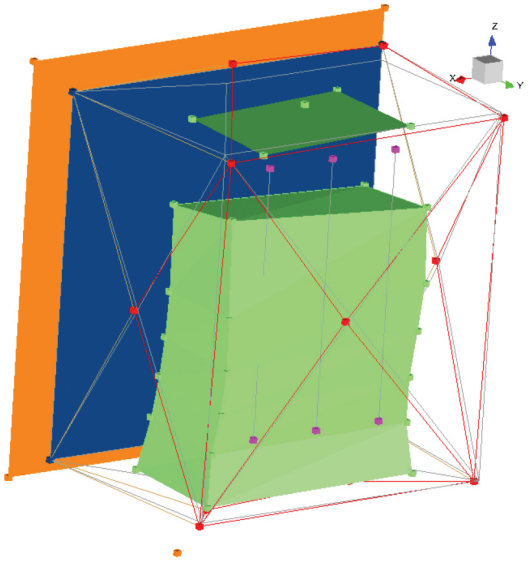

Fig. 18 Corrected FB longitudinal mode obtained with the Frequency-based approach. $ST2 = 105\%C3$

Table 4 Summary of results of Frequency-based approach as a function of selected table shapes.

Bare table modes		
1	2	3
128 Hz 143 Hz	128 Hz 232 Hz	143 Hz 232 Hz
Correction result modal approach		
1	2	3
$126\%C3$	$149\%C3$	$151\%C3$

Another notable aspect is that the modes obtained through the correction show a slight increase in modal complexity. The results are highly sensitive to the table modes used, especially regarding frequency estimation.

Because of the high sensitivity to table mode selection, the Singular value decomposition based approach was also applied, as it avoids the need for bare table modes and appears more effective for frequency correction [35]. The first attempt applied SVD to the $ST2$ mode and used the resulting $\mathbf{U}\boldsymbol{\Psi}_{ST2,c}$ as $\boldsymbol{\Phi}_c$ to constrain the DOFs. The frequency changed from $87\%C3$ before correction to $99.9\%C3$, very close to the reference, but the correction did not significantly change the modal shape; the fixture still showed motion.

The second attempt applied SVD to the entire assembly matrix (boundary DOFs only), retaining the two dominant singular values. The resulting mode shape (see Figure 20) shows nearly zero cage motion. The MAC value is 88% relative to the CUBE longitudinal mode (higher than the 82% MAC of the slip table longitudinal mode). However, the frequency is $123\%C3$, the best obtained with this approach.

Decoupling of bending and torsion

The same procedure was also attempted for other modes, such as the torsional about Z ($C8$ and $ST8$) and the 2nd bending about X ($C9$ and $ST9$). A thorough study is still required to identify which table modes should be considered for effective correction. The Singular value decomposition based approach was used to avoid manually selecting table modes, relying only on the assembly's modal shape matrix. However, for the torsional mode, results remained inconclusive, suggesting that further investigation is needed.

For the 2nd bending about X, while the SVD method increased mode complexity, the corrected frequency was 98% of $C9$, improving from the original value of $90\%C9$ before the correction. The corrected modal shape is shown in Figure 21.

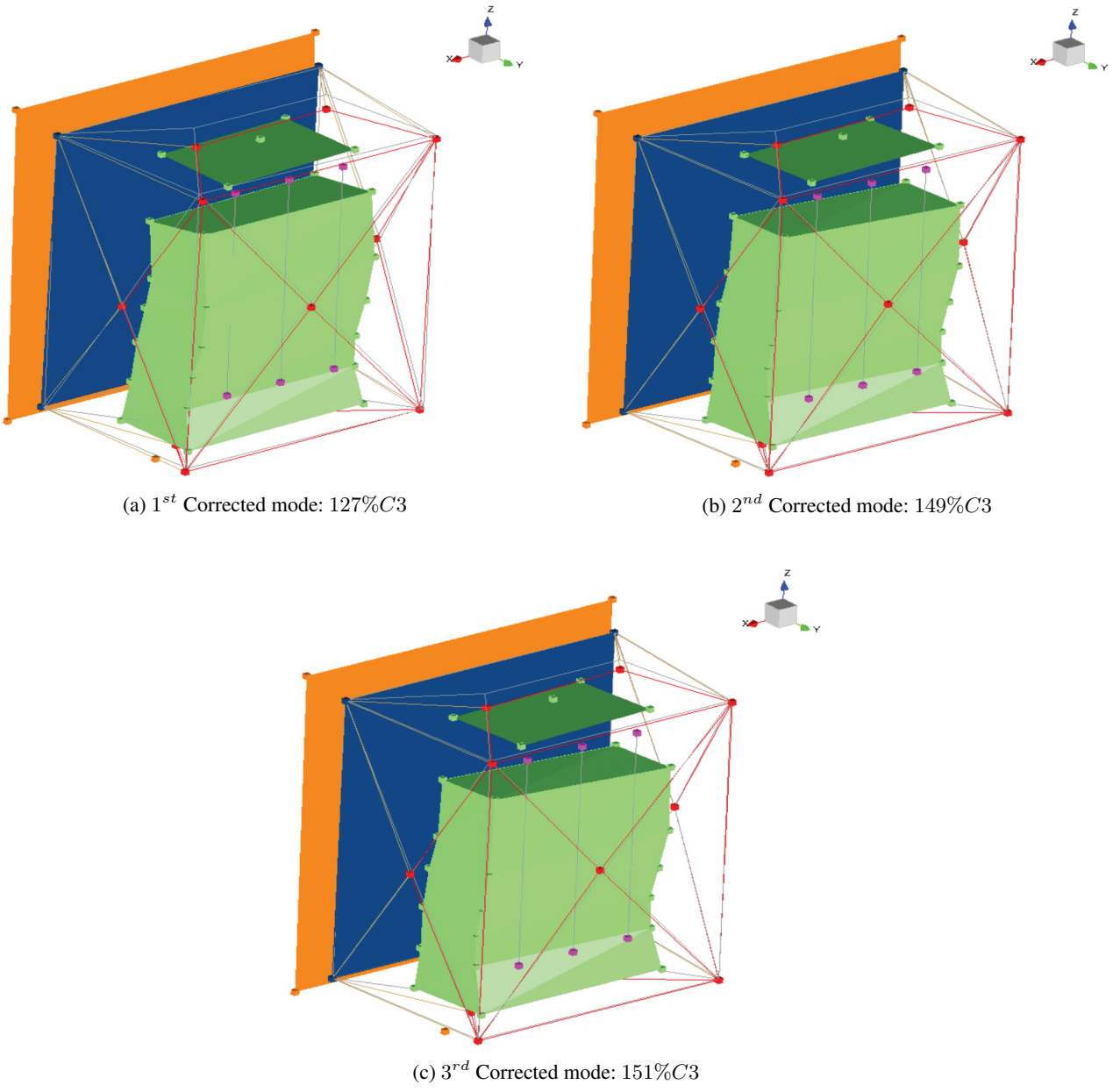

(a) 1st Corrected mode: $127\%C3$

(b) 2nd Corrected mode: $149\%C3$

(c) 3rd Corrected mode: $151\%C3$

Fig. 19 Modal shape correction results for the longitudinal mode: Modal-based approach.

Comments and summary of decoupling results

In performing these corrections, the DOFs of the fixture were treated as boundary conditions—taken as a first approximation to be equivalent to those of the cage (i.e., the actual structural component). This was motivated by the observation that, without fixing these DOFs, the correction process did not adequately suppress the fixture's motion, resulting in inaccurate results. This may suggest that the relative motion between the fixture and cage plays a non-negligible role in the dynamics. A more rigorous approach could involve placing additional accelerometers directly on the cage to capture and account for its motion relative to the fixture. Since fixture and cage are bolted together, their interface introduces a further layer of complexity to the system's dynamics, which would benefit from a more comprehensive instrumentation setup.

This preliminary application of the decoupling method focuses on correcting a few of the most coupled modes per time, but the approach has inherent limitations. Correction accuracy depends on proper identification of table modes and precise estimation of coupling effects. Future work could expand the analysis to include all highly coupled modes (longitudinal,

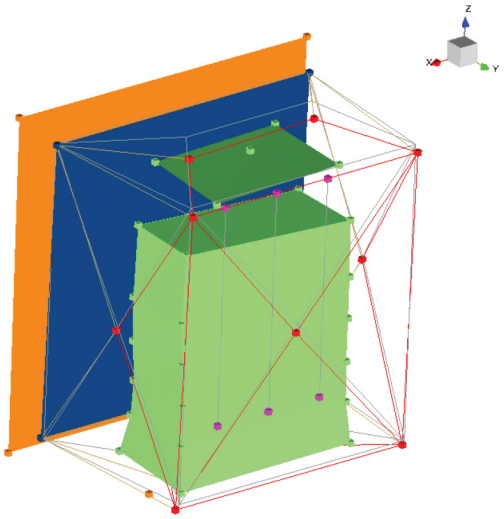

Fig. 20 Longitudinal mode corrected using the Singular value decomposition based approach: $123\%C3$

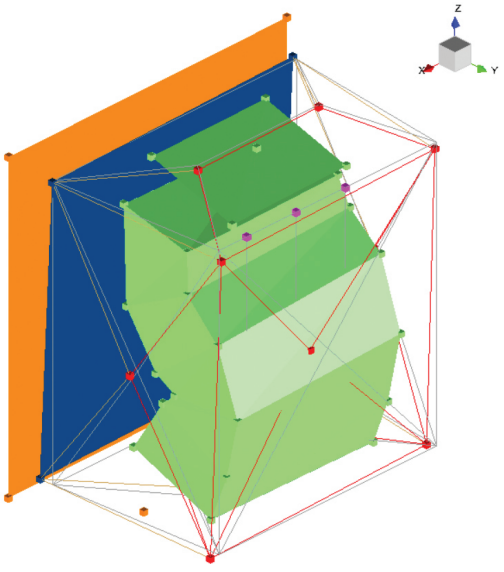

Fig. 21 2nd bending about X, corrected using the Singular value decomposition based approach: $98\%C9$.

torsional, and bending) simultaneously, allowing for a more comprehensive validation and deeper insight into the slip table–structure interaction.

It is important to note that if the table mode shape is directly extracted from the assembly modes—considering only the boundary DOFs of the longitudinal coupled mode—and used for correction, the longitudinal mode may completely disappear. This indicates the method's sensitivity to the proper selection of the correction basis.

Among the three approaches of the method, the Singular value decomposition based approach was able to retrieve the corrected FB modal shape for the longitudinal mode, with a higher MAC value than the shape obtained on the CUBE (used here as reference), although the frequency was not corrected. When the same method was applied using exactly the table's DOFs in the assembly matrix, the frequency obtained was very close to the CUBE value.

The same procedure applied to another coupled mode allowed the method to fix the fixture and achieve a frequency close to the CUBE reference, despite increased mode complexity.

It is important to note that including more columns from $\mathbf{T_{ref}}$ after SVD degrades results and causes loss of information, causing the correction to fail. This is consistent with [35], which reports that including more modes than necessary results in the correction affecting the actual structural modes as well.

Conclusions

This study addressed the dynamic characterization of a fuel cell stack through experimental testing, modal analysis, finite element model (FEM) updating, and fixture coupling neutralization, with a focus on supporting the development and qualification of vibration-robust hydrogen fuel cell systems for aviation.

The main conclusions from each step of the workflow, as well as points of synergy between the activities, are as follows:

- **Shaker Testing and Experimental Modal Analysis:** The thorough experimental campaign, utilizing multiple shaker platforms and a dense array of accelerometers, enabled high-quality data collection for a wide range of excitation conditions. The comprehensive modal survey provided reliable identification of natural frequencies, damping ratios, and mode shapes, while also revealing amplitude-dependent nonlinearities, particularly due to friction. Robust validation of the modal dataset was achieved through auto-MAC assessment, modal synthesis, and complexity analysis, yielding a highly credible experimental modal model.
- **FEM Updating and Test-Analysis Correlation:** The availability of an accurate experimental modal model proved fundamental for the successful updating and validation of the FEM. By directly using the experimental mode shapes and frequencies as targets, design variables (including material properties and interface spring stiffnesses) could be refined. This process led to excellent test-analysis correlation in both frequency (within 5% error for relevant modes) and MAC (most modes above 75%). The update also highlighted the importance of including realistic boundary and connection conditions in the FEM, corroborated by experimental observations on the true dynamic response of the stack. The improved FEM, validated against a trustworthy modal reference, forms a solid foundation for structural durability assessment and numerical vibration immunity studies.
- **Fixture Coupling Neutralization:** The experimental results demonstrated clear evidence of fixture coupling, in the form of additional resonances, altered mode shapes, and frequency shifts, especially on the slip table configuration. Various state-of-the-art decoupling techniques (frequency-based, modal-based, and SVD-based) were implemented and evaluated. Their successful application critically depended on the accurate experimental modal model for synthesizing fixed-base characteristics and the selection of the relevant table modes. The SVD-based approach was particularly attractive for its flexibility, though all approaches required careful parameter tuning to avoid over-constraining or losing structural information.
- **Synergies and Research Outlook:** The workflow established in this paper clearly demonstrates that the accuracy of later steps—model updating and fixture decoupling—relies intrinsically on the quality of the experimental modal data. Any uncertainty or error in the modal survey propagates to both FEM correlation and decoupling, and vice versa. Indeed, in the case a fixed-base setup is not available, decoupling is fundamental to identify a modeset to be used for FEM correlation. In turn, a well-updated FEM assists in interpreting residual discrepancies in the test data, separating fixture from structure effects, and refining fixture decoupling procedures. The interplay between accurate experiment, model updating, and decoupling methods is therefore fundamental for robust vibration qualification and design of critical components such as fuel cell stacks for aerospace applications.
- **Recommendations:** Future work should focus on improving the automation and robustness of table mode identification, integrating multi-axial excitation strategies, and extending sensor instrumentation to better capture interface dynamics. Joint consideration of experimental modal analysis, FEM updating, and fixture decoupling in a closed-loop manner can lead to further gains in accuracy and reliability for vibration qualification in demanding engineering scenarios.

Acknowledgments The NEWBORN project is supported by the Clean Aviation Joint Undertaking and its members. Funded by the European Union under Grant Agreement No. 101101967.

Views and opinions expressed are, however, those of the authors only and do not necessarily reflect those of the European Union or Clean Aviation Joint Undertaking. Neither the European Union nor the granting authority can be held responsible for them.

References

1. CORDIS European Commission. “NEWBORN - NExt generation high poWer fuel cells for airBORNe applications”. https://cordis.europa.eu/project/id/101101967/reporting, 2023. Project ID: 101101967.
2. NEWBORN Project Consortium. “NEWBORN Project Official Website”. https://newborn-project.eu/, 2023.
3. PowerCell Group. “PowerCell Sweden AB”. https://powercellgroup.com/.

4. RTCA, Inc. "DO-160G Environmental Conditions and Test Procedures for Airborne Equipment, Section 8 Vibration". Technical report, Federal Aviation Administration, 2010.
5. D. J. Ewins. *Modal Testing: Theory, Practice and Application*. Research Studies Press, Baldock, UK, 2nd edition, 2000.
6. KU Leuven. "The CUBE". https://www.mech.kuleuven.be/en/mod/services-consulting-depreciated/cube.
7. Siemens Digital Industries Software. "Simcenter SCADAS Lab". https://plm.sw.siemens.com/en-US/simcenter/physical-testing/scadas/lab/, 2024.
8. Siemens Digital Industries Software. "Simcenter Testlab". https://plm.sw.siemens.com/en-US/simcenter/physical-testing/testlab/, 2024.
9. Gaëtan Kerschen, Keith Worden, Alexander F. Vakakis, and Jean Claude Golinval. "Past, present and future of nonlinear system identification in structural dynamics". *Mechanical Systems and Signal Processing*, 20(3):505 – 592, 2006.
10. Bart Peeters, Herman Van der Auweraer, Patrick Guillaume, and Jan Leuridan. "The polymax frequency-domain method: A new standard for modal parameter estimation?". *Shock and Vibration*, 11, 2004.
11. Randall J Allemang and David L Brown. "A correlation coefficient for modal vector analysis". *Proceedings of the 1st international modal analysis conference*, 1:110–116, 1982.
12. Herman Van der Auweraer and Dirk Hartmann. "The executable digital twin: merging the digital and the physics worlds". 2023.
13. Giovanni Fasulo, Simone Gallas, Hervé Denayer, Oskar Ekblad, Giancarlo Kosova, and Mattia Barbarino. "A modeling approach for assessing vibration immunity in hydrogen fuel cell stack for aeronautical applications". For submission to *Applied Sciences*, Special Issue: Advances in Aerostructural Analysis, Design, and Optimization., in preparation.
14. "Simcenter Nastran". https://plm.sw.siemens.com/en-US/simcenter/mechanical-simulation/nastran/, 2024.
15. "Simcenter Nastran SOL200 – Structural Optimization". https://plm.sw.siemens.com/en-US/simcenter/mechanical-simulation/nastran/sol200-optimization/, 2024.
16. "Simcenter 3D". https://plm.sw.siemens.com/en-US/simcenter/mechanical-simulation/simcenter-3d/, 2024.
17. Ulrich Füllekrug. "Determination of Effective Masses and Modal Masses from Base- Driven Tests". In *Proceedings of 7th International Congress on Sound and Vibration*, 1996.
18. M. Sinapius. "Identification of Free and Fixed Normal Modes by Base Excitation.". In *Proceedings of 14th International Modal Analysis Conference*, 1996.
19. Carsten Schedlinski and Michael Link. "Identification of Frequency Response Functions and Modal Data from Base Excitation Tests Using Measured Interface Forces". In *Proceedings of the ASME Conference On Noise & Vibration, Boston, Massachusetts*, 1995.
20. Mario Razeto, Jean-Claude Golinval, and Michel Géradin. "Modal Identification and Determination of Effective Mass Using Environmental Vibration Testing on an Electro-dynamic Shaker". In *Proceedings of the 12th International Modal Analysis Conference, Honolulu, Hawaii*, 1994.
21. Thomas G Carne, David R Martinez, and Arlo R Nord. "A comparison of fixed-base and driven-base modal testing of an electronics package". Technical report, Sandia National Labs., Albuquerque, NM (USA), 1989.
22. J.-G. Béliveau, F.R. Vigneron, Y. Soucy, and S. Draisey. "Modal parameter estimation from base excitation". *Journal of Sound and Vibration*, 107(3), 1986.
23. Randy Mayes and Lynn Bridgers. "Extracting Fixed Base Modal Models from Vibration Tests on Flexible Tables". In *Proceedings of the Society for Experimental Mechanics Series*, 2009.
24. Randy Mayes and Mathew Allen. "Converting a Driven Base Vibration Test to a Fixed Base Modal Analysis". In *Proceedings of the 29th International Modal Analysis Conference*, 2011.
25. Benjamin Pacini and R. Mayes. "Computing Effective Mass Using the Modal Craig Bampton Framework". *Experimental Techniques*, 48, 2024.
26. Randy L. Mayes. "Refinements on estimating fixed base modes on a slip table". In *Topics in Modal Analysis I, Volume 5*, pages 359–365, 2012.
27. Peter A. Kerrian. "A Comparison of Different Boundary Condition Correction Methods". In Brandon Dilworth and Michael Mains, editors, *Topics in Modal Analysis & Testing, Volume 8*, 2021.
28. Kevin Napolitano and Nathanael Yoder. "Fixed Base FRF Using Boundary Measurements as References: Analytical Derivation". In *Proceedings of the 30th International Modal Analysis Conference*, 2012.
29. Kevin Napolitano, Nathanael Yoder, and William Fladung. "Extraction of Fixed-Base Modes of a Structure Mounted on a Shake Table". In *Proceedings of the 31st International Modal Analysis Conference*, 2013.
30. Lucas D. Staab, James P. Winkel, Vicente J. Suarez, Trevor M. Jones, and Kevin L. Napolitano. "Fixed Base Modal Testing Using the NASA GRC Mechanical Vibration Facility". In *Proceedings of the 34th International Modal Analysis Conference*, 2016.
31. James Winkel, James Akers, Vicente Suarez, Lucas Staab, and Kevin Napolitano. "Modal Survey of the MPCV Orion European Service Module Structural Test Article Using a Multi-axis Shake Table". In *Proceedings of the 36th International Modal Analysis Conference*, 2017.
32. Kevin L. Napolitano. "Feasibility Study to Extract Artemis-1 Fixed Base Modes While Mounted on a Dynamically Active Mobile Launch Platform". In Chad Walber, Patrick Walter, and Steve Seidlitz, editors, *Sensors and Instrumentation, Aircraft/Aerospace, Energy Harvesting & Dynamic Environments Testing, Volume 7*, 2021.
33. Peter Adam Kerrian and Kevin L. Napolitano. "Pretest Analysis for Modal Survey Tests Using Fixed Base Correction Method". In *Proceedings of the 37th International Modal Analysis Conference*, 2019.
34. Randy L. Mayes, Tyler F. Schoenherr, Jill Blecke, and Daniel P. Rohe. "Efficient Method of Measuring Effective Mass of a System". In *Topics in Experimental Dynamic Substructuring, Volume 2*. Springer New York, 2014.
35. Randy L. Mayes and Matthew S. Allen. "Converting a Driven Base Vibration Test to a Fixed Base Modal Analysis". In Tom Proulx, editor, *Rotating Machinery, Structural Health Monitoring, Shock and Vibration, Volume 5*. Springer New York, 2011.
36. Nathanael Yoder and Kevin Napolitano. "Fixed Base FRF Using Boundary Measurements as References: Experimental Results". In *Proceedings of the 30th International Modal Analysis Conference*, 2012.
37. Natalie Spivey, Rachel Saltzman, Carol Wieseman, Kevin Napolitano, and Benjamin Smith. *Passive Aeroelastic Tailored Wing Modal Test Using the Fixed Base Correction Method*, pages 61–83. Springer International Publishing, 2021.

River Rapids

Dynamic Evironments and Durability Testing, Volume 7

Dagny Beale ■ Cora Taylor ■ Shannon Danforth

Dynamic Environments and Durability Testing, Volume 7: Proceedings of the 44th IMAC, A Conference and Exposition on Structural Dynamics, 2026, the seventh volume of ten from the Conference brings together contributions to this important area of research and engineering. The collection presents early findings and case studies on fundamental and applied aspects Dynamic Environments Testing including papers on:

- Dynamic Environment Definition and Specification
- Dynamic Testing Fixture Design and Fixture Neutralization
- Measurement Sensitivity to Test Design
- Multi-Degree of Freedom Shaker Testing and Environments Specification
- Resonant Plate Shock Testing

ISBN 978-87-438-1446-7

9 788743 814467

River Publishers